UNCLASSIFIED

SECURITY CLASSIFICATION OF THIS PAGE *(When Data Entered)*

AD-A197 152

REPORT DOCUMENTATION PAGE		READ INSTRUCTIONS BEFORE COMPLETING FORM
1. REPORT NUMBER AFIT/CI/NR 88- 174	2. GOVT ACCESSION NO.	3. RECIPIENT'S CATALOG NUMBER DTIC FILE COPY
TITLE *(and Subtitle)* NONLINEAR EFFECTS IN PHOTOREFRACTIVE CRYSTALS		5. TYPE OF REPORT & PERIOD COVERED MS THESIS
		6. PERFORMING ORG. REPORT NUMBER
AUTHOR(s) DONALD ROSS ERBSCHLOE		8. CONTRACT OR GRANT NUMBER(s)
PERFORMING ORGANIZATION NAME AND ADDRESS AFIT STUDENT AT: UNIVERSITY OF OXFORK - U.K.		10. PROGRAM ELEMENT, PROJECT, TASK AREA & WORK UNIT NUMBERS
CONTROLLING OFFICE NAME AND ADDRESS		12. REPORT DATE 1988 13. NUMBER OF PAGES 199
14. MONITORING AGENCY NAME & ADDRESS*(if different from Controlling Office)* AFIT/NR Wright-Patterson AFB OH 45433-6583		15. SECURITY CLASS. *(of this report)* UNCLASSIFIED 15a. DECLASSIFICATION/DOWNGRADING SCHEDULE

16. DISTRIBUTION STATEMENT *(of this Report)*

DISTRIBUTED UNLIMITED: APPROVED FOR PUBLIC RELEASE

17. DISTRIBUTION STATEMENT *(of the abstract entered in Block 20, if different from Report)*

SAME AS REPORT

18. SUPPLEMENTARY NOTES

Approved for Public Release: IAW AFR 190-1
LYNN E. WOLAVER
Dean for Research and Professional Development
Air Force Institute of Technology
Wright-Patterson AFB OH 45433-6583

19. KEY WORDS *(Continue on reverse side if necessary and identify by block number)*

20. ABSTRACT *(Continue on reverse side if necessary and identify by block number)*

ATTACHED

DTIC
ELECTE
AUG 1 7 1988
S D
H

DD FORM 1 JAN 73 1473 EDITION OF 1 NOV 65 IS OBSOLETE

UNCLASSIFIED

SECURITY CLASSIFICATION OF THIS PAGE *(When Data Entered)*

NONLINEAR EFFECTS IN PHOTOREFRACTIVE CRYSTALS

By

Donald Ross Erbschloe

Merton College

Trinity Term, 1988

A THESIS

SUBMITTED FOR THE D. PHIL. DEGREE

AT THE UNIVERSITY OF OXFORD

The Department of Engineering Science

Parks Road

Oxford

'88 8 16 014

ABSTRACT

Donald Ross Erbschloe

Merton College

Thesis submitted for D.Phil. degree

Trinity Term 1988

NONLINEAR EFFECTS IN PHOTOREFRACTIVE CRYSTALS

Photorefractive crystals are materials whose index of refraction is altered under illumination by light. These crystals are both photoconductive and electrooptic. When a nonuniform light intensity pattern is present in the material, photocarriers are generated and redistributed, creating space charge electric fields which change the refractive index locally. These crystals are ideal media for real-time holography, and applications include wave amplification, image processing, phase conjugation, and laser beam steering for optical interconnects.

This thesis investigates many novel aspects of the photorefractive effect. A study of nonreciprocal behaviour identifies a new important consideration in the theory of two-wave mixing between counterpropagating beams—namely the presence of a photocurrent, or frequency detuning between the beams results in a spatially varying beam coupling. A numerical treatment of these important cases provides the first systematic theoretical assessment of the control of nonreciprocal transmission and phase shift in lithium niobate, a representative photorefractive crystal. A comparison between crystal types suggests candidates for nonreciprocal applications such as an optical diode.

A study of bismuth silicon oxide, $Bi_{12}SiO_{20}$, as the active gain medium in an oscillator reveals a novel feature, the presence of a light intensity threshold. For one crystal sample no oscillation occurred for incident intensities less than 0.8 mW/cm^2. A surprising new result is the appearance of higher diffracted orders in a crystal sample with a small wedge angle (0.036°) due to wave mixing between an incident beam and its first codirectional multiple reflection. Several applications for this new means of obtaining beam interaction are discussed—including the study of the photorefractive coupling for very large grating spacings, the investigation of transient phenomena, and laser beam steering.

A new gain mechanism for wave mixing in photorefractive crystals is verified experimentally using the unidirectional ring resonator and the linear resonator. The new mechanism depends on two, frequency detuned pump beams and off-Bragg coupling. A comparison with the traditional gain mechanism for wave amplification, using a single pump beam, reveals that the intensity of the oscillating beam with the new mechanism can be four times larger than with a single pump beam. We provide the first quantitative measurement of oscillation in the linear resonator using $Bi_{12}SiO_{20}$.

QUALITY INSPECTED 7

Justification
By
Distribution/
Availability Codes
Dist | Special
A-1

For

my grandfather: whose curiosity has never dimmed,

my father: who showed me the way,

and my son: who holds no wonder too small.

Acknowledgements

This thesis could not have been written without the love and support of my wife, *Vickie*, and my son, *Spenser*. They calmly endured my late nights, the absences while I was at conferences, my unpredictable schedules, and temperamental moods—from fretting to exhiliration. My mother and father, sisters, and grandparents gave me encouragement throughout, even when it seemed I did not have the time to thank them. My appreciation and love to them all.

It was an honour and a rare privilege to work jointly with *Dr. Laszlo Solymar* and *Dr. Tony Wilson*. I owe them a debt impossible to repay. I can only promise that when I teach again, I will strive to show my students the same patience, care, and enthusiasm they gave me. My mentor in the laboratory was *Dr. Jeno Takacs*. His insight saved the day on more than one occasion.

My thanks to all my fellow graduate students—a unique collection of extraordinarily talented individuals. The discussions and advice they gave focused my efforts considerably. Special credit goes to *Andrew Ward* and *Grahame Faulkner* for their expert technical help.

I would like to acknowledge my cherished friends *Kathy* and *Fred Roggero* and their daughters, *Mandy* and *Claire*, who shared so much with my family during our concurrent assignments to Great Britain. Thanks to *Dr. Gerry McCrum* and *Caroline McKinnon* for their warm friendship to these strangers in a strange land.

A deep debt of gratitude goes to *Judith Takacs* for her beautiful diagrams.

I would like to thank the United States Air Force, and particularly the US Air Force Academy, for the remarkable opportunity of studying at Oxford. I am grateful to Merton College (and *Dr. N. J. Richardson*) for the funds to attend a conference at Cambridge. Thanks as well to the Science and Engineering Research Council who funded the project on nonreciprocal effects.

Finally, my thanks to *Grace Slick*, *Linda Ronstadt*, and *Carlos Santana* whose music sustained me during the long and difficult nights of thesis writing.

Contents

Chapter 1

Introduction

A page of history is worth a volume of logic.

Oliver Wendell Holmes, Jr.

The driving mechanism for the optical properties of a crystal lies in the regular arrangement of its atoms or molecules. It seems natural that crystals should be used to investigate the character of light and vice versa. Perhaps this is why the evolution of optics is coincident with (indeed, often inextricably linked to) the study of crystals. The twentieth century has witnessed tremendous parallel advances in technology in the fields of optics and solid-state physics. Developments such as the laser and semiconductor devices have infiltrated and revolutionized everyday life. More than ever we exploit that which we purport to know.

In 1966 [5] an investigation of nonlinear optical properties of a crystal of lithium niobate ($LiNbO_3$) opened a new front of study—the photorefractive effect. This effect truly embodies the union of crystals and optics. In this process, as the name suggests, the refractive index is influenced by light. A photorefractive material exhibits both photoconductivity and the linear electrooptic effect. In fact the best photorefractive materials such as bismuth silicon oxide ($Bi_{12}SiO_{20}$) have moderate to large electrooptic coefficients, large photoconductivity parameters and low

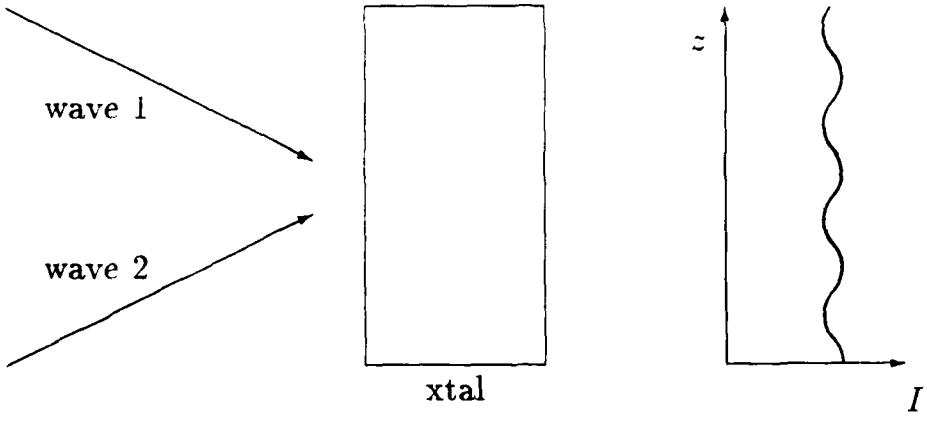

Figure 1: Intensity pattern created by two interfering sinusoidal waves.

dark conductivities. How a (semi-) permanent grating can be established in such a material is summarized below. If two monochromatic plane waves intersect as in Figure 1, an interference pattern is established in which the intensity, I, is modulated according to:

$$I(z) = I_0(1 + m\cos(Kz)) \tag{1}$$

where I_0 is the total intensity, K is the length of the grating vector formed by the two mixing waves and m is the intensity modulation ratio. If this space-varying sinusoidal intensity pattern falls upon a photorefractive crystal the following processes occur. These materials are semiconductors so where the irradiance is high, electrons from donor atoms are excited into the conduction band. By either drift or diffusion the free electrons move to darker regions where recombination occurs. The electrons may recombine and be re-excited many times before final trapping occurs. Motion of charge carriers will eventually reach an equilibrium when drift and diffusion effects are balanced by internal fields caused by space charge effects. A modulated charge density builds up inside the crystal, mimicking the modulated intensity pattern. The success of the imitation will depend on a number of features, such as drift and diffusion lengths, strength of applied field, etc., and in the steady

state manifests itself in a phase mismatch angle Φ_g between the intensity fringes and the charge concentration. The gradient of the charge density expresses the space charge electric field associated with it. This field will vary sinusoidally in space and through the linear electrooptic effect, the index of refraction is modulated and a grating is formed.

This grating is a phase hologram [115]. A hologram uses a reference and an "object" beam to create an interference pattern. This interference pattern, which is stored in the recording medium, contains phase and amplitude information about the two "writing" beams. If the hologram is replayed by the reference beam alone, part of the reference is diffracted and reconstructs the object beam. We may consider this *static* or *stationary* holography, and this describes the situation for steady-state wave-mixing in photorefractive materials. However, to reach steady-state we must first go through a complicated *dynamic* process. The writing beams undergo diffraction as the grating is being formed thus the hologram is being written and read at the same time. These diffracted beams also contribute to the interference field and so hologram formation exhibits a wealth of transient effects before settling down to equilibrium.

The interest and effort into the study of photorefractivity has grown steadily in its 22 year history. Only a handful of articles and papers appeared on the subject in the late 1960's. Now such publications as *Physics Reports* (1982), *The Journal of the Optical Society of America* (February 1986), and *The IEEE Journal of Quantum Electronics* (August 1986, December 1987) devote issues to it. Photorefractivity even merits special dedicated conferences such as a 1986 Meeting on Progress in Scientific Culture at Erice, Sicily and the July 1987 Los Angeles meeting of the Optical Society of America.

There is more to the utility of photorefractive materials than just as erasable, real-time media in which to store display holograms. These materials are optically nonlinear, which means the polarisation of the medium is not strictly proportional to an applied electric field. (It is an unfortunate consequence of an overly useful

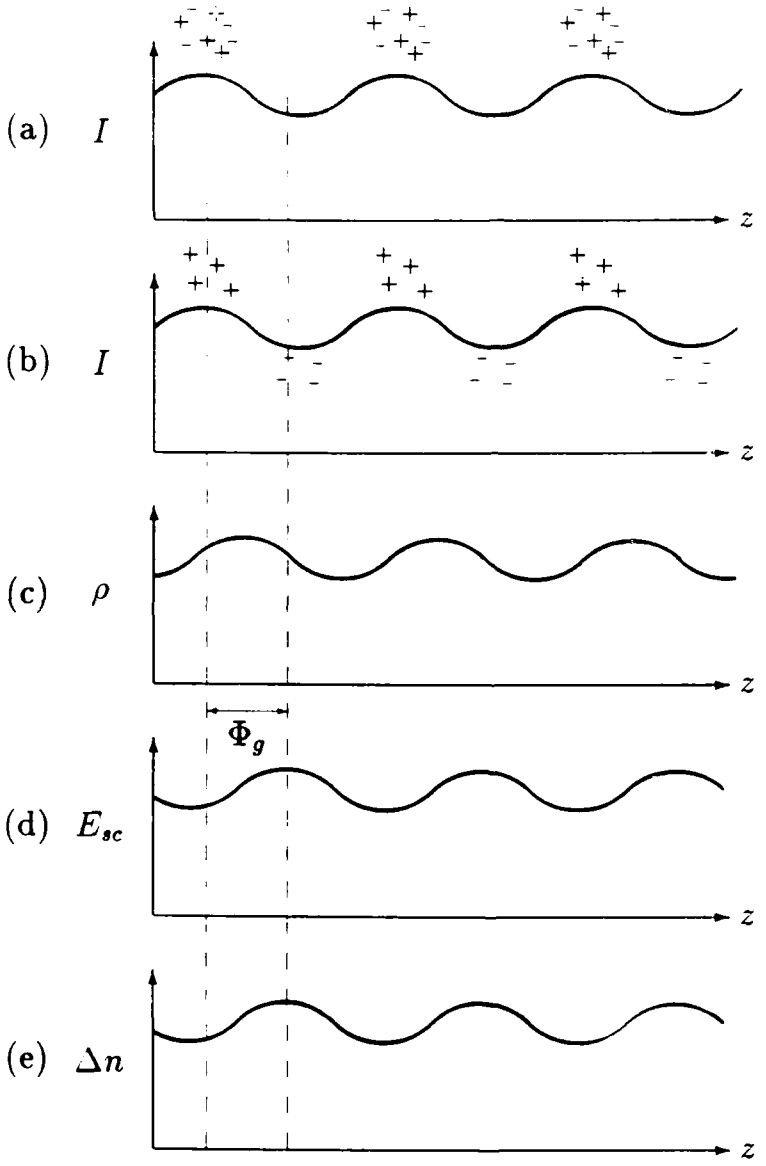

Figure 2: Photorefractive grating formation: (a) Carrier photogeneration. (b) Drift, diffusion and trapping of carriers. (c) Space charge distribution. (d) Space charge electric field (gradient of space charge distribution) may be out of phase, Φ_g, with intensity. (e) Modulated refractive index (via electrooptic effect.)

term like "linear" that the coefficients of the *linear* electrooptic effect can be directly related to the second-order optical *nonlinear* susceptibility coefficients. [135]) Two- and four-wave mixing in photorefractive materials yield such nonlinear phenomena as energy exchange between the interacting waves [76], phase conjugation [24], and nonreciprocal effects [140].

As we approach the twenty-first century our information-hungry society demands more and more from its technologies. There is a never ending quest for faster computers and improved and increased communications capability. Optical engineering has become an important arena for priority research. Much of the early thrust of this research was to develop optical analogues of electronic components such as switches (bistable optical devices [111]), optical diodes [86], and logical gates [80], but increasingly, applications aim at areas where optics has inherent strengths, for example parallel processing in associative memories [26] and neural networks [81]. Photorefractive materials are versatile and figure prominently in many proposed schemes for the devices mentioned.

Before we discuss studies of photorefractive crystals, it is worthwhile to review their place in the history of crystal optics.

1.1 History of Crystal Optics

Crystals were certainly known and valued to the ancients in the forms of gems and precious stones. The first scientific mention of the regular shape of a crystal (garnet) appears in Theophrastus' (372-287BC) *Concerning Stones* [32]. To the geographer Strabo (63BC- 24AD), pieces of quartz were so reminiscent of ice that he proposed a common origin. Thus our word "crystal" comes from his description "$\kappa\rho\upsilon\sigma\tau\alpha\lambda\lambda\omicron\sigma$". It means "to freeze, or to congeal with frost" [1]. Pliny the Elder propagated this myth in his marvelous compendium of misinformation, *Natural History*. However, he did note the characteristic six angles of quartz crystals [10].

The ice-crystal explanation dominated until the 18th century. In this regard

Strabo's view was to crystals what the Aristotalean view was to mechanics -- and nearly as long-lived. One of the more eloquent expressions of the theory comes from John Wycliffe (1320-1384) [1]

> When the colde northwynde bloweth harde Christall cometh of the water

As with Aristotalean dynamics, though, there were a few dissenting voices through the centuries. Agricola (Georg Bauer, 1490-1555) dismissed the idea of frozen crystals as he noted the presence of crystalline materials near Hecla, an active volcano [101]. The fact that if crystals were a form of ice it was different from typical water-ice was mentioned by Robert Boyle (1627-1691). Essentially his argument was that if one dropped a crystal and a piece of ice into some water there will be a difference. The crystal will not float. A charming refutation of the then-current hypothesis of crystals from frozen dew appears in *Philosophical Transactions* in 1672. P. Francisco Lana, while travelling in Italy, was given some six-sided crystals found exclusively in some narrow crevices in a large meadow. "I was told, that they were produced from the dews, because (forsooth!) being gather'd over night, the next morning there would be found others at such a time only, when it was a serene and dewy sky . . . ." To Lana's credit, he argued [82]

> It therefore ought not to be affirm'd, that a dewy vapour is of it self able to be form'd into a solid gem; because, if that were so, such vapours being easily carried by any motion of the Air from those narrow places, and falling down in dew far from the same, Crystals would be formed in those other places.

In 1669 Steno (Niels Stenson, 1638-1686) set down the law of constancy of interfacial angles for quartz. This law was extended in the classification hundreds of types and shapes of crystals by such researchers as Dominic Guglielmi and Jean Baptiste Rome Deslisle [32]. Strabo's simple concept was no longer adequate to explain this complicated situation. The ice theory melted into oblivion.

If crystals weren't ice, what were they? Robert Hooke (1635-1703) spectulated in his *Micrographia* that crystals are ultimately composed of spherical particles [51].

> . . . all these regular features arise onely from three or four several positions or postures of globular particles . . . and this I have ad oculum demonstrated with a company of bullets and some few other simple bodies . . . even almost by shaking them.

It was a fortuitous accident which established the science of crystallography. Rene Just Haüy (1743-1822) dropped and broke one of a group of calcite crystals belonging to a friend. He noticed that the fragments had the same characteristic rhomb shape. According to Bishop [10],

> After breaking up many more calcite crystals of differing external shapes he concluded that all were composed of a repetition of a minute structural unit . . . called integrant molecules.

(Presumably he first asked his friend's permission, else this is an example of experimental science at its most callous.)

In the 19th century the study of crystal structure passed on to the mathematicians with research into crystal classes and group theory. Experimental work was left to the study of interactions of light with crystals. As early as 1669, Erasmus Bartholinus (1625-1698) observed double refraction in Icelandic feldspar [9]. In trying to explain this phenomenon, Christian Huyghens (1629-1695) discovered the polarisation of light. Further advances in study of polarised light in crystals were made by David Brewster [13] (1781-1868) and Etienne Louis Malus (1776-1812), culminating in the discovery in 1816 that two rays polarised at right angles will not interfere. This definitive demonstration that light waves are transverse was made by Augustin Jean Fresnel (1788-1827) and Dominique Jean Francois Arago (1786-1853) with the explanation coming from Thomas Young (1773-1829). Fresnel worked out the details of wave propagation in crystals, a feat which Born and Wolf call "one of the greatest achievements of natural science" [11].

Polarisation of light is easily demonstrable and it appealed greatly to the most eminent popularizer of science in the 19th century, Micheal Faraday (1791-1867). In the 1840's he conducted a series of experiments investigating the influence of electric and magnetic fields on light. He discovered the Faraday effect (a non-reciprocal rotation of the polarisation axis in a crystal subjected to a magnetic field) in 1845 [33] but failed to find a comparable effect using an electric field. It took until 1875 and better laboratory equipment for this latter observation. In that year John Kerr (1824-1907) demonstrated the quadratic electrooptic effect[68], a change in the refractive index proportional to the square of the applied electric field. The linear electrooptic effect followed in 1893 from the studies of Friedrich Carl Alwin Pockels (1865- 1913) [50].

For centuries crystals had been used to divulge the properties of light. The history of light and crystals comes full circle in 1912 when light in the form of X-rays was used to investigate the fundamental nature of crystals. The classic experiment exhibiting X-ray diffraction was suggested by Max von Laue and performed by W. Friedrich and P. Knipping. Using Laue photographs produced by a sodium chloride crystal, the father-son team of W.H. and W.L. Bragg ascertained its structure. The thorough (and personal) history of the early years in X-ray diffraction is told in chapter 12 of the Braggs' classic text *The Crystalline State* [12].

A resurgence in interest in crystals came with this new technology. The timing was right for the 1920's saw the first stirrings of quantum mechanics. An early success of the theory was the discovery that a periodic potential function leads to allowed energy states in the form of bands [124]. This finding helped explain electrical conduction, and led to the ultimate exploitation of semiconductors.

1.2 History of the Photorefractive Effect

In 1966, Ashkin, Boyd and their group of co-workers at Bell Telephone discovered "optically-induced refractive index inhomogeneities" in crystals of lithium niobate

($LiNbO_3$) and lithium tantalate ($LiTaO_3$). Because of their known nonlinear optical properties, the crystals were being tested in applications such as second harmonic generation and as electrooptic modulators. Exposure of the crystals to focused or unfocused visible laser light created nonuniform changes primarily in the extraordinary refractive index. If left alone there was some relaxation of the change, but effects would still persist for days or months. Heating the crystal ($\approx 170°$ C) accelerated the restoration of the crystal to the neutral state. They surmised that the electrooptic effect could explain the index change but a more fundamental mechanism was needed to explain the fields required to induce the electrooptic effect. Among the mechanisms suggested were pyroelectricity (a spontaneous polarization due to a temperature change), microdomain reversals, or a change in the structure of the crystal cell [5].

Chen found in 1967 that potassium tantalate niobate (KTN) suffered laser induced "damage" as well. In his experiment a crystal was illuminated with 633 nm He-Ne laser light while a transverse external electric field was being applied. Chen felt a long-lived space charge field could be established by the drift of photoexcited electrons from traps in the illuminated area and their subsequent recapture in traps in darker regions [18]. In a later paper, Chen, LaMacchia and Fraser demonstrated the ability of this "optical damage" in recording a volume hologram inside lithium niobate. The crystal had excellent resolution properties, greater than 1600 lines/mm [20]. No applied field was necessary and the question as to the driving mechanism of photoexcited carriers in lithium niobate became important. Johnston in 1970 claimed that a type of spontaneous polarisation similar to the pyroelectric effect was responsible [63]. This idea appealed to Townsend and LaMacchia who created volume holograms using barium titanate ($BaTiO_3$) [125]. Chen likened the effect to persistent internal polarisation [19], an effect well known in ferroelectric materials in which strong internal fields could last for days after space charge fields were established by using radiation to excite electrons which can then drift out of the irradiated area and be trapped [66].

In 1971, Amodei reported that thermal diffusion could account for the motion of excited free carriers [3]. Later that year he and co-author, Staebler, published a classic paper in which Kogelnik's coupled-wave theory was applied to hologram writing and reading. Both diffusion and drift of carriers were considered. They also predicted a one-way energy transfer between recording beams [119].

With this 1971 paper, a coherent picture of what was later to be called the photorefractive effect began to emerge. (The earliest reference I have found in which the term "photorefractive" is used is in a 1976 article by Magnusson and Gaylord [87].)

The 1970s saw tremendous refinements to the physical picture of the photorefractive effect and the development of a powerful predictive theory. Ninomiya was the first to consider dynamic processes in hologram formation. He considered the index modulation as being linear with the exposure (the time-average of the irradiance) [95]. Magnusson and Gaylord tested Ninomiya's theory experimentally with the result that they qualtitatively verified many predictions of the theory (i.e., such as rapidly varying writing and reading results which previous authors had taken as "experimental problems"). They suggested coupling experiment with theory to diagnose material parameters of recording media [87]. Vahey used an approach similar to Ninomiya, but considered the index modulation as being proportional to the writing irradiance multiplied by an arbitrary time dependent function. He also succeeded in deriving an expression for diffraction efficiency (how much of the reading beam is diffracted by the grating) of the hologram [127]. Kim et al. considered feedback between the space charge field and the free electron density and thus were pioneers in the incorporation of materials effects in the dynamic theory. However they did not consider how the feedback would affect the writing beams [69]. This oversight was included in the work of Moharam and Young who also included the photovoltaic effect [93], an internal electric field which can drive an intensity-dependent photocurrent [41]. 1979 saw the publication of the two most successful theories to date, theories which looked closely at material properties. Feinberg et

al. proposed the hopping model in which charges are fixed to certain sites in the dark, but under illumination can move to neighboring sites with an irradiance dependent probability. This approach had very good success in describing effects seen using $BaTiO_3$[36]. The most general theory, and the one most favoured today, is from Kukhtarev et al. [77,76]. Chapter 2 will review the important equations and provide an example of their theory.

1.3 Applications of Photorefractive Materials

It would be impractical to present an exhaustive list of proposed applications for photorefractive materials here. As Eichler noted in his introduction to the special issue on "Dynamic Gratings and Four-Wave Mixing" in the *IEEE Journal of Quantum Electronics* in 1986, "...more than 500 papers have been published up to 1985" [29]. Our time would be better spent cataloguing areas of suggested uses with references to one or two representative papers.

The first division of applications is that of static (storage or display) versus dynamic (real-time) holography. Certainly the first proposed use for a photorefractive material, ($LiNbO_3$), was as a medium in which to store holograms. A reasonable question to ask is how equal are they to this task? The answer, as it so often is in science, is "that depends". It depends on what type of crystal we are discussing. Some crystals, such as $Bi_{12}SiO_{20}$ and $Bi_{12}GeO_{20}$, are very sensitive to light and are very quick (grating writing times for moderate ($\approx$ 10 mW/cm^2) intensities are on the order of milliseconds). They compare favorably with high resolution photographic plates, but suffer from short storage times (20–30 hours) [54]. Other crystals, like $LiNbO_3$ and $LiTaO_3$, respond in seconds to minutes, but have much longer storage times (1-10 years) [44]. The benefit with photorefractives, of course, is that you have a self-developing, erasable medium. However it is possible to "fix" the holograms in these crystals by writing the hologram at a high temperature (160°

C) and reading it at room temperature. Staebler, et al. estimate that the resulting storage time for a fixed hologram in $LiNbO_3$ is 10^5 years. Because these are volume holograms, the angular selectivity is very strong—one must be very near to Bragg conditions for high efficiency [115], one can store many holograms in the same crystal by slightly altering the angle with each exposure. In one experiment a whopping 500 holograms were recorded in a single, 2 mm thick sample of $LiNbO_3$. Each hologram had a diffraction efficiency of 2.5% or better [120]. As promising as these results sound, very few papers appear nowadays on holographic storage in photorefractives—perhaps the feeling is that all the work possible on this subject has been done, or the cost of materials (a 1 cm^3 cube of $Bi_{12}SiO_{20}$ sells, typically, for £500) is too high.

In dynamic holography we take advantage of the ability to simultaneously write and read a hologram in a photorefractive material. A useful way to characterise dynamic applications is by the number of interacting waves.

In wave mixing, as in an argument, the minimum number required to produce interference is two. The simplest case is when the writing beams are uniform plane waves and, as we have already discussed, this creates a sinusoidal diffraction grating. The process works just as well if one of the beams has temporal or spatial distributions, and two-wave mixing has been used to generate real-time interferograms. An interferogram is a means of measuring the relative spatial displacement between two surfaces. Departures from parallelism result in bright and dark fringes: dark where the separation is a half-odd multiple of the wavelength, corresponding to destructive interference; and bright where the interference is constructive. You can use the same surface if you superimpose two images taken at different times, which is particularly useful if your object of interest is vibrating. As mentioned above the response time in $Bi_{12}SiO_{20}$ can be on the order of milliseconds. If the period of the vibrating object is much less than this response time, the mixture of the object beam and reference beam produces a continuous interferometric pattern [54,67]. In $LiNbO_3$, where the response time is much longer, it is more convenient

to use the crystal as a storage hologram and make a double exposure interferogram [88].

Two-wave mixing in photorefractives generally involves power transfer. In Chapter 2 we will discuss this phenomenon in great detail, but we should mention here that in $Bi_{12}SiO_{20}$ this transfer can be dramatically increased if there is a slight difference in frequency between the waves (detuning typically of a few hundred Hertz). Thus we can use two-wave mixing to amplify weak signals. In $Bi_{12}SiO_{20}$ gains of 10^3 and in $BaTiO_3$ gains of $4x10^3$ have been reported [109,126]. This suggests using photorefractive materials for laser beam steering. In this scheme a crystal is illuminated with a strong, uniform pump beam. A weak probe beam (frequency shifted if necessary) is turned on in the required direction. The large amplification of this beam essentially redirects part of the pump beam in the desired orientation [108].

We have discussed how to form a holographic grating with an object and a reference wave. A third wave can be diffracted off this grating and, if it is sufficiently intense and near the same wavelength, may interact and contribute to the dynamic diffraction process. Of particular interest is when the third beam is counterpropagating to the reference beam. Then part of the third beam will be diffracted from the original grating *from behind.* This diffracted beam runs counter to, and retraces the path of, the object beam. Its phase is the reverse of the object beam. This latter property gives the diffracted beam its name—a phase conjugate. It has been likened to time reversal [133].

Although we started with three beams, we ended up with four, so this scheme falls under the category of four-wave mixing. The arrangement described above which produces a phase conjugate wave is often labelled a phase conjugate mirror (PCM). These mirrors are characterised by a threshold [70]. Any sufficiently intense beam incident on the PCM produces a reflected conjugate beam. (In analogy with a classical mirror, the conjugate is the "reflected wave". However, considering the conjugate's turn tail character, perhaps, the term "retreating wave" is more apt.)

It is possible for a single input beam to generate a phase conjugate. The photorefractive crystal can act as the gain medium in a linear resonator. Optical noise from the input can be captured and amplified in the resonator, creating the required counterpropagating beams [131]. An even more intriguing arrangement is the CAT mirror (named for the discoverer's pet feline, whose portrait ignominiously was aberrated for the experiment) using $BaTiO_3$, in which internal reflections provide all the necessary beams [37].

Phase conjugate mirrors play important roles in a wide variety of applications. We can use their phase reversing properties to clean up beams from unwanted aberations [21] or compress frequency dispersed pulses in optical fibres [99]. Since the amplitude of the conjugate wave is related to the product of the amplitudes of the other three mixing waves, PCMs are useful for image processing tasks such as image division [60], image subtraction [80], intensity inversion [132] or edge enhancement [35]. The thresholding property of PCMs can be used for correlation [40] and associative memories [134].

The response time of photorefractives is proportional to the incident intensity. Very intense pulses can be used to write gratings on nano- or even pico-second time scales [83,114]. Thus some of the applications discussed in this section may be possible on ultra-fast time scales. The limitation is the ability of the crystal to dissipate the power. For pulses of gigawatt instantaneous power, the repetition frequency must be no higher than a few Hertz [138].

1.4 Outline of the Thesis

Our exploration of photorefractivity begins in Chapter 2 with a discussion of the theory describing two-wave interactions. This comparatively simple case is the springboard to more complicated geometries, and the recipe we develop to handle it will serve us well in later chapters.

Two-wave mixing in photorefractive crystals has been studied for nearly twenty

years and one might think that there are no new wrinkles to the problem. We can classify these interactions in terms of the grating spacing of the mixing beams (a small interbeam angle means a large grating spacing and vice versa). Certainly the range of grating spacings from submicrons up to 100 microns has been studied (see for example J.M. Heaton's D.Phil. thesis [49]). However, in Chapter 3 we bring up important considerations for the case of counterpropagating beams (grating spacing equals one half wavelength — the smallest possible length), and explore nonreciprocal effects.

With Chapter 4 we lean towards the other extreme of the grating spacing scale. Significant gain is possible in $Bi_{12}SiO_{20}$ for large (10-50 microns) grating spacings with moving intensity fringes. We use this effect in a unidirectional ring resonator. At these large grating spacings, conditions are favourable for energy transfer to higher diffracted orders.

Chapter 5 describes theory and experiments involving a new mechanism for gain in photorefractive materials. This amplification depends on off-Bragg coupling and is more efficient in many cases than our stalwart gain mechanism derived in Chapter 2.

The production of higher diffracted orders is investigated in Chapter 6 using a novel techninque–we take advantage of a very slight wedge angle in a crystal sample. Two-wave mixing is provided by a single incident beam and its nearly coincident internal reflection.

We finish up with conclusions, suggestions for future work, and some relevant appendices.

Chapter 2

Two-Wave Mixing in Photorefractive Crystals

"The revelation came to me while doing homework on partial differential equations. I was a junior and I had to calculate the torsional modes of vibration in a metal beam. That was when I realized that solving a differential equation gives you a feeling of accomplishment, but not one of justice."

"Then you were doing it wrong, son."

"The Paradoxical Case of the Relativity Twins"

To create a dynamic holographic grating in a photorefractive material three processes must occur.

1. Transport of photoinduced carriers.

2. Modulation of the refractive index via the linear electrooptic effect.

3. Diffraction of the writing beams as the grating forms.

The first process can be described in terms of materials equations; the second is worked out by considering the electrooptic tensor; and the third is specified by field equations. In this chapter we adopt the strategy of divide and conquer—each

process will handled separately. This makes the problem much more tenable and allows the luxury of pausing occasionally to discuss the physics involved. By the end of the chapter we will have derived an expression for power transfer for two-wave mixing and we will consider means to control and optimize this effect.

Two-wave mixing is fundamental to understanding the whys, hows and wherefores of the photorefractive effect. The interaction of several waves often can be reduced to a linear combination of mixing of all the possible pairs of waves.

2.1 The Materials Equations

One of the most quoted papers dealing with photorefractivity appeared in two parts in *Ferroelectrics* in 1979. N. V. Kukhtarev and his coworkers [77,76] laid down a consistent framework of materials equations describing the generation and recombination of charge carriers, their transport in the form of a current density, and the establishment of a space charge field.

2.1.1 The rate equations

In this band transport model charge carriers are liberated from fixed donor sites in the bandgap. Thus one way to monitor the carrier concentration, n, is to consider the ionized donor density, N_D^+ (here we assume an n-type semiconductor). (There are also negatively charged traps, whose concentration is given by N_A^-—this will appear in a later equation.) These ionized donors act as traps for unwary carriers and thus both n and N_D^+ can be depleted.

The first materials equation describes the time rate change of N_D^+.

$$\frac{\partial N_D^+}{\partial t} = (sI + \beta)\left(N_D - N_D^+\right) - \gamma_r n N_D^+ \tag{1}$$

The first term on the right hand side of the equation is the creation term. There are two avenues of increasing N_D^+: photo- or thermal generation. s is the photoionization constant, I is the driving light intensity and β is the thermal generation

coefficient. Note that the production of ionized donors is proportional to the density of un-ionized donors ($N_D - N_D^+$).

The second term describes recombination. γ_r is the recombination coefficient, and we see the depletion of N_D^+ is proportional to the *product* of the carrier and trap densities. This means the recombination term is nonlinear.

The donor sites are fixed. Whenever a photon or a phonon begets an ionized donor a charge carrier is produced. But the charge carriers are mobile— there is an additional process by which the carrier density can change. That is via a current density. Our second materials equations is:

$$\frac{\partial n}{\partial t} = \frac{\partial N_D^+}{\partial t} - \frac{1}{e}\nabla \cdot \vec{J} \tag{2}$$

This equation should look familiar to anyone well versed in electromagnetic theory. It is the continuity equation, where e is the unit electric charge and $\vec{J}$ is the current density. It is a statement of the conservation of charge.

2.1.2 The current density

The flow of a current requires some agent to move the charges. Our third materials equation considers three possible processes:

$$\vec{J} = \mu e n \vec{E}_s + \vec{p} I \left(N_D - N_D^+\right) - \mu k_B T \nabla n \tag{3}$$

The first two terms on the right hand side of the equation are drift current densities. The first is due to a space charge electric field, E_s, which we allow to include any background field due to an applied voltage. Here μ is the carrier mobility. The second term is a photovoltaic drift current density which is proportional to the intensity and the density of un-ionized donors. The constant of proportionality is the photovoltaic coeffcient, p.

The final term is the diffusion current density, which depends on the gradient of the carrier concentration. Here k_B is Boltzmann's constant and T is the absolute temperature.

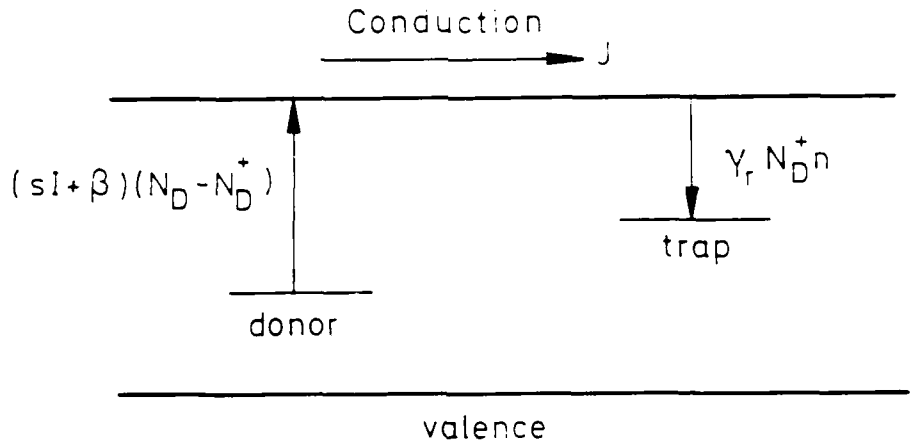

Figure 1: Band transport model: Generation, transport and trapping of n-type charge carriers. Donors and traps lie in the bandgap between the conduction and valence bands.

Fig. 1 summarizes the first three materials equations. In photorefractive ferroelectric crystals, such as $LiNbO_3$ and $BaTiO_3$, the donor and trap sites are impurities, mainly transition metals such as Fe, Cu and Mn [72,71]. In Fe doped $LiNbO_3$, for example, the charge transport occurs between Fe^{2+} and Fe^{3+} [73]. The donor sites in $Bi_{12}SiO_{20}$ crystals are silicon vacancies that lie 2.6 eV below the conduction band (the band gap energy is 3.25 eV [52]). The nature of the traps in $Bi_{12}SiO_{20}$ is not well understood, but they lie 0.6 eV below the conduction band. Luminescence centres (2.25 eV below the band when occupied by an electron, 1.3 eV when not occupied) may also contribute to charge transport [44].

2.1.3 The space charge field

Our last equation is Poisson's equation. The divergence of the space charge field is related to the charge density.

$$\nabla \cdot \vec{E}_s = \frac{e}{\epsilon_s}\left(N_A^- + n - N_D^+\right) \tag{4}$$

ϵ_s is the permittivity of the medium and N_A^- is an ionized acceptor density. The presence of ionized acceptors is necessary to insure charge neutrality because we will assume, for most practical cases, $N_D^+ \gg n$. That is, in a Fourier expansion of N_D^+ and n, the coefficients obey $N_{D_i}^+ \gg n_i$ where i is an index. Normally we take this expansion out to first order.

2.1.4 Simplifying assumptions

In theory we could apply any driving intensity, I, to Eqns 1-4 and find the resulting space charge electric field, E_s. (That is our goal, for this is the field which will modulate the refractive index through the electrooptic effect.) In practice, though, our first step is to reduce the complexity of the equations by making some simplifying assumptions. Here we list each assumption and briefly discuss its validity.

1. *There is only one species of charge carriers.* Implicit in the statement of the Kukhtarev model is that only one type of charge carrier, electrons or holes, is involved in the transport process. Orlowski and Krätzig have demonstrated that the transport of both holes and electrons is deleterious to photorefractivity [100]. However, simultaneous electron/hole transport does occur in Fe-doped $LiNbO_3$[130] and $BaTiO_3$[71]. The acceptor/donor concentration ratio (Fe^{2+}/ Fe^{3+}) can be controlled during the crystal growth process, and this ratio determines, to a large extent, the relative contributions of the electrons and holes to photoconductivity. Thus by judicious doping one can regain single charge carrier status. Valley [128] and Strohkendl, et al. [123] independently have developed charge transport models for the presence of both electrons and holes. These models are based on Kukhtarev's theory and contain similar expressions of Eqns 1-3 for holes. Valley considered two cases—one in which the recombination/donor centres are the same for holes and electrons, and one in which they are different. In $Bi_{12}SiO_{20}$ electron transport dominates, while in $Bi_{12}GeO_{20}$ either holes or electrons govern photoconductivity [102].

2. *Thermal generation of carriers is negligible.* The justification for this assumption comes from the low dark conductivities of most photorefractive crystals [44]. Our own measurements of dark current in $Bi_{12}SiO_{20}$ (applied voltage but no illumination) gave values typically in the picoamp range, while with moderate incident intensities ($\approx$ 10 mW/cm^2) the current rose to microamps. Thermal generation in Eqn 1 can be neglected except for very low light intensities.

3. *The carrier density, n, is negligible compared with the ionized donor density, N_D^+.* Several authors have measured trap densities in photorefractive crystals. In $LiNbO_3$[16], $BaTiO_3$[36], and $Bi_{12}SiO_{20}$[94] the densities are on the order of magnitude of 10^{22} m^{-3}. Carrier densities are usually much lower than this. For example, a uniform illumination of 100 mW/cm^2 in $Bi_{12}SiO_{20}$ produces a carrier density of $\approx$ 2 x 10^{17} m^{-3}. Thus $N_D^+ - n \approx N_D^+$.

4. *The ionized donor density, N_D^+, is negligible compared with the donor density, N_D.* Here again measurements provide the justification. In $Bi_{12}SiO_{20}$, N_D is on the order of 10^{25} m^{-3} [109], while in $LiNbO_3$ it is 10^{23} m^{-3} [16]. Therefore $N_D - N_D^+ \approx N_D$.

5. *The ionized acceptor density, N_A^-, is constant.* Ionized acceptors must be present to offset the initial ionized donor density to insure charge neutrality. We assume these acceptors play no active role in the charge transport process.

2.1.5 The driving light intensity

Consider the intensity pattern formed by the superposition of two waves of nearly the same wavelength as shown in Fig. 2a. This is referred to as nearly degenerate two wave mixing. The grating vector (the spatial angular frequency of the intensity pattern) is seen in Fig. 2b.

$$I(\vec{r}) \sim |E_+ e^{j(\omega_+ t - \vec{k_+}\cdot\vec{r})} + E_- e^{j(\omega_- t - \vec{k_-}\cdot\vec{r})}|^2 = I_0 + I_1 e^{j(\delta\omega t - \vec{K}\cdot\vec{r})} + c.c. \qquad (5)$$

where $I_0 = I_+ + I_- \sim |E_+|^2 + |E_-|^2$ is the background intensity, $I_1 = \sqrt{I_+ I_-}$ is the modulated intensity, $k_{+/-} = 2\pi/\lambda_{+/-}$ is the $+/-$ wave vector, with $\lambda_{+/-}$ the

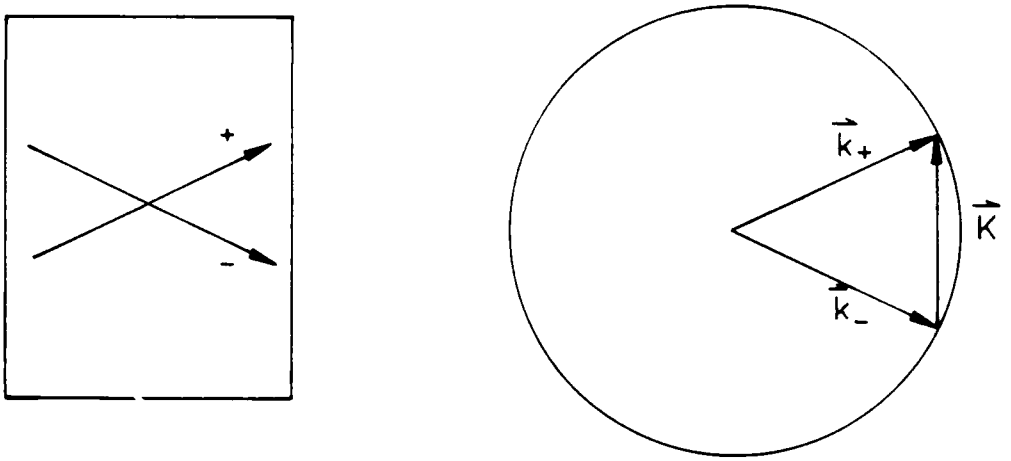

Figure 2: Two-wave mixing. (a) The waves inside the medium. (b) The grating vector in reciprocal space.

wavelength in the medium, $|\vec{K}| = |\vec{k_+} - \vec{k_-}| = 2\pi/\Lambda$ is length of the grating vector with Λ the grating spacing, $\delta\omega = \omega_+ - \omega_-$ is the frequency detuning, and *c.c.* means complex conjugate. For $\delta\omega \neq 0$ this intensity pattern consists of sinusoidal fringes moving with velocity $v = \delta\omega/K$. It is common practice to set up a coordinate system in which $\vec{K}$ is parallel to one of the axes, say z, so $\vec{K} \cdot \vec{r} = K\,z$. This total light intensity will drive the materials equations.

At this point it is convenient to introduce normalized quantities for n, N_D^+, E_s, and J. Experience shows that this will save a lot of algebra later. With our simplifying assumptions our normalized materials equations may be written:

$$h\frac{\partial N_n}{\partial t} = \left(1 + m\,e^{jK(vt-z)} + c.c.\right) - \frac{1}{n_{na}} n_n N_n \tag{6}$$

$$\frac{\partial N_n}{\partial t} = \mu E_q \nabla \cdot \vec{J}_n \tag{7}$$

$$\vec{J}_n = n_n \vec{E}_n + n_{na}\frac{\vec{E}_p}{E_q}\left(1 + m\,e^{jK(vt-z)} + c.c.\right) - \frac{1}{K}\frac{E_t}{E_q}\nabla n_n \tag{8}$$

$$\frac{1}{K}\nabla \cdot E_n = 1 - N_n \tag{9}$$

where our normalized quantities are $N_n = N_D^+/N_A^-$, n_n =n/N_A^-, $E_n = E_s/E_q$, J_n= $J/\mu e N_A^- E_q$. The constants are $h = N_A^-/sI_0N_D$, $m = I_1/I_0$, $n_{na} = h/\tau_r$, $\tau_r = 1/\gamma_r N_A^-$. The characteristic electric fields are $E_q = eN_A^-/\epsilon_s K$, $E_t = k_BTK/e$, $E_p = p\gamma_r N_A^-/se\mu$.

The next step is to assume the solutions to Eqns 6-9 are driven by I and thus have the same general functional form.

$$F_n(z,t) = F_{n0} + F_{n1}e^{jK(vt-z)} + c.c. \tag{10}$$

Note we assume steady-state conditions for the coefficients F_{n0} and F_{n1}. These are the first two coefficients in a spatial Fourier series. We will take the directions of $\vec{E}_n$, $\vec{E}_p$ and $\vec{J}_n$ to be $\hat{z}$, i.e. parallel to $\vec{K}$.

There is one more obstacle to overcome. Eqns 6 and 8 are nonlinear (they contain the terms n_nN_n and n_nE_n). To overcome this difficulty we invoke linearization. We assume the amplitude of the first order term is much smaller than the amplitude of the zero order term. This is a reasonable assumption if the intensity modulation is very small ($m \ll 1$). Then we may ignore products of first order terms. Making the substitutions of Eqn 10 and applying linearization, we next equate coefficients of the static (d.c.) and exponential (a.c.) terms. This gives us eight equations and eight unknowns.

2.1.6 The d.c. equations

$$n_{n0} = n_{na} \tag{11}$$

$$N_{n0} = 1 \tag{12}$$

$$J_{n0} = n_{n0}E_{n0} + n_{na}\frac{E_p}{E_q} \tag{13}$$

$$E_{n0} = \frac{E_{s0}}{E_q} \tag{14}$$

Here E_{s0} is the static electric field due to any applied voltage.

2.1.7 The a.c. equations.

$$m = \frac{1}{n_{na}}n_{n1} + (1 - jKvh)N_{n1} \tag{15}$$

$$N_{n1} = -\frac{\mu E_q}{v}J_{n1} \tag{16}$$

$$J_{n1} = n_{na}E_{n1} + \left(E_{n0} - j\frac{E_t}{E_q}\right)n_{n1} + n_{na}m\frac{E_p}{E_q} \tag{17}$$

$$E_{n1} = jN_{n1} \tag{18}$$

2.1.8 The modulated space charge field

Our goal was to find the modulated space charge field, E_{s1}, and we now have the means. The following method works well. From the a.c. equations eliminate J_{n1}, then n_{n1}, and lastly N_{n1}. The final result is:

$$E_{s1} = -mE_\omega \tag{19}$$

$$E_\omega = \frac{E_{s0} + E_p - jE_t}{1 + \frac{E_t}{E_q} + b\frac{E_{s0}}{E_m} + j\left(\frac{E_{s0}}{E_q} - b(1 + \frac{E_t}{E_m})\right)} \tag{20}$$

where $E_m = \gamma_r N_A^- / \mu K$, $b = Kv\tau_d$ and $\tau_d = \epsilon_s \gamma_r N_A^- / e\mu s I_0 N_D$ is the dielectric relaxation time.

We will defer a full discussion of the physical meaning of Eqn 20 until later in the chapter when we have worked out the rest of the photorefractive process. We should notice, however, that E_{sc} is directly proportional to the intensity modulation, m, and it is complex. This means the field can be out of phase with the intensity pattern. This is what we dubbed the phase mismatch angle, Φ_g, in Fig. 2 in chapter 1.

2.2 The Linear Electrooptic Effect

The next question to ask is what influence the space charge field, $\vec{E}_s$, will have on the photorefractive medium. The answer comes from considering the linear electrooptic effect. In this effect geometry and orientation are crucial.

In many problems we have the luxury of choosing a convenient coordinate system. For example, in the previous section we chose the z axis as being parallel to the grating vector, $\vec{K}$. We are much more restricted when we consider propagation of light in an anisotropic medium, such as a crystal. Optically speaking there is only one preferred set of axes—the principal coordinate system.

Simply put, the principal coordinate system is the one in which the dielectric tensor, $\bar{\epsilon}$, is diagonal. When an electric field, $\vec{E}$, is applied to a dielectric the medium is polarized. The electric displacement, $\vec{D}$, is related to this field by:

$$\vec{D} = \bar{\epsilon}\vec{E} \tag{21}$$

In the principal coordinate system, $\epsilon_{ij} = 0$ for $i \neq j$. Along the axes, $\vec{D}$ is in the same direction as $\vec{E}$ [46].

If the medium is homogeneous, nonabsorbing and magnetically isotropic then the electric energy density is given by:

$$W_E = \frac{1}{2}\vec{E}\cdot\vec{D} = \frac{1}{2}\sum_{i=1}^{3}\frac{D_i^2}{\epsilon_{ii}} \tag{22}$$

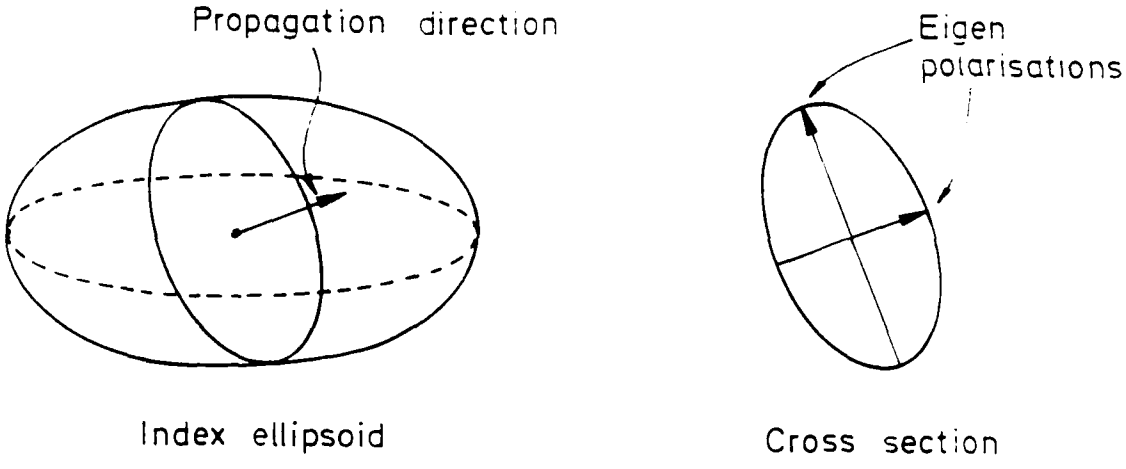

Figure 3: (a) The index ellipsoid with propagation direction, $\vec{s}$. (b) Propagation eigenstates from the cross-section ellipse.

Making a change of variable, $x_i = D_i/\sqrt{2W_E\epsilon_0}$, and recalling the refractive index $n_i = \sqrt{\epsilon_0\epsilon_i}$ gives:

$$\sum_{i=1}^{3} \frac{x_i^2}{n_i^2} = 1 \tag{23}$$

The above is the equation defining the index ellipsoid. The x_is are the principal axes coordinates. Thus in the principal coordinate system the index ellipsoid has a particularly simple form.

The index ellipsoid is used to describe propagation of light in anisotropic media. For any propagation direction there are generally two eigenstates, each characterised by a polarisation and a phase velocity (refractive index). By eigenstate we mean an incident wave polarised in one of these characteristic directions will maintain its polarisation state as it progresses through the medium. Fig 3 shows how to find these eigenstates. Construct a plane passing through the origin of the index ellipsoid whose normal is in the desired propagation direction. The intersection of this plane and the ellipsoid is an ellipse. The directions of the major and minor axes give the eigenpolarisations while the lengths of the semiaxes are the corresponding refractive indices.

The treatment for the index ellipsoid concerned the optical electric field. An applied field, such as the space charge field developed in Sec 1, may perturb the distribution of charges in the medium and alter the index ellipsoid. This is known as electrooptic effect and the perturbation may be proportional to the applied field (linear or Pockel's effect) or to the square of the applied field (quadratic or Kerr effect).

In photorefractivity it is the linear electrooptic effect which is important. Using the contracted index notation of Yariv and Yeh [135] an applied field transforms the index ellipsoid into:

$$\left(\frac{1}{n_1^2} + r_{1j}E_j\right)x_1^2 + \left(\frac{1}{n_2^2} + r_{2j}E_j\right)x_2^2 + \left(\frac{1}{n_3^2} + r_{3j}E_j\right)x_3^2 + 2r_{4j}E_j x_2 x_3 + 2r_{5j}E_j x_1 x_3 + 2r_{6j}E_j x_1 x_2 = 1 \qquad (24)$$

with repeated summation over $j = 1,2,3$. The r_{ij}s are the coefficients of the electrooptic tensor. The form of this tensor depends on the symmetry of the crystal class [30]. For example, several crystal classes are centrosymmetric; that is they have a centre of symmetry and are invariant under an inversion (replacing the electrooptic tensor **r** with -**r**). Performing this inversion in Eqn 24 gives a different form for the index ellipsoid unless all the r_{ij}s are zero. Thus a necessary (but not sufficient) condition for exhibition of the linear electrooptic effect is that a crystal be noncentrosymmetric. Ref [135] contains a list of forms for the electrooptic tensor for all the crystal classes as well as the individual coefficients for several crystals.

Eqn 24 represents a transformation of the original index ellipsoid. In this transformation the lengths of the ellipsoid semi-major and -minor axes may change and their orientation may suffer a rotation. In other words we might have a new principal coordinate system with the application of an electric field.

Most of our experimental work with photorefractive crystals will involve $Bi_{12}SiO_{20}$ in the configuration shown in Fig 4a. The Miller index notation gives us the orientation of the principal coordinate system with no applied field. Fig 4b shows the new orientation of the principal axes for a field applied along the 001 or x_3 crystal

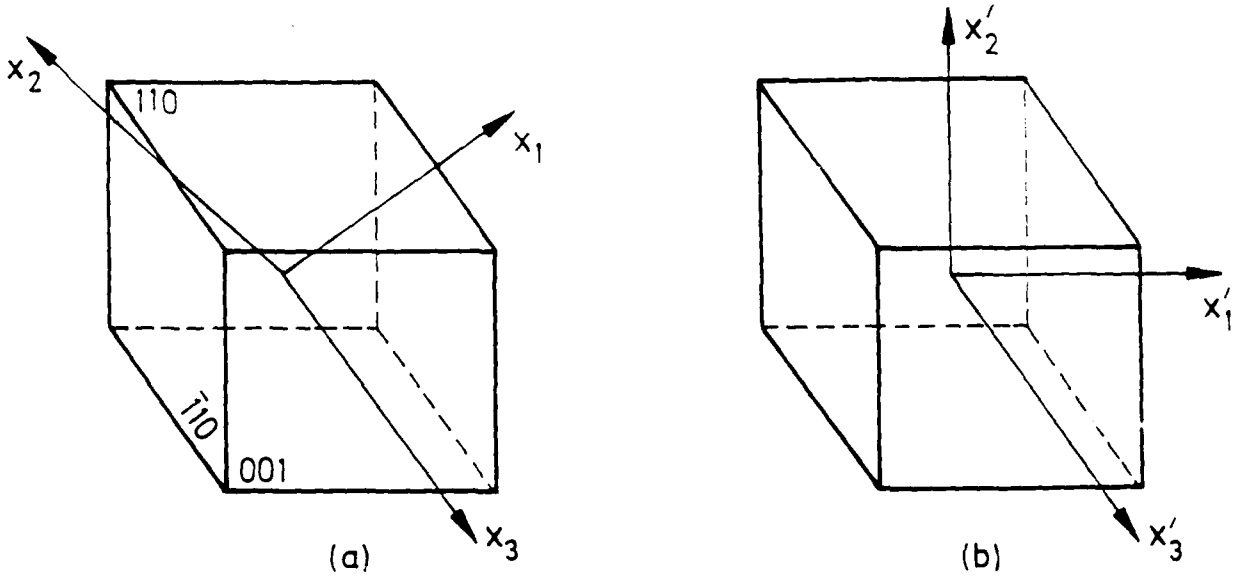

Figure 4: a) Principal coordinate system (dark axes) for $Bi_{12}SiO_{20}$. b) Reoriented principal coordinate system for applied field along the x_3 axis.

axis. The analysis of this case is as follows. $Bi_{12}SiO_{20}$ belongs to crystal class 23. It is a cubic crystal so with no applied field the index ellipsoid is a sphere of radius n. The only non-zero elements of the electrooptic tensor are r_{41}, r_{52}, and r_{63}, all of which are equal. Assuming an electric field $\vec{E}$ applied along the principal x_3 axis, our index ellipsoid is transformed into:

$$\frac{x_1^2}{n^2} + \frac{x_2^2}{n^2} + \frac{x_3^2}{n^2} + 2r_{63}Ex_1x_2 = 1 \tag{25}$$

In the new principal axes system the index ellipsoid has the form given by Eqn 23. The appropriate transformation is:

$$x_1' = \frac{1}{\sqrt{2}}(x_1 + x_2) \tag{26}$$

$$x_2' = \frac{1}{\sqrt{2}}(-x_1 + x_2) \tag{27}$$

$$x_3' = x_3 \tag{28}$$

This is merely a rotation about the x_3 axis through 45°. In the new primed principal

coordinate system the index ellipsoid is:

$$\left(\frac{1}{n^2} - r_{63}E\right) x_1'^2 + \left(\frac{1}{n^2} - r_{63}E\right) x_2'^2 + \frac{x_3'^2}{n^2} = 1 \tag{29}$$

The quantity $r_{63}E \ll 1/n^2$ so the new ellipsoid axes lengths are

$$n_1 = n + \frac{1}{2}n^3 r_{63}E \tag{30}$$

$$n_2 = n - \frac{1}{2}n^3 r_{63}E \tag{31}$$

$$n_3 = n \tag{32}$$

In the primed principal coordinate system light polarised in the x_1' or x_2' direction will experience a refractive index change, but light polarised along the x_3' axis will not.

In general we can describe the change in refractive index in terms of a change in the dielectric constant (for optical frequencies) given below:

$$\Delta\epsilon_r = \epsilon_r{}^2 r_{\text{eff}} E \tag{33}$$

where r_{eff} is the appropriate electrooptic tensor component or combination of components.

2.3 The Field Equations

Consider the mixing of two waves in a photorefractive medium as shown in Fig 5. How will the modulated refractive index found in Sec 2.2 affect the waves? We need to find the expression of the governing wave equation. Here we will neglect any vectorial complications such as optical activity or birefringence. These effects will be discussed briefly later in the chapter.

The superposition of the two waves is given by:

$$E = E_+(z)e^{-j(\vec{k}_+ \cdot \vec{r} - \omega_+ t)} + E_-(z)e^{-j(\vec{k}_- \cdot \vec{r} - \omega_- t)} \tag{34}$$

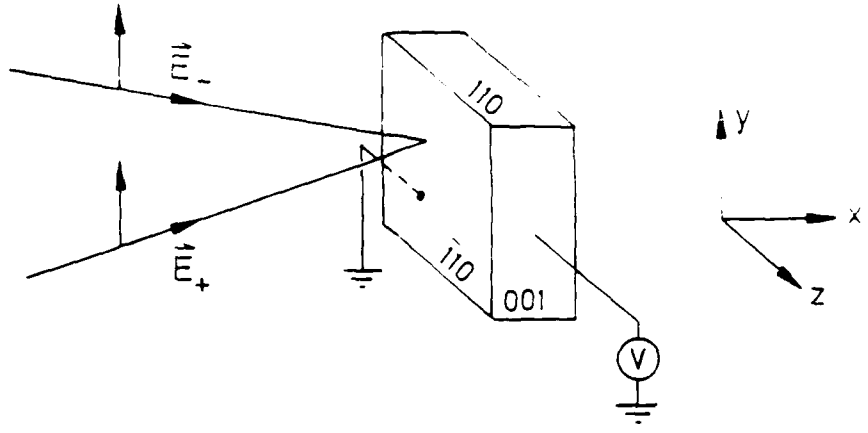

Figure 5: Orientation for two-wave mixing

The modulated dielectric constant is:

$$\epsilon_r = \epsilon_{r0} + \Delta\epsilon_r e^{j(\vec{K}\cdot\vec{r}-\delta\omega t)} + \Delta\epsilon_r{}^* e^{-j(\vec{K}\cdot\vec{r}-\delta\omega t)} \tag{35}$$

Here "*" means complex conjugate.

The derivation of the scalar wave equation is a straightforward exercise and can be found, for example, in Ref [115]. We take advantage of the fact that the angular frequency difference, $\delta\omega$, between the waves is very small compared to either angular frequency. Thus $\omega_+ \approx \omega_-$. This also means the time derivatives of ϵ are much smaller than the time derivatives of E. The scalar wave equation is given by:

$$\nabla^2 E + \omega^2 \mu_0 \epsilon_r \epsilon_0 E = 0 \tag{36}$$

where ω is the angular frequency of the two waves, μ_0 is the permeability of free space, ϵ_r is the relative dielectric constant of the medium, ϵ_0 is the permittivity of free space, and E is the total complex amplitude.

Putting Eqns 34 and 35 into 36 yields:

$$\begin{aligned}
&\left(\nabla^2 E_+ - 2j\vec{k}_+ \cdot \nabla E_+ - k^2 E_+\right) e^{-j(\vec{k}_+\cdot\vec{r}-\omega_+ t)} + \\
&\left(\nabla^2 E_- - 2j\vec{k}_- \cdot \nabla E_- - k^2 E_-\right) e^{-j(\vec{k}_-\cdot\vec{r}-\omega_- t)} + \\
&\omega^2 \mu_0 \epsilon_0 \left(\epsilon_{r0} + \Delta\epsilon_r e^{j(\vec{K}\cdot\vec{r}-\delta\omega t)} + \Delta\epsilon_r{}^* e^{-j(\vec{K}\cdot\vec{r}-\delta\omega t)}\right) \\
&\left(E_+ e^{-j(\vec{k}_+\cdot\vec{r}-\omega_+ t)} + E_- e^{-j(\vec{k}_-\cdot\vec{r}-\omega_- t)}\right) = 0
\end{aligned} \tag{37}$$

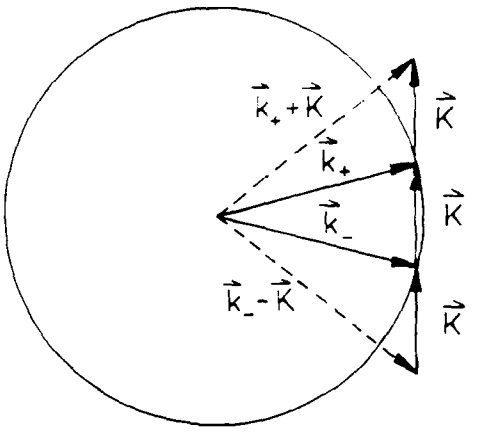

Figure 6: Bragg closure. The propagation directions corresponding to $\vec{k}_- - \vec{K}$ and $\vec{k}_- - \vec{K}$ are neglected.

where $|\vec{k}_+| \approx |\vec{k}_-| = k$.

As is stands the above equation is difficult to work with. It is time for some simplifying assumptions.

2.3.1 More simplifying assumptions

1) *Neglect terms involving the second derivative.* This is reasonable because E_+ and E_- vary slowly in space. It is a common assumption and is known as the "slowly varying amplitude" approximation [44]. An alternative way of reaching this conclusion is to look at the first derivative terms. These are multiplied by k which is a very large number. Thus these terms dominate the second derivatives.

2) *Neglect higher diffracted orders.* The vectors $\vec{k}_+$, $\vec{k}_-$, and $\vec{K}$ form a Bragg closure. In Eqn 37, $e^{-j(\vec{k}_+ \cdot \vec{r} - \omega_+ t)} e^{j(\vec{K} \cdot \vec{r} - \delta\omega t)} = e^{-j(\vec{k}_- \cdot \vec{r} - \omega_- t)}$ and $e^{-j(\vec{k}_- \cdot \vec{r} - \omega_- t)} e^{-j(\vec{K} \cdot \vec{r} - \delta\omega t)} = e^{-j(\vec{k}_+ \cdot \vec{r} - \omega_+ t)}$. These products correspond to valid propagation directions for the solution given by Eqn 34. The products $e^{-j(\vec{k}_+ \cdot \vec{r} - \omega_+ t)} e^{-j(\vec{K} \cdot \vec{r} - \delta\omega t)}$ and $e^{-j(\vec{k}_- \cdot \vec{r} - \omega_- t)} e^{j(\vec{K} \cdot \vec{r} - \delta\omega t)}$ suggest higher diffracted orders which do not fit the Bragg closure. In a volume grating angular selectivity is very strong and any departure from the Bragg condition greatly reduces the diffraction efficiency [115]. This assumption will be valid

except for very small interbeam angles.

3) *Use one dimensional theory.* Assume the incident beams make very small angles with the x axis so $\vec{k}_{-} \cdot \vec{r} \approx kx$.

With these three assumptions and the relationship

$$k^2 = \omega^2 \mu_0 \epsilon_0 \epsilon_{r0} \tag{38}$$

we obtain

$$\frac{dE_{+}}{dx} = -j\frac{\Delta\epsilon_r^* k}{2\epsilon_{r0}} E_{-} \tag{39}$$

$$\frac{dE_{-}}{dx} = -j\frac{\Delta\epsilon_r k}{4\epsilon_{r0}} E_{+} \tag{40}$$

(In reflection geometry (see Fig 2.7c) the right hand side of Eqn 40 is positive rather than negative.)

2.3.2 Two-wave mixing coupled wave equations

Using Eqn 33, Eqns 39 and 40 can be written:

$$\frac{dE_{+}}{dx} = j\Gamma e^{-j\Phi_g} \frac{I_{-}}{I_{+} + I_{-}} E_{+} \tag{41}$$

$$\frac{dE_{-}}{dx} = j\Gamma e^{j\Phi_g} \frac{I_{+}}{I_{+} + I_{-}} E_{-} \tag{42}$$

where $\Gamma = \frac{1}{2} k_0 n^3 r_{\text{eff}} |E_\omega|$ with k_0, the free space wave number, and $\Phi_g = \arg(E_\omega)$. In terms of the intensity and phase of each wave we may write:

$$\frac{dI_{+}}{dx} = 2\Gamma \sin\Phi_g \frac{I_{+} I_{-}}{I_{+} + I_{-}} \tag{43}$$

$$\frac{dI_{-}}{dx} = -a2\Gamma \sin\Phi_g \frac{I_{+} I_{-}}{I_{+} + I_{-}} \tag{44}$$

$$\frac{d\phi_{+}}{dx} = \Gamma \cos\Phi_g \frac{I_{-}}{I_{+} + I_{-}} \tag{45}$$

$$\frac{d\phi_{-}}{dx} = a\Gamma \cos\Phi_g \frac{I_{+}}{I_{+} + I_{-}} \tag{46}$$

Here $a = +1$ for transmission geometry and -1 for reflection geometry.

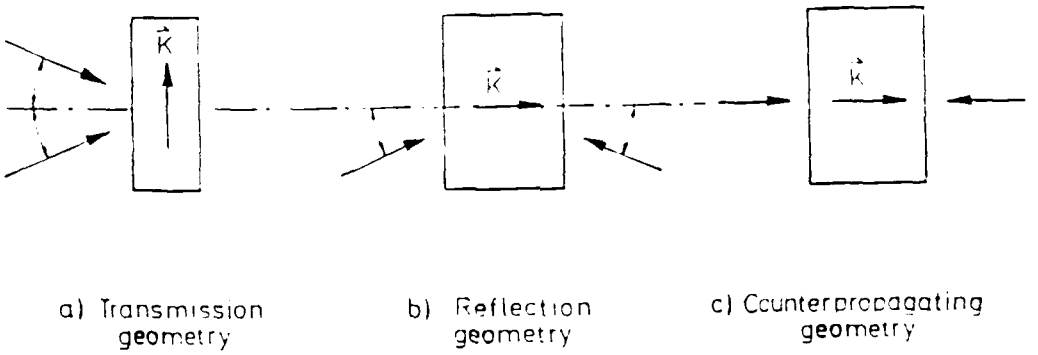

Figure 7: Geometries for Two-Wave Mixing. (a) Transmission. (b) Reflection. (c) Counterpropagating.

2.3.3 Consequences of the coupled wave equations

The coupling in Eqns 43 - 46 is highly dependent on the phase mismatch angle, Φ_g. If $\Phi_g = 0$ there is no coupling in intensity between the beams. When $\Phi_g = 90°$ the coupling is strongest and we may expect maximum power transfer. The reverse is true for the phase equations. But what does coupling of the phase mean physically? It means the phase difference between the beams can change as one moves across the crystal. This means the fringes of the steady-state grating are bent [93].

Consider the symmetric geometries shown in Fig 7. We should point out that in general the crystal orientations differ between transmission and reflection geometries to take best advantage of the electrooptic effect. The counterpropagating beam configuration is a special case of the reflection geometry and will be discussed in detail in Chapter 3. In this antiparallel case the steady-state grating fringes are not bent, but chirped as a result of the phase difference in the beams.

Power conservation is different for transmission and reflection geometries. For the transmission case the sum $I_+ + I_-$ is constant while it is easily shown that the reflection case gives constant $I_+ - I_-$. We can use power conservation to obtain

solutions for the coupled wave equations. For the transmission case, substitute $I_+ = I_0 - I_-$ into the differential equations and solve.

$$I_+(x) = \frac{\beta_r \exp(2\Gamma \sin \Phi_g x)}{1 + \beta_r \exp(2\Gamma \sin \Phi_g x)} I_0 \quad (47)$$

$$I_-(x) = \frac{1}{1 + \beta_r \exp(2\Gamma \sin \Phi_g x)} I_0 \quad (48)$$

$$\phi_+(x) = \phi_+(0) + \Gamma \cos \Phi_g x + \frac{1}{2} \cot \Phi_g \ln \frac{1 + \beta_r}{1 + \beta_r \exp(2\Gamma \sin \Phi_g x)} \quad (49)$$

$$\phi_-(x) = \phi_-(0) - \frac{1}{2} \cot \Phi_g \ln \frac{1 + \beta_r}{1 + \beta_r \exp(2\Gamma \sin \Phi_g x)} \quad (50)$$

Here $\beta_r = I_+(0)/I_-(0)$, the input beam ratio.

2.3.4 Crystal parameters

Different crystal types generally have different photorefractive responses. There may even be variation between crystals of the same type but from different manufacturers [31]. The presence of impurities or dopants may lead to variation in effects such as absorption, relative concentrations of acceptors and donors, or the strength of the photovoltaic field. Ultimately the individual behaviour of a crystal sample is due to its distinct combination of crystal parameters.

Table 1 lists typical values from the literature for the parameters which make up E_{sl} for $Bi_{12}SiO_{20}$, $LiNbO_3$, and $BaTiO_3$. These are the crystals we will consider theoretically and experimentally in the rest of the thesis. $LiNbO_3$ and $BaTiO_3$ are uniaxial crystals and have ordinary (n_o) and extraordinary (n_e) refractive indicies. There are two important electrooptic tensor components for the applied electric field and grating vector direction along the 001 axis. In $LiNbO_3$ r_{33} is the appropriate value for transmission geometry and r_{13} for reflection geometry. We have taken p as 1.0×10^{-30} m^3/V to give a photovoltaic field of 2.5 kV/cm, a value we measured for one sample of $LiNbO_3$. The photovoltaic effect is negligible in $BaTiO_3$ and $Bi_{12}SiO_{20}$. $BaTiO_3$ has a very large electrooptic tensor component, r_{51}, which enhances two-wave mixing in transmission geometry. The r_{13} component is important

Parameter	$Bi_{12}SiO_{20}$	$LiNbO_3$	$BaTiO_3$
$N_D(m^{-3})$	$1.0x10^{25}$	$1.0x10^{23}$	$1.0x10^{25}$
$N_A^-(m^{-3})$	$1.0x10^{22}$	$1.0x10^{22}$	$2.0x10^{22}$
ϵ_s	56	$\epsilon_{11} = 78$	$\epsilon_{11} = 4300$
		$\epsilon_{33} = 32$	$\epsilon_{33} = 168$
n (refractive index)	2.62	$n_o = 2.29$	$n_o = 2.44$
		$n_e = 2.20$	$n_e = 2.37$
r_{eff} (m/V)	$3.4x10^{-12}$	$r_{13} = 9.6x10^{-12}$	$r_{13} = 2.6x10^{-11}$
		$r_{33} = 3.1x10^{-11}$	$r_{51} = 1.6x10^{-9}$
μ (m^2/Vs)	$3.0x10^{-6}$	$1.0x10^{-5}$	$5x10^{-5}$
s (m^2/J)	$2.0x10^{-5}$	$2.5x10^{-5}$	$3x10^{-6}$
p (m^3/V)	0	$1.0x10^{-30}$	0
$\gamma_r(m^3/s)$	$1.6x10^{-17}$	$1.0x10^{-15}$	$5x10^{-14}$

Table 1: Crystal parameters for $Bi_{12}SiO_{20}$, $LiNbO_3$, and $BaTiO_3$ for $\lambda = 514$ nm. Refs [49,135,130,16,86]

in reflection geometry. The values listed are for a wavelength of 514 nm.

2.3.5 Optimization of intensity coupling

The characteristic fields are E_t, E_q, E_m, and E_p. E_t is a diffusion field. E_q is proportional to the maximum value the space charge field can have. It is $1/2\pi$ times the field due to the separation of ionized donors and acceptors by one grating spacing [117]. E_m is a consideration during the transient period while the grating forms [49] or when moving fringes are present, i.e. when the two mixing beams have different frequencies [121]. The photovoltaic field is E_p. It is a constant field and can be present in ferroelectric materials such as $LiNbO_3$ and has been measured in some samples to be as strong as 100 kV/cm [72].

E_t, E_q, and E_m depend on K and therefore on the interbeam angle. Fig 8 depicts the relative strengths of these fields as functions of the interbeam angle for $Bi_{12}SiO_{20}$ illuminated by light of wavelength 514 nm at a temperature of 293 K. Here the interbeam angle is measured in the medium. As the angle between the beams increases the grating spacing decreases. This has the expected effects of

increasing E_t, but decreasing E_q. For small interbeam angles ($\theta < 5°$) we may take $E_t \ll E_q$. In all cases $E_m \ll E_q$. $E_t \ll E_m$ only for very small ($< 1°$) angles but for angles $> 10°$ the reverse is true.

The above approximations may be used to simplify the expression for E_{s1}. The interbeam angle ranges (small/large) where the approximations are valid are useful to delineate photorefractive behaviour. Consider the case with no moving fringes ($b = 0$). For small interbeam angles (large grating spacings) we take $E_q \gg E_{s0} \gg E_t$. Then

$$E_{s1} \approx -mE_{s0} \tag{51}$$

Since m is real, E_{s1} is in phase with the intensity pattern and $\Phi_g = 0$.

There are two cases in which E_{s1} becomes pure imaginary. If there is no applied field, $E_{s0} = 0$, then for $E_q \gg E_t$

$$E_{s1} \approx jmE_t \tag{52}$$

For large interbeam angles, $E_q \ll E_t$ and

$$E_{s1} \approx jmE_q \tag{53}$$

Here the modulated space charge field is 90° out of phase with the intensity pattern.

The small interbeam angle case is called ***drift dominated*** and is characterized by little or no intensity coupling, but pronounced bending of the hologram fringes at steady-state due to strong phase coupling. When the interbeam angle is large (small grating spacing) or when no external field is applied, the diffusion process governs charge transport. This is called the ***diffusion dominated*** regime. Now significant power transfer between the beams is possible. Staebler and Amodei [119] were the first to describe these two extremes.

Figs 9a-e demonstrate these effects for $Bi_{12}SiO_{20}$ using the crystal parameter values of Table 1. In the first the phase mismatch angle is plotted as a function of applied field, E_{s0}, for five interbeam angles (1°, 2°, 5°, 10°, and 20°). At $E_{s0} = 0$ the only possible process for charge transport is diffusion, thus we expect $\Phi_g = 90°$.

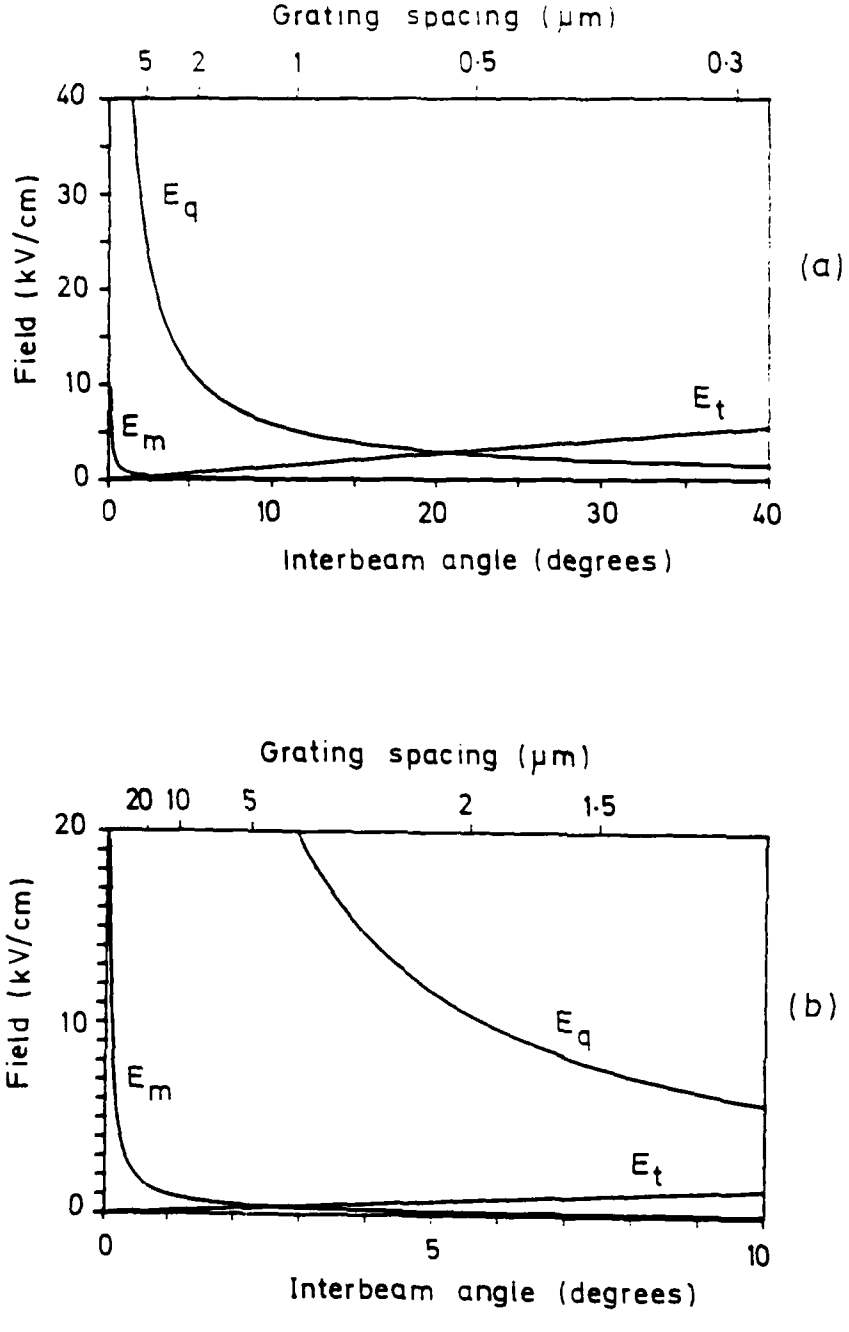

Figure 8: Characteristic fields versus interbeam angle (in the medium). (a) Transmission geometry. (b) Expanded view of (a).

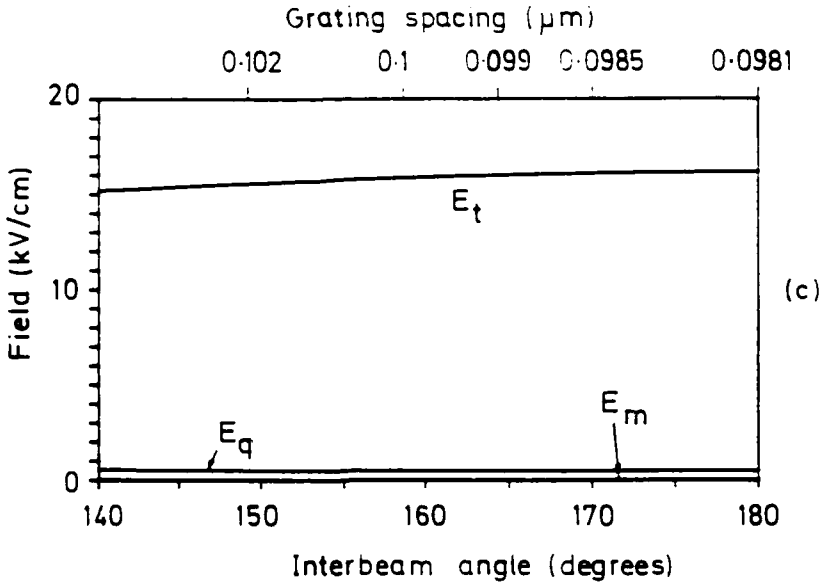

Figure 8: Characteristic fields versus interbeam angle (in the medium). (c) Reflection geometry.

For small interbeam angles even small electric fields push Φ_g towards 0 or 180°, while for large angles, diffusion continues to dominate over drift. Fig 9b shows the symmetric dependence of the magnitude of the coupling term Γ on E_{s0}. It is symmetric because we have no moving fringes and no photovoltaic field. This plot illustrates an important trade-off, the phase mismatch is more favourable for power transfer in the diffusion dominated case, but in the presence of an applied field the coupling coefficient, Γ, has a smaller magnitude than for the drift dominated case. The intensity coupling depends on $2\Gamma \sin \Phi_g$ and we might expect the magnitude of this term to be optimized for a particular interbeam angle (or grating spacing). Fig 9c shows that coupling gets stronger with increasing interbeam angle for small applied fields, but not necessarily for greater fields. Fig 9d plots $2\Gamma \sin \Phi_g$ versus interbeam angle for E_{s0}= 0, 2, 5, 8, and 10 kV/cm. There is a clear optimum angle for the stronger fields. In Fig 9e we plot the gain $(I_-(d)/I_-(0))$, given by Eqn 48, for an interaction length of 1 cm, no moving fringes and an applied field of 10 kV/cm

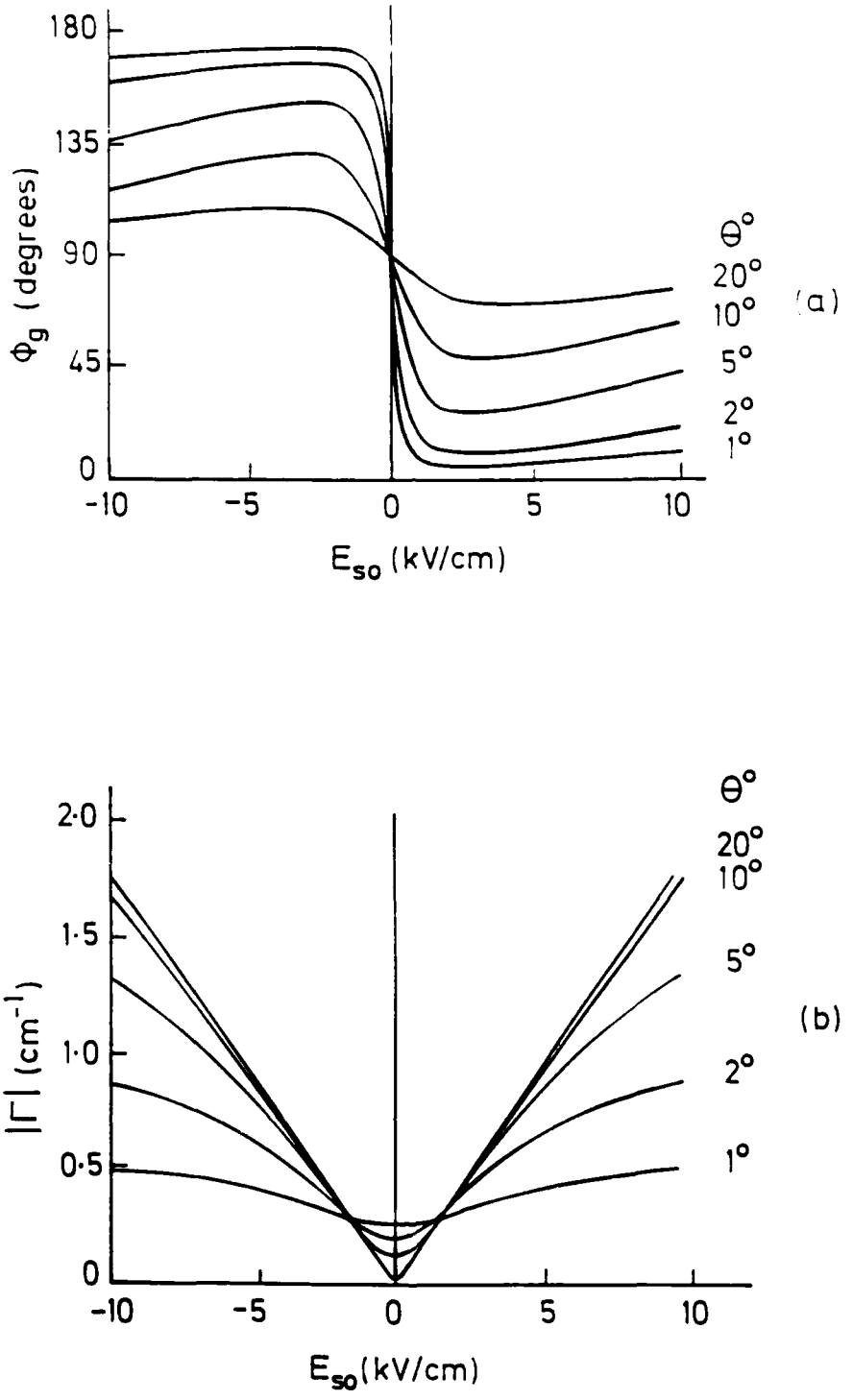

Figure 9: Coupling in degenerate two-wave mixing. (a) Φ_g vs E_{s0}. (b) Γ vs E_{s0}. For all plots: $\lambda = 514$ nm, T = 293 K.

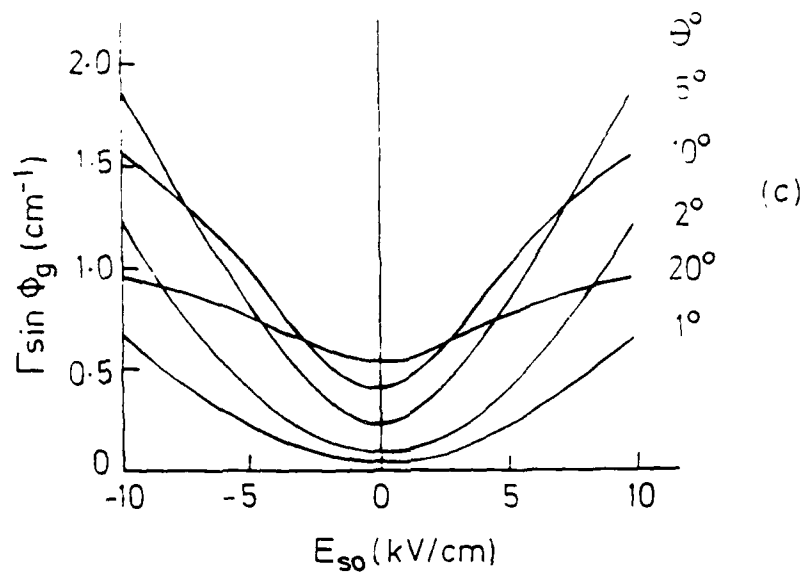

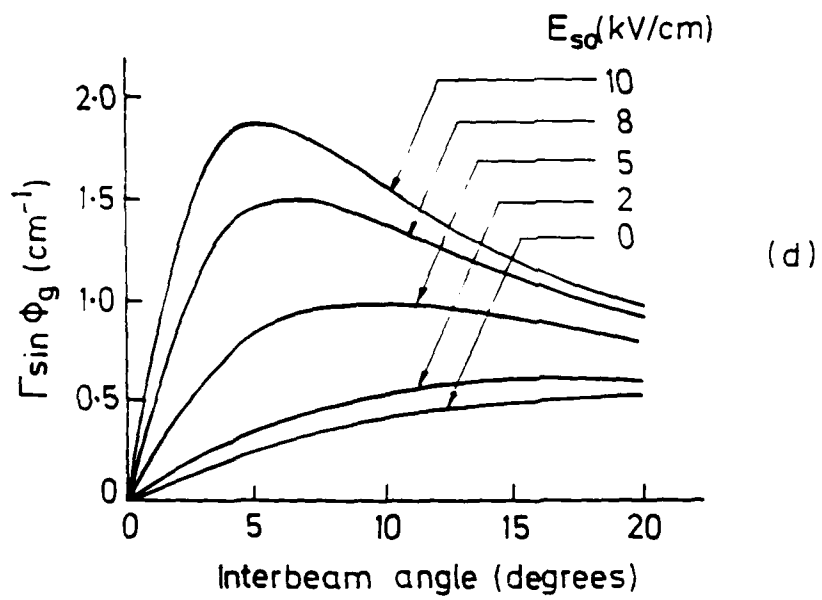

Figure 9: Coupling in degenerate two-wave mixing. (c) $\Gamma \sin \Phi_g$ vs E_{s0}. (d) $\Gamma \sin \Phi_g$ vs interbeam angle.

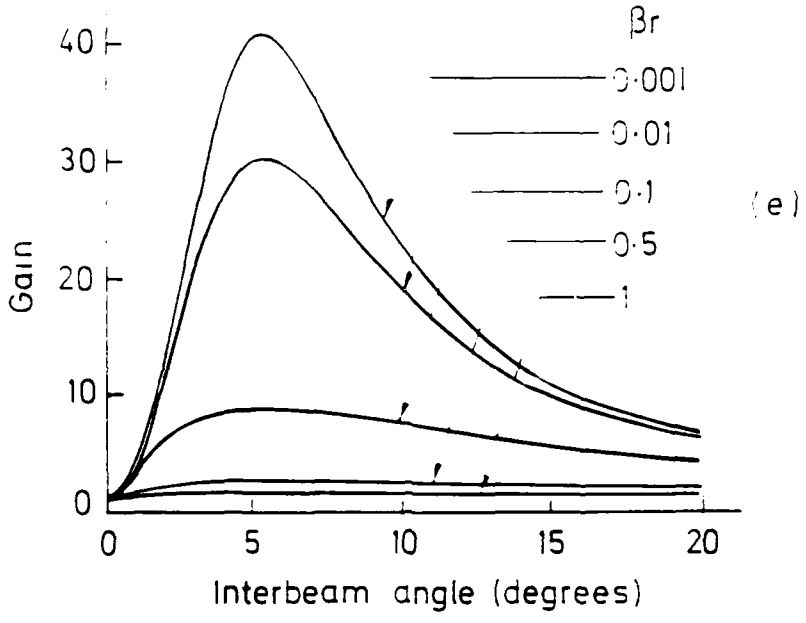

Figure 9: Coupling in degenerate two-wave mixing. (e) Gain (I_+ (d)/ $I_+(0)$) vs interbeam angle.

for various incident beam ratios, β_r. The beam ratio has no effect on the optimum interbeam angle. The smaller β_r is, the greater the gain. Thus for $\beta_r = 10^{-3}$ the gain can be as high as 40.

Another key feature borne out by Figs 9c and 9d is that the energy transfer is just in one direction. That is the coupling term has the same sign regardless of the combination of beam ratio, interbeam angle, and applied field. In our example, I_+ always gains at the expense of I_-.

For the applications oriented reader, it is evident from Fig 9c that the applied field is a useful control parameter for beam coupling in $Bi_{12}SiO_{20}$, particularly for small interbeam angles. Changing the interbeam angle also influences the beam coupling, but shifting beam directions is undesirable in applications requiring fixed optics.

2.3.6 Optimization with moving fringes

The preceding discussion highlights an unfortunate aspect of photorefractivity with $Bi_{12}SiO_{20}$. An applied field is necessary to obtain a large coupling coefficient, Γ, but this field takes us away from the high gain, diffusion-dominated regime.

Fortunately there is a way to have the best of both worlds, to maximize Γ and have $\Phi_g = 90°$. The trick is to use moving fringes. This was first demonstrated experimentally in 1981 by Huignard and Marrakchi [56]. The following year Stepanov, et al. explained this effect in terms of "running" holograms [121]. The process of reading a hologram in a photorefractive material in the presence of an electric field results in a moving grating. A resonant condition is achieved if the recording intensity pattern runs synchronously with this moving grating. Treatments of moving gratings have been provided theoretically by Valley [129] and both experimentally and theoretically by Refregier, et al. [109], Günter [45], and Huignard and Marrakchi [57].

Let us reconsider Eqn 20 for the case $b \neq 0$. Using the approximations of Sec 2. we obtain for large interbeam angles

$$E_{s1} = -\frac{mE_q}{b\frac{E_q}{E_m} + j} \tag{54}$$

For negligible b, we are still in the diffusion dominated regime with $\Phi_g = \pm 90°$. As the fringe velocity grows in magnitude the real part of E_{s1} becomes increasingly important. For $|bE_q/E_m| \gg 1$, $E_{s1} \approx -mE_m/bE_q$. Here $\Phi_g = 0$ and we have no power transfer between the beams. Clearly moving fringes will not facilitate intensity coupling for large interbeam angles.

For small interbeam angles

$$E_{s1} = -m\frac{E_{s0}}{1 + b\frac{E_{s0}}{E_m} + j(\frac{E_{s0}}{E_q} - b)} \tag{55}$$

With a bit of algebra we can show that the imaginary part of E_{s1} has a maximum for $b = -E_m/E_{s0}$ in the limit $E_{s0} \gg E_m$. Figs 10a-d give a comparative study of

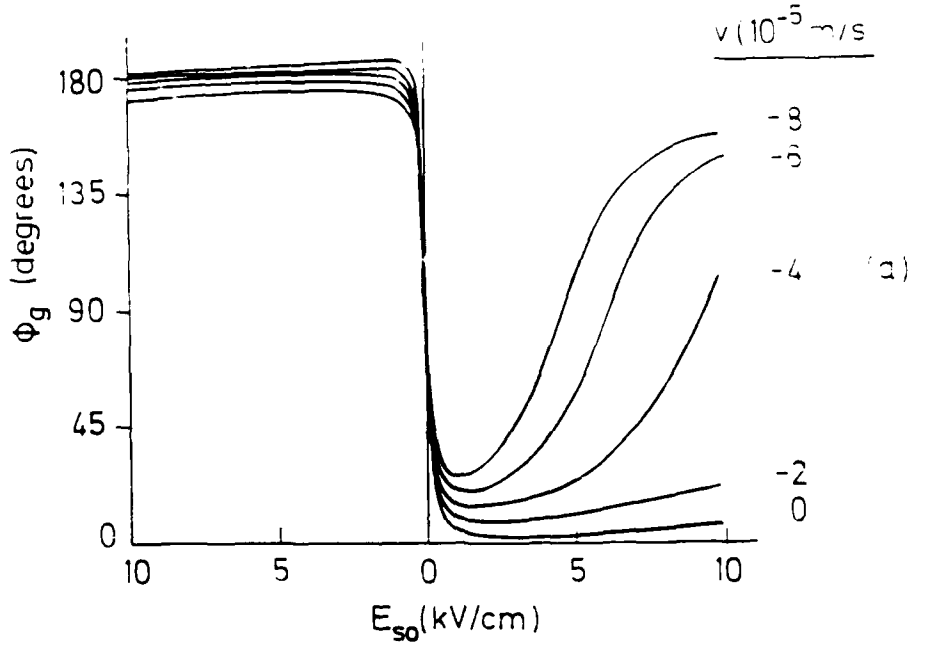

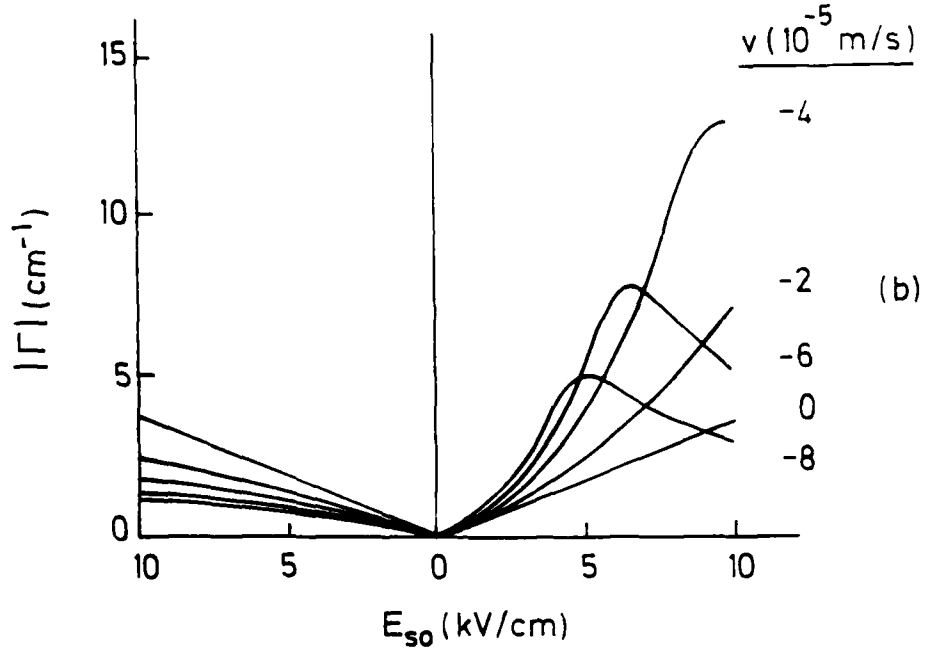

Figure 10: Coupling in nearly degenerate two-wave mixing. (a) Φ_g vs E_{s0}. (b) Γ vs E_{s0}. For all plots: λ = 514 nm, T = 293 K, interbeam angle = 0.75°.

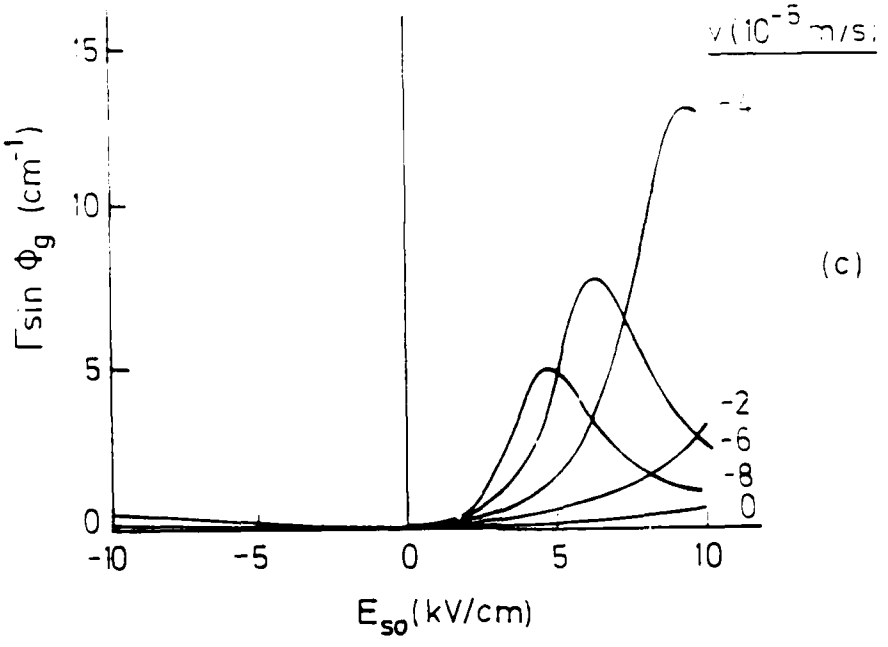

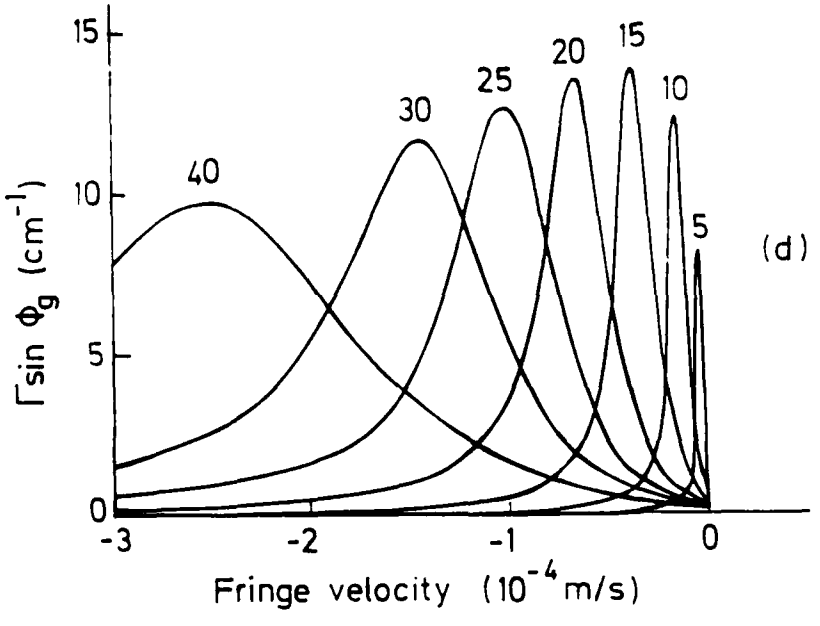

Figure 10: Coupling in nearly degenerate two-wave mixing. (c) $\Gamma \sin \Phi_g$ vs E_{s0}. (d) $\Gamma \sin \Phi_g$ vs fringe velocity. In (d) the different curves refer to grating spacings (μm).

Φ_g, Γ and coupling in $Bi_{12}SiO_{20}$ to that for zero fringe velocity. We have chosen one particular interbeam angle, 0.75°, corresponding to a grating spacing of 15 μm. Fig 10a shows Φ_g as a function of E_{s0} for various fringe velocities. We see that $\Phi_g = 90°$ is realizable for $E_{s0} \neq 0$ with an appropriate fringe velocity. Happily this combination of field and velocity is also where Γ has its peak, as seen in Fig 10b. The resonant condition is apparent with applied field as the control parameter in Fig 10c and with fringe velocity as the control parameter in Fig 10d.

$\Gamma \sin \Phi_g$ for moving fringes is nearly an order of magnitude larger than that obtained with no moving fringes. If we tried to reproduce Fig 9e for gain with a 1 cm long crystal, we would find essentially complete power transfer between the beams.

Highly efficient gain in $Bi_{12}SiO_{20}$ and related crystals may be achieved using an applied a.c. field. First proposed by Stepanov and Petrov [122] this method employs an a.c. field of frequency $\omega_{ac} \gg \tau_d$. The photoinduced carriers do not have time to move far before the direction of the applied field changes. Thus the time average for Φ_g is 90° and optimum gain is realized. This technique has recently been used in photorefractive gallium arsenide [78].

2.3.7 Other effects

In the course of our treatment of the photorefractive effect we have made several simplifying assumptions. Some, such as neglecting thermal generation of carriers, have a sound basis in experimental evidence. Other assumptions were made for the ease of the theory. Let us discuss briefly the modifications necessary if we were to include these effects.

1. *Large modulations.* To linearize the materials equations we expanded n, N_D^+, J, and E_s out to first order terms in a Fourier series and then neglected products of first order terms. In other words we assumed small modulations. It is easy to show that each first order coefficient is proportional to the intensity modulation,

m. If the gain is large (strong coupling or large interaction lengths) then m might not be small. This problem has been addressed by Refregier, et al. [109], Ochoa, et al. [97], and most recently by Au and Solymar [6]. Higher order Fourier terms are included in a pertubation treatment. Ref [6] modeled $Bi_{12}SiO_{20}$ and found that, in general, the imaginary part of E_{s1} decreased for larger modulation depths. We also made the claim that $N_D^+ \gtrsim n$, or specifically, $N_{D1}^+ \gg n_1$. If we look at the a.c. Eqns 15-18, then this latter condition is no longer true for very small interbeam angles and very weak applied fields. For example, using $Bi_{12}SiO_{20}$ with no applied field, no moving fringes, an interbeam angle of 0.1°, a temperature of 300°, and a wavelength of 514 nm, we find that $|N_{D1}^+| \approx |n_1|$. Fortunately, most of our applications will involve larger interbeam angles, stronger applied fields, or both.

2. *Absorption.* The photorefractive process would not work without attenuation of the mixing waves. If none of the incident light was absorbed, no photocarriers would be produced, and there would be no space charge field or refractive index modulation. With moving fringes there is another way in which absorption reduces the gain. The total intensity will not be constant across the medium. The dielectric relaxation time is inversely proportional to the total intensity. A spatially varying intensity means the optimum fringe velocity changes across the crystal. Only one "slice" of the crystal will be at the resonance condition.

For the transmission geometry there are analytic solutions to the coupled wave equations in the presence of absorption (see Chap 4) but a numerical treatment is necessary for the reflection case.

3. *Vectorial Effects.* We used a scalar treatment for the field equations. But the vectorial nature of the problem is important when we consider birefringence or optical activity. For example, the optical activity of $Bi_{12}SiO_{20}$ (the rotation of the polarisation axis is $\approx 38°$/mm for 514 nm) will reduce photorefractive gain. To see why, consider the transmission geometry for the crystal orientation in Fig 5. Take the two incident beams polarised in the y direction to maximize the electrooptic effect. If the crystal is 10 mm long then the polarisation of the waves will undergo a

little more than one complete revolution during transit. Half the interaction length will be spent with polarisations close to the z direction. But the electrooptic effect is null for beams polarised in z. There will be little or no coupling in these regions and therefore the overall gain is reduced.

John Heaton's D.Phil. thesis gives a thorough treatment of absorption, optical activity, and birefringence [49]. One must resort to numerical methods to include these effects.

2.4 The Photorefractive Effect as a Nonlinear Problem

The term *nonlinear* has cropped up many times in the course of this chapter. We finish our discussion of two-wave mixing by reviewing the inherent nonlinearity of the photorefractive process.

The most important nonlinear character was mentioned in Section 2.2. The polarisation of the medium is described by $\vec{D} = \bar{\epsilon}\vec{E}$. But the dielectric tensor, $\bar{\epsilon}$, itself depends on E, thus we have a nonlinear relationship. In particular, $\bar{\epsilon}$, via the electrooptic effect due to the modulated space charge field, depends on the product of the mixing optical field amplitudes. When writers describe photorefractive materials as being nonlinear, this is the property to which they refer.

The material equations are nonlinear in the sense that they contain products of intensity driven terms such as the space charge electric field and carrier concentration. We resorted to a linearization process to arrive at analytic expressions for the modulated space charge field.

Finally the field (coupled wave) equations were expressed in terms of the product of complex amplitudes. The lossless case given by Eqns 43 and 44 is a pair of nonlinear coupled differential equations. Fortunately these equations have an analytic solution.

Chapter 3

Nonreciprocal Effects in Photorefractive Materials

So flew the god and the virgin—he on wings of love, and she on wings of fear.

The Legend of Apollo and Daphne

Bullfinch's Mythology

In Chapter 2 we learned that the phases of two mixing waves could be coupled in a nonlinear photorefractive medium. The particular case of counterpropagating beams was investigated first by Yeh [136,139]. A 1985 Letter by Solymar and Wilson proposed a novel application for this phase coupling [118]. They suggested using photorefractive materials in a controllable nonreciprocal (NR) optical phase shifter. This is a device through which a beam transitting in one direction will suffer a certain phase shift, but a beam travelling in the opposite direction may undergo a different phase shift.

NR devices, such as phase shifters, are well known in microwave applications [23] and more recently have become important in optical waveguides [98,17,92]. Many applications involve a 180°phase shift (gyrator) and the devices invariably depend on a gyrotropic or Faraday rotation effect. NR phase shifts of up to 360° are available

using these devices so, to be competitive, a photorefractive NR phase shifter should be able to produce similar sized effects. Solymar and Wilson suggested using the NR phase shifter in a fibre-optic gyroscope to compensate for the Sagnac phase shift. This operation would be analogous to slewing a mechanical gyroscope to a new orientation. Yeh has proposed using the effect to decouple counterpropagating modes in a bidirectional ring resonator [139]. This latter use has recently been demonstrated in a resonator using $BaTiO_3$ as the gain medium [62].

In this chapter we will explore the feasibility of a NR phase shifter using photorefractive materials. First we look at an analytic treatment of two-wave mixing for counterpropagating waves [59,136]. We then argue that this approach requires a numerical treatment for several important cases, and we will compare results using analytical and numerical methods. Once we have an effective means to solve the coupled wave equations, we can look in detail at NR transmission and phase shift, the expected magnitude of these effects, and the means to control them. The chapter finishes with an overall appraisal of using photorefractives for NR applications and a discussion of the limitations of our treatment.

3.1 Reflection Holograms

3.1.1 Background

Most applications of two-wave mixing in photorefractive materials use transmission geometry. There are several reasons why reflection geometry is less popular.

1. Large interbeam angles, such as would be used in reflection geometry, are associated with the diffusion dominated region with the phase mismatch angle, Φ_g, close to 90°. Unfortunately, overall gain is generally reduced. For example, in Chapter 2 we found in $Bi_{12}SiO_{20}$ the interbeam angle for optimum gain was usually less than 10°.

2. Reflection geometry often involves different crystal orientations than those for the transmission case to exploit fully the electrooptic effect. This requires different polished faces, or perhaps, an alternative crystal cut. There is a greater demand for transmission geometry orientations, and these are what the crystal suppliers provide.

3. Experimental layout for reflection geometry is generally more complicated. In general, a greater number of optical elements are required to get a split beam around the crystal to send it through the rear face.

4. In the reflection case the coupled wave equations have a two-point boundary condition. This increases the difficulty of a mathematical solution.

There are certainly fewer papers dealing with reflection geometry as opposed to transmission geometry for photorefractive materials. Counterpropagating beams impinging on a crystal exhibiting optical activity was studied by Kukhtarev, Dovgalenko and Starkov [74]. Diffraction efficiency in both reflection and transmission geometries was the subject of a paper by Heaton, et al. [47] A reflection grating can form when a single beam interacts with its reflection off the back face of a crystal. The treatment of this case was studied theoretically by Yeh [137] and experimentally by MacDonald, et al., in $BaTiO_3$[86], and by Zha and Günter in $KNbO_3$[140]. Ja generalized two-wave mixing with multiple reflections [58]. Dynamic self-enhancement in lithium niobate using reflection geometry has been demonstrated by Shvarts, et al. [113]

3.1.2 An analytic treatment

Two of the most detailed theoretical studies of mixing of counterpropagating beams come from Yeh [136] and Ja [59]. This latter paper includes a numerical treatment for the lossy case. The method for the lossless case follows.

We start with the coupled wave equations:

$$\frac{dI_+}{dz} = 2\Gamma \sin\Phi_g \frac{I_+ I_-}{I_+ + I_-} \quad (1)$$

$$\frac{dI_-}{dz} = 2\Gamma \sin\Phi_g \frac{I_+ I_-}{I_+ + I_-} \quad (2)$$

$$\frac{d\phi_+}{dz} = \Gamma \cos\Phi_g \frac{I_-}{I_+ + I_-} \quad (3)$$

$$\frac{d\phi_-}{dz} = -\Gamma \cos\Phi_g \frac{I_+}{I_+ + I_-} \quad (4)$$

To solve the intensity equations, introduce $\Delta = I_+ - I_-$ and $\Sigma = I_+ + I_-$. Then we can rewrite Eqns 1 and 2 as

$$\frac{d\Delta}{dz} = 0\,, \quad \Delta = \text{constant} \quad (5)$$

$$\frac{d\Sigma}{dz} = \Gamma \sin\Phi_g \frac{\Sigma^2 - \Delta^2}{\Sigma} \quad (6)$$

These two equations lead us to

$$I_+(z) = \tfrac{1}{2} I_{+0} \left(\sqrt{1-\beta_{ro})^2 + 4\beta_{ro} e^{2\Gamma \sin\Phi_g z}} + (1-\beta_{ro}) \right) \quad (7)$$

$$I_-(z) = \tfrac{1}{2} I_{+0} \left(\sqrt{1-\beta_{ro})^2 + 4\beta_{ro} e^{2\Gamma \sin\Phi_g z}} - (1-\beta_{ro}) \right) \quad (8)$$

where $I_{+0} = I_+(0)$ and $\beta_{ro} = I_-(0)/I_+(0)$. The above two expressions are inconvenient in that we rarely know $I_-(0)$ in advance. It is useful to introduce $\beta_r = I_-(d)/I_+(0)$, the input beam ratio, where d is the crystal length. It is a straightforward calculation to show

$$\beta_{ro} = \frac{\beta_r(1+\beta_r)}{\beta_r + e^{2\Gamma \sin\Phi_g d}} \quad (9)$$

Using this we obtain

$$I_+(z) = -C + \sqrt{C^2 + B e^{2\Gamma \sin\Phi_g z}} \quad (10)$$

$$I_-(z) = C + \sqrt{C^2 + B e^{2\Gamma \sin\Phi_g z}} \quad (11)$$

$$B = \beta_{ro} I_{+0}{}^2$$
$$= \beta_r I_{+0}{}^2 \frac{1+\beta_r}{\beta_r + e^{2\Gamma \sin\Phi_g d}} \quad (12)$$
$$C = \tfrac{1}{2} I_{+0}(\beta_{ro} - 1)$$
$$= \tfrac{1}{2} I_{+0} \frac{\beta_r{}^2 - e^{2\Gamma \sin\Phi_g d}}{\beta_r + e^{2\Gamma \sin\Phi_g d}} \quad (13)$$

Eqns 10 and 11 can be put into the phase equations to obtain

$$\phi_+(z) = \phi_+(0) + \tfrac{1}{2}\Gamma \cos\Phi_g z + \tfrac{1}{4}\cot\Phi_g \ln(T_+ T_-) \quad (14)$$
$$\phi_-(z) = \phi_-(0) - \tfrac{1}{2}\Gamma \cos\Phi_g z + \tfrac{1}{4}\cot\Phi_g \ln(T_+ T_-) \quad (15)$$

where $T_+ = I_+(d)/I_+(0)$ and $T_- = I_-(0)/I_-(d)$ are the transmissions of the two waves. A useful relationship is

$$I_+(z) I_-(z) = B e^{2\Gamma \sin\Phi_g z} \quad (16)$$

We can use this to show the transmissions are

$$T_+ = \frac{(1+\beta_r) e^{2\Gamma \sin\Phi_g d}}{\beta_r + e^{2\Gamma \sin\Phi_g d}} \quad (17)$$
$$T_- = \frac{1+\beta_r}{\beta_r + e^{2\Gamma \sin\Phi_g d}} \quad (18)$$

We next obtain the expression for the NR phase shift, $\Delta\phi$.

$$\Delta\phi = (\phi_+(d) - \phi_+(0)) - (\phi_-(0) - \phi_-(d)) \quad (19)$$
$$= \tfrac{1}{2}\cot\Phi_g \ln \frac{(\beta_r + 1) e^{\Gamma \sin\Phi_g d}}{\beta_r + e^{2\Gamma \sin\Phi_g d}} \quad (20)$$

In the limit $\Phi_g \to 0$, Eqn 20 becomes

$$\Delta\phi = \tfrac{1}{2}\Gamma d \frac{\beta_r - 1}{\beta_r + 1} \quad (21)$$

The above expression is what prompted Solymar and Wilson to suggest a NR phase shifter. A large product Γd for an input beam ratio much different than 1 can lead to a substantial NR phase shift. Numerical results from the previous chapter suggest values for Γ close to 15 cm^{-1} for $Bi_{12}SiO_{20}$ are possible. This was for transmission geometry and moving fringes. The question we need to ask is how large can the coupling term be for reflection geometry?

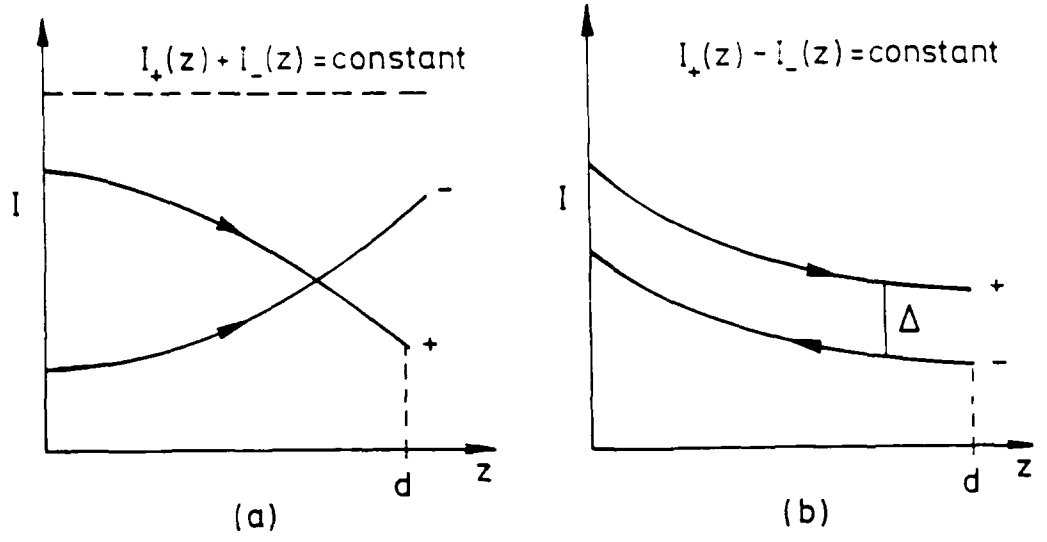

Figure 1: Power conservation in two-wave mixing. (a) Transmission geometry. (b) Reflection geometry.

3.1.3 A numerical treatment

To answer the question of the size of the coupling term we need to obtain an expression for the modulated space charge field, E_{s1}. Before using the procedure of Chapter 2, we should consider power conservation in the reflection geometry. Fig 1 gives a comparison of the two geometries. In the transmission case the total intensity is constant. For wave mixing in the reflection case, $\Delta = I_+ - I_-$. In our analytic treatment this constant difference, $\Delta = -2C$. The important feature is that the total intensity varies across the crystal.

How will a background intensity gradient affect our previous treatment? The d.c. equations in Section 2.1.6 will not be changed. This means the zero order (or background) current density, J_0, is constant. This is a flow, and is the product of a density and a velocity. The density is given by the carrier density, n_0, which is proportional to the total intensity in a given region. The velocity is the drift velocity, and this is proportional to the field E_{s0}. Since J_0 is constant but n_0 is not, this means E_{s0} must vary in space. This is an effect not considered by previous researchers. There is an additional consideration when moving intensity fringes are

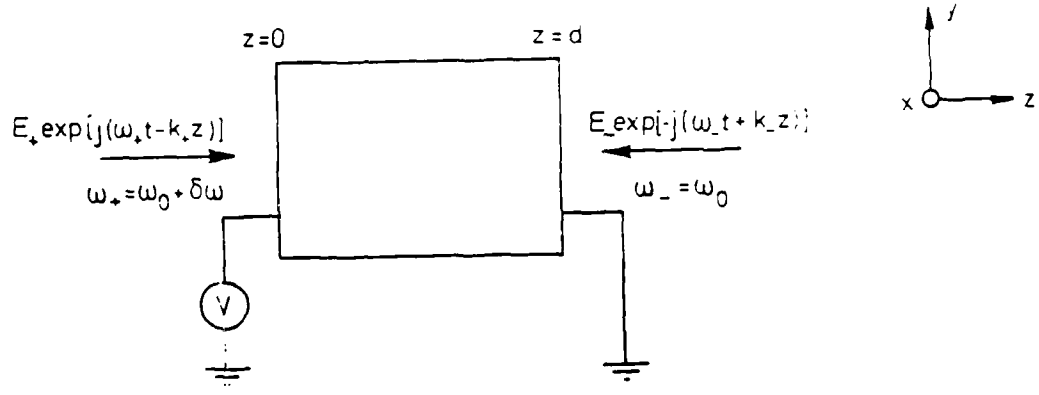

Figure 2: Nearly degenerate two-wave mixing of counterpropagating waves.

present. This is essentially the same argument given in Chapter 2 for gain reduction when absorption is present. Coupling is optimized, for a given total intensity, for one particular fringe velocity. If the total intensity varies across the crystal, then one fringe velocity cannot satisfy the optimum condition everywhere—the gain is less.

The treatment of Sec 2.1 can be modified easily to include a spatially varying intensity. Here the input waves are as shown in Fig 2. Analogous to Eqns 2.5 and 2.10 the driving intensity and normalized quantities have the forms:

$$I(z,t) = I_0(z) + I_1(z)e^{jK(vt-z)} + c.c. \quad (22)$$

$$F_n(z,t) = F_{n0}(z) + F_{n1}(z)e^{jK(vt-z)} + c.c. \quad (23)$$

We assume steady-state conditions for the coefficients. The procedure to find E_{s1} is exactly as outlined in Chapter 2, except all the terms involving the total intensity, such as b and h can have z dependence. One final assumption is needed, namely, the zero order terms vary slowly in space. On the scale of a grating spacing their derivatives with respect to z are negligible compared with those of the first order terms.

With these assumptions, we obtain the following results

$$E_{s0}(z) = \frac{J_0}{\mu e n_0} - E_p \tag{24}$$

$$E_{s1}(z) = -m\frac{E_{s0}(z) + E_p - jE_t}{1 + \frac{E_t}{E_q} + b(z)\frac{E_{s0}(z)}{E_m} + j\left(\frac{E_{s0}(z)}{E_q} - b(z)(1 + \frac{E_t}{E_m})\right)} \tag{25}$$

We should mention that in the derivation of the above, J_0 was found to be constant. As long as a current is present, E_{s0} varies spatially, since the background carrier density, n_0, depends on the total intensity. In this case a further condition on E_{s0} is

$$V = \int_0^d E_{s0}(z)\,dz \tag{26}$$

where V is any applied voltage (possibly equal to zero for the case where only the photovoltaic field drives the current). If E_{s0} varies spatially, so does E_{s1}. If there is no current, then E_{s0} is constant, but E_{s1} will still be spatially dependent if $b \neq 0$.

Previous experiments demonstrating NR transmission used crystals in open circuit configurations [86,140], that is no electrodes or wires and no current flow. If no voltage is applied and $J = 0$, then E_{s0} is constant. This leads to

$$E_{s1\text{open}}(z) = m\frac{jE_t}{1 + \frac{E_t}{E_q} - b(z)\frac{E_p}{E_m} - j\left(\frac{E_p}{E_q} + b(z)\frac{E_t}{E_m}\right)} \tag{27}$$

This is identical to Eqn 25 for $E_{s0} = -E_p$, except the last term in the denominator was $b(1 + E_t/E_m)$. For reflection geometry, $E_t/E_m \gg 1$, so the two expressions reduce to the same thing. In other words, the open circuit configuration can be included as a special case of the closed circuit treatment, for $E_{s0} = -E_p$.

The coupled wave equations are given by Eqns 1-4, except now Γ and Φ_g may vary spatially.

3.1.4 A comparison of the treatments

It is important to compare results using variable coupling with those using constant coupling. The two crystals we will consider are $Bi_{12}SiO_{20}$ and $LiNbO_3$. $LiNbO_3$

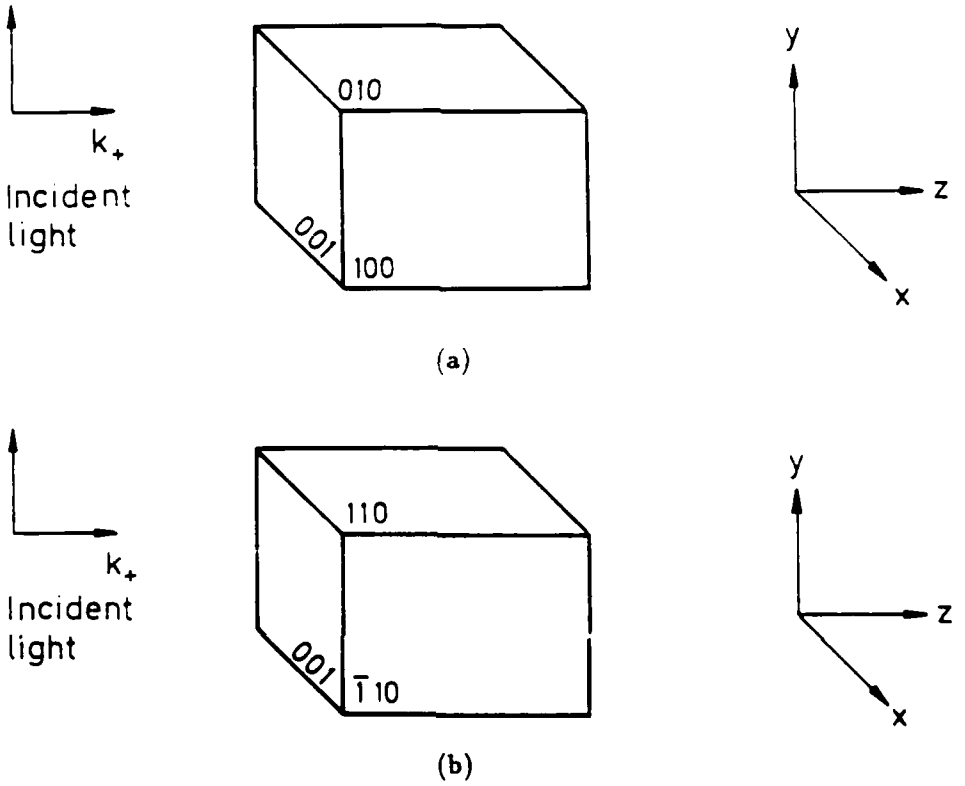

Figure 3: Crystal orientations for counterpropagating waves. (a) $LiNbO_3$. (b) $Bi_{12}SiO_{20}$.

has the advantages of a larger electrooptic coefficient and a photovoltaic effect. The crystal orientations for counterpropagating beams are shown in Fig 3. In both cases any applied voltage will be in the z direction.

Consideration of the electrooptic effect

The photovoltaic field in $LiNbO_3$ acts along the 001 axis. To take full advantage of this field, the two-wave mixing grating vector needs to be in this direction as well.

$LiNbO_3$ belongs to crystal class 3m. In the contracted notation of Yariv and Yeh [135], the electrooptic tensor is

$$\begin{vmatrix} 0 & -r_{22} & r_{13} \\ 0 & r_{22} & r_{13} \\ 0 & 0 & r_{33} \\ 0 & r_{51} & 0 \\ r_{51} & 0 & 0 \\ -r_{22} & 0 & 0 \end{vmatrix}$$

An electric field applied along the 001 (or z or crystal c) axis does not rotate the principal axes, but changes their lengths.

$$\Delta n_{x,y} = -\tfrac{1}{2} n_o^3 r_{13} E \quad (28)$$

$$\Delta n_z = -\tfrac{1}{2} n_e^3 r_{33} E \quad (29)$$

For light polarised in either the x or y direction the relevant electrooptic coefficient is r_{13}. This component is roughly one third that of the largest coefficient (r_{33}), but this orientation was chosen specifically to take full advantage of the photovoltaic field.

For $Bi_{12}SiO_{20}$ the field will be along the 001 axis to optimize the electrooptic effect. This case was worked out in Chapter 2 and we will use the same input polarisations, either in the x or y directions.

The numerical method

The variable coupling terms and the mixed boundary conditions require a numerical treatment for the solution of the coupled wave equations. A common technique to handle mixed boundary conditions is the shooting method [104,61]. The basic approach is to make reasonable guesses for all unspecified function values at one boundary, integrate to the other boundary and compare the computed function values with the known boundary conditions. Revised guesses are made and the cycle repeats until the final function values are within a set tolerance.

In our case we do not know $I_-(0)$ in advance. We use the analytic solution in Eqn 11 to make our first guess. (Here we take the total intensity as $I_+(0) + I_-(d)$

and $E_{s0} = V/d$ in calculating Φ_g and Γ.) $I_-(0)$ is known, and, for convenience, we take $\varphi_+(0) = \varphi_-(0) = 0$. This is justified since, as revealed in Eqns 14 and 15, there is an undetermined constant in each solution.

The set of four coupled differential equations is integrated using a fourth-order Runge-Kutta routine. If the calculated value for $I_-(d)$ is not within a tolerance of 0.1 % then a new guess for $I_-(0)$ is found via a Newton-Raphson method.

A further integration is required after each iterative cycle to choose J_0 such that the condition in Eqn 26 is satisfied. Combining Eqns 25 and 26 gives

$$J_0 = \mu e \frac{V + E_p d}{\int_0^d dz / n_0(I)} \tag{30}$$

where the total intensity, $I(z)$, is updated on each iteration.

Figs 4-6 show comparisons between the numerical method outlined here and the analytic and numerical methods of Refs [59,136] which assume constant coupling. In all plots the crystal length is taken to be 1 cm, the wavelength of the incident light is 514 nm, and the temperature is 300 K. For $LiNbO_3$ the photovoltaic field is chosen to be 15 kV/cm, a typical value.

The coupling in $LiNbO_3$ is strong and there is significant variation of intensity across the crystal. This is seen in both the intensity and phase solutions to the coupled wave equations (Figs 4a,b and 5a,b). Figs 4c and 5c depict the variation of E_{s0}. Figs 4d and 5d illustrate that the coupling terms do vary across the crystal.

The conditions for Fig 4 were chosen to illustrate the case of no moving fringes. The input beam ratio is 0.1 and the variable coupling solution for intensity shows less power transferred between the beams. The difference between the analytic and numerical treatments shown in Fig 5a, where only the photovoltaic field drives the current, is not as disparate. That is because the intensity coupling term, $\Gamma \sin \Phi_g$, does not have a large spatial variation. What is interesting, though, is that the phase coupling term, $\Gamma \cos \Phi_g$, changes sign as we move across the crystal. The difference in behaviour for the phase solutions between the two methods, as seen in Fig 5b, is quite dramatic.

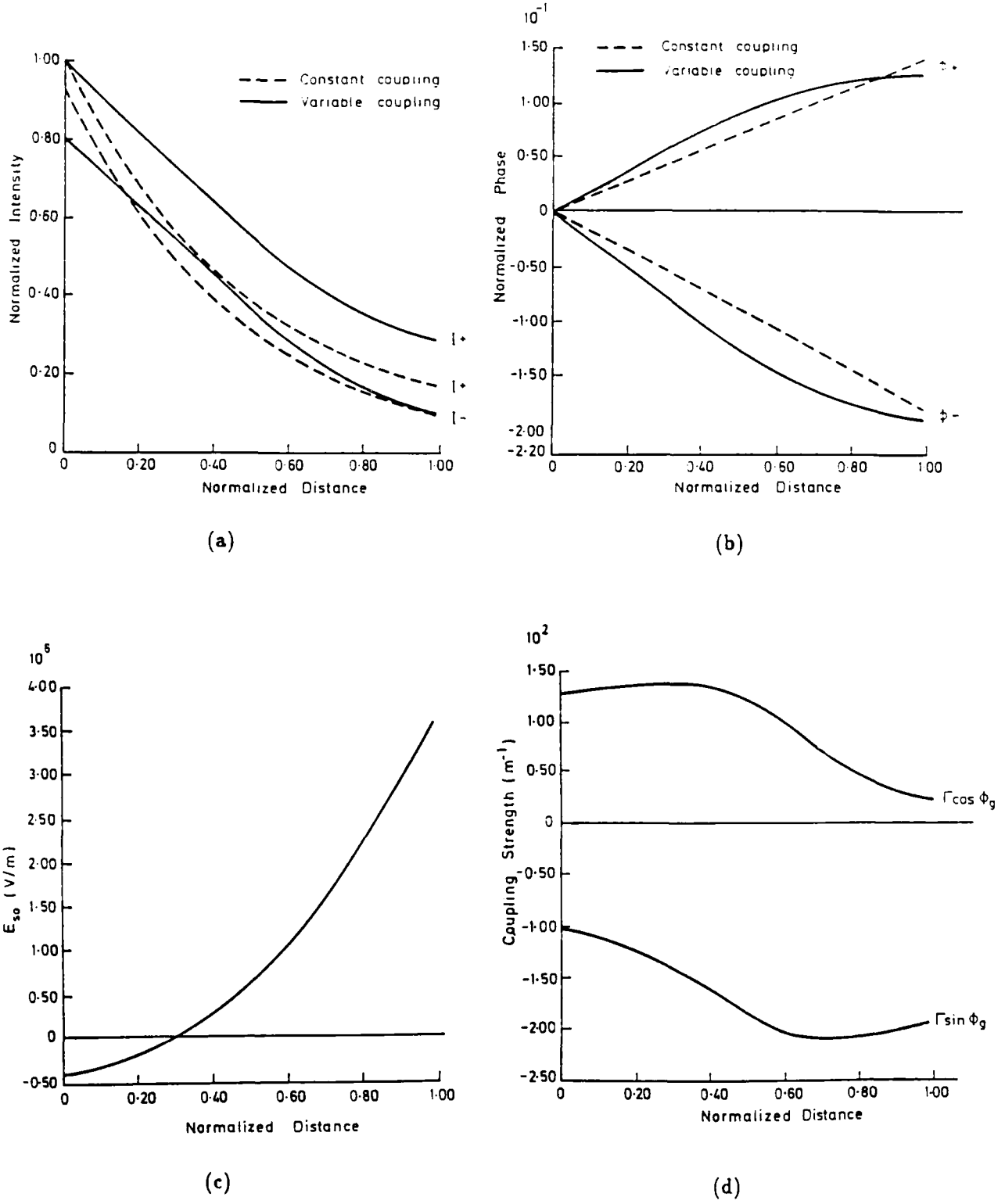

Figure 4: $LiNbO_3$. $V = 10$ kV, $I_+(0) = 10$ mW/cm^2, $J_0 = 8.01 \times 10^{-5}$ A/m^2, fringe velocity = 0, no absorption. Intensity is normalised to $I_+(0)$, phase is normalised to π

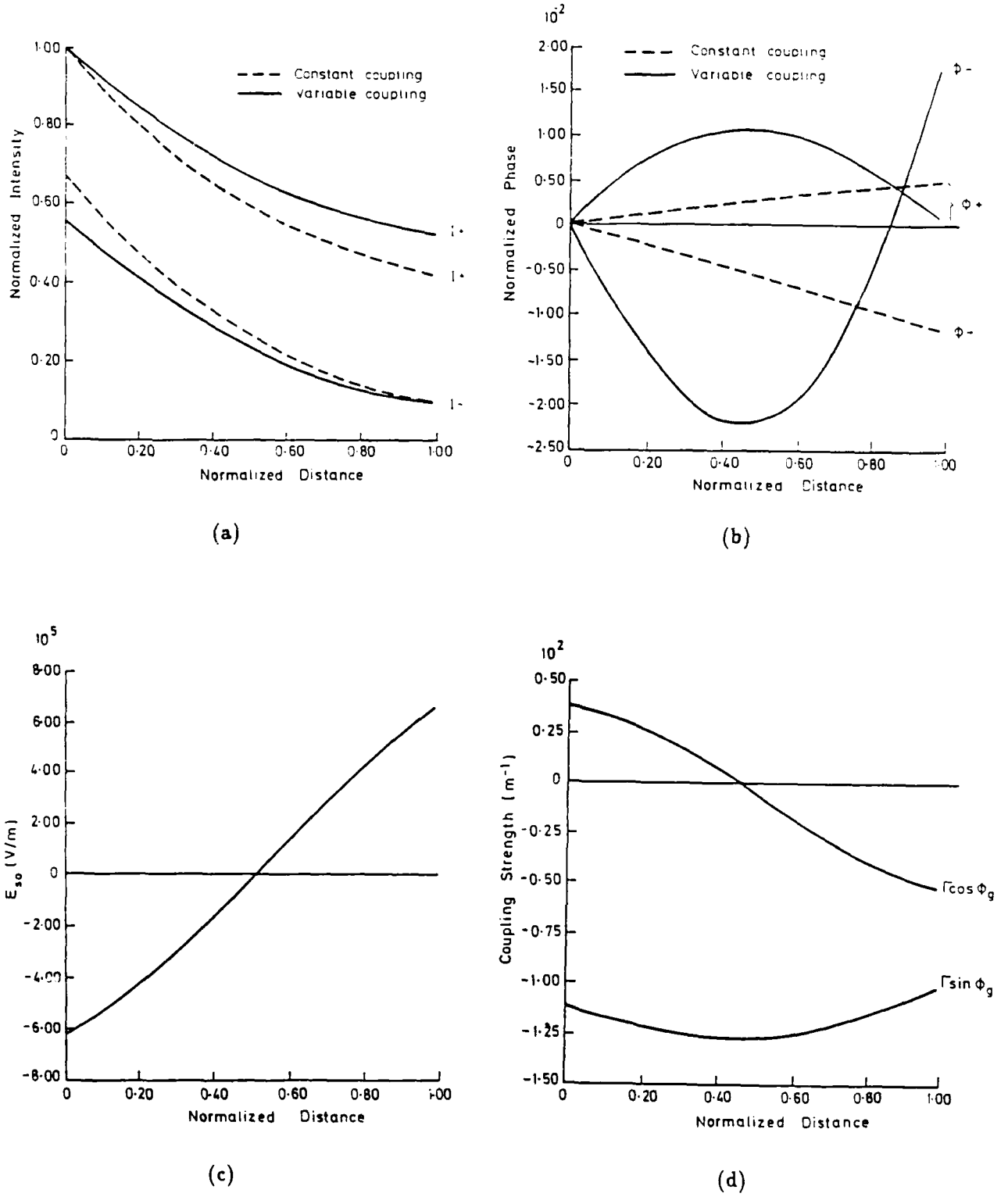

Figure 5: $LiNbO_3$. $V = 0$, $I_+(0) = 100$ mW/cm^2, $J_0 = 5.52 \times 10^{-5}$ A/m^2, fringe velocity $= -5.0 \times 10^{-9}$ m/s, no absorption. Intensity is normalised to $I_+(0)$, phase is normalised to π

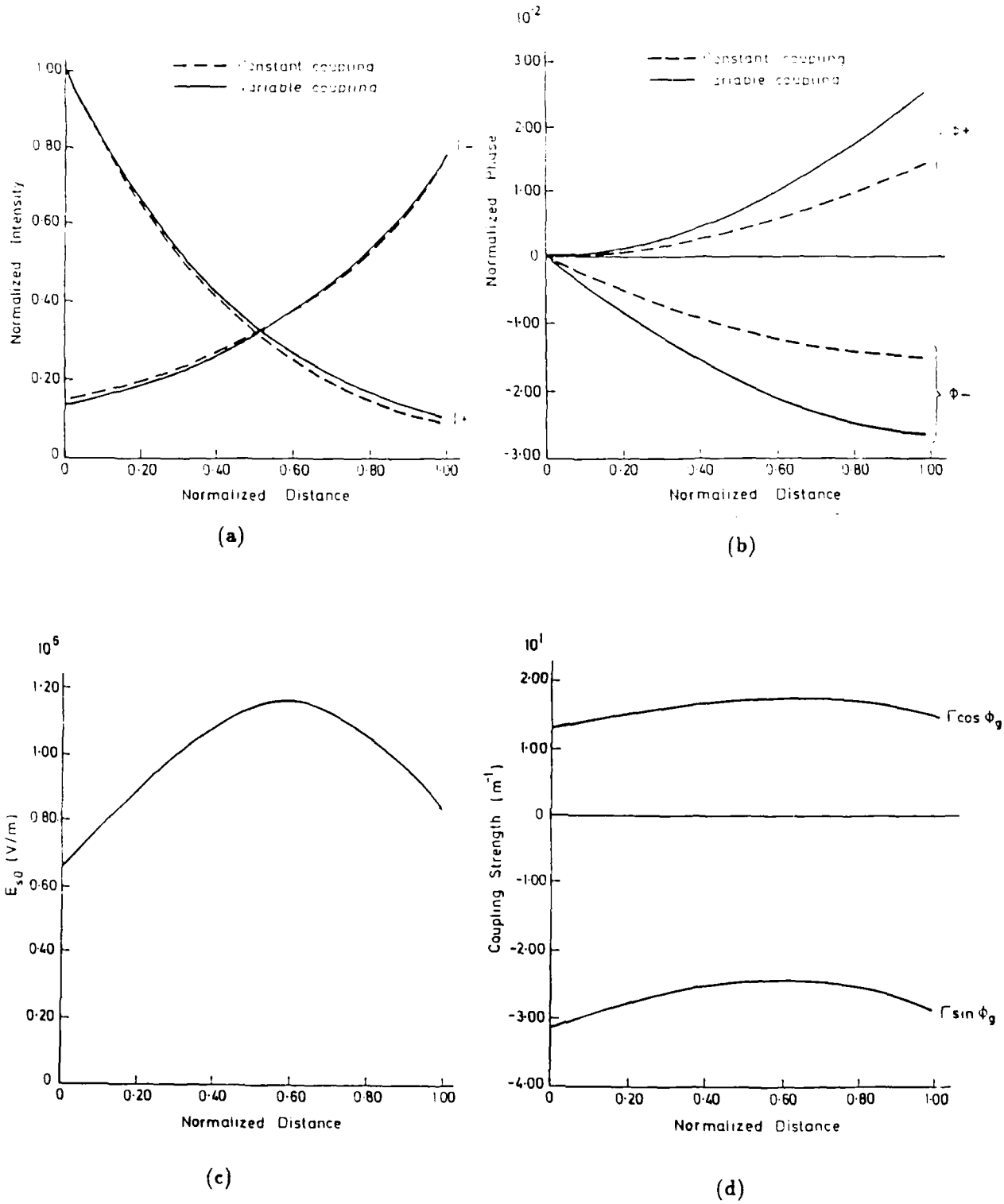

Figure 6: $Bi_{12}SiO_{20}$. V = 10 kV, $I_+(0)$ = 10 mW/cm^2, J_0= 0.0456 A/m^2, fringe velocity = 1.5x 10^{-8} m/s, α = 2 cm^{-1}. Intensity is normalised to $I_+(0)$, phase is normalised to π.

Coupling is not strong in $Bi_{12}SiO_{20}$ and the two treatments yield essentially the same solutions. If absorption is present, though, the intensity variation across the crystal is greater, and some divergence between the methods might be expected. Since we are using a numerical method to treat the variable coupling case, it is relatively simple to include absorption in our treatment. The intensity coupled equations become

$$\frac{dI_+}{dz} = 2\Gamma \sin\Phi_g \frac{I_+ I_-}{I_+ + I_-} - \alpha I_+ \tag{31}$$

$$\frac{dI_-}{dz} = 2\Gamma \sin\Phi_g \frac{I_+ I_-}{I_+ + I_-} - \alpha I_- \tag{32}$$

We can compare this with the numerical treatment with absorption for constant coupling in Ref [59]. Figs 6a-d consider absorption in the case of $Bi_{12}SiO_{20}$. Here α is taken as 2 cm^{-1}, a value found experimentally for some $Bi_{12}SiO_{20}$ samples [31]. The difference in the two treatments is more apparent in the phase solutions.

We argued at the beginning of this subsection, from physical principles, that moving fringes, absorption, or a photocurrent leads to variable coupling in reflection geometry. That was confirmed in the derivation of E_{s1}. That this variable coupling is a significant effect is seen in Figs 4-6.

We have a suitable numerical treatment with which to solve the coupled wave equations for counterpropagating beams. Now we have the means to calculate NR effects and consider various control parameters. Two potential control parameters are applied voltage and fringe velocity. It is unfortunate that these represent the cases where we most need the numerical treatment.

3.2 Nonreciprocal Effects

The origin of the laurel tree, according to ancient Greeks, began with an unkind remark. One day Apollo chided Cupid for playing with arrows—such devices were surely meant for more mature hands. Apollo's assessment of Cupid's character was spot on, for no sooner had he turned his back, but Cupid fired a gold-tipped arrow

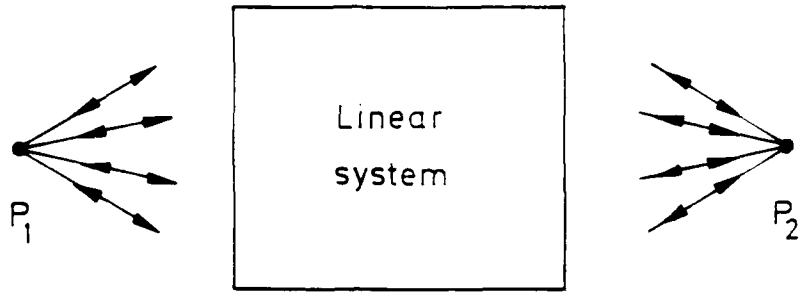

Figure 7: Principle of reciprocity. Source at P_1 and detector at P_2 may be interchanged and still produce the same effect.

at him. This caused Apollo to fall hopelessly in love with Daphne, a wood nymph. The god of love then struck Daphne with a lead-tipped arrow. Her heart hardened and she could love no man, particularly Apollo. She fled and Apollo pursued. He had nearly overtaken the nymph when her father, Peneus, interceded and changed her into a laurel tree. This is an interesting and early example of the dramatic consequences of nonreciprocity.

To understand NR effects, we should start with the principle of reciprocity. Fig 7 illustrates this principle, most commonly attributed to Helmholtz [42]. A source and a detector may be placed, one at P_1 and the other at P_2. If the system through which the light signal passes is linear, then reciprocity holds: the measured signal (amplitude and phase) will be the same whether the source is at P_1 and the detector is at P_2 or vice versa. If the intervening system is nonlinear, then NR behaviour is possible.

For two-wave mixing in photorefractive materials there are two types of NR effects—transmission and phase shift.

3.2.1 Nonreciprocal transmission

NR transmission is merely a fancy name for power transfer. If one mixing wave gains at the expense of the other, then $T_+ = T_-$. This effect was demonstrated experimentally in $KNbO_3$:Mn by Zha and Günter [140]. For an open circuit crystal with beams of equal input intensity, they measured $T_+ = 113\%$ and $T_- = 57\%$. MacDonald, et al., used $BaTiO_3$ to investigate "assymmetric transmission" [85]. A single input beam was used and the counterpropagating beam was the back surface reflection of the input. They found the transmission through the crystal depended on whether the input was parallel to the crystal c axis ($T = 52\%$) or antiparallel ($T = 39\%$). The asymmetry is a consequence of the one-way power transfer in photorefractive crystals. For one orientation of the c axis the reflected beam gained at the expense of the input, for the opposite orientation it lost power. A complete treatment of the problem involves multiple reflections. The reflection at the rear surface depends on the steady-state intensity solution. This is worked out in detail in Ref [137]. If this effect could be enhanced, one could use a photorefractive crystal as an optical diode.

The potential control parameters for NR effects are applied voltage, beam ratio and fringe velocity. We investigate these controls using $LiNbO_3$ as the medium, and, in most cases, consider the effect of different values for the photovoltaic field. In all plots the crystal length was 1 cm, the temperature 300 K, and the wavelength 514 nm. The crystal parameters are taken from Table 2.1.

Figs 8 a and b show the transmissions as functions of applied voltage for input beam ratios, β_r, of 1 and 0.1 with no moving fringes. Substantial power is transferred from the plus beam to the minus beam. Physically this is due to being in the diffusion dominated regime and having a long interaction length. The photovoltaic field is taken to act in the $+z$ direction, so a positive polarity voltage enhances the NR transmission, while a negative polarity detracts.

Transmission (T_-) as a function of beam ratio is shown in Fig 9 for no

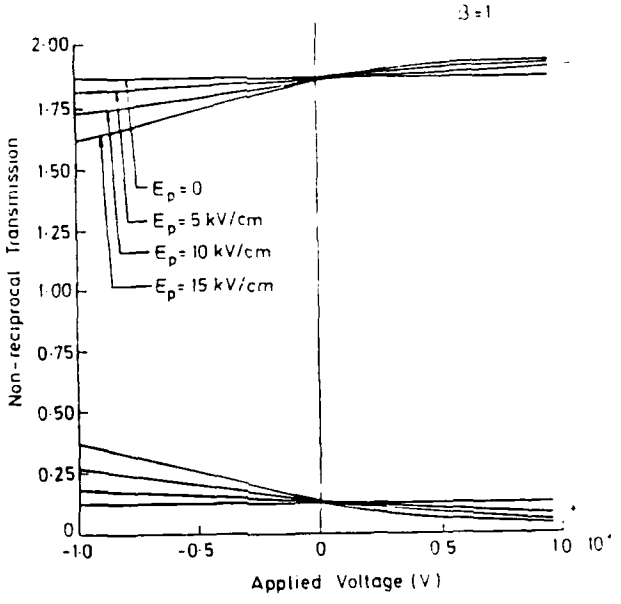

(a)

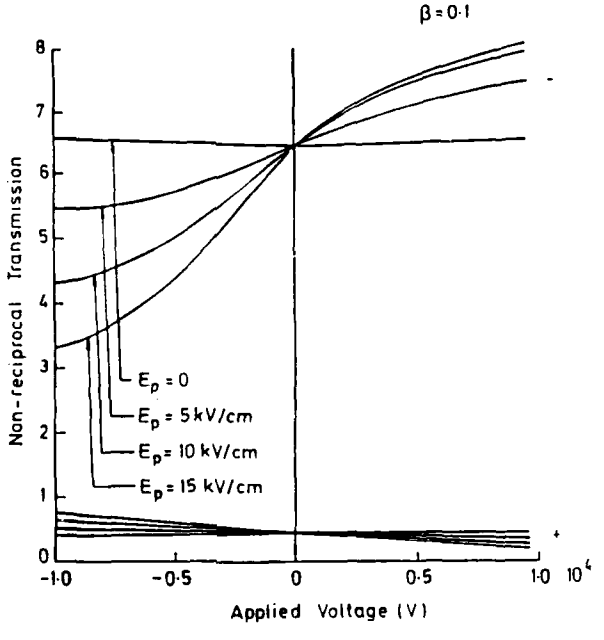

(b)

Figure 8: Transmission vs applied voltage. (a) $\beta_r = 1$. (b) $\beta_r = 0.1$.

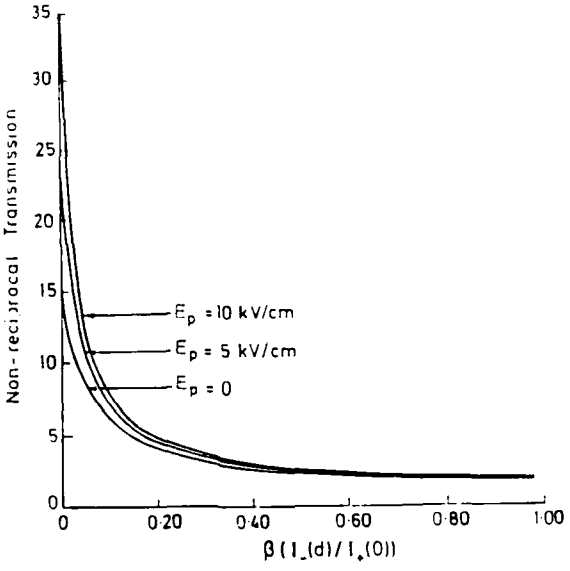

Figure 9: Transmission vs beam ratio.

applied voltage and no moving fringes. A photovoltaic field increases the transmission, and the gain is larger for smaller beam ratios.

Some interesting effects are seen when moving intensity fringes are present (Fig 10a). Here no voltage is applied, the beam ratio is 1, and the total input intensity is 200 mW/cm^2. With no photovoltaic field the coupling is still strong and the behaviour is symmetric. As this field increases the asymmetry with fringe velocity is more apparent. The maximum NR transmission is no longer at $v = 0$, and for positive fringe velocity it is possible to change the direction of power transfer. The key feature here is that moving fringes can be used to reduce the NR effect. The magnitude of fringe velocity ($\sim 10^{-8}$ m/s) at this relatively strong intensity is very small. This corresponds to a detuning frequency of 0.7 Hz. If the intensity is reduced, the detuning frequency required to achieve the same effect goes down.

In Fig 10b, $E_p = 15$ kV/cm, $V = 10$ kV, $\beta_r = 0.1$, and the total intensity is 200 mW/cm^2. Here we plot J_0 as well. Notice that J_0 has a minimum close to the fringe

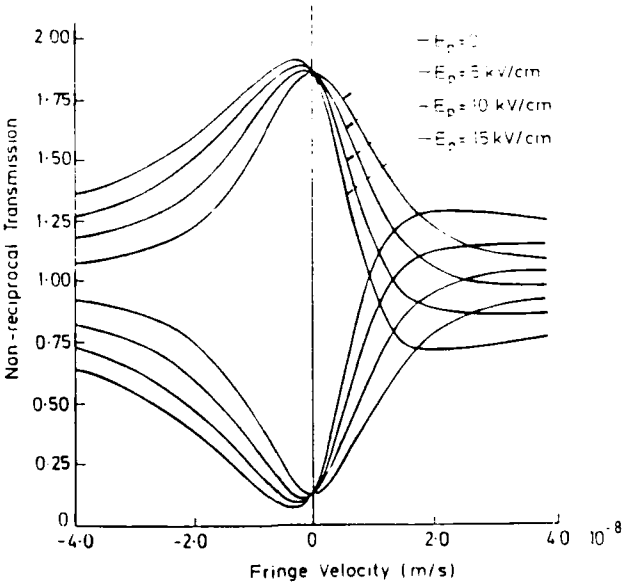

(a)

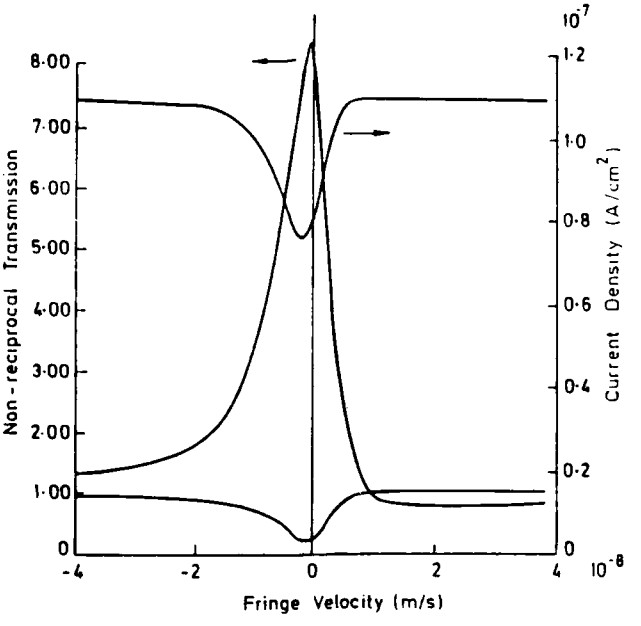

(b)

Figure 10: Transmission vs fringe velocity. (a) $\beta_r = 1$. (b) $\beta_r = 0.1$. Also plotted is the current density.

velocity at which the NR transmission is optimized. Physically we can understand this by looking at Fig 4a for the solution to the intensity coupled wave equations. The steady-state background current density depends on the background carrier density, which is driven by the total itensity. For very strong coupling, the space average total intensity is *less* than the total input intensity. This means the current density is reduced. This is a useful effect for device applications. We can monitor beam coupling by measuring the photocurrent—there is no need to sample either of the beams.

3.2.2 Nonreciprocal phase shift

Phase coupling between counterpropagating beams was evident in Figs 4-6. Thus we expect a difference in phase shifts encountered by the two mixing waves. We need to investigate the influence of various control parameters on this effect.

We define NR phase shift, $\Delta\phi$, as in Eqn 19. We use $LiNbO_3$, a crystal length of 1 cm, temperature of 300 K, and a wavelength of 514 nm. Figs 11a and b show $\Delta\phi$ as a function of applied voltage for no moving fringes and beam ratios of 1 and 0.1. Here the NR phase shift is normalised to π. A photovoltaic field is necessary to produce an appreciable effect. It is evident the sign of $\Delta\phi$ depends on beam ratio. This is shown in Fig 12 for an applied voltage of 10 kV.

The effect of fringe velocity is seen in Figs 13a-d. Here $V = 10$ kV and $I_+(0) = 100$ mW/cm^2. Three values of β_r, 1, 0.4, and 0.01, are shown. Note the difference in behaviour for the plots $\beta_r = 1$ and $\beta_r = 0.01$. The sign of $\Delta\phi$ for a given fringe velocity is essentially reversed between the two cases. $\beta_r = 0.4$ lies in the transition range.

The largest NR phase shift is roughly $-\pi/2$ for $E_p = 15$ kV/cm and $\beta_r = 0.01$. Fig 13d shows the close relationship between input intensity and optimum fringe velocity. The beam ratio in this figure is kept constant while the intensity, as given by $I_+(0)$, varies. Each curve represents a different fringe velocity and each one has

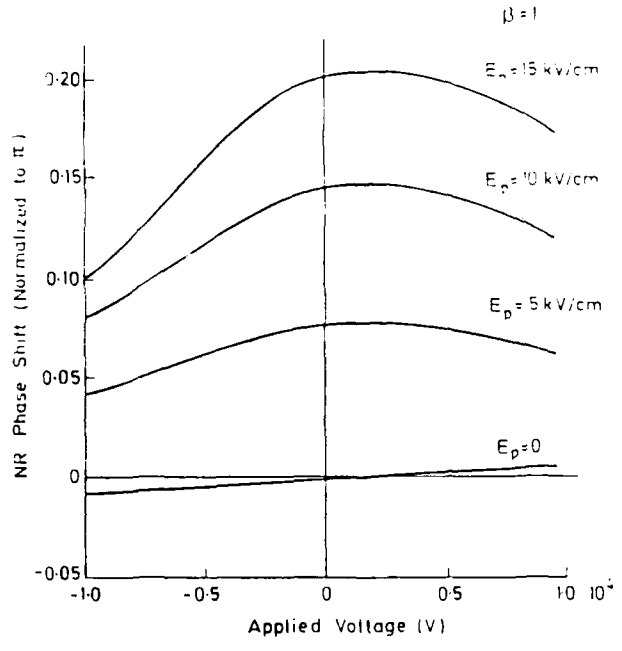

(a)

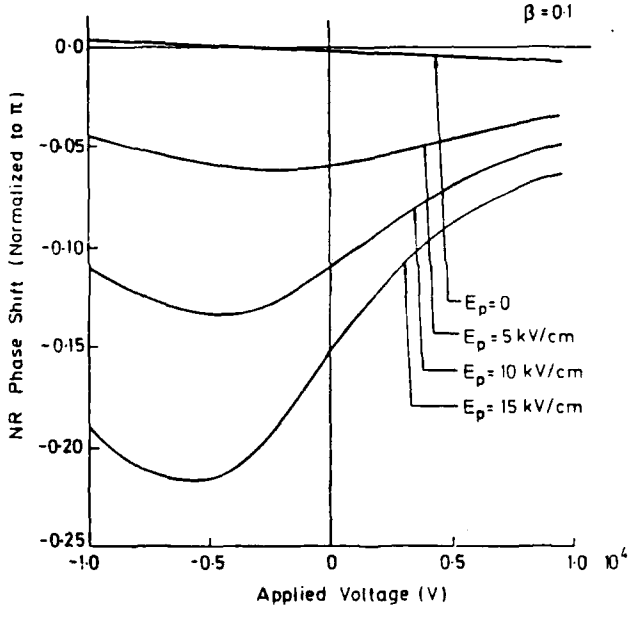

(b)

Figure 11: NR phase shift vs applied voltage. (a) $\beta_r = 1$. (b) $\beta_r = 0.1$.

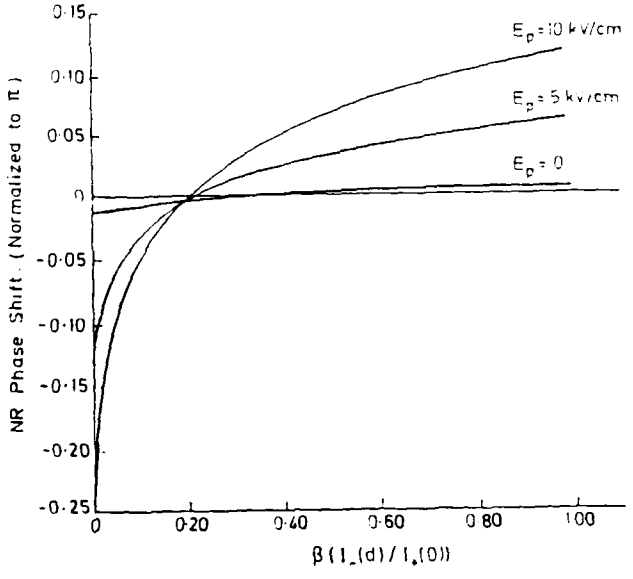

Figure 12: NR phase shift vs beam ratio.

an optimum for a different value of $I_+(0)$. (The guiding principle for photorefractives is the greater the intensity, the faster the reaction.) The optimum value of $\Delta\phi$ is the same for each curve. This suggests that a device capable of seeking out this optimum could be used to measure intensity by varying fringe velocity, or to detect movement by varying intensity.

3.3 Assessment and Design Considerations

3.3.1 Control parameters

In the previous section three control parameters were studied—applied voltage, beam ratio, and fringe velocity. (The effect of a fourth parameter, the input intensity was found to be dependent upon the fringe velocity.) Let us discuss each control separately.

1. ***Applied voltage.*** In the absence of a photovoltaic field, applied voltage is

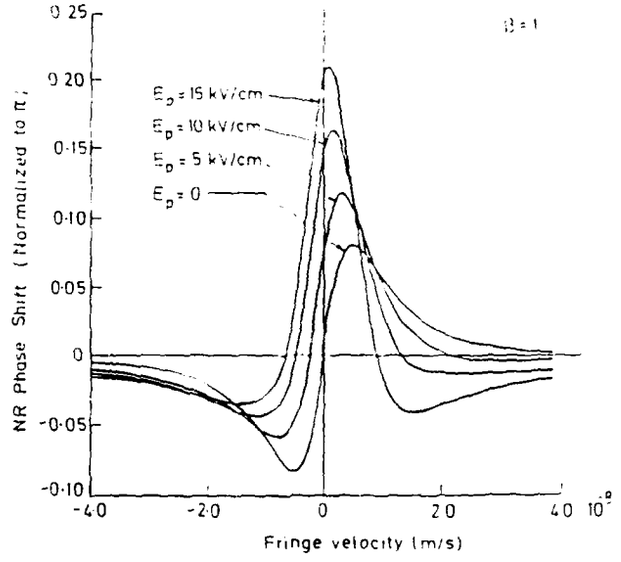

(a)

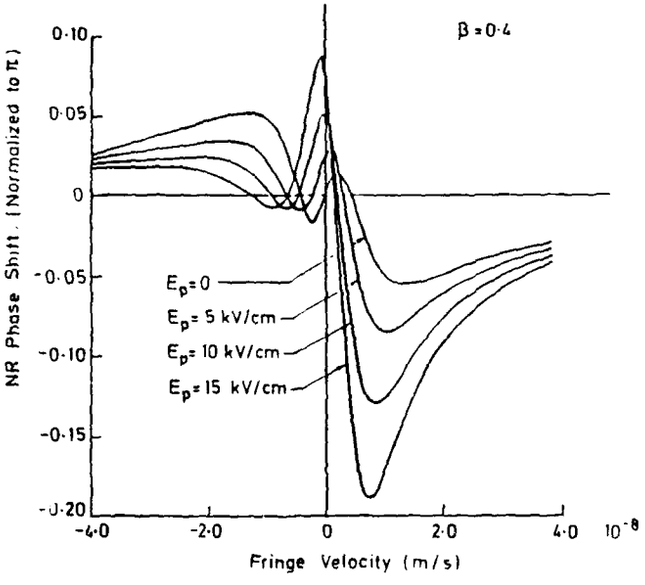

(b)

Figure 13: NR phase shift vs fringe velocity. (a) $\beta_r = 1$. (b) $\beta_r = 0.4$.

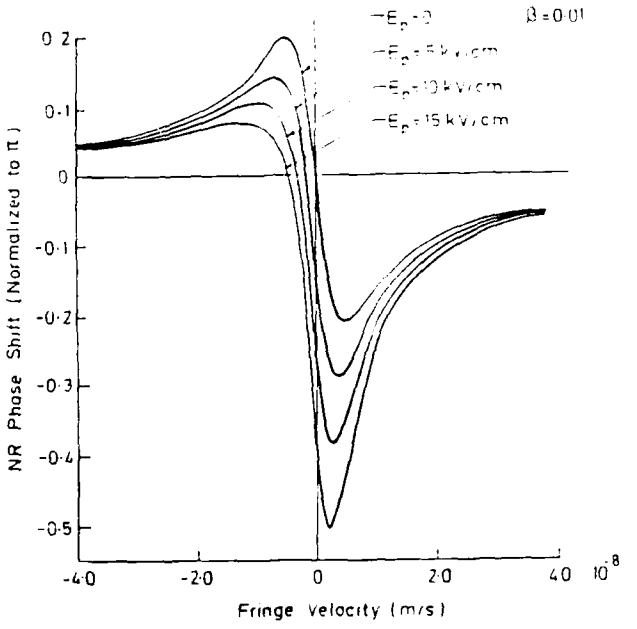

(c)

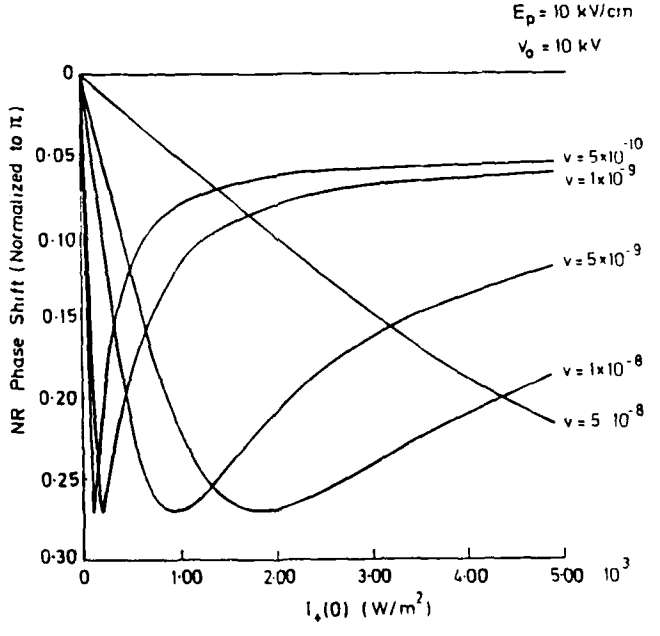

(d)

Figure 13: NR phase shift vs (c) fringe velocity for $\beta_r = 0.01$. (d) $I_+(0)$ for $\beta_r = 0.1$. In (d) the different curves refer to different fringe velocities (m/s).

not a useful control parameter for NR behaviour. Its effectiveness is increased for smaller beam ratios. To apply a voltage, transparent electrodes are required.

2. *Beam ratio.* In most practical applications, the input beam ratio will be fixed in advance, or allowed to reach some steady-state value (such as in a feedback circuit like a bidirectional ring resonator). Thus this parameter has limited potential as a control. In general, the lower the input beam ratio, the greater the NR effects. For a given fringe velocity, the beam ratio determines the sign of the NR phase shift.

3. *Fringe velocity.* This is the best candidate for a control parameter as it offers the widest range for NR effects. The reason it is so effective is that coupling between the beams is only strong for a small range of fringe velocities close to 0. If a strong photovoltaic field exists, one can use fringe velocity to change the direction of power transfer. There are two drawbacks to using fringe velocity as a control. In many applications it will be undesirable to frequency shift one beam relative to the other. In such a case moving fringes can be produced by moving the crystal at the desired speed by mounting the crystal on a piezoelectric translator driven by an applied sawtooth voltage. The second drawback is the very slow velocities required to achieve strong NR effects, even for moderate intensities. Fringe velocity may be impractical to use for low intensity two-wave mixing.

3.3.2 Comparison of crystal types

The previous section concentrated on $LiNbO_3$ as the nonlinear medium. Table 1 compares NR effects for three crystal types ($Bi_{12}SiO_{20}$, $BaTiO_3$, and $LiNbO_3$), using fringe velocity as the control. These are representative values for similar conditions. In each case the crystal length was 1 cm, the wavelength 514 nm, the temperature 300 K, the input beam ratio was 1, the total input intensity was 200 mW/cm^2, and the beams propagated along the crystal c axis. There will be some minor differences between the crystals, though, to increase NR effects—namely, the $LiNbO_3$ sample should have a photovoltaic field (we took the value 10 kV/cm in our comparison),

Crystal	*Maximum Transmission*	*Maximum NR Phase Shift*	*Fringe Velocity Scale (m/s)*
$Bi_{12}SiO_{20}$	1.33	$6.1 \times 10^{-3}\pi$	10^{-6}
$BaTiO_3$	1.92	$0.12\ \pi$	10^{-7}
$LiNbO_3$	1.91	$0.17\ \pi$	10^{-8}

Table 1: Comparison of NR effects for different crystals.

while in $Bi_{12}SiO_{20}$ we should apply a voltage (here we used a value of 10 kV). $LiNbO_3$ seems to give the best combination of transmission and NR phase shift, but requires the slowest fringe movement. If a strong photovoltaic field is present, one can use fringe velocity to change the direction of power transfer.

3.3.3 Magnitude of nonreciprocal effects

This study revealed that the largest calculated NR phase shift ($< \pi/2$) is less than expected from Eqn 21. In that expression, when $\Phi_g \rightarrow 0$ then, for small beam ratios, $\Delta\phi \approx \Gamma d$. The difficulty with this simple analysis is that Γ and Φ_g do not have constant values for the combinations of control parameters necessary for drift domination. But we can consider what happens when intensity coupling is reduced—this should correspond to conditions where phase coupling is strong. For example, in Fig 10a there are specific values of fringe velocity where $T_+ = T_-$. For these velocities, the spatial average of Φ_g should be close to 0. When we compare $\Delta\phi$ in Fig 13a we see these velocities are not where the NR phase shift is optimized. In other words, conditions which take the average value of Φ_g to 0 also tend to reduce the magnitude of Γ. This makes sense, Γ and Φ_g are not independent, but are linked through E_{sc1}.

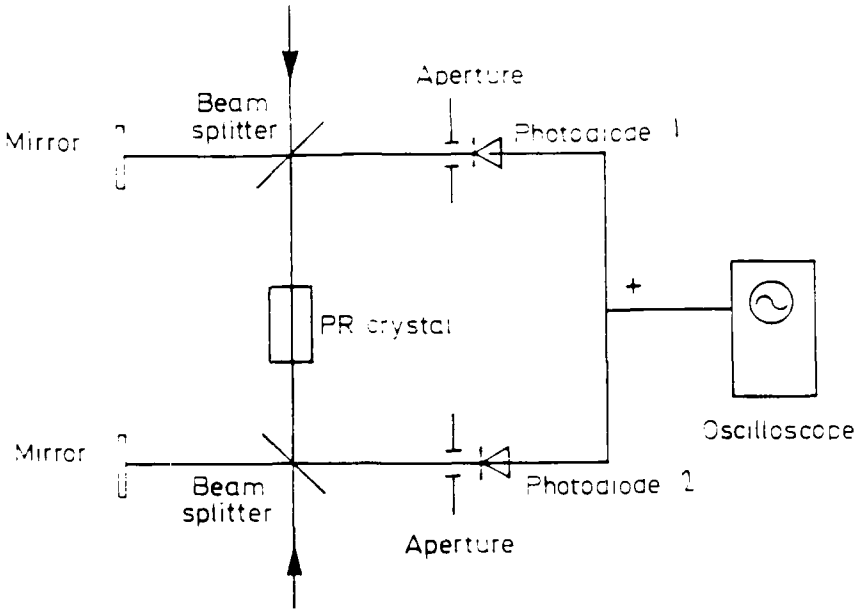

Figure 14: Measurement of NR phase shift for nondegenerate two-wave mixing.

3.3.4 Measurement of nonreciprocal phase shift

It is difficult to measure the phase of a wave directly. Instead it is common practice to combine the wave with a reference wave (of unspecified phase) and measure the phase difference. This, in essence, is what is done in an interferometer. In a similar way we do not measure the NR phase shift, but its change as we adjust control parameters. A scheme involving frequency shifted input beams is illustrated in Fig 14. After mixing in the crystal each transmitted beam is combined with a reference beam in a Mach-Zehnder interferometer arrangement to produce a moving interference fringe pattern which can be measured by photodetectors 1 and 2. Both intensity patterns have the same angular frequency but independent phases. Part of the difference in phases is due to the NR phase shift, $\Delta\phi_{NR}$, the rest a consequence of optical path differences between the various combining waves, $\Delta\phi_{OPL}$. For convenience we may separate these phases and consider the intensity patterns

to be described by $A_1 \sin(\delta\omega t - \Delta\phi_{OPL})$ and $A_2 \sin(\delta\omega t - \Delta\phi_{NR})$. The combination of these two signals gives another sinusoidal function with amplitude A_T. The total phase difference is related to the amplitudes of these three signals by

$$\Delta\phi_{NR} - \Delta\phi_{OPL} = \cos^{-1} \frac{A_T^2 - (A_1^2 + A_2^2)}{2A_1A_2} \tag{33}$$

We can eliminate $\Delta\phi_{OPL}$ by changing control parameters and making a second measurement. We are left with the change in $\Delta\phi_{NR}$. A bit more algebra is required to extract the transmissions from the amplitudes.

3.3.5 Experimental attempts

Our $LiNbO_3$ samples proved very difficult to work with. Previous research with crystal samples in the group was plagued by noise and non-repeatability [91]. The noisiness of signals hampered our effects as well. Of the dozen or so crystals of $LiNbO_3$ available, only one was found with the proper cut—polished faces normal to the c axis. No $Bi_{12}SiO_{20}$ crystals had the proper orientation. The sample had a large interaction length, 1.3 cm, and the crystal was used in an open circuit configuration. A set-up was similar to Fig 14 except the detectors just measured the transmitted signal—the mirrors were blocked off and no moving fringes were produced at the detectors. Moderate intensity (10-30 mW/cm^2) input beams produced independent, noisy, transmitted signals. The fringe velocity was limited to no slower than 5×10^{-9} m/s and for this value, little power transfer was expected. A new attempt was made mixing unexpanded beams. Fig 15 shows typical simultaneous readings. Coupling between the beams is evident in that one trace has peaks where the other trace has depressions and vice versa. The noise was not due to any fluctuations in the laser output. Removing the crystal produced flat, steady signals at the detectors.

We borrowed a second sample of $LiNbO_3$ with polished c faces from the University of Osnabruk. This had a large photovoltaic field (35 kV/cm) but a very small interaction length (2 mm), and produced similar noisy traces with hints of beam coupling.

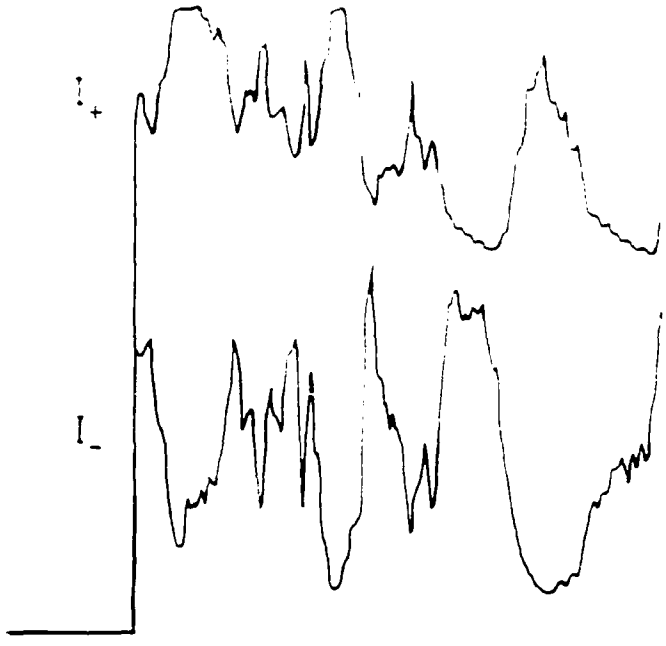

Figure 15: Typical traces for transmitted beam intensities. The signals are very noisy, but beam coupling is evident.

One cannot make sweeping generalizations from looking at just two samples, but obtaining poor results from two crystals of very different origins bodes ill for the use of $LiNbO_3$ in nonreciprocal applications.

3.3.6 Limitations

Numerical methods, particularly ones involving iteration, are prone to instability. Our treatment was no exception. For values of E_p greater than 15 kV/cm and positive fringe velocities, the computer program would not converge to a particular solution. Instead it seemed to oscillate between two solutions. Nonlinear materials often exhibit bistable behaviour, and the mathematical model may be pointing to a region where $LiNbO_3$ is optically bistable—two possible intensity states for the same input.

The presence of absorption dramatically slowed down convergence, and scores

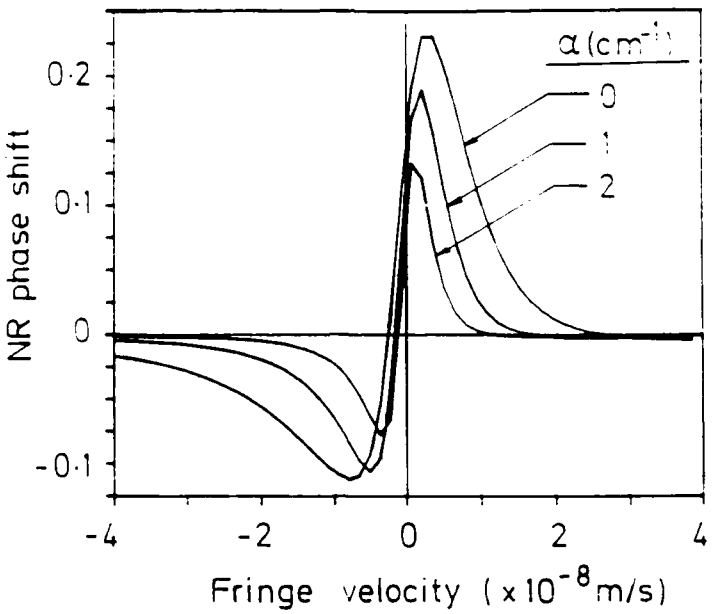

Figure 16: NR phase shift vs fringe velocity for various values of absorption.

of iterations typically were required. This is likely due to the poor initial guess calculated from the numerical treatment of Ref [59]. But absorption has been studied, and Fig 16 shows that a healthy attenuation constant of 2 cm^{-1} reduces the maximum NR phase shift by a factor of 2. The conditions are the same for Fig 13a with $E_p = 10$ kV/cm.

The question of modulation depth is important here. The solutions to the intensity coupled wave equations shown in Figs 4a, 5a and 6a reveal there are regions in the crystal in which m is not much smaller than 1. Indeed, for the $Bi_{12}SiO_{20}$ plot, the intensity solutions cross, so there is one point where $m = 1$. As suggested by Ref [8], we may expect a reduction in photorefractive coupling for higher modulation depths. Taking this into account may lower the expected magnitude of NR effects.

3.4 Conclusions

This chapter began by posing the question: Can photorefractive materials be used in the design of a nonreciprocal phase shifter? The answer is yes, but there are several drawbacks.

The effect is small, several times less than that obtainable from magnetooptic NR phase shifters. For use in a fibre-optic ring laser gyroscope, this might be adequate, for the round-trip optical path difference between counterpropagating beams is typically much less than a wavelength [22]. However there is a concurrent effect which might be undesirable in a resonator—power is transferred between the beams. Decoupling these effects would be difficult. The best control parameter, fringe velocity, requires delicate and precise movement of either a mirror or the crystal itself. Of the three crystal types studied, the material with the largest theoretical NR behaviour, $LiNbO_3$, has produced poor experimental results.

Our research has shown, however, that NR transmission effects in photorefractive materials have great potential. It has been suggested to use a photorefractive crystal as an optical diode, but we have shown that using fringe velocity one can control the strength of the beam coupling, reduce it to negligible coupling, or even change the direction of power transfer.

An interesting byproduct of this study is a numerical method for treating two-wave mixing with spatially variable coupling. The techniques described should be readily adaptable to other geometries.

Chapter 4

Unidirectional Ring Resonator

One ring to bring them all and in the darkness bind them.

J.R.R. Tolkein

(a fellow Mertonian)

Beam coupling in photorefractive materials often results in power transfer. As discussed in Chapter 2, this light intensity interchange is described by a gain coefficient, $2\,\Gamma \sin \Phi_g$, which has a maximum in $Bi_{12}SiO_{20}$ with moving fringes when $\Phi_g = 90°$. A photorefractive crystal with high gain can be used as the active medium in a resonator. Oscillation will occur as long as the photorefractive gain exceeds losses due to absorption, diffraction and reflection from optical elements in the cavity. We will see that the oscillating beam chooses a path whose length satisfies the phase condition for resonance—namely one roundtrip represents an accumulated phase which is an integer multiple of 2π.

Optical resonators with photorefractive gain are the subject of keen interest, particularly in concert with phase conjugating mirrors [28]. The interest is understandable—phase conjugating mirrors retroreflect incident light, reversing the phase, so any aberrating effects in the resonator cavity may be corrected, and the reflectivity can exceed unity. (Of course there are different theoretical considerations

in a system which, in effect, folds the optical path. For example, the concept of cavity length loses its meaning.) Many of the applications of photorefractive crystals discussed in Chapter 1, such as in optical computing, image processing, and associative memories, utilise such optical resonators.

Most of the work with these resonators uses $BaTiO_3$, and many configurations are discussed in Ref [131]. We were interested in seeing if one design in particular, the linear resonator, would work using $Bi_{12}SiO_{20}$ as the gain medium. (The linear resonator is discussed in greater detail in Chapter 5.)

A good starting place for the understanding of resonator operation with photorefractives is the unidirectional ring resonator (URR). In this tried-and-true arrangement, a photorefractive crystal is placed in a leg of a resonator formed by three or more mirrors (see Fig 1). A single input beam incident on the crystal generates scatter, some of which may be captured in the resonator and amplified. This arrangement has been explored using $BaTiO_3$ by White, et al. [131], Kwong, et al. [79], and Fischer [38]. $BaTiO_3$ has very high gain due to its large electrooptic effect and one can induce oscillation at very low light intensities ($\approx 50\mu W/cm^2$ at 633 nm), and may even achieve bidirectional operation. Rajbenbach and Huignard reported a study of the URR using $Bi_{12}SiO_{20}$[105]. In a material like $Bi_{12}SiO_{20}$ wave propagation in the resonator is unidirectional because the applied electric field enhances the gain for beams in the transmission geometry, but not in the reflection geometry.

A URR is relatively easy to set up (as much as any resonator can be), oscillation is self-starting (no need for a seed beam), and the gain can be quite large. We felt the experience gained in working with the URR would serve us well later.

We start this chapter with a short review of the pertinent theory of two-wave mixing and derive an analytic solution to the intensity coupled wave equations in the presence of absorption. Then we consider the feedback of the amplified beam in the ring resonator geometry. Next we discuss experimental results. Although our work reproduced many of the findings of Rajbenbach and Huignard, we concentrate

on new observations or quantify some of their qualitative results. In particular we discuss the appearance of diverse higher diffracted orders.

The thrust of this and the next two chapters is experimental, and they follow a particular sequence of experiments. The fruition of our labours with the URR comes to bear in Chapter 5, in which we consider a new gain mechanism for photorefractive materials [110]. This mechanism is different from that discussed in Chapter 2 (that one depended on the imaginary part of the space charge field). This new gain process is very similar to one proposed recently in which higher diffracted orders may amplify a weak mixing wave [6]. We employ this new mechanism successfully in a ring and linear resonator. Finally in Chapter 6 we look more closely at the higher diffracted orders discussed at the end of this chapter with a special eye towards applications.

4.1 Background

4.1.1 Optimum frequency detuning and grating spacing

In two-wave mixing the combination of small interbeam angles and a large applied electric field leads to drift dominated behaviour. In this regime, except for very small interbeam angles or weak applied fields, $E_q \gg E_{s0} \gg E_m \gg E_t$. Our expression for the modulated space charge field in this limit is given by Eqn 2.55. The imaginary part of E_{s1} has extrema for $b = \pm E_m/E_{s0}$. The maximum value occurs for $b_{\rm opt} = -E_m/E_{s0}$ and the positive root, $b_{\rm min}$, gives the minimum value. For $b_{\rm opt}$

$$E_{s1} = jm\,\frac{{E_{s0}}^2 E_q}{{E_{s0}}^2 + E_m E_q} \tag{1}$$

in other words, pure imaginary so $\Phi_g = 90°$. For $b_{\rm min}$

$$E_{s1} = -\tfrac{1}{2} m\, E_{s0} \tag{2}$$

Here $\Phi_g = 0$. This positive root is not discussed in the literature, but it gives insight into the resonance condition for b. The ratio E_m/E_{s0} is small, therefore there is

little separation of $b_{\rm opt}$ and $b_{\rm min}$—the resonance is sharp.

For fixed E_m and E_{s0} (ie. constant interbeam angle and applied field), $b_{\rm opt}$ is constant. But $b_{\rm opt} = \delta\omega_{\rm opt}\tau_d$, where $\delta\omega_{\rm opt}$ is the optimum detuning frequency for the fixed grating spacing. Using the definition of τ_d and E_m from Chapter 2 we obtain

$$\delta\omega_{\rm opt} = b_{\rm opt}\frac{e\mu s N_D}{\epsilon_s\gamma_r N_A^-} I_0 = -\frac{esN_D}{\epsilon_s K E_{s0}} I_0 \tag{3}$$

The optimum detuning frequency is linearly dependent upon the total intensity.

Both E_m and E_q are proportional to the grating spacing, Λ. We can optimize the imaginary part of E_{s1} in Eqn 1 for a particular grating spacing. The condition to be satisfied is ${E_{s0}}^2 = E_m E_q$, which leads to

$$\Lambda_{\rm opt} = \frac{2\pi E_{s0}}{N_A^-}\sqrt{\frac{e\mu}{\epsilon_s\gamma_r}} \tag{4}$$

For the crystal parameters in Table 2.1, $\Lambda_{\rm opt} = 15\mu$m. Any grating spacing close to this value will insure high gain at the optimum detuning frequency.

We have considered conditions favourable to high gain. Now we need to consider losses.

4.1.2 Coupled intensity equations with absorption

The results of Chapter 2 show that for waves mixing at the optimum detuning frequency, $\Phi_g = 90°$. That is, there is maximum intensity coupling ($\Gamma\sin\Phi_g = \Gamma$), and no phase coupling. Consider two waves mixing as in Fig 2.5 at optimum detuning. We make the assumption that absorption losses are sufficiently small that Γ is constant through the medium. Then our coupled intensity equations are

$$\frac{dI_+}{dx} = 2\Gamma\frac{I_+I_-}{I_+ + I_-} - \alpha I_+ \tag{5}$$

$$\frac{dI_-}{dx} = -2\Gamma\frac{I_+I_-}{I_+ + I_-} - \alpha I_- \tag{6}$$

where α is the absorption constant.

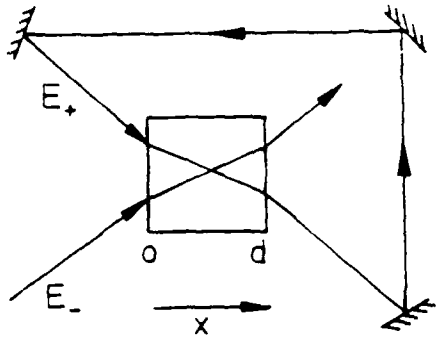

Figure 1: Unidirectional ring resonator geometry.

Introduce the quantities $\Sigma = I_+ - I_-$ and $Q = I_+/I_-$. Eqns 5 and 6 can be written in terms of these quantities as

$$\frac{d\Sigma}{dx} = -\alpha\Sigma, \quad \Sigma(x) = \Sigma_0 \exp(-\alpha x) \tag{7}$$

$$\frac{dQ}{dx} = 2\Gamma Q, \quad Q(x) = Q_0 \exp(2\Gamma x) \tag{8}$$

where the subscript "0" denotes the value at $x = 0$.

$$I_+(x) = \frac{\Sigma}{1+1/Q} = \frac{I(0)\exp(-\alpha x)}{1+\frac{I_-(0)}{I_+(0)}\exp(-2\Gamma x)} \tag{9}$$

$$I_-(x) = \frac{\Sigma}{1+Q} = \frac{I(0)\exp(-\alpha x)}{1+\frac{I_+(0)}{I_-(0)}\exp(2\Gamma x)} \tag{10}$$

where $I(0) = I_+(0) + I_-(0)$.

4.1.3 Ring resonator

We may now consider two wave mixing in which the amplified, oscillating beam undergoes feedback as shown in Fig 1. Rajbenbach and Huignard have shown that in $Bi_{12}SiO_{20}$ the oscillating beam can arise from the noise spectrum of a pump beam [105]. In other words, oscillation is self-starting. The particular frequency component of the noise spectrum corresponding to the optimum frequency detuning will

achieve the highest gain, thus the frequency of the oscillating beam is automatically detuned to the optimum value. This means the intensity expression of Eqn 9 is valid.

At steady-state, the condition for oscillation is that both the amplitude and phase of $E_\perp$ return to their original values after one complete circuit. The amplitude condition can be expressed in terms of the intensity

$$I_+(0) = R\, I_-(d) \tag{11}$$

where R is the combined reflectivity of the resonator for one round trip. We ignore diffraction losses in this treatment. Substituting Eqn 9 at $x = d$ into the above expression yields

$$\beta_{ro} = \frac{I_+(0)}{I_-(0)} = \frac{1 - e^{-2\Gamma d}}{1 - Re^{-\alpha d}} - 1 \tag{12}$$

For oscillation to occur, this ratio must be greater than 0, so Γ must satisfy

$$2\Gamma d > \alpha d - \ln R \tag{13}$$

Eqn 12 gives the steady-state beam ratio of the resonator.

The phase condition for oscillation is that the phase delay of the round trip must be an integer multiple of 2π. This is not a very restrictive condition—there are many components of the noise spectrum of the input pump beam which can find optical paths around the resonator satisfying the phase requirement.

In $Bi_{12}SiO_{20}$ oscillation in a ring resonator is unidirectional. For the set-up in Fig 1 we take the crystal orientation to give efficient power transfer for transmission geometry. A counterpropagating beam would mix with the pump beam to form a reflection grating with $\vec{K}$ in the x direction. But the applied field (necessary for high gain in $Bi_{12}SiO_{20}$) is in the z direction and cannot enhance the reflection coupling. Thus the gain for the reflection case will not be large enough to sustain oscillation.

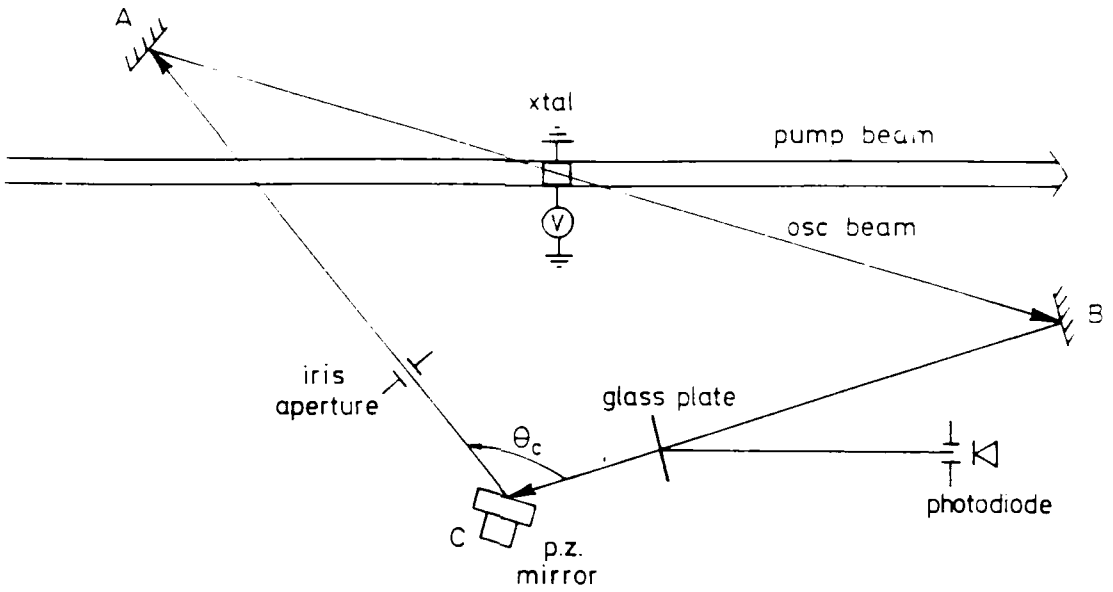

Figure 2: Experimental layout.

4.2 Experimental Results

4.2.1 Layout and resonator alignment

The layout of the URR we studied is shown in Fig 2. The resonator cavity was formed by 3 dielectric plane mirrors. One mirror (C) was mounted on a piezoelectric driven translation stage, and by applying a voltage to the driver, the geometry of the cavity could be slightly changed. The $Bi_{12}SiO_{20}$ crystal sample had 5mm x 5mm front and rear faces and a length of 5.33mm. The crystal had silver painted electrodes on the 001 face, and the orientation used was as in Fig 2.5. The crystal was mounted in the holder described in John M. Heaton's D.Phil. thesis [49]. This holder has plunger type contacts and was connected to a Brandenburg HV power supply. Unless otherwise stated, the applied voltage was 4.5 kV. Reflection off a glass plate inserted in one leg of the resonator provided a sample of the oscillating beam. The strength of the oscillating signal was measured using a photodiode. An iris aperture allowed only low order modes to oscillate in the resonator when it was stopped down (variable down to slightly less than 1 mm in diameter).

The pump beam was the expanded, spatially filtered and collimated output of an argon ion laser. The wavelength was 514 nm and the light was vertically polarised. Part of this beam was split off to provide a normalising signal, as well as a reference beam for interferometric measurements.

The resonator alignment is critical to achieve oscillation. A systematic placement of the mirrors using the following method worked well. The resonator was built up "backwards", using an injected beam from a He-Ne laser source. The He-Ne laser was put in the position of the photodiode in Fig 2. The He-Ne beam was parallel to the optical table and the beam height was level with the centre of the crystal. Mirrors A, B, and C were positioned sequentially, forming the general arrangement of the ring resonator. The line AB was at an angle of $\approx 1.9°$ to the pump beam to give a grating spacing of 15 μm. The height at which the He-Ne beam struck each mirror was constant. Any uphill or downhill slope to the alignment beam was detected easily using a stopped down iris aperture of the correct height. Care was taken to insure the reflection off mirror C hit the glass plate at the exact spot as the injection of the beam from the He-Ne laser. The iris aperture was placed downstream of the glass plate now. Any misalignment resulted in the beam reflected off mirror C missing the aperture. Each mirror mount had vertical and horizontal tilt controls and these were adjusted until any reflected beam retraced the path of the original alignment beam. When this was accomplished, the resonator was sufficiently lined up to obtain some sort of oscillation.

Additional fine-tuning of the resonator was made in two stages. First the iris aperture was opened to its maximum diameter. The pump beam was turned on, a voltage applied, and oscillation started. The oscillating beam consisted of a writhing, complicated, superimposed mode structure. We replaced the He-Ne laser with the photodiode and mirror C was adjusted to optimize the signal strength of the oscillating beam sample. (We found, by trial and error, that this signal was most sensitive to changes in the tilt of mirror C, off which the oscillating beam had the largest angle of incidence.) The second stage was to close the iris aperture to

its minimum diameter and then adjust the mirrors to optimize the symmetry in the lower order modes. For this tuning, mirror B worked best.

4.2.2 Comparison with previously reported results

Oscillation was self-starting in our ring resonator. As mentioned above the aperture could be used to select single modes. Not a specific lower order mode, but one of many. A sample of these modes, as well as an example of the structure with a fully open aperture, is given in Fig 3. There are two images in each photograph because there were reflections off both the front and rear surfaces of the glass plate. Here the photodiode in Fig 2 was replaced by a lens and a camera back.

The main difference between these modes and those reported by Rajbenbach and Huignard is the obvious rectangular symmetry. Ref [105] reported modes exhibiting circular symmetry. This means in our resonator the limiting aperture must be the crystal itself.

Mode stability was fairly good—from a few seconds to two minutes. High frequency vibration, such as produced by rapping on the optical table did not initiate mode transition, but low frequency disturbances, such as caused by air currents, did. Often a particular oscillating mode would fade and there would be a delay of some tens of seconds before oscillation would build up again. At other times a single stable mode would give way to a waver of competing modes. The struggle would have a single stable mode emerge as the victor. This competition occured most frequently between modes TEM_{00} and TEM_{11}, or between modes TEM_{10} and TEM_{02}. Ref [25] describes mode competition in a URR using $Bi_{12}SiO_{20}$. In particular, by placing lenses in the resonator, the authors were able to emulate a confocal resonator and limit the number of higher order modes by decreasing the Fresnel number of the system.

We used low input intensities, less than 15 mW/cm^2. This is an order of magnitude less than that used by Rajbenbach and Huignard. One reason we chose to

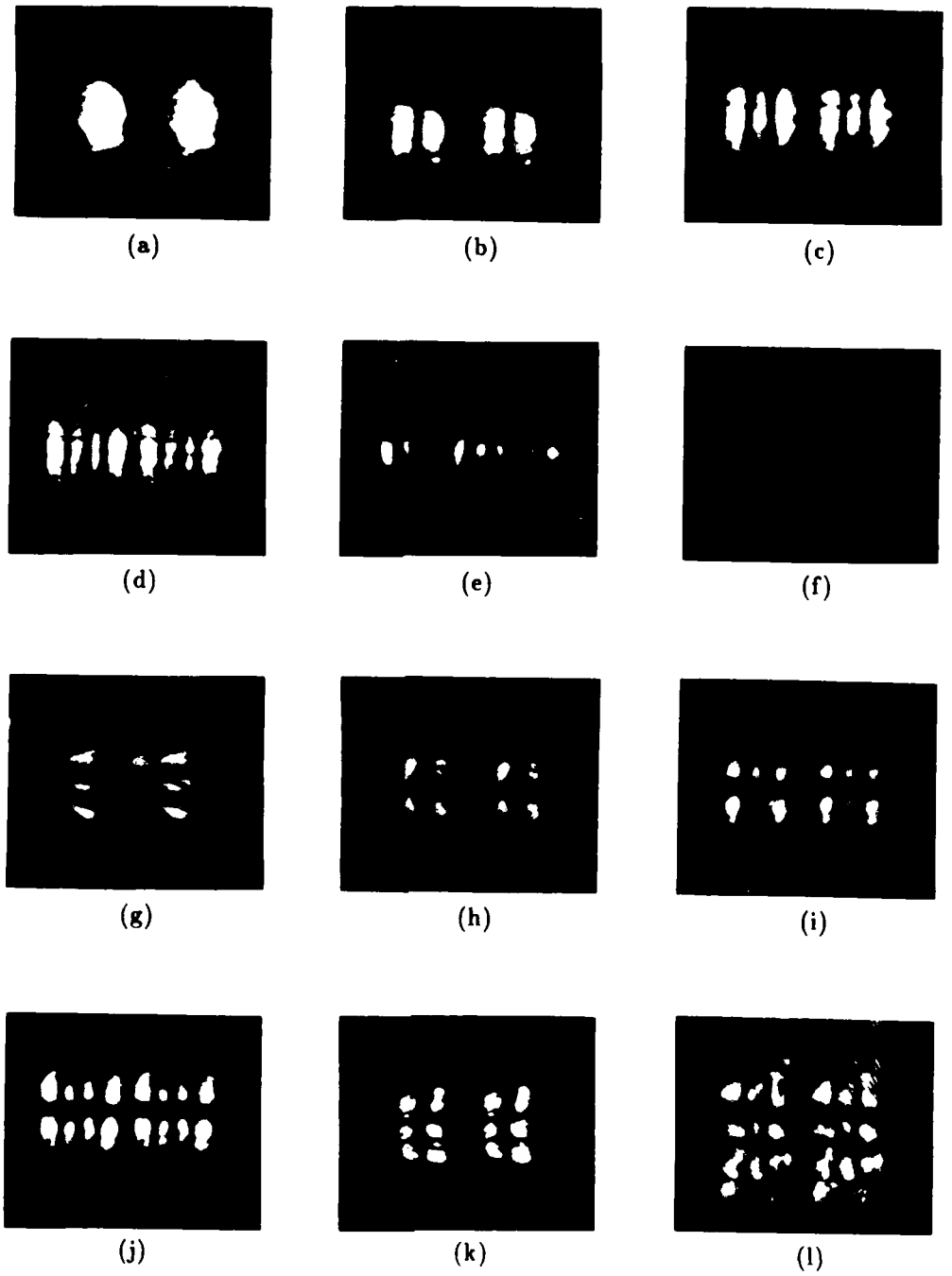

Figure 3: Resonator TEM modes. (a) 00 (b) 10 (c) 20 (d) 30 (e) 40 (f) 01 (g) 02 (h) 11 (i) 21 (j) 31 (k) 12 (l) Superposition of modes.

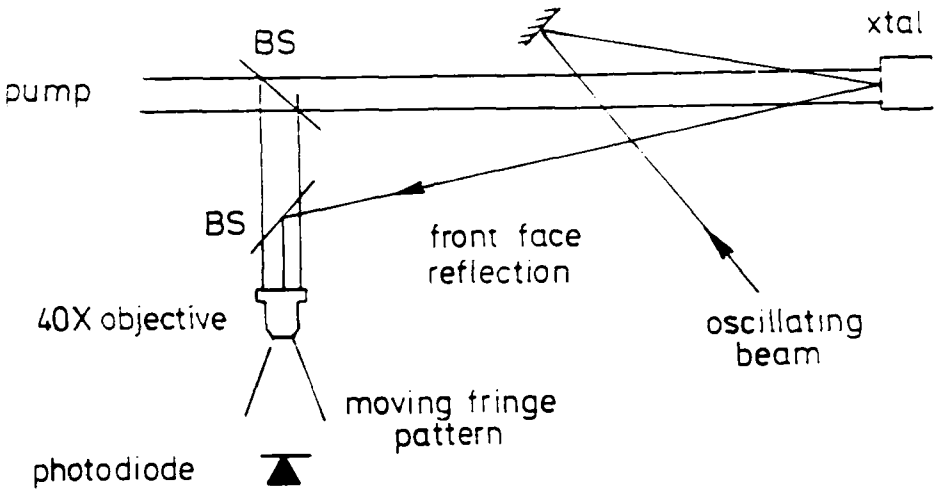

Figure 4: Measurement of detuning frequency.

work in this range was necessity. Our laser output was less stable at high power settings. A second reason was that it was more convenient when performing interferometric time studies. The frequencies we measured were on the order of hertz to tens of hertz instead of the hundreds of hertz characteristic of high light intensities.

The interferometric arrangement is shown in Fig 4. The reflection of the oscillating beam off the front face ($\approx 20\%$) is combined with part of the input beam in a Mach-Zehnder scheme. Any frequency difference between the two beams results in an interference pattern of fringes moving at the detuning frequency. This frequency can be measured by analysis of an oscilloscope trace.

We had a number of questions about the detuning frequency we wanted to answer.

1. Does the detuning frequency depend on mode?

2. Is the behaviour linear with input intensity, as suggested by Eqn 3?

3. How will changing the length of the cavity affect the detuning frequency?

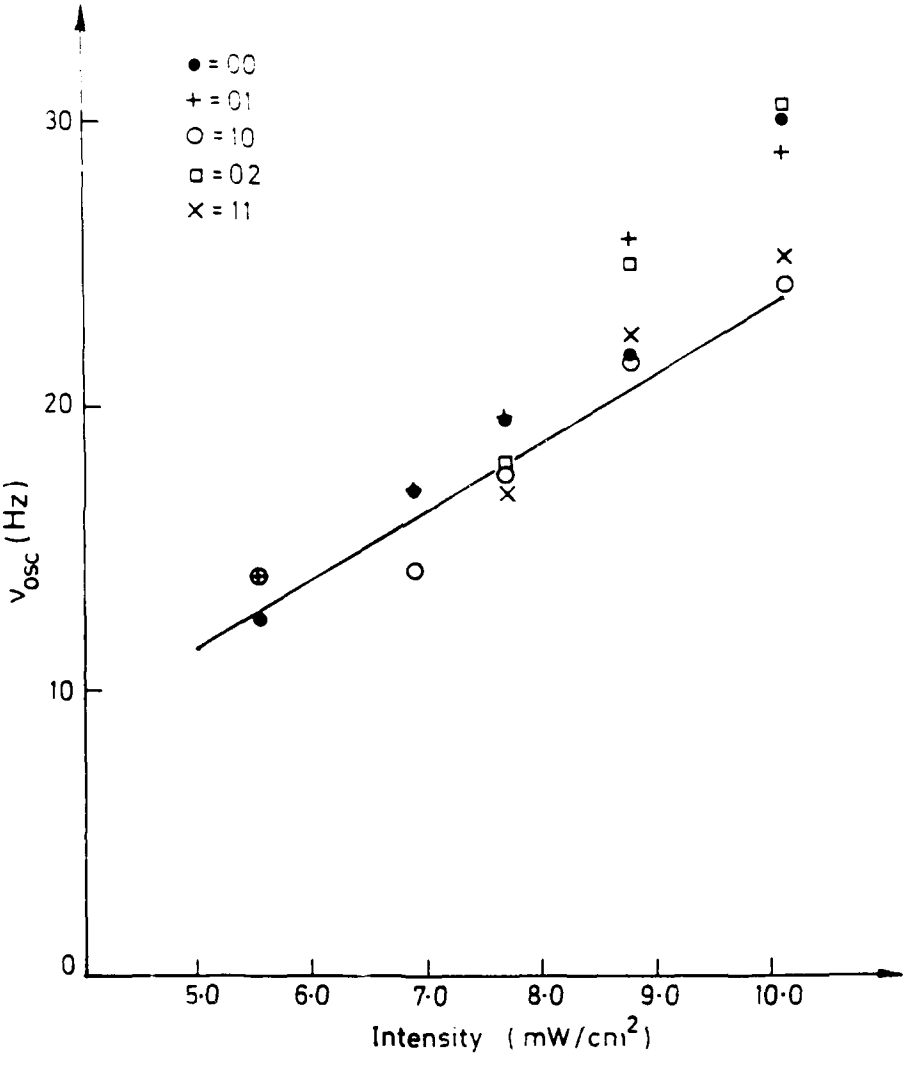

Figure 5: Detuning frequency, $\delta\nu$ vs input pump intensity. Symbols refer to various TEM modes.

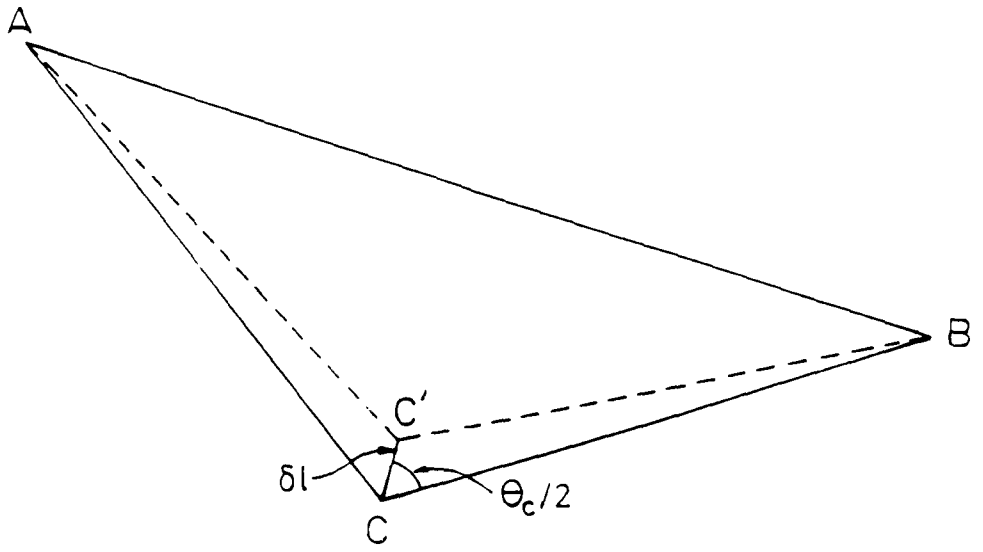

Figure 6: Change in cavity length due to displacement of mirror C. For our case: AB = 65.2 cm, BC = 33.0 cm, CA = 56.5 cm.

Fig 5 shows the frequency difference, $\delta\nu = \delta\omega/2\pi$, for various modes as a function of input pump intensity. Each data point is a statistical average of up to ten measurements taken for a particular mode and a given intensity. Error bars are not shown in this figure. but typical error bars for these interferometric measurements appear in Fig 7a. The scatter is somewhat broad, but there is no discernible trend difference between the modes. Within experimental error every mode seems to have roughly the same detuning frequency for the same intensity. The dependence of $\delta\nu$ on the input intensity appears linear in this region. The straight line is based on a linear regression fit to the function $\delta\nu = cI_0$, where c is the slope. We may take $I_0 = I_-(0)$ because the oscillating beam intensity is very weak compared to the pump intensity. The best fit slope is 0.23 m^2/Ws. This is over eight times larger than the slope predicted by Eqn 3 using the crystal parameters of Table 2.1. Two factors may account for this discrepancy. The table parameter values were chosen as representative of the literature. There may be significant variation among crystal

samples. In particular, this $Bi_{12}SiO_{20}$ sample produced photocurrent densities (proportional to sN_D) nearly four times larger than those for other $Bi_{12}SiO_{20}$ samples for a given input intensity [31]. The second factor concerns the size of the applied field. Some authors report that the applied electric field in $Bi_{12}SiO_{20}$ is often less than that expected from the applied voltage (ie. $E_{s0} < V/d$). For example, Jonathan, et al., found their applied field was half as large as expected [64]. This decrease in field strength may be due to shadowing effects at the electrodes, or a loss due to poor ohmic contact of the electrode to the crystal. A combination of higher values for sN_D and a smaller E_{s0} would result in a larger slope in Eqn 3.

In $BaTiO_3$ one can change the detuning frequency by displacing one resonator mirror slightly [79]. This changes the cavity length and the difference in detuning is necessary to satisfy the phase condition for oscillation. The detuning frequency can take on positive or negative values, and is periodic with the mirror shift.

We would not expect a change in cavity length to produce such a large range of detuning frequencies in $Bi_{12}SiO_{20}$ because the gain is very strong only for values close to $\delta\omega_{opt}$. It is likely that oscillation would cease before a large change in detuning took place.

Fig 6 shows the change in geometry when mirror C is displaced a distance δl along the bisector of $\angle ACB$. Both sides AC' and BC' are shortened by a length $\delta l \cos\frac{1}{2}\theta_C$. The total change in cavity length is

$$\Delta L = -2\delta l \cos\tfrac{1}{2}\theta_C \tag{14}$$

For our case $\theta_C = 89.5°$. The piezoelectric translator had an elongation of 1 μm /100 V. Thus applying 10 V gave $\delta l = 0.1\mu$m. This resulted in $\Delta L = 0.28\lambda$, where $\lambda = 514$ nm. This change in length was confirmed by injecting a beam into the resonator with no applied field to the crystal (no beam coupling) and setting up an interferometer as in Fig 4. An applied voltage of 40 V to the piezoelectric translator shifted the interference pattern by almost exactly one fringe.

Fig 7a shows the results of mirror displacement on the detuning frequency of

mode TEM_{10} for an incident intensity of 9.7 mW cm^2. The error bars represent one standard deviation of the experimental values. Fig 7b includes various modes. Again the different modes all seem to be at roughly the same detuning frequency and this is independent of mirror displacement.

The ordinate axis in Figs 7a and b has quotation marks around the word "change". Did we really change the cavity length by displacing mirror C? As soon as the voltage to the piezoelectric translator was modified, the oscillation in the URR immediately stopped. After several seconds to a few minutes, the oscillating beam would reappear—equally intense and at the same detuning frequency. It is likely that after the original oscillation was disturbed by shifting mirror C, the new oscillating beam travels along a slightly different path which satisfies the twin conditions of optimum detuning and proper cavity length. We still obtained oscillation when the path choices were restricted by putting in one or two small apertures in the system. In this regard oscillation in the URR is very forgiving.

One benefit of using low incident power was the discovery of a threshold for oscillation. No oscillation occured for pump intensities less than 0.8 mW/cm^2. This is seen in Fig 8. Here the ratio, β_r, of the intensity of the oscillating beam ($I_+(d)$) to the pump intensity ($I_-(0)$) is plotted as a function of input intensity. According to Eqns 9 and 10, $\beta_r = \beta_{r_0}/R$ and thus depends on Γ, R, and α, all of which are independent of intensity. We should mention that Rajbenbach has reported a region of reduced gain in $Bi_{12}SiO_{20}$, for nearly degenerate two-wave mixing at similar intensities [106]. It is possible that at low light intensities not all acceptor sites are filled, ie. N_A^- is reduced, which leads to reduced coupling.

Threshold devices are increasingly important in many optical applications such as image processing [70] and associative memories [112]. A URR using $Bi_{12}SiO_{20}$ could be used as a threshold detector, however the mode structure of the oscillating beam would be a limiting factor on the spatial resolution of the output.

The highest beam ratio we measured was 0.08. This is lower than the steady-state beam ratio of 0.6 reported in Ref [107]. However, Rajbenbach and Huignard

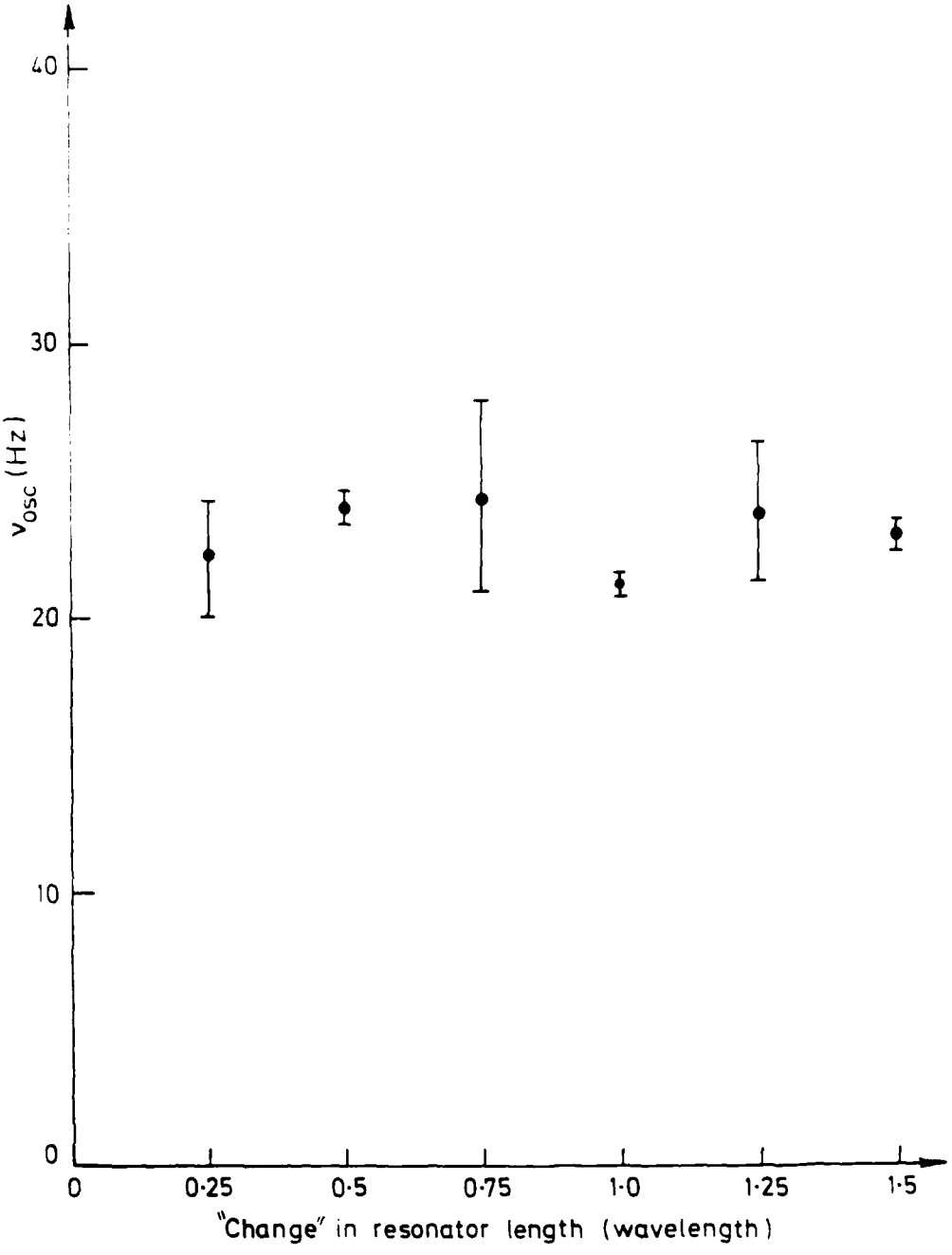

Figure 7: Detuning frequency, $\delta\nu$, vs "change" in cavity length, that is, a mirror displacement designed to give this change in length. (a) TEM_{10}. Error bars represent one standard deviation.

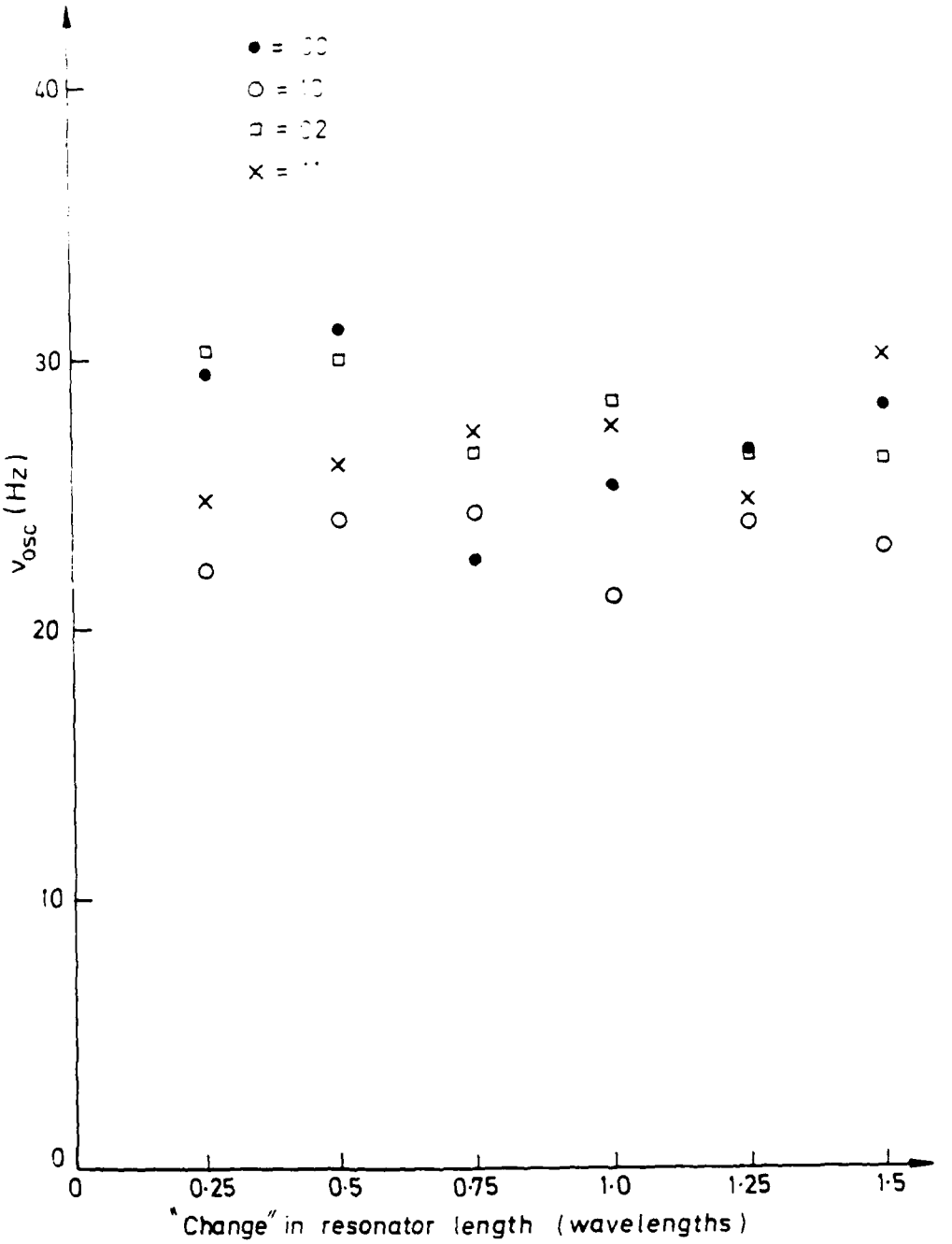

Figure 7: Detuning frequency, $\delta\nu$, vs "change" in cavity length, that is, a mirror displacement designed to give this change in length. (b) Various modes.

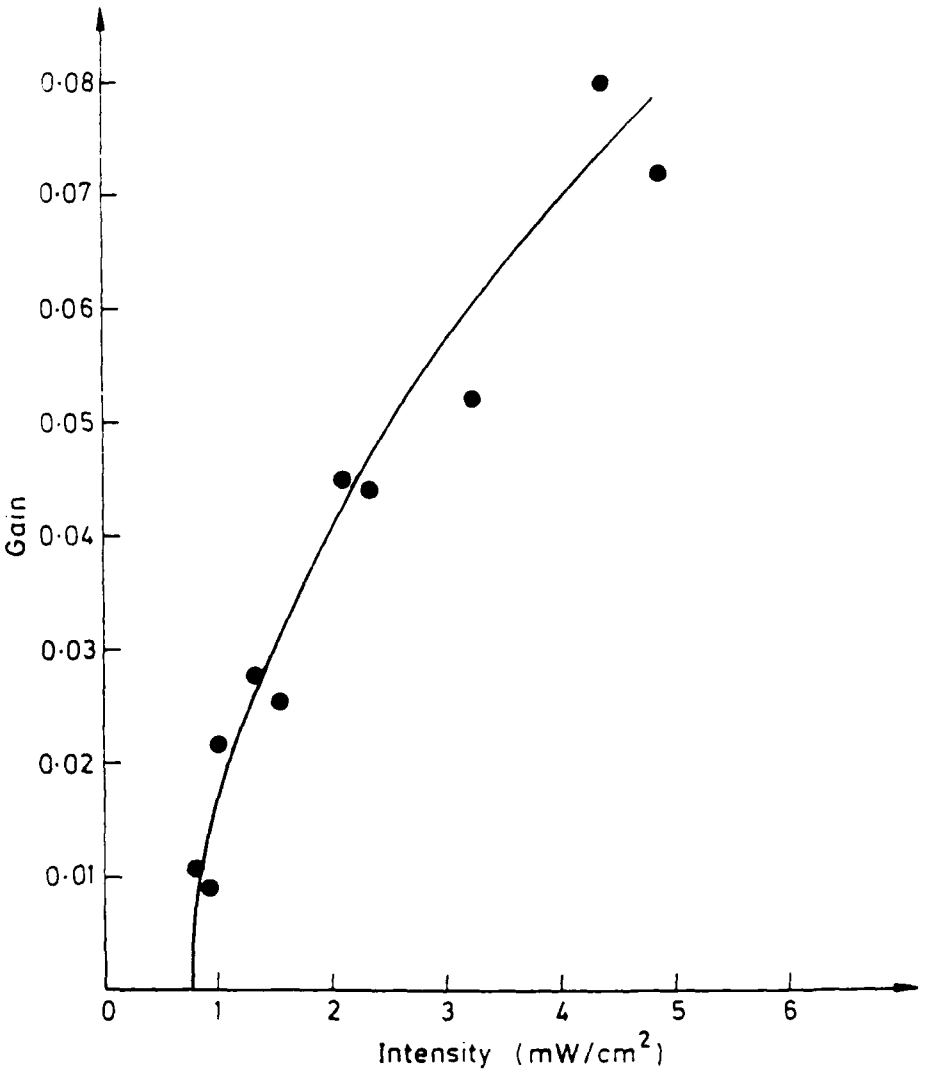

Figure 8: Ratio of oscillating intensity to input intensity, β_r, vs input intensity. No oscillation occurred for an input less than 0.8 mW/cm^2.

used a longer wavelength (568 nm) to reduce the absorption loss, and had a longer interaction length (1 cm). We can use our value and Eqn 10 to estimate the gain coefficient in our system. For this crystal $\alpha = 1.1$ cm^{-1}, $d = 0.53$ cm, and $R = 0.65$. (To calculate R: Mirrors A and B had reflectivities of 0.95, C had a reflectivity of 0.98, the transmission of the glass plate was 0.92, and there was a 20% reflection loss off the front face of the crystal.) In terms of β_r

$$\Gamma = -\frac{1}{2d}\ln\left(R\left(e^{-\alpha d}(1 + R\beta_r) - \beta_r\right)\right) \tag{15}$$

For our experimental values, $\Gamma = 1.05$ cm^{-1}. This is lower (by a factor of ten) than that calculated from the treatment of Secs 2.1.8 and 2.3.2, but those did not take into account optical activity or higher diffracted orders. Further, as we have discussed, E_{s0} may be reduced.

4.3 Higher Diffracted Orders

4.3.1 Emergence of higher diffracted orders

In the derivation of the coupled wave equations in Chapter 2 we neglected coupling to higher diffracted orders (see Fig 2.6). We argued there that this simplification was valid if the interbeam angle was large. However, to get the high gain necessary for oscillation in the URR using $Bi_{12}SiO_{20}$ the interbeam angle must be small. Higher diffracted orders (HDOs) were visible whenever the oscillating beam was present. In general, besides the pump beam (0 order) and the oscillating beam (-1 order), the +1, -2, and -3 orders were seen (see Fig 9a).

Au and Solymar have described the emergence of higher diffracted orders and have shown that significant power transfer to these orders is possible [7]. They have also identified an off-Bragg coupling mechanism by which power transfer between the principal mixing waves may occur, even when the phase mismatch angle, Φ_g, equals 0 [6]. We will not go into the full theory in this thesis, but an off-Bragg coupling mechanism similar to that presented in Ref [6] is described in Chapter 5.

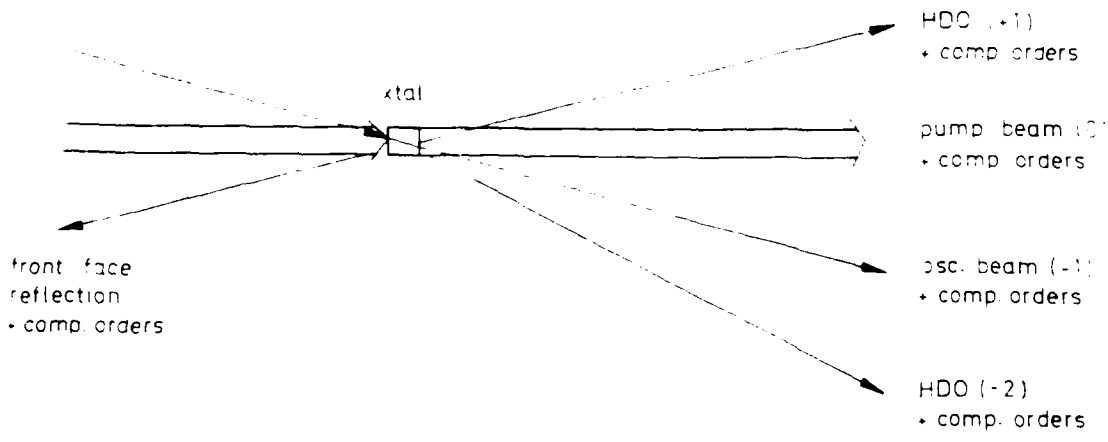

(a)

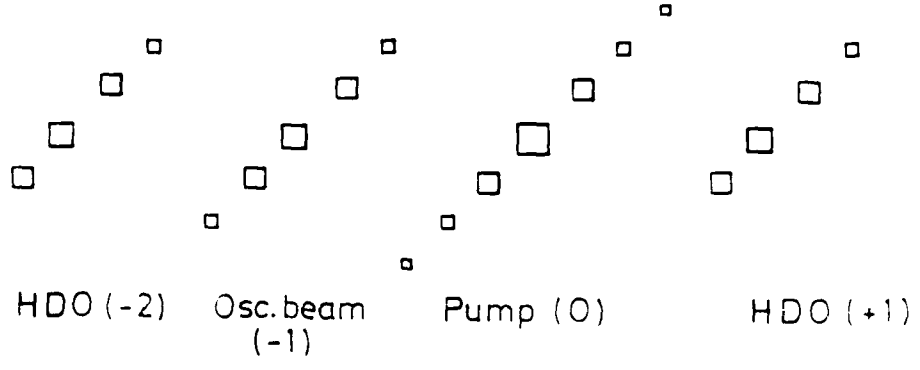

(b)

Figure 9: Two species of higher diffracted orders in the URR. (a) HDOs. (b) Companion orders.

The key feature here is that conditions for HDOs improve as the interbeam angle becomes smaller.

4.3.2 Companion orders

The reflection of the oscillating beam off the glass plate revealed an interesting phenomenon. The oscillating beam had an entourage. A number of other beams (which we shall call *companion orders*) were visible. These represented a different "species" of higher diffracted orders. They appeared on either side of the oscillating beam and were evenly spaced along a line some 35° out of the plane of the resonator.

Closer inspection revealed that companion orders also appeared around the pump beam, the HDOs, and, surprisingly, the reflection of the oscillating beam off the front crystal face. (We shall call the pump and oscillating beams and the HDOs due to their two-wave mixing the *principal beams*, in relation to the companion orders.) Several views of these companion orders are seen in Fig 10.

Several observations may be made here:

- The angular separation of companion orders was much smaller than that for the HDOs. (We will measure this separation in the next subsection.)
- There seemed to be a focusing effect in the companion orders—as one moved away from the principal beam, on one side the orders became increasingly focused while on the other side the companion orders were increasingly defocused.
- The companion orders shared the same mode structure as the principal beam.
- The spacing and orientation of the companion orders were not affected by a decrease in interbeam angle between the pump and oscillating beam to 1.44°.
- The number of companion orders around each principal beam diminished as the order of the HDO got larger (i.e. as one moved away from the pump

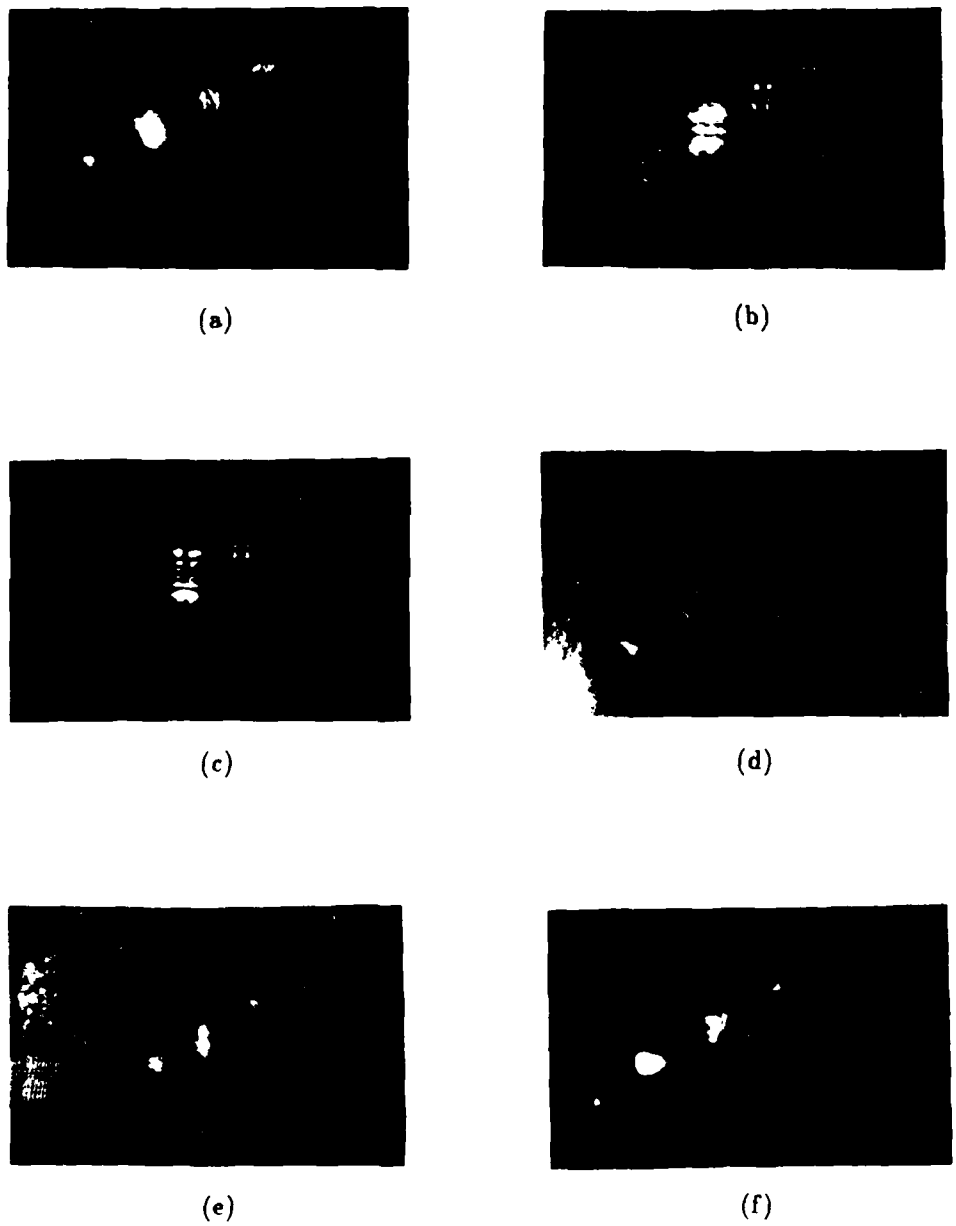

Figure 10: Companion Orders in the Ring Resonator. (a)-(c) Oscillating beam. (d) Pump beam (one side only). (e) Higher diffracted -2 order. (f) Reflection of oscillating beam off front face. In all but (d), the principal beam is the second from the bottom.

beam). The pump beam usually had eight or nine companion orders, the oscillating beam five to seven, HDOs -2 and -1 three or four and HDO -3 two or three. It was not unusual to find that a single input to the crystal, the pump beam, produced over 30 separate beams. This was a very prolific crystal!

How do the companion orders arise? It should be emphasized that because of the iris aperture and the angular separation of the companion orders, only the oscillating beam could circumnavigate the resonator and be reinforced. Only the oscillating and pump beam entered the front face of the crystal. The companion orders were not due to any reflection external to the crystal, they had to be produced inside the crystal.

One possibility we considered was that the companion orders were some type of preferential, amplified scatter from the noise spectrum of the principal beams. The question we asked was, is the electrooptic effect in $Bi_{12}SiO_{20}$ enhanced for a grating vector out of the plane of the resonator at 35°? The answer, as demonstrated in Appendix B, is no.

A telling clue to the origin of the companion orders is seen in Fig 11. An expanded, incident beam with no voltage applied to the crystal produced a transmitted beam as well as a second beam at an angle of 35°. It seemed our crystal sample had a slight wedge angle.

4.3.3 Measurement of the wedge angle

This particular crystal of $Bi_{12}SiO_{20}$ had come back recently from being recut and polished. It was part of a crystal of original dimensions 5mm x 5mm x 10mm. After a long and protracted bout with an internal fracture, the first crystal split in two (see Appendix A describing damage in $Bi_{12}SiO_{20}$ crystals). The larger piece was saved and became the crystal we used for these experiments. It is very likely that during the cutting or polishing the wedge was introduced.

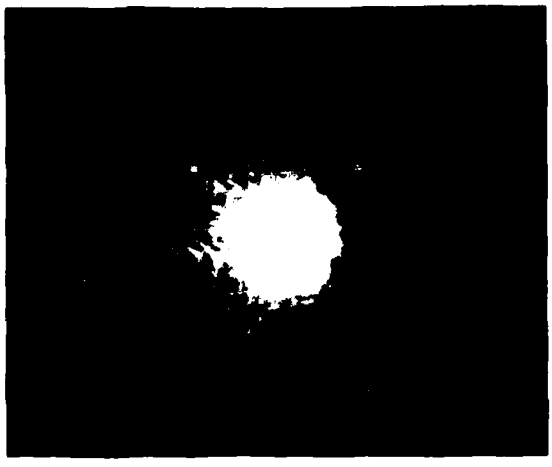

Figure 11: Transmission of a uniform beam through the crystal sample. The presence of a multiple reflection suggests a wedge angle.

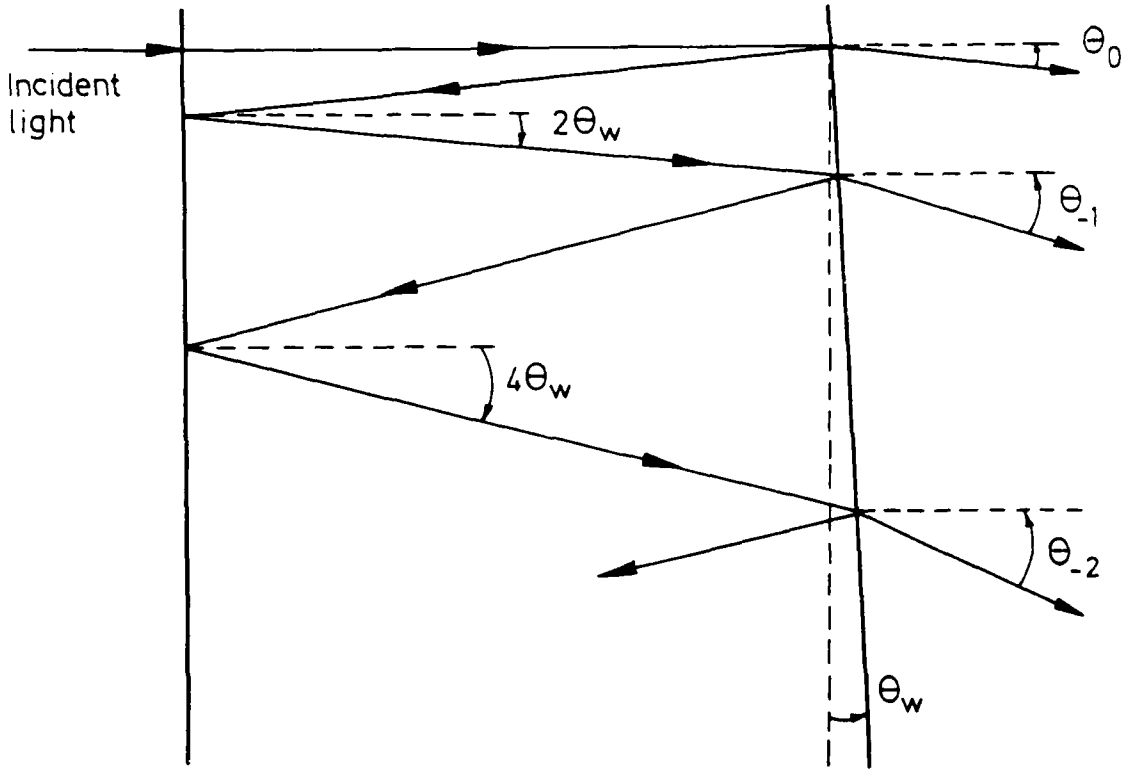

Figure 12: Multiple reflections in a crystal with a wedge angle.

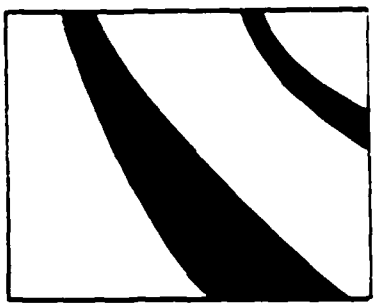

Figure 13: Interferometric measurement of wedge in $Bi_{12}SiO_{20}$ crystal.

The angular separation of the companion orders in air, $\Delta\theta$, was measured as the ratio of spatial separation over a given distance behind the crystal. This was found to be 0.19° for all the companion orders observed.

As shown in Fig 12, the wedge angle, θ_w, is related to this angular spacing by

$$\Delta\theta = \theta_{-1} - \theta_0 = 2n\theta_w \tag{16}$$

where n is the index of refraction. For our measurement, $\theta_w = 0.036°$. Notice that the angular separation of multiple reflections with the input beam is a multiple of $2\theta_w$. In other words, the higher multiple reflections are at the same angular spacing as higher diffracted orders produced by two-wave mixing of the input beam and the first co-directional multiple reflection.

The presence of a wedge in the crystal was confirmed using a Specac interferometer. This is shown in Fig 13, a sketch of the interference pattern. A fringe analysis was difficult because both the wedge angle and crystal face were small. The orientation of the fringes were at approximately 35° to the 001 crystal axis. The fringes were bent, suggesting one or both surfaces were curved. This may explain the focusing effects we saw. The two interference fringes is too small a number to give a value for the wedge angle of 0.036°, but reflection off the curved surfaces might emulate a larger wedge angle.

4.3.4 Nature of the companion orders

Are the companion orders merely the result of amplification of multiple reflections? This cannot be the complete answer because we see companion orders on either side of the principal beam. Multiple reflections exist only on one side. In the same way the interaction of the pump and oscillating beams produce HDOs, the two-wave mixing between any principal beam and its first codirectional multiple reflection gives rise to higher diffracted "companion" orders. Additional weak multiple reflections at the proper angular displacements may well facilitate the emergence of higher diffracted companion orders. Because the wedge angle was smaller than the interbeam angle between the pump beam and the oscillating beam (roughly ten times smaller), a greater number of companion orders were present than HDOs. Moving out from the pump beam, the intensity of the principal beams decreased, and thus fewer companion orders were seen.

Once the HDOs and companion orders are established, an intricate network of beam coupling builds up. For example, each separate beam couples to the pump beam. This is evident because when the oscillating beam is suddenly interrupted, the HDOs and their companion orders decrease in brightness, then gradually fade away completely. Clearly the pump beam is reading/erasing a number of gratings. A complete description, in which each beam is coupled to every other beam, would be complicated indeed.

4.4 Conclusions

Our goal in these experiments was to gain expertise with a resonator using $Bi_{12}SiO_{20}$ as an active medium. In the course of the experiments we have put numbers to many qualitative findings previously reported, and have found reasonable agreement with theory, if one allows for variation in crystal parameters and applied fields. We have demonstrated the crucial importance of the optimum detuning frequency

to oscillator operation. We discovered that oscillation in a URR resonator using $Bi_{12}SiO_{20}$ has a threshold for incident intensity. For our crystal sample no oscillation occurred for intensities less than 0.8 mW/cm^2. And we have observed and explained the presence of various higher diffracted orders, some of which are due to a slight wedge angle in the crystal sample we used. In Chapter 6 we will discuss potential applications for a crystal with a wedge angle.

Chapter 5

Wave Amplification with Two Pump Beams

So we grew together,
Like to a double cherry, seeming parted,
But yet an union in partition;
Two lovely berries moulded on one stem.

A Midsummer Night's Dream
Act III, Scene II

Thus far we have looked at wave mixing in photorefractive materials with two input beams. A characteristic of the wave interaction is power transfer in one direction, eg. I_+ increases at the expense of I_-, but not vice versa. The coupling term which describes the power transfer depends on the imaginary part of the modulated space charge field.

But there are other means of redistributing energy if a greater number of waves interact and the interbeam angles are small. A recent article by Ringhofer and Solymar suggested a new mechanism for wave amplification in this case [110]. In this new scheme, four waves interact as shown in Fig 1. Power is transferred inwards from the pump beams. Unlike our traditional two-wave mixing mechanism which is necessarily on-Bragg (the beams which write the grating, simultaneously read it

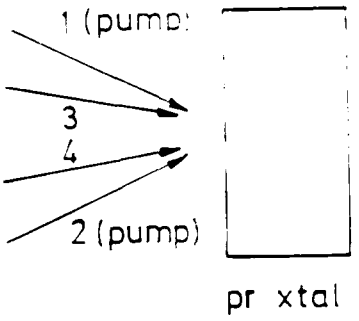

Figure 1: Four wave mixing. Beams 1 and 2 are strong pump beams.

directly), this new mechanism depends on an indirect, off-Bragg coupling. This is similar to the process by which beams can be amplified via a higher diffracted order [6].

In this chapter we review the theory of Ref [110] (which gives only the final expression for the gain coefficient). We will concentrate on qualitative features of the theory. One important criterion is that, for high gain, the four mixing waves must be frequency shifted relative to one another. A common method of achieving this small frequency shift experimentally is to introduce a Doppler shift by reflection off a slowly moving mirror. The mirror is typically mounted on a piezoelectric translator driven by a sawtooth voltage signal [109]. This works fine for one beam, but coordinating the motions of two or three mirrors to get multiple frequency shifts is difficult and requires more equipment than we had available to us. One way out is to use a ring resonator. The oscillating beam in the ring resonator is automatically frequency shifted to give optimum gain. In this arrangement, one of the internal beams (3 or 4 in Fig 1) is reinforced in a resonator, and one needs only a single moving mirror to detune a second pump beam. The remainder of the chapter relates experimental work with this resonator and a similar arrangement—a linear resonator.

Our goals in the experiments were to verify the existence of the new gain mechanism, to test certain qualitative features of the theory, and to establish some

benchmark by which the new mechanism could be compared to the traditional gain mechanism.

5.1 Theory

Consider the four waves mixing in Fig 1. The interference pattern produced by the overlapping of these waves is merely a superposition of those patterns produced by each pair of waves. The total intensity is

$$\begin{aligned} I(\vec{r}) &\sim |E|^2 = |\sum_{l=1}^{4} E_l e^{j(\omega_l t - \vec{k}_l \cdot \vec{r})}|^2 \\ &= I_0 + \sum_{l=1}^{4}\sum_{m=1}^{4} E_l^* E_m e^{j(\delta\omega_{lm} t - \vec{K}_{lm}\cdot\vec{r})} \qquad l \neq m \end{aligned} \tag{1}$$

where $\delta\omega_{lm} = \omega_l - \omega_m$ are the detuning frequencies, and $\vec{K}_{lm} = \vec{k}_l - \vec{k}_m$ are the resulting grating vectors. We assume nearly degenerate mixing.

We can follow the general treatment of Chapter 2 and derive a modulated space charge field for each grating. As in that chapter, we neglect higher diffracted orders and assume small modulation. We can reduce the complexity somewhat by assuming beams 1 and 2 are very much stronger than beams 3 and 4. Thus we may neglect coupling between beams 3 and 4. In Chapter 2 we found that power transfer was in one direction only. Let us take this direction in a clockwise sense in reciprocal space (Fig 2a) so power is transferred $1 \rightarrow 3 \rightarrow 4 \rightarrow 2$. We let our subscripts reflect this direction. The modulated dielectric constant is

$$\begin{aligned} \epsilon_r &= \epsilon_{r0} + \epsilon_r{}^2 r \left(E_{\omega_{13}} \frac{I_{12}}{I_0} e^{-j(\vec{K}_{12}\cdot\vec{r} - \delta\omega_{12} t)} + E_{\omega_{13}} \frac{I_{13}}{I_0} e^{-j(\vec{K}_{13}\cdot\vec{r} - \delta\omega_{13} t)} \right. \\ &\quad + E_{\omega_{14}} \frac{I_{14}}{I_0} e^{-j(\vec{K}_{14}\cdot\vec{r} - \delta\omega_{14} t)} + E_{\omega_{32}} \frac{I_{32}}{I_0} e^{-j(\vec{K}_{32}\cdot\vec{r} - \delta\omega_{32} t)} + \\ &\quad \left. + E_{\omega_{42}} \frac{I_{42}}{I_0} e^{-j(\vec{K}_{42}\cdot\vec{r} - \delta\omega_{42} t)} + c.c. \right) \end{aligned} \tag{2}$$

where $I_{lm} = E_l^* E_m$ and

$$E_{\omega_{lm}} = \frac{E_{s0}}{1 + b_{lm}\frac{E_{s0}}{E_{m_{lm}}} + j\left(\frac{E_{s0}}{E_{q_{lm}}} - b_{lm}\right)} \tag{3}$$

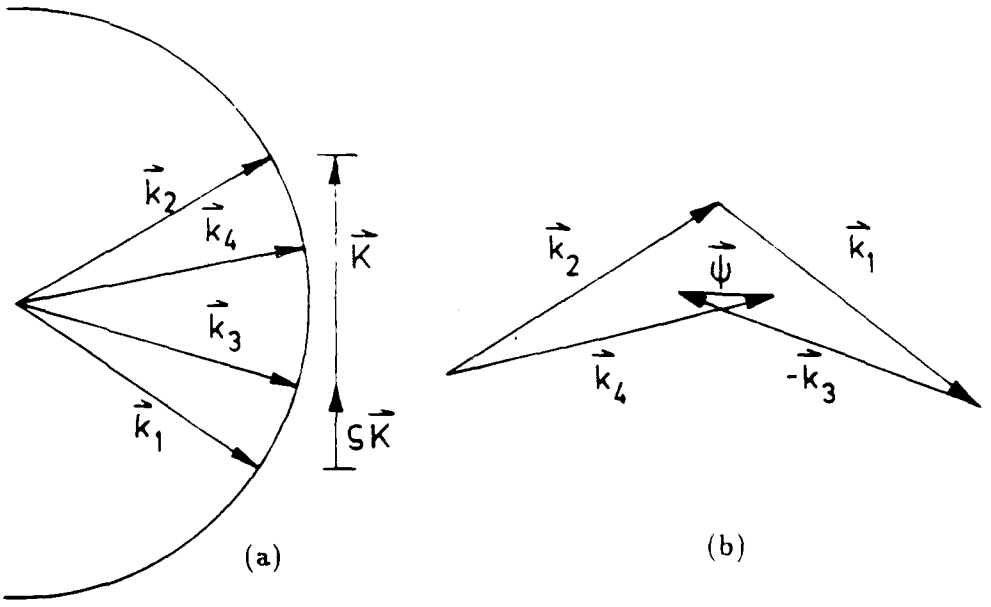

Figure 2: Nearly degenerate four-wave mixing. (a) Propagation vectors in reciprocal space. $\vec{K} = \vec{k}_1 - \vec{k}_2$. (b) Off-Bragg parameter, $\vec{\psi}$.

reflects the fact that the interbeam angles are small and we are in the drift dominated regime. Here $b_{lm} = \delta\omega_{lm}\tau_d$, $E_{m_{lm}} = \gamma_r N_A^- / \mu K_{lm}$, and $E_{q_{lm}} = eN_A^- / \epsilon_s K_{lm}$.

5.1.1 On-Bragg and off-Bragg coupling

The writing beams read the various gratings formed in the photorefractive medium. Finding the coupling between the beams is rather like doing a jigsaw puzzle. We need to find some combination of a writing beam and a grating vector which will exactly reproduce any one of the writing beams, ie. duplicate the propagation vector and frequency. If the pieces fit, we have vector closure, and the on-Bragg condition of Fig 2.6 is satisfied. For example, beam 1 combines with grating vector $\vec{K}_{13}$ and part of it is diffracted into beam 3.

Sometimes the jigsaw pieces do not meet exactly, and we need a hammer to force the fit. The hammer is the off-Bragg vector, $\vec{\psi}$, shown in Fig 2b. Vector closure is given by

$$\vec{k}_3 = \vec{k}_1 + \vec{k}_2 - \vec{k}_4 + \vec{\psi} \tag{4}$$

Thus, for example, beam 1 combines with grating vector $\vec{K}_{42}$ *and* $\vec{w}$ to reproduce beam 3. This is indirect, or off-Bragg, coupling. Note, for this to work in general, we must match the frequency detunings, $\delta\omega_{13} = \delta\omega_{42} = \zeta\delta\omega_{12}$ and $\delta\omega_{14} = \delta\omega_{23} = (1-\zeta)\delta\omega_{12}$, where ζ is the scaling parameter shown in Fig 2a. This condition suggests itself, regardless, because of the symmetry of the mixing. This also ensures that all gratings move at the same velocity.

In the undepleted pump approximation, where $I_3, I_4 \ll I_1, I_2$, the coupled differential equations for E_3 and E_4 become

$$\frac{dE_3}{dx} = -j\frac{q}{I_0}\left(E_{\omega_{13}}I_1 + E_{\omega_{32}}{}^*I_2\right)E_3 - j\frac{q}{I_0}\left(E_{\omega_{14}}{}^* + E_{\omega_{32}}\right)E_1E_2E_4^*e^{-j\psi x} \quad (5)$$

$$\frac{dE_4}{dx} = -j\frac{q}{I_0}\left(E_{\omega_{14}}I_1 + E_{\omega_{42}}{}^*I_2\right)E_4 - j\frac{q}{I_0}\left(E_{\omega_{13}}{}^* + E_{\omega_{42}}\right)E_1E_2E_3^*e^{-j\psi x} \quad (6)$$

where $q = \frac{1}{2}k_0n^3r$. The first term on the right hand side of the above equations represents on-Bragg coupling, the second term off-Bragg.

5.1.2 Analytic treatment of the coupled equations

To make Eqns 5 and 6 more tenable, we introduce a change of variables

$$B_3 = E_3\exp(j\frac{\psi x}{2}), \quad B_4 = E_4^*\exp(-j\frac{\psi x}{2}) \quad (7)$$

Then our coupled equations become

$$\frac{dB_3}{dx} = -jq\left(\frac{\beta_{ro}}{1+\beta_{ro}}E_{\omega_{13}} + \frac{1}{1+\beta_{ro}}E_{\omega_{32}}{}^* - \frac{\psi}{2q}\right)B_3 - jq\left(E_{\omega_{14}}{}^* + E_{\omega_{42}}\right)\frac{\sqrt{\beta_{ro}}}{1+\beta_{ro}}B_4 \quad (8)$$

$$\frac{dB_4}{dx} = jq\left(\frac{\beta_{ro}}{1+\beta_{ro}}E_{\omega_{14}}{}^* + \frac{1}{1+\beta_{ro}}E_{\omega_{42}} - \frac{\psi}{2q}\right)B_4 + + jq\left(E_{\omega_{13}}{}^* + E_{\omega_{32}}\right)\frac{\sqrt{\beta_{ro}}}{1+\beta_{ro}}B_3 \quad (9)$$

where $\beta_{ro} = I_1/I_2$. These equations are of the form

$$B_3' = -j(a_{11}B_3 + a_{12}B_4) \quad (10)$$

$$B_4' = -j(a_{21}B_3 + a_{22}B_4) \quad (11)$$

where

$$a_{11} = q\left(\frac{\beta_{ro}}{1+\beta_{ro}}E_{\omega_{13}} - \frac{1}{1+\beta_{ro}}E_{\omega_{32}}^{*} - \frac{\psi}{2q}\right) \quad a_{12} = q\frac{\sqrt{\beta_{ro}}}{1+\beta_{ro}}(E_{\omega_{14}}^{*} - E_{\omega_{42}})$$

$$a_{21} = -q\frac{\sqrt{\beta_{ro}}}{1+\beta_{ro}}(E_{\omega_{32}}^{*} - E_{\omega_{13}}) \quad a_{22} = -q\left(\frac{\beta_{ro}}{1+\beta_{ro}}E_{\omega_{14}}^{*} - \frac{1}{1+\beta_{ro}}E_{\omega_{42}} - \frac{\psi}{2q}\right)$$

The solutions are

$$E_3(x) = B_3\exp(-j\frac{\psi x}{2}) = E_3(0)\exp(-j(\Upsilon + \frac{\psi}{2})x) \tag{12}$$

$$E_4(x) = B_4\exp(j\frac{\psi x}{2}) = E_4(0)\exp(j(\Upsilon^{*} - \frac{\psi}{2})x) \tag{13}$$

where

$$\Upsilon = \tfrac{1}{2}(a_{11} - a_{22}) \pm \tfrac{1}{2}\sqrt{(a_{11} - a_{22})^2 + 4a_{12}a_{21}} \tag{14}$$

5.1.3 The gain coefficient

The coupling term Υ is complex. Let $\Upsilon = \Upsilon_r + j\Upsilon_i$. Then

$$E_3(x) = E_3(0)\exp(\Upsilon_i x - j(\Upsilon_r + \tfrac{1}{2}\psi)x) \tag{15}$$

$$E_4(x) = E_4(0)\exp(\Upsilon_i x + j(\Upsilon_r - \tfrac{1}{2}\psi)x) \tag{16}$$

The intensities, I_3 and I_4, will exhibit simple exponential gain, expressed by a gain coefficient, $2\Upsilon_i$, which is the new mechanism analogue of $2\Gamma\sin\Phi_g$. An interesting feature is the phase. If $\frac{1}{2}\psi \ll \Upsilon_r$, then beams 3 and 4 are phase conjugates.

Let us look at Υ more closely. We can simplify Eqn 14 somewhat by noting $E_{\omega_{13}} = E_{\omega_{42}}$ and $E_{\omega_{14}} = E_{\omega_{32}}$. So $a_{12} = -a_{21}$. Our general expression for Υ is

$$\Upsilon = \tfrac{1}{2}q\frac{1-\beta_{ro}}{1+\beta_{ro}}(E_{\omega_{14}}^{*} - E_{\omega_{42}}) \pm \tfrac{1}{2}\sqrt{q^2\frac{(1-\beta_{ro})^2}{(1+\beta_{ro})^2}(E_{\omega_{42}} + E_{\omega_{14}}^{*})^2 - 2q\psi(E_{\omega_{42}} + E_{\omega_{14}}^{*}) + \psi^2} \tag{17}$$

So our gain term for intensity is

$$2\Upsilon_i = \mathrm{Re}\left[jq\frac{1-\beta_{ro}}{1+\beta_{ro}}(E_{\omega_{42}} - E_{\omega_{14}}^{*}) + \sqrt{2q\psi(E_{\omega_{42}} + E_{\omega_{14}}^{*}) - \psi^2 - q^2\frac{(1-\beta_{ro})^2}{(1+\beta_{ro})^2}(E_{\omega_{42}} + E_{\omega_{14}}^{*})^2}\right] \tag{18}$$

The first term on the right hand side of the equation is due to on-Bragg coupling between the internal beam and the two pump beams. Power is transferred from pump 2 to the internal beam, but lost to pump 1. The second term is due to off-Bragg coupling.

It is worthwhile to look at two special cases.

I. *Three-wave mixing.* $\zeta = \frac{1}{2}$.

Here both internal waves are coincident, so we have in effect three-wave mixing. In this case, $E_{\omega_{14}} = E_{\omega_{42}}$. Eqn 18 becomes

$$2\Upsilon_i = -2q\frac{1-\beta_{ro}}{1+\beta_{ro}}\,Im(E_{\omega_{14}}) + \sqrt{4q\psi\,\mathrm{Re}(E_{\omega_{14}}) - \psi^2 - 4q^2\frac{(1-\beta_{ro})^2}{(1+\beta_{ro})^2}\,(\mathrm{Re}(E_{\omega_{14}}))^2} \tag{19}$$

Here it is obvious that on-Bragg coupling depends on the imaginary part of the modulated space charge field, and the off-Bragg coupling on the real part. Two other features are important here. The sign of q, which depends on r_{eff}, can be positive or negative by virtue of crystal orientation. This is a consideration in optimizing $2\Upsilon_i$. For example, to get large gain when q is positive, we must minimise $\mathrm{Im}(E_{\omega_{14}})$ and balance the two terms containing $\mathrm{Re}(E_{\omega_{14}})$ simultaneously. The second feature is the pump ratio, β_{ro}. For positive q and $\mathrm{Im}(E_{\omega_{14}})$, a beam ratio greater than one is necessary for effective on-Bragg coupling. If the beam ratio is less than one, then this term detracts from the overall gain.

II. *Equal pump intensities.* $\beta_{ro} = 1$.

Here

$$2\Upsilon_i = \mathrm{Re}\left(\sqrt{2q\psi\,(E_{\omega_{42}} + E_{\omega_{14}}{}^{*}) - \psi^2}\right) \tag{20}$$

This is the expression from Ref [110]. There are two strategies, mathematically, for maximising the real part of this square root (we assume $\zeta \neq \frac{1}{2}$). Which strategy we choose depends on the the size of the off-Bragg parameter, ψ. It has to be different from zero to have gain, but if it is too large, the ψ^2 term dominates and gain is reduced or lost completely. In our jigsaw puzzle analogy, when the hammer is too large it smashes the pieces rather than making them fit. Therefore we expect the

gain to be effective for small interbeam angles. However, for very large values of w one can achieve high gain if the real part of $(E_{\omega_{42}} - E_{\omega_{14}}^{*})$ is minimised while its imaginary part is maximised (and has a positive sign). For this to be effective, though, ζ must be different from $\frac{1}{2}$. In the case of three-wave mixing then

$$2\Upsilon_i = \sqrt{4q\psi\,\mathrm{Re}(E_{\omega_{14}}) - w^2} \tag{21}$$

The best test for the presence of the new gain mechanism is to have equal pump intensities. There is no on-Bragg coupling in this case.

5.1.4 Optimization of the gain

Let us look at the problem of achieving high gain for a particular case. We will restrict ourselves to the combination of three-wave mixing and equal pump intensities. The gain is optimized for the maximum value of $q\ \mathrm{Re}(E_{\omega_{14}})$. For the case $E_{q_{14}} \gg E_{s0}$ we have

$$\mathrm{Re}(E_{\omega_{14}}) = \frac{E_{s0}\left(1 + b_{14}\frac{E_{s0}}{E_{m_{14}}}\right)}{\left(1 + b_{14}\frac{E_{s0}}{E_{m_{14}}}\right)^2 + {b_{14}}^2} \tag{22}$$

which has extrema for

$$b_{14} = -\frac{E_{m_{14}}}{E_{s0}}\left(1 \pm \frac{1}{\sqrt{1 + {E_{s0}}^2/{E_{m_{14}}}^2}}\right) \tag{23}$$

Fig 3 shows $2\Upsilon_i$ as a function of pump detuning frequency ($\delta\nu_{12}$) for various interpump angles. Fig 3a is for positive q, and Fig 3b is for negative q. For all the theoretical plots in this chapter the crystal parameter values are those which give a good qualitative fit to the experimental data—that is, providing the correct peak frequency detuning for the symmetric case of three-wave mixing. The differences between these and those in Table 2.1 are $N_A^- = 2 \times 10^{22}$ m^{-3}, and the ratio $\mu/\gamma_r = 1.9 \times 10^{12}$ (V-m)$^{-1}$. We use an applied field of 8 kV/cm and a total pump intensity of 15 mW/cm^2.

It is clear there is one best overall interpump angle. For these parameters, it is approximately 3.2° for both positive and negative q. This angle gave us the best

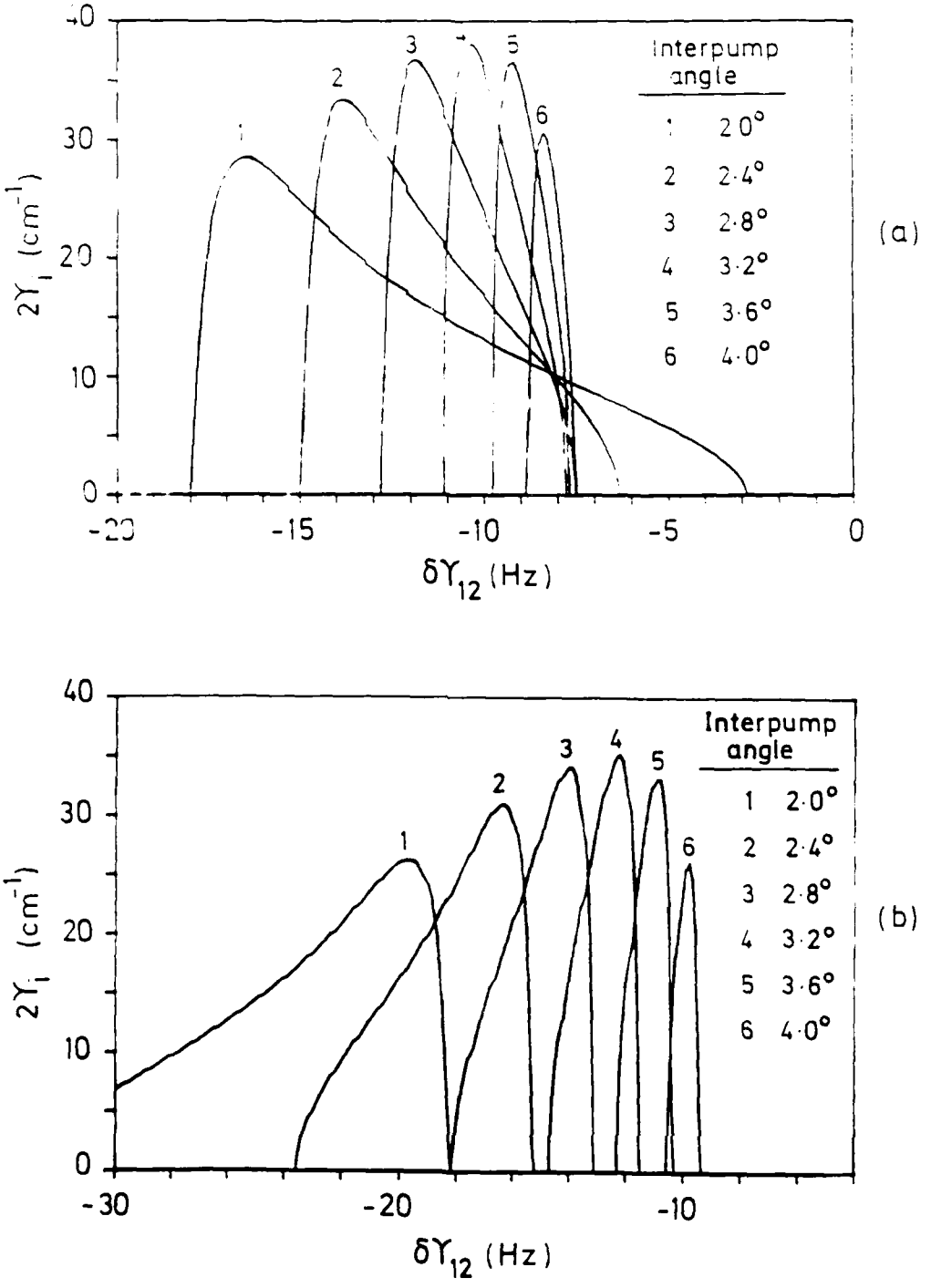

Figure 3: Gain coefficient, $2\Upsilon_i$ vs pump detuning frequency for various interpump angles (in air). (a) q positive. (b) q negative.

experimental gain. An important point is the magnitude of the gain coefficient. At optimum detuning and grating spacing, the gain is 37 cm^{-1}. In the case of nearly degenerate two-wave mixing, we found at small angles, $E_{\omega opt} = E_q$. If we compare mixing between pump 1 and the inside beam, then the same for the same crystal parameters the largest expected gain coefficient is 35.5 cm^{-1}. (Note: These values are theoretical values. In practice, because of loss, this gain coefficient is much less—a typical optimum value in $Bi_{12}SiO_{20}$ is 12 cm^{-1}.) This new gain mechanism seems to be slightly more efficient than the traditional mechanism.

5.1.5 Variation in ζ

If $\zeta \neq \frac{1}{2}$ then we have four-wave mixing. Fig 4 shows the gain coefficient as a function of ζ for various pump detuning frequencies for two extremes of in-air angles between the pump beams. Fig 4a is for an interpump angle of 1.6° and positive q, and Fig 4b for negative q. For a given value of ζ there is an optimum detuning frequency. Figs 4c and 4d show an interpump angle of 10°. This gain is only possible when the imaginary part of $(E_{\omega_{42}} + E_{\omega_{14}}{}^*)$ is maximised and ζ much different than $\frac{1}{2}$. The symmetry and interrelatedness of the internal beams is very important in these plots. Both beams experience the same gain.

At this point we should mention the appearance of spatial subharmonics between mixing beams in $Bi_{12}SiO_{20}$. This has been reported by Mallick, et al. [89]. The authors observed $K/2, K/3$, and $K/4$ subharmonics (where K is the grating vector formed by two nearly-degenerate mixing waves). These are very distinct beams which may attain an intensity relative to the pump beams of 40%. Which submultiples were visible depended on the amount of frequency detuning. Ref [89] suggested these beams were diffracted orders which overlapped and were mutually reinforced.

The spatial subharmonics reported correspond to $\zeta = 1/2, 1/3$, and $1/4$ for our four-wave mixing. Fig 4 shows that high gain is possible for these, and other, values

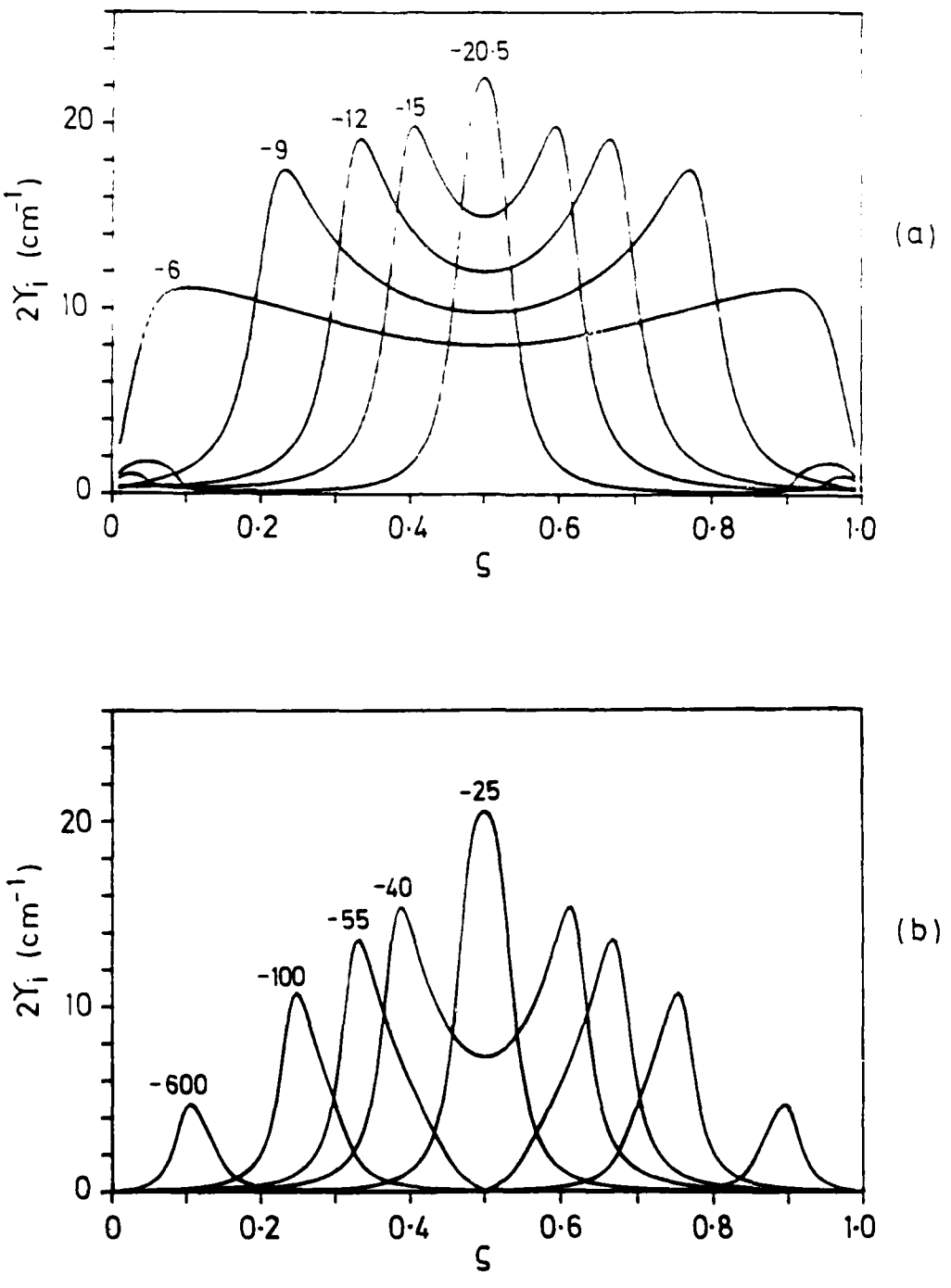

Figure 4: Gain coefficient, $2\Upsilon_i$ vs ζ for various pump detuning frequencies, $\delta\nu_{12}$ (Hz). Interpump angle (in air) = 1.6°. (a) q positive. (b) q negative.

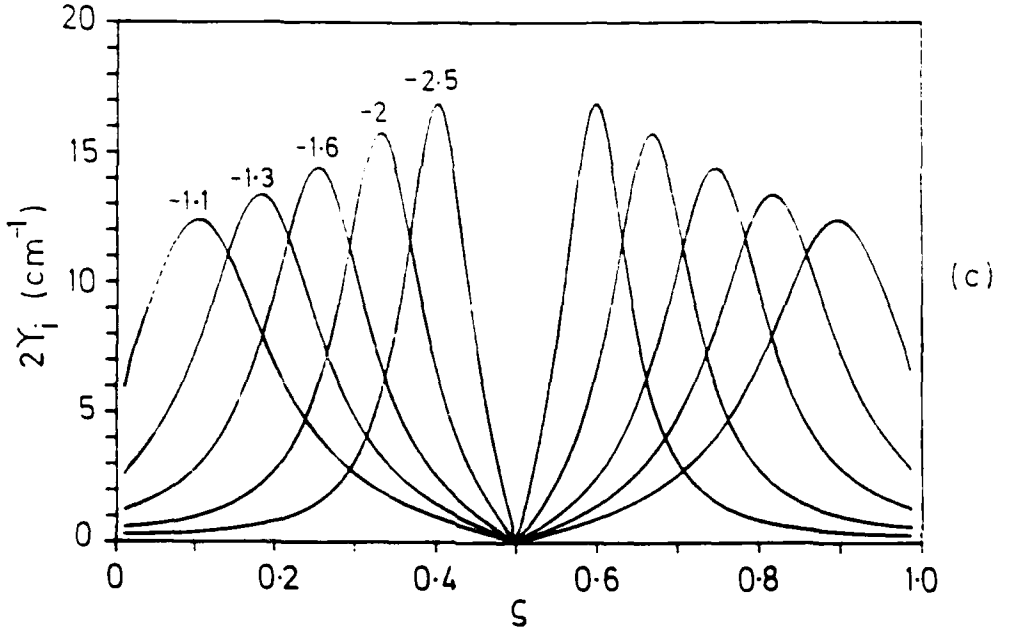

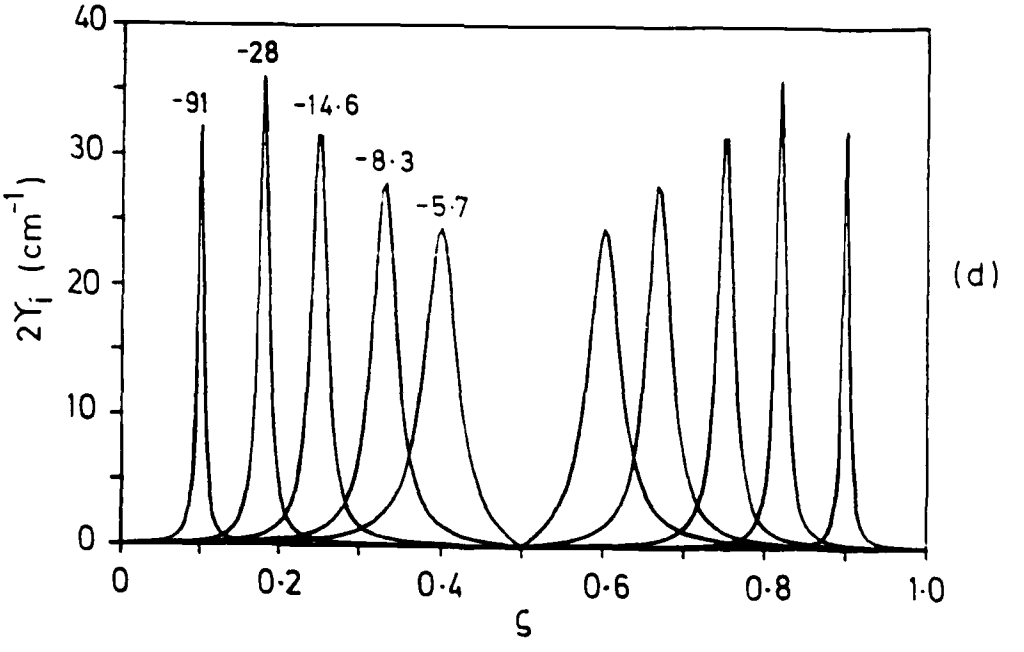

Figure 4: Gain coefficient, $2\Upsilon_i$ vs ζ for various pump detuning frequencies, $\delta\nu_{12}$ (Hz). Interpump angle (in air) = 10°. (c) q positive. (d) q negative.

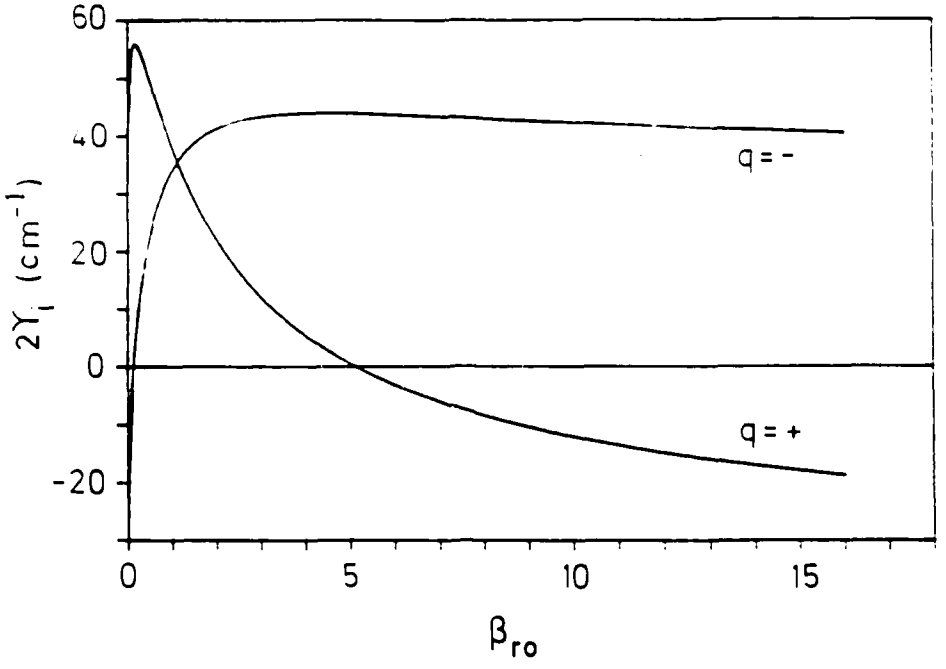

Figure 5: Gain coefficient, $2\Upsilon_i$ vs pump beam ratio for positive and negative q.

of ζ. Perhaps these intrapump beams arise from noise amplified by a combination of the gain mechanism described in this chapter, and a reinforcing mechanism. The phenomenon of subharmonics does not seem to be a general characteristic of $Bi_{12}SiO_{20}$—we have looked for it, but have never observed distinct subharmonics in any of our crystal samples.

5.1.6 Variation in pump beam ratio

The relative strength of the pump beams is important to the gain term. If the ratio is much different than 1, the on-Bragg coupling becomes important and may dominate the gain. In any case, pumps of unequal intensity produce a term inside the square root of Eqn 19 which detracts from the off-Bragg coupling.

The effect of changing β_{ro} on the gain coefficient is seen in Fig 5. Here $\zeta = \frac{1}{2}$, the interpump angle is 3.2° and for positive q, $\delta\nu_{12}$ is taken as -10.5 Hz, while for negative q, $\delta\nu_{12}$ is -12.5 Hz. These frequencies maximise the gain coefficient for $\beta_{ro} = 1$.

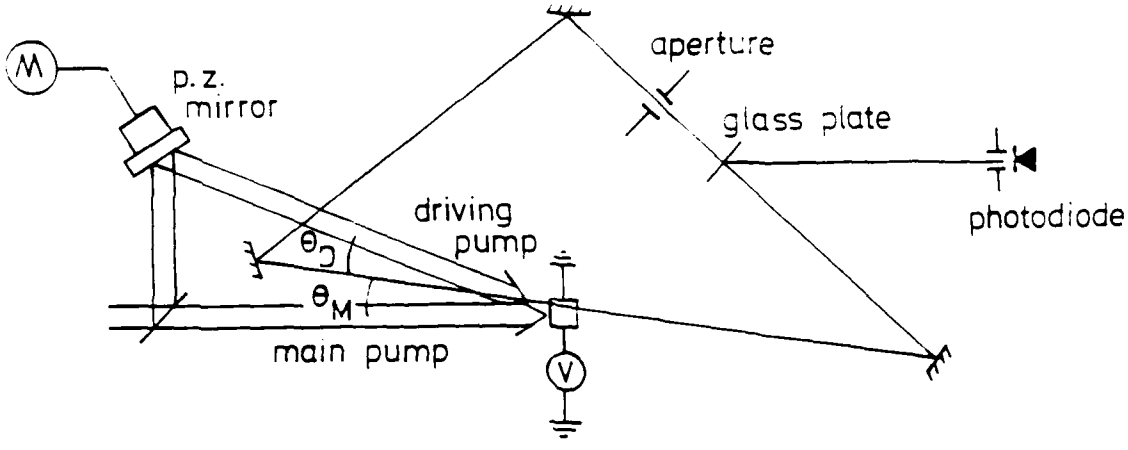

Figure 6: Unidirectional ring resonator with two pump beams.

5.2 Unidirectional Ring Resonator: Experimental Results

5.2.1 Experimental layout

We set about to prove experimentally the existence of the new gain mechanism. The obvious way of doing the experiment is to have 3 or 4 input beams and measure the power transfer into the signal beams. But the difficulty is then to adjust carefully the frequency detuning of each beam needed to maximise the interaction. We opted for a different experimental set-up (Fig 6) in which there are only two input beams (the two pump beams) and then one of the signal beams may emerge from the noise. In order to help the emergence of the signal beam we created a feedback loop by constructing a three-mirror resonator. This is not an ideal test of the theory because the interaction will now depend on additional phenomena like the scattering of the input pump beams and on new parameters like the resonant frequency of the cavity, and in our undepleted pump approximation there would be no limit to the exponential growth of the signal beam. However, this beam can only emerge in the

resonator if there is an amplification mechanism. Therefore the present experiments can prove the existence of the mechanism, but they are not suitable for checking quantitatively the predictions of the theory.

The photorefractive material used was the $Bi_{12}SiO_{20}$ sample described in Chapter 4. For all runs a 4 kV d.c. voltage was applied along the 001 crystal axis. Vertically polarized light of wavelength 514 nm was incident on the $\bar{1}10$ face. One pump beam (which we shall call driving pump) was Doppler shifted using a mirror mounted on a piezoelectric translator. The input signal to the translator was a triangular wave. During half the period the frequency shift was favourable for oscillation and amplification, and during the other half conditions were unfavourable. The ring resonator cavity was aligned using the main pump beam. An iris aperture in one of the cavity legs allowed only low order modes to oscillate. The oscillating beam was sampled from reflection off a glass plate.

5.2.2 Verification of new gain mechanism.

First the set-up was aligned so that the angle between the main pump beam and the oscillating beam, θ_M, was the same as the angle between the driving pump beam and the oscillating beam, θ_D. Then we switched on the main beam on its own and, as expected, obtained oscillation due to the traditional gain mechanism, that is the oscillating beam adjusted its own frequency detuning so as to maximise the imaginary part of the space charge field. Next we switched on the driving beam of the same intensity as the main beam. The oscillation stopped, as predicted, because the two pump beams worked against each other. The oscillating beam, however, reappeared if we slightly detuned the driving beam. Such detuning would not have helped the traditional gain mechanism (recall there is no gain via the imaginary part of the space charge field when there are two pump beams of equal intensity) but could maximise the new gain mechanism. Hence the reappearance of the oscillating beam is a proof for the existence of the new gain mechanism.

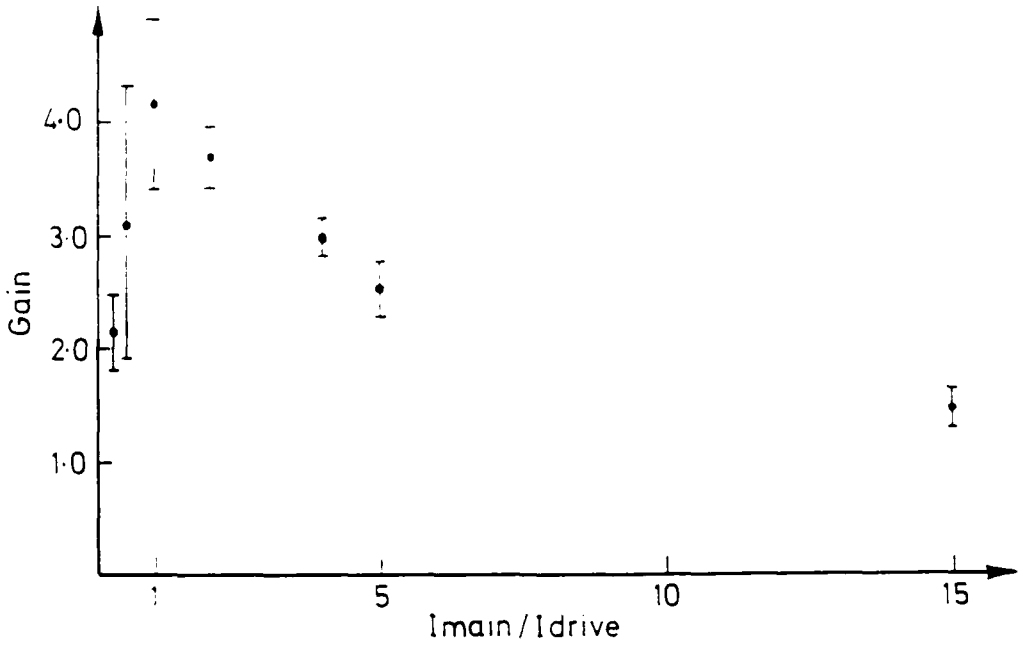

Figure 7: Gain vs ratio of pump beam intensities. Gain is defined as the photodiode signal with both pumps over the photodiode signal with only the main pump.

5.2.3 Comparison with traditional gain mechanism

The relative intensity of the oscillating beam as a function of pump beam ratio is plotted in Fig. 7. The interpump angle in air was 3.2° with the oscillating beam bisecting this angle. The intensity ratio (I_{main}/I_{drive}) was varied using a neutral density filter wheel. The photodiode signal was taken at optimum driving pump detuning frequency and this value was normalised to the average signal for oscillation with no driving pump. The driving pump had no noticeable effect for ratios $\geq$ 50:1—the oscillating signal was indistinguishable from that due to the main pump alone. For ratios $\leq$ 1:10 oscillation was surpressed. Presumably for very weak main pumps the new gain mechanism is not efficient—the direction of energy exchange from the driving pump for the traditional gain mechanism is wrong for our geometry. The optimum beam ratio was unity, giving an increase in signal intensity by about a factor of four. This overall behaviour agrees qualitatively with Fig 4a (for the case of negative q), although the peak there did not occur for $\beta_{ro} = 1$. Our crystal was set up so the energy transfer was $2 \rightarrow 4 \rightarrow 3 \rightarrow 1$, corresponding to negative q. We also see that the new gain mechanism is more efficient than the

traditional one. In a system with feedback, such as this resonator, a small increase in $2\Upsilon_i$ can be magnified into a large increase in gain.

Each data point represents the average of the photodiode signal for 10-30 cycles of the triangular input to the piezoelectric translator. The error bars represent one standard deviation for the data. The likely reason for the noisiness of the data is the rather short interaction length of the crystal, only 5.3 mm, thus giving only a limited amount of amplification. The overall plot and trends, however, were easily repeatable.

5.2.4 Optimization of gain

The dependence of the oscillating signal on the driving pump beam detuning is shown for a pumpbeam ratio of 1:2 (driving pump intensity = 10 mW/cm^2). Fig 8a shows the symmetric case of $\theta_M = \theta_D = 1.6°$, with error bars. The next two plots (without error bars) show the effect of keeping $\theta_M = 1.6°$ and varying θ_D, and for $\theta_D = 1.6°$ and varying θ_M. The trends are quite clear. In all cases there is an optimum detuning and the signal declines as θ_D or θ_M increases.

5.2.5 Search for subharmonics

Let us discuss some further experiments related to those of Mallick et al. who also had two pump beams incident on a $Bi_{12}SiO_{20}$ crystal and observed spontaneously emerging output beams at subharmonic positions. We asked the following question: Is the signal beam in the oscillator higher at a subharmonic position that in its vicinity, or in other words, are subharmonic positions in any way distinguished?

To answer this question we set $\theta_M = 1.6°$ and $\theta_D = 3.2°$, that is when the oscillating beam trisects the inter-pump angle and we chose unity beam ratio. This corresponds to the position of the third subharmonic. By varying either θ_M or θ_D or both we did not observe any preference for the subharmonic position. This seems to indicate that, as predicted by the theory of Ref [110], the subharmonic positions

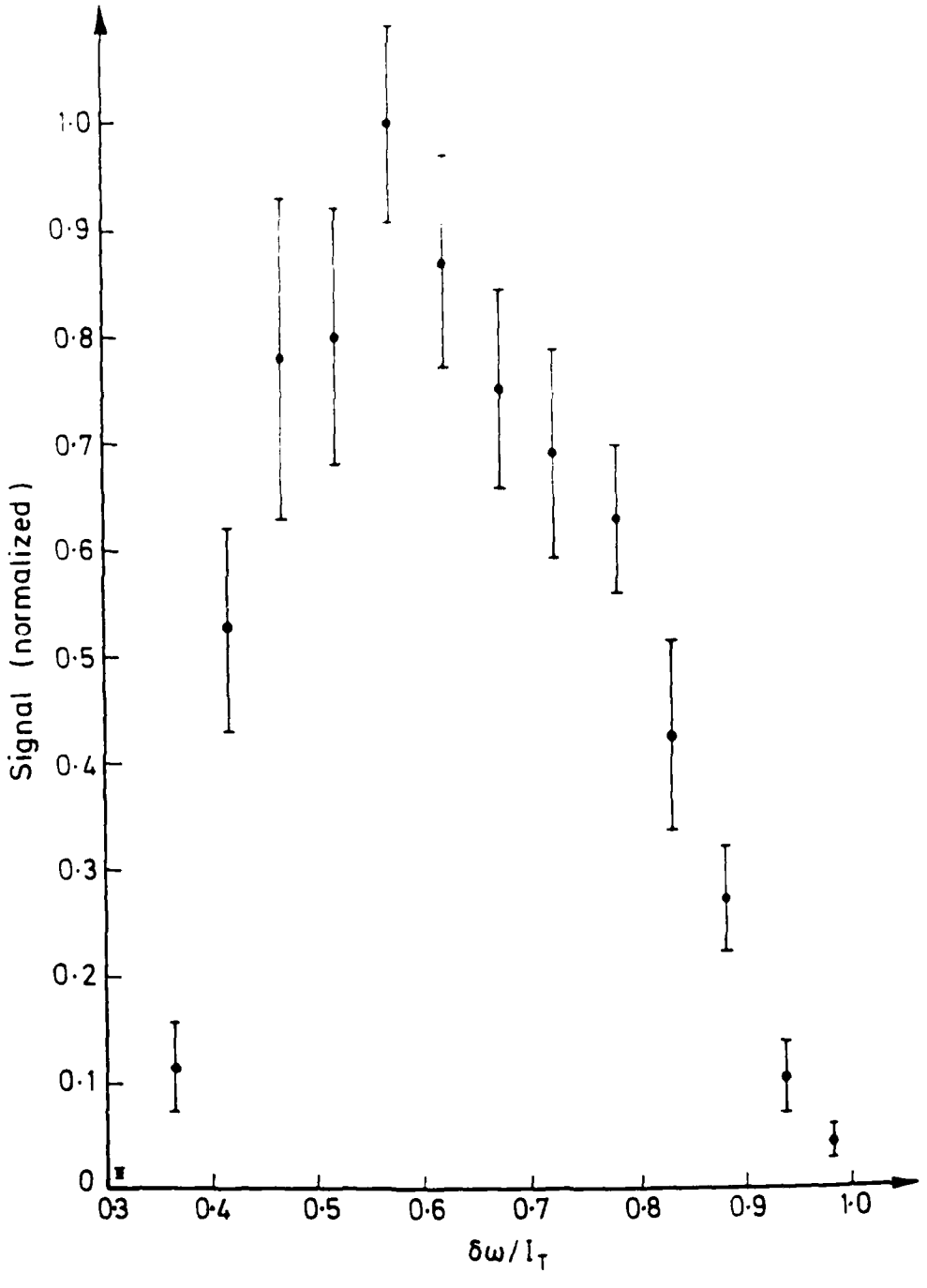

Figure 8: Normalised photodiode signal vs normalised driving pump beam detuning. (a) $\theta_D = \theta_M = 1.6°$ run. Error bars represent one standard deviation for the data.

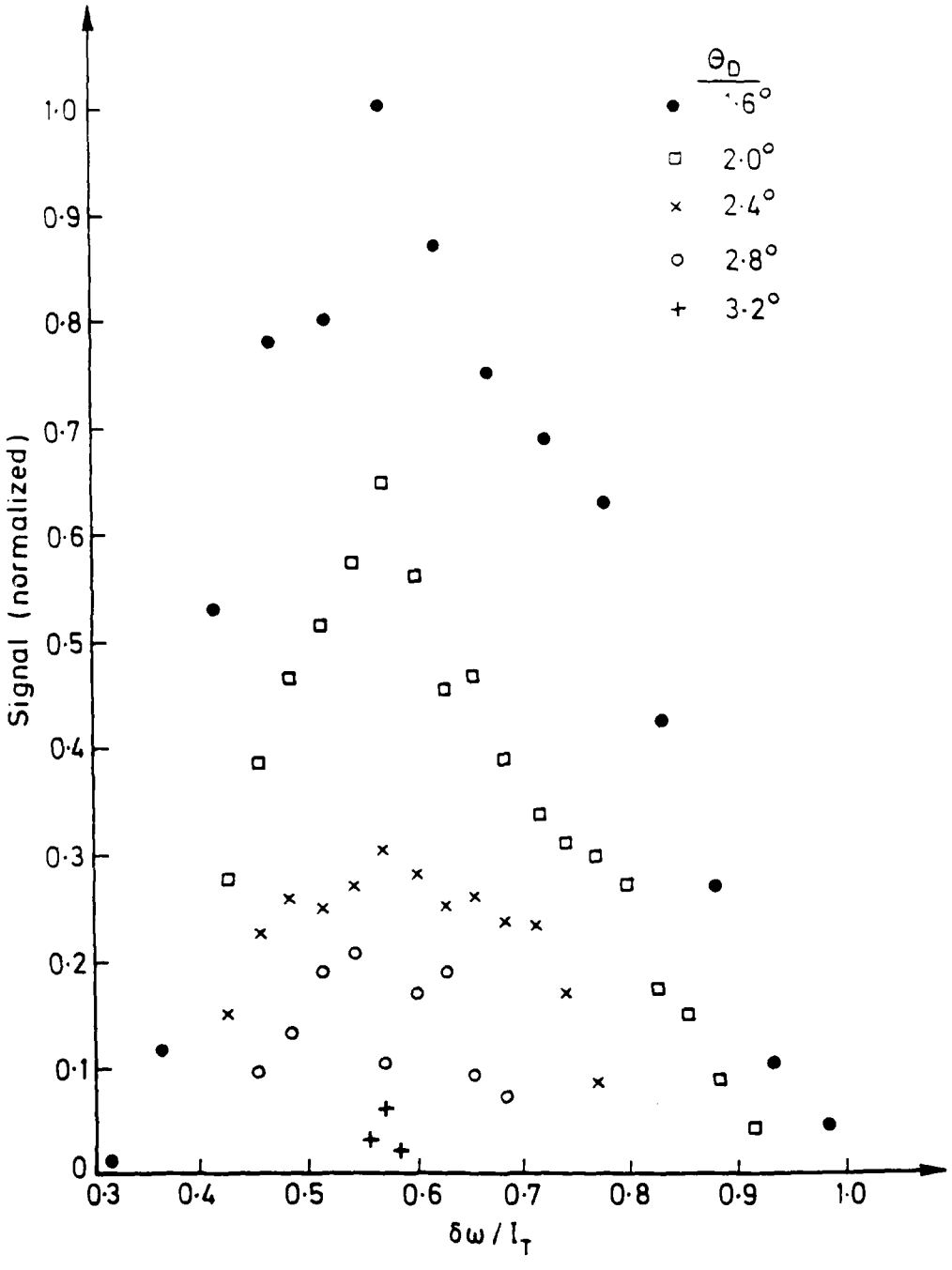

Figure 8: (b) Variation in oscillating beam-driving pump angle θ_D for $\theta_M = 1.6°$.

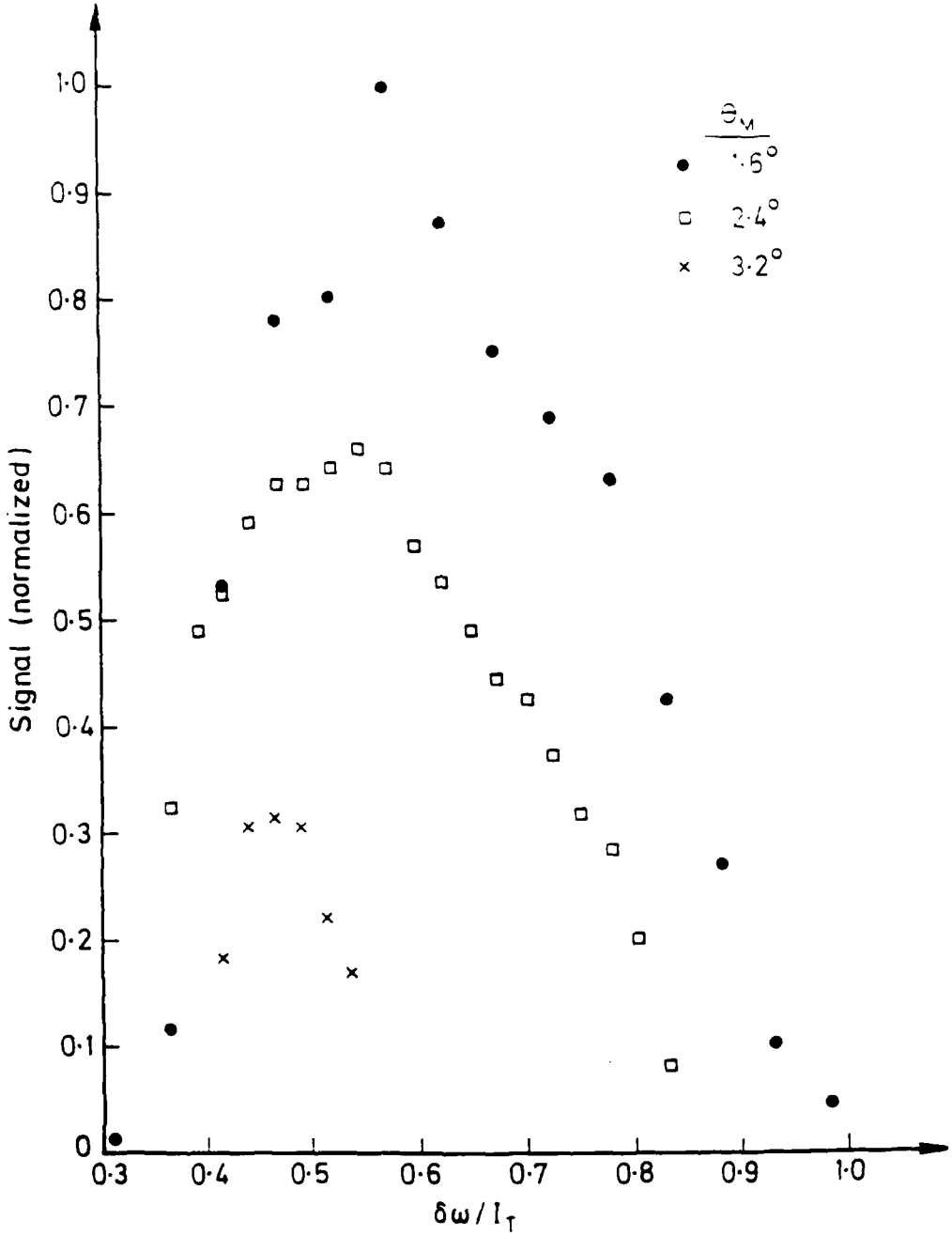

Figure 8: (c) Variation in oscillating beam-driving pump angle θ_M for $\theta_D = 1.6°$.

are by no means preferred and gain is *continuously* present for the range of θ_M's and θ_D's measured, not only in discrete positions.

There is no doubt that subharmonics were observed repeatedly and reproducibly by Mallick et al. Why is it then that neither the theory of Ref [110] nor our experiments can find any preference for subharmonics? It is possible the theory fails to find the subharmonics because of the approximations used, namely small modulation and no higher diffracted orders. Our experiments might miss the subharmonics because for some reason it is the presence of the resonator that ensures the continuously available gain. Another possibility is that the subharmonics found by Mallick, et al. are due to some properties of their experimental set-up, e.g. those of the piezoelectric drive.

We should mention an effect observed when in the range of pump frequency detuning correspoding to high gain. If the resonator was not aligned, or a screen was placed in one of the cavity legs, no oscillation occurred. However, a large patch of optical noise appeared in between the pump beams when the driving mirror movement direction was favourable for gain. This region could be fairly intense, roughly 20 times less than that for the oscillating beam. There were even "higher diffracted orders" produced— less intense regions of noise on either side of the pumps. It is clear from Fig 4a that gain is high, for small angles, for a range of ζ around $\frac{1}{2}$. Noise in this region undergoes high amplification.

5.2.6 The second signal beam

The appearance of the second signal beam is an important verification of the theory. The new gain mechanism depends on four-wave mixing. We cannot have amplification of one signal beam in the absence of the other. There is a crucial symmetry in these beams. In one experiment, we varied the interpump angle from 3.4° to 5.8°, keeping the angle θ_M constant as 1.7°. The angle between the second signal beam and the driving pump was measured at 1.7° in every instance.

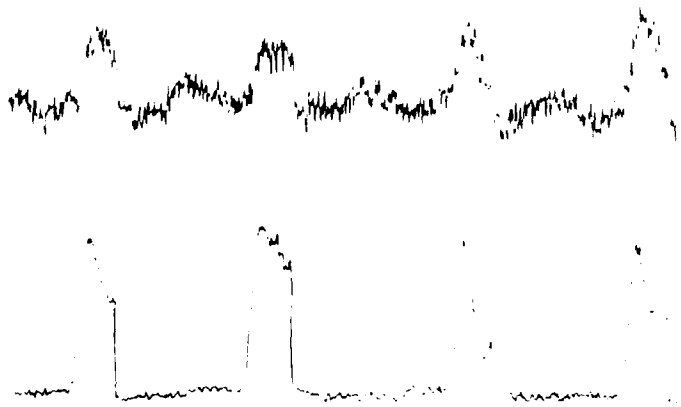

Figure 9: Simultaneous oscilloscope traces of signal strength of beams 3 and 4. Bottom trace is oscillating beam.

Both signal beams could be sampled using a photodiode. Fig 9 shows a typical simultaneous trace for the emergence of the two beams. The second signal beam was weaker (by a factor of 5 to 10), but the close relationship between the beams is unmistakable. If the oscillating beam was suddenly interrupted, both oscilloscope traces immediately dropped to background level.

5.3 Linear Resonator with Two Pump Beams

A significant finding of the last section was that for the ring resonator the gain in the system with two pumps was larger that using a single pump (i.e. exploiting the traditional photorefractive gain mechanism). This gave us encouragement to try the two pumps with a linear resonator arrangement with $Bi_{12}SiO_{20}$. Using just a single pump we have been unable to obtain oscillation in $Bi_{12}SiO_{20}$ with this geometry.

The linear resonator using photorefractive crystals as the gain medium has been investigated theoretically [24,65] and experimentally using $BaTiO_3$[131]. In these studies, a cavity is formed by two mirrors (see Fig 10), and a single pump is sufficient

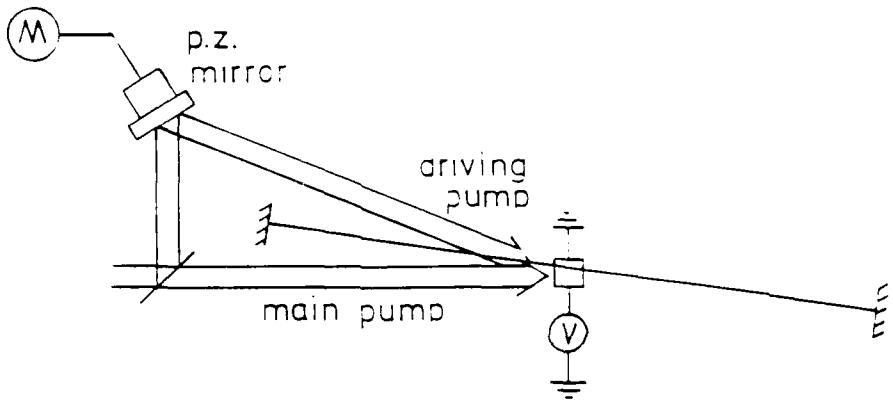

Figure 10: Linear Resonator: Experimental layout.

for oscillation to begin. The oscillating beams arise from the noise spectrum of the input pump beam. Those components which satisfy cavity resonance conditions and which have the appropriate frequency detuning can be amplified. If these counterpropagating beams are sufficiently intense, a phase conjugate of the input pump beam is produced.

That oscillation in the linear resonator is more difficult to start and sustain is readily seen in Fig 10. Amplification is effective only when the oscillating beam is codirectional with the pump beams. The oscillating beam must traverse the crystal twice to get back to a direction where gain is possible. We have twice the absorption loss. The situation is reminiscent of the ferrymen who hauled supplies and convicts out to the prison on Alcatraz island in San Francisco Bay—the trip was only profitable on the way out. This configuration using $Bi_{12}SiO_{20}$ was described by Rajbenbach and Huignard [105], but it is unclear what success, if any, they had in achieving oscillation.

Everything about the layout was the same as for the ring resonator, except a d.c. voltage of 4.75 kV was used. Both pumps had intensities of 4 mW/cm^2. The interpump angle was 3.2° in air and the oscillating beam bisected this angle. As before, the driving pump was detuned using a mirror mounted on a piezoelectric translator. We used a triangular ramp signal to drive the mirror. This effectively changes the sign of the frequency detuning halfway through each cycle and for one

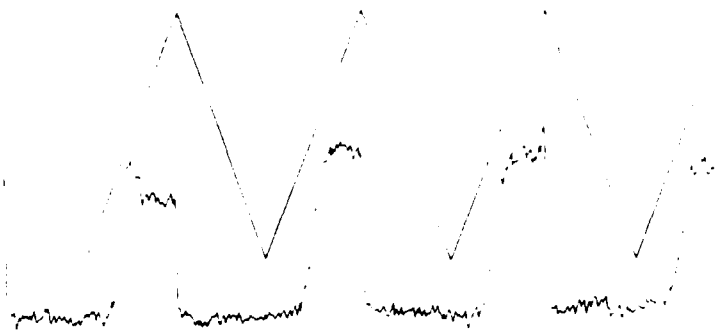

(a)

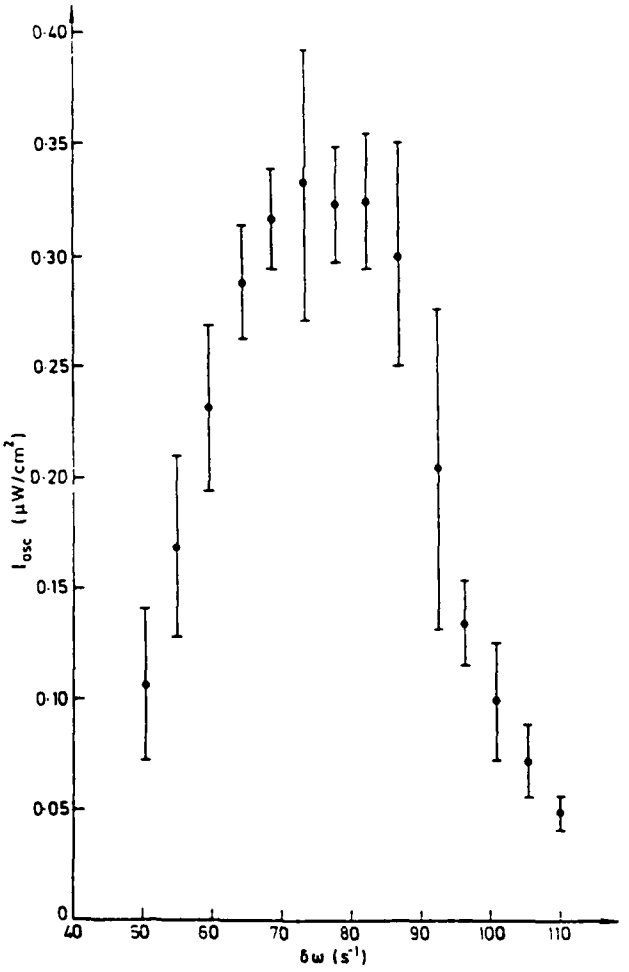

(b)

Figure 11: (a) Typical data for Linear Resonator. Top trace is ramp signal to piezoelectric mirror. (b) Oscillating beam intensity vs pump detuning frequency.

direction of mirror motion we expect favourable gain, but none for the opposite direction. This effect is readily seen in Fig 11a which depicts some sample data. Here $\delta\omega = 87\ s^{-1}$. There is a slight delay as the ramp voltage increases before oscillation begins. This might be explained, in part, by an initial slow amplification from the noise spectrum. More likely it is due to some chirp in the detuning of the driving pump beam due to inertia as the mirror changes direction of motion.

It was essential for both pump beams to be present to maintain oscillation. There was no oscillation for either pump alone. Thus it appears that, as for the case of the ring resonator, this new gain mechanism is more efficient than the traditional one.

The oscillating beam was sampled using the reflection (20%) off the front face of the crystal. Fig 11b shows the variation of the oscillating beam intensity as a function of the frequency detuning of the driving pump beam. There is clearly an optimum value. Unfortunately the intensity of the oscillating beam was not high enough to observe phase conjugate reflection.

5.4 Conclusions

In this chapter we have investigated a new mechanism for wave amplification in photorefractive materials. This mechanism uses two pump beams and is very effective in $Bi_{12}SiO_{20}$ at small interbeam angles where the off-Bragg parameter is small. Therefore it seems to be a useful complement to nearly-degenerate two-wave mixing described in Ref [109]. We have used this mechanism successfully in two different resonator configurations.

Chapter 6

Applications of Wave-Mixing in a Crystal Sample with a Wedge Angle

There is nothing insignificant.

Samuel Taylor Coleridge

The photorefractive effect, when first reported, was nearly dismissed as a mere nuisance. The opening paragraph of the paper by Ashkin, et al. [5] addressed the optically-induced refractive index inhomogeneity in $LiNbO_3$ and $LiTaO_3$:

> The effect, although interesting in its own right, is highly detrimental to the optics of nonlinear devices based on these crystals.

And the closing remarks proclaim (italics mine):

> Work on this mechanism and its *possible elimination* is continuing.

Chen recognized the potential of the change in refractive index as a means of storing volume holograms [20] and the rest, as described in Chapter 1, is history.

The moral here, of course, is that in the construction of technology, sometimes stumbling blocks make the best building material.

In our experiments with the unidirectional ring resonator described in Chapter 4, we discovered a crystal sample of $Bi_{12}SiO_{20}$ with a wedge angle. The multiple reflections created by the wedge and their resulting higher diffracted orders introduced new channels through which incident power was transferred. The result was a loss in efficiency of the resonator. It would be simple to denounce the wedge angle as an unfortunate mishap and have the sample repolished. But before taking that step we should ask: Is there any use for a crystal with a wedge angle?

One application is immediately obvious and was mentioned in Chapter 4. One can produce many output beams with a single input beam. Since the wedge angle is fixed, the results are highly reproducible—something not always guaranteed with photorefractive crystals.

This chapter addresses other ways of utilizing our "unfortunate mishap". First we look at some interesting transient phenomena when the applied voltage is first turned on. This provides some insight into how power is transferred among the higher diffracted orders. Finally we use a He-Ne 633 nm beam to probe the grating formed by argon ion laser light of 514 nm. The probe beam was coincident with the writing beam. We observed a field/intensity dependent scattering that has potential application in laser beam steering.

6.1 Transient Effects in Higher Diffracted Orders

6.1.1 Transient energy transfer between mixing beams

There is a certain inertia during grating formation in photorefractive materials. It takes time for the space charge field to build up to modulate the refractive index. The build-up period is characterised by transient effects and these can be quite spectacular. For example, in drift-dominated two-wave mixing, the power transfer

is oscillatory and during the undulations of intensity, a weak signal beam can nearly deplete a strong pump beam [45].

The time dependence of the modulated space charge field produced by two mixing waves is described by the well-known differential equation [116]

$$\frac{\partial E_{s1}}{\partial t} - gE_{s1} = f\,m \tag{1}$$

where m is the modulation ratio of the the mixing waves and

$$g = \frac{1}{\tau_d}\frac{A}{D},\quad f = \frac{1}{\tau_d}\frac{C}{D},\quad A = 1 + \frac{E_t}{E_q} + b\frac{E_{s0}}{E_m} + j\left(\frac{E_{s0}}{E_q} - b\left(1 + \frac{E_t}{E_m}\right)\right)$$

$$C = -\frac{E_{s0}}{E_q} + j\frac{E_t}{E_q},\quad D = 1 + \frac{E_t}{E_m} + j\frac{E_{s0}}{E_m}$$

Eqn 1 reduces (as it must) to Eqn 2.19 in the steady-state. Because the coefficients are complex in this first order differential equation, the time behaviour of E_{s1} can be oscillatory.

In short, transient effects are described by Eqn 1 and the coupled wave equations. John M. Heaton's D.Phil. thesis provides many theoretical and experimental details of two-wave mixing transient behaviour in $Bi_{12}SiO_{20}$ [49]. In particular he developed both numerical and analytic solutions to the coupled time and space differential equations. Both treatments, though, are computationally complicated. For example, the analytic solution works only for the undepleted pump approximation and requires complex integration and the evaluation of Bessel functions with complex arguments. Appendix C reveals a new, simple, analytic formula we have developed for the signal beam complex amplitude which agrees remarkably well to the numerical solution of Heaton and Solymar [48] for a wide range of important and practical cases. The savings in computer time is marked. A typical calculation of 220 time points using either method of Heaton takes 20 minutes on an IBM personal computer, while the computation of the same number of points using the simple formula requires less than 5 seconds.

Transient effects have been studied experimentally in two-wave mixing in $LiNbO_3$ [75], $Bi_{12}GeO_{20}$ [45], and $Bi_{12}SiO_{20}$ [49,64]. Observed effects are

- Power is transferred from the strong beam to the weak beam.
- For small interbeam angles and small applied fields the transfer is oscillatory.
- For strong applied fields the grating writing times are longer.
- For smaller grating spacings (larger interbeam angles) the grating writing times are longer.

Our study is the first experimental look at transient power transfer among higher diffracted orders.

6.1.2 Videotape studies

The business of applying a voltage to a crystal may seem rather mundane, but there are definite considerations. $Bi_{12}SiO_{20}$ is a very good insulator in the dark (resistivity = 5 x $10^{13}\,\Omega$ cm [2]). One must be careful of having a high voltage across an unilluminated crystal. The danger is an in-air spark between the electrodes which might damage the crystal (see Appendix A). The crystal must be flooded with light to reduce the resistivity several orders of magnitude before the voltage is applied.

The turn-on characteristics of our HV power supplies were not step-functions. There was no instantaneous jump from 0 V to the desired potential difference. Instead the voltage (as measured from the current across a fixed 10 GΩ resistor—a value close to the resistance of our illuminated crystal) had rise time constants on the order of a few milliseconds, and generally experienced some type of overshoot above the final steady-state voltage. For example, if the power supply was turned to 1 kV, the voltage peaked at 2.7 kV (an overshoot of 1.7 kV) before dropping back to 1 kV. For a desired voltage of 4.0 kV the rise time was longer and the overshoot was 1.0 kV (underdamped behaviour).

Modelling a time-varying applied field like this is difficult, and, for the most part, unnecessary. Studies of transient behaviour in photorefractive crystals employ

choppers or shutters for one of the mixing beams with the applied voltage at its steady-state value [49].

But the simple fact remains: at some instant, one has to turn on the voltage with the crystal illuminated. Not so simple is that when this occurs, a pulse of light energy escapes from the crystal, away from the region of transmitted light.

This effect is observed to some extent, in all of our $Bi_{12}SiO_{20}$ crystal samples. The pulse duration is short—less than one second for intensities on the order of 1 mW/cm^2. This is too fast for ordinary camera film to pick up, but not for a TV camera. We observed scores of transient sequences and recorded on videotape several of them for varying crystal sample, incident intensity, and magnitude and polarity of applied voltage.

Figs 1a-f show a transient sequence for one crystal. This was a sample from Sumitomo Electrics. Its front face was a 1 cm square and it measured 3mm thick. A voltage of 5 kV was applied along the 001 axis and the incident light was vertically polarised, of wavelength 514 nm, and intensity 0.3 mW/cm^2. Fig 1a starts with the transmitted light with no applied field. Scatter is seen predominantly on sides of the crystal image. The top and bottom scatter regions are due to an incomplete fit of the crystal in its holder—there were gaps through which light could pass. It is likely the scatter on the left results from a reflection off an internal surface, although we took efforts to ensure the incident light was normal to the front surface. The subsequent photographs show the emergence of the light pulse on the left side at intervals of 20 ms. The pulse manifests itself as somewhat staccato horizontal streamers that reach out from the main transmitted beam. There are two counterpropagating pulses—one on either side of the crystal, but the one corresponding to the primary direction of energy transfer is the most prominent.

We can explain this pulse in terms of amplification of scatter noise. As soon as a voltage is applied to the crystal, power can be transferred to scattered beams making small angles with the incident light. These beams are amplified, generating

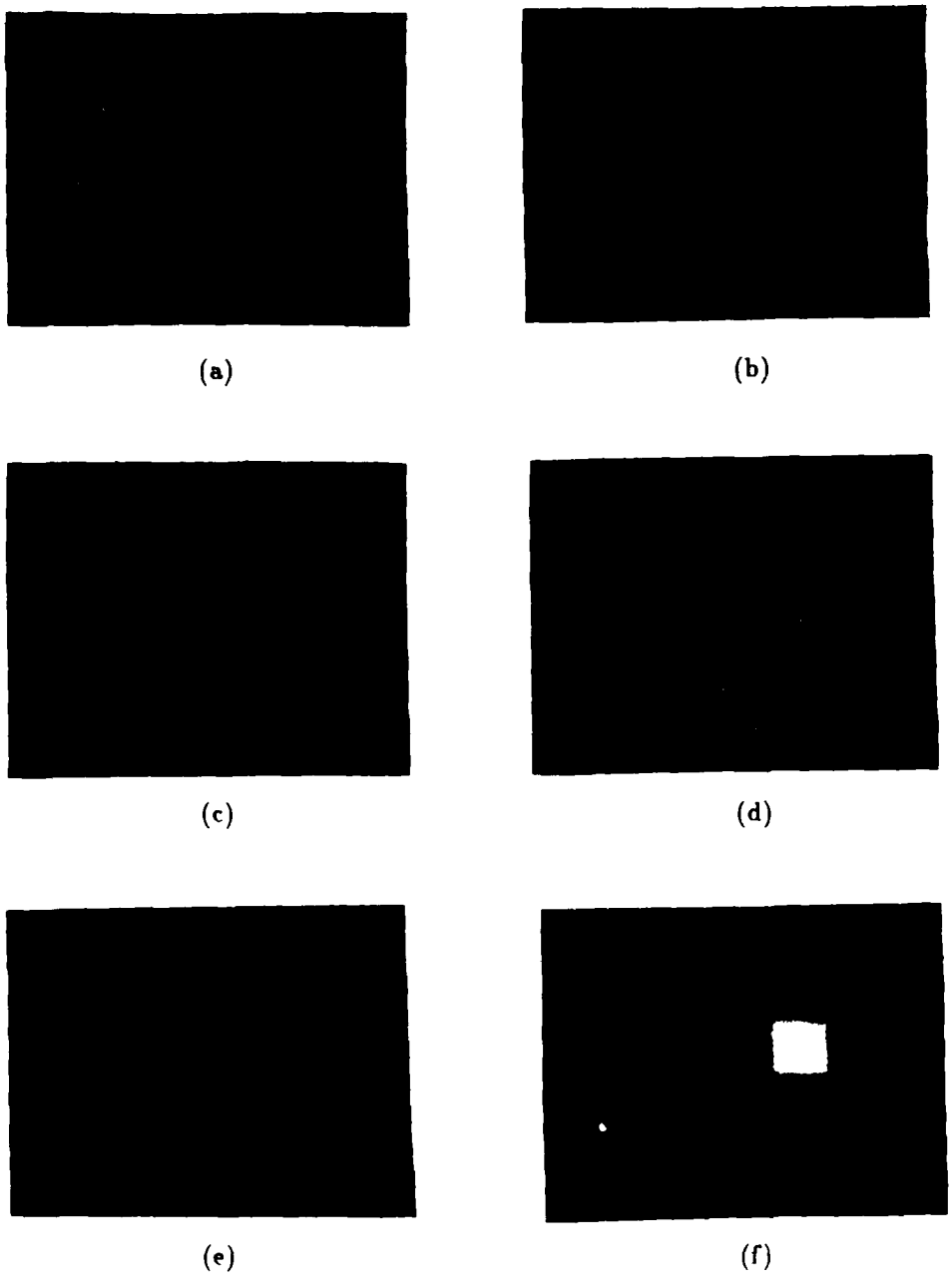

Figure 1: Transient effects in Sumitomo $Bi_{12}SiO_{20}$ crystal sample. (a) No applied field. (b) 20 ms after application of field. (c) 40 ms. (d) 60 ms. (e) 80 ms. (f) 100 ms.

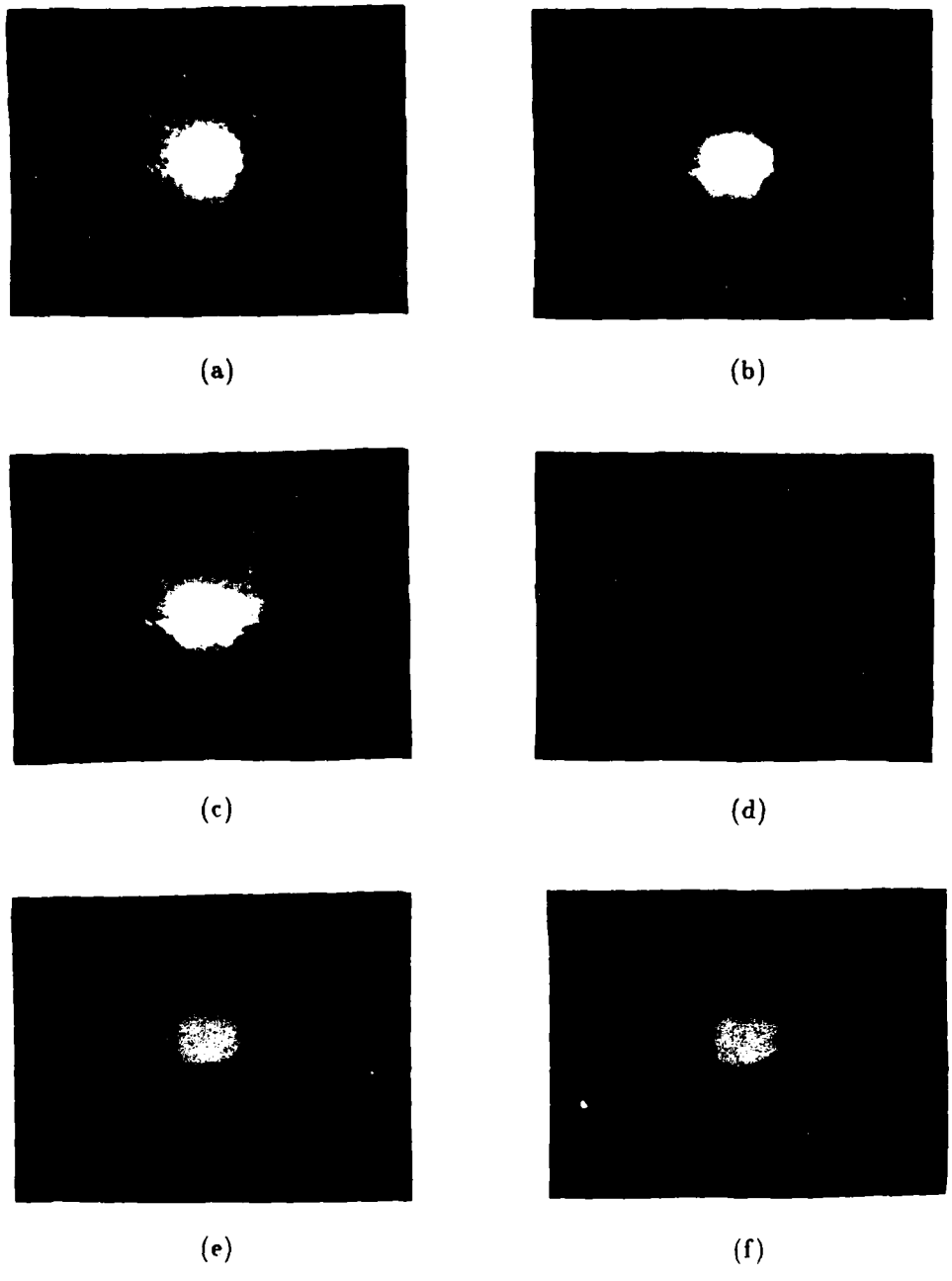

Figure 2: Transient effects in Crystal Technology $Bi_{12}SiO_{20}$ crystal sample. (a) No applied field. (b) Field turn on. (c) 20 ms after application of field. (d) 60 ms. (e) 80 ms. (f) 100 ms.

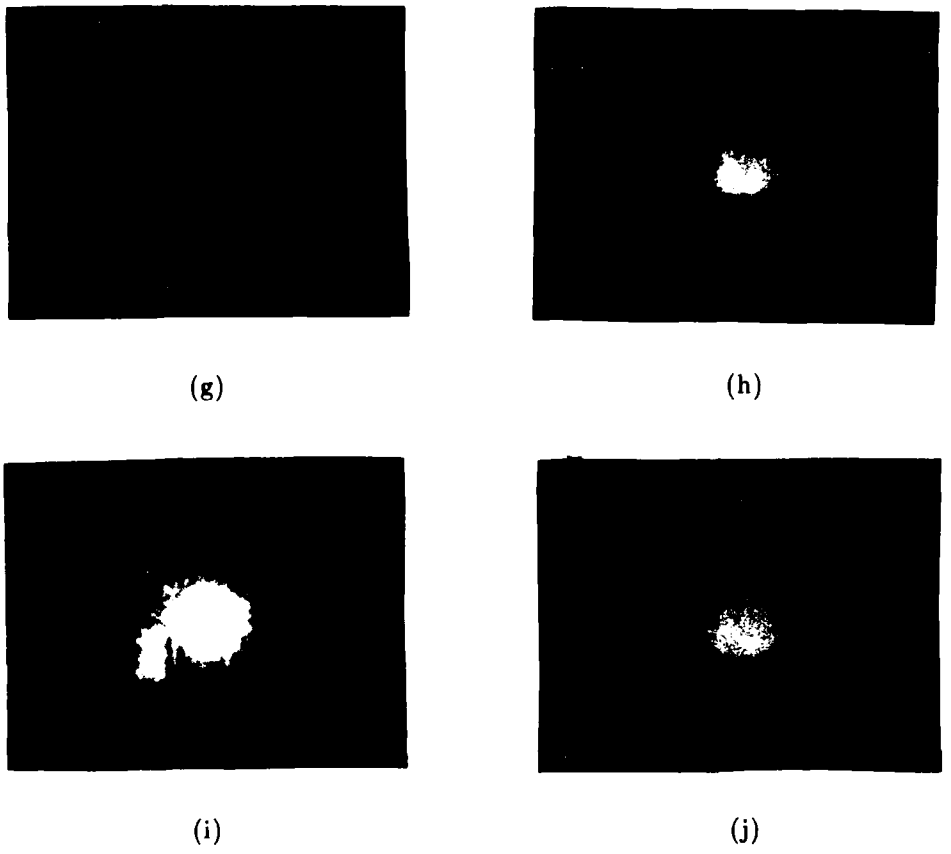

Figure 2: Transient effects in Crystal Technology $Bi_{12}SiO_{20}$ crystal sample. (g) 120 ms. (h) 160 ms. (i) 200 ms. (j) 400 ms.

more scatter which can be amplified, creating additional scatter and so on. Power is passed on like the baton in a relay race. This transfer is very effective in the transient phase because of the presence of moving fringes [49].

Through our studies we can make these observations. Keeping everything else constant:

- Pulse duration increases with decreasing incident illumination.
- Pulse duration and spatial extent decreases with decreasing applied voltage.
- The pulse is seen predominantly on the side corresponding to the direction of normal power transfer.
- The pulse reoccurs when the voltage is turned off.

Figs 2a-j show the Crystal Technology $Bi_{12}SiO_{20}$ sample with the wedge angle (0.036°). Here the bright pulse of light moves horizontally to the right (the correct direction for normal power transfer for this orientation), and we see the higher diffracted orders emerge on either side in sequence. This is a very pretty thing to watch. The intensity of the orders undulates as another pulse moves out along the 35° line.

Clearly this phenomenon gives us rare insight into energy transfer among higher diffracted orders. It is worth looking at this in greater detail.

6.1.3 Photodiode measurements

A closer inspection of the transient behaviour was made using the experimental layout in Fig 3. The path length from crystal to photodetector was approximately 3 meters. This length was necessary to provide adequate spatial separation of the orders to steer them to the appropriate detector. A storage oscilloscope monitored two orders at a time. We numbered the orders as in Fig 4.9a, that is the main incident beam was the 0 order, the first multiple reflection (on top) -1, the second

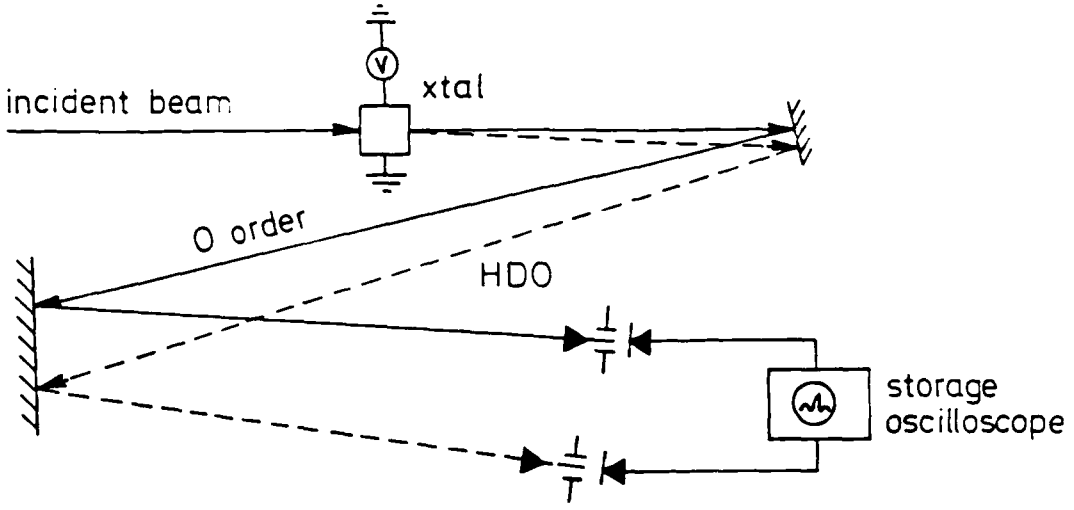

Figure 3: Study of transients in higher diffracted orders. Experimental layout.

-2, etc. Those orders below the 0 order wave were numbered +1, +2, and so on. The -1 order was always monitored and this provided a reference. An attempt to measure the main beam revealed no discernible change in intensity during transient effects, ie. an undepleted pump. Repeatibility was excellent in these runs.

Fig 4 shows some typical data. This is for an applied voltage of 4 kV and incident intensity of 1.4 mW/cm^2 for beams -1 and +1. We see that both beams gain in intensity after the field is applied, but beam +1 gains more slowly and peaks while beam -1 is losing strength. Both beams show ringing effects, but in beam +1 the oscillations are more damped.

Fig 5 shows oscilloscope traces for beams +1, +2, -1 and -2 (the only beams measurable) for the same intensity of 0.45 mW/cm^2 and an applied field of 4 kV. This is a composite of 3 plots in which the -1 traces were matched. The dashed line marks the instant the voltage is first applied. The important feature here is the confirmation of what was observed in the video runs. The intensity peaks move out sequentially from the main beam. Also higher diffracted orders seem to grow in pairs—orders +1 and -2 peak at roughly the same time.

We can explain the relative delay in power transfer to the outlying orders in two

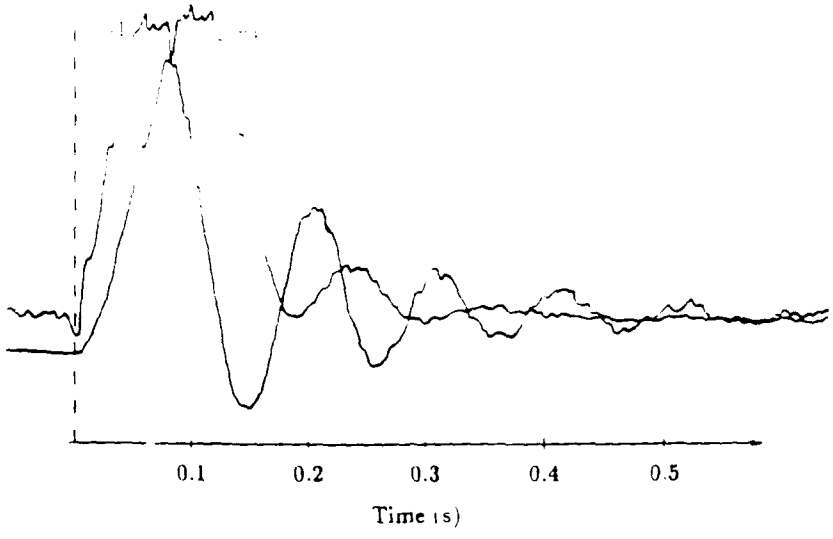

Figure 4: Simultaneous oscilloscope traces for photodiode signals of beams -1 and +1. Incident intensity is 1.4 mW/cm^2. Applied voltage is 4 kV. Dashed line represents the instant voltage is first applied.

ways. First, efficient power transfer depends on a strong modulated space charge field. The coupling of an order to its adjacent orders is expressed in the modulation ratio, m, in Eqn 1. Until the adjacent order amplitude grows large, the driving term, fm, is weak. Thus the growth of one order couples it more strongly to the next order and so on. This is why optical intensity seems to be handed from order to order. The second effect is due to coupling with the main beam. The larger the interbeam angle, the longer the grating writing time. So receiving power directly from the main beam takes more time for distant orders.

We can take the time from first applying the voltage to the first peak in intensity as a repeatible, representative time value for the photorefractive transient effect. Because we are using low light intensities the transient behaviour has time constants on the order of tenths of seconds or longer. The time constants for the rise of the voltage delivered by the power supply was on the order of milliseconds—so we may neglect transient circuit effects. Fig 6a shows the reciprocal of this time value plotted as a function of incident intensity for the -1 beam. The fit is remarkably

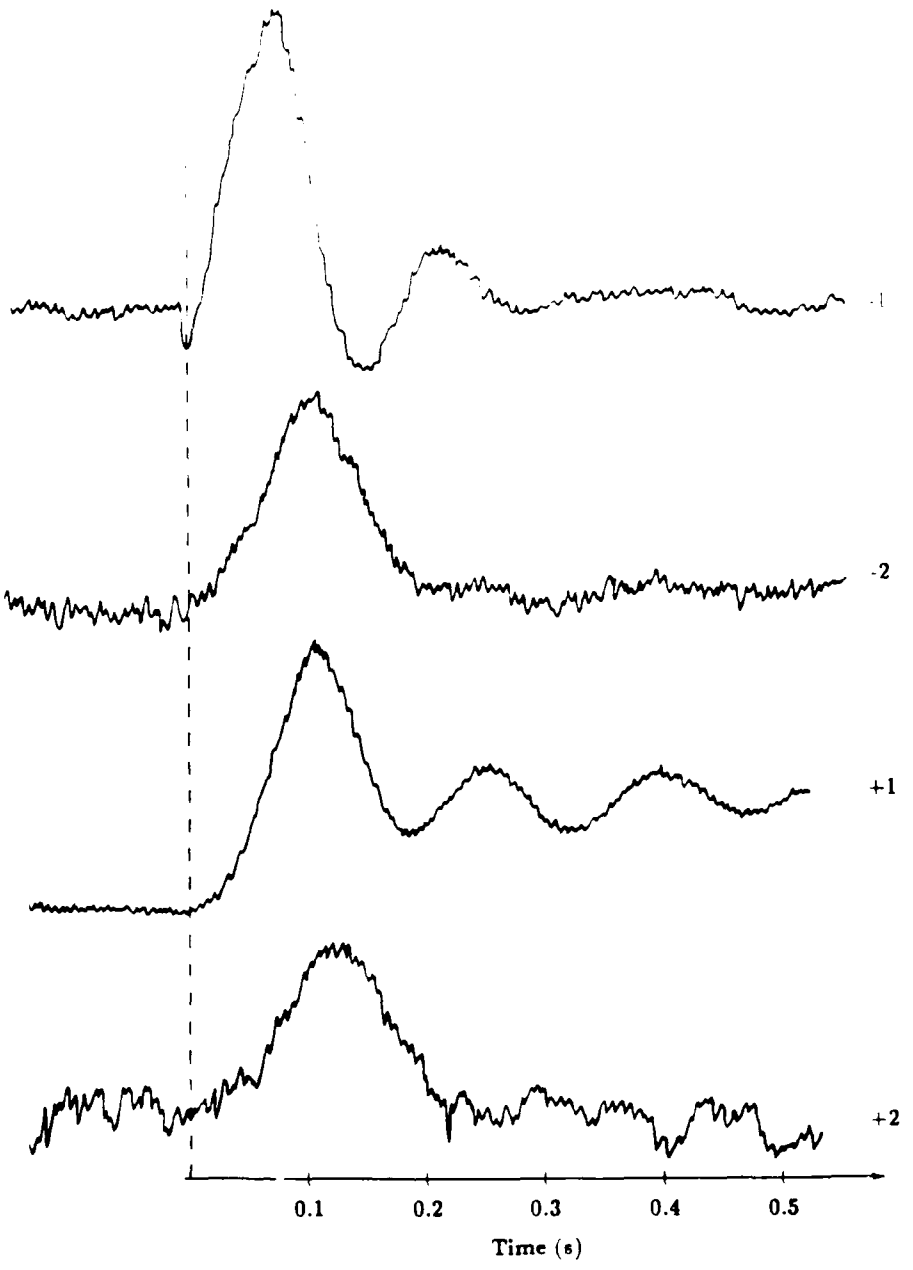

Figure 5: Composite of oscilloscope traces for photodiode signals of beams -1,-2, +1 and +2. Incident intensity is 1.45 mW/cm^2. Applied voltage is 4 kV. Dashed line represents the instant voltage is first applied.

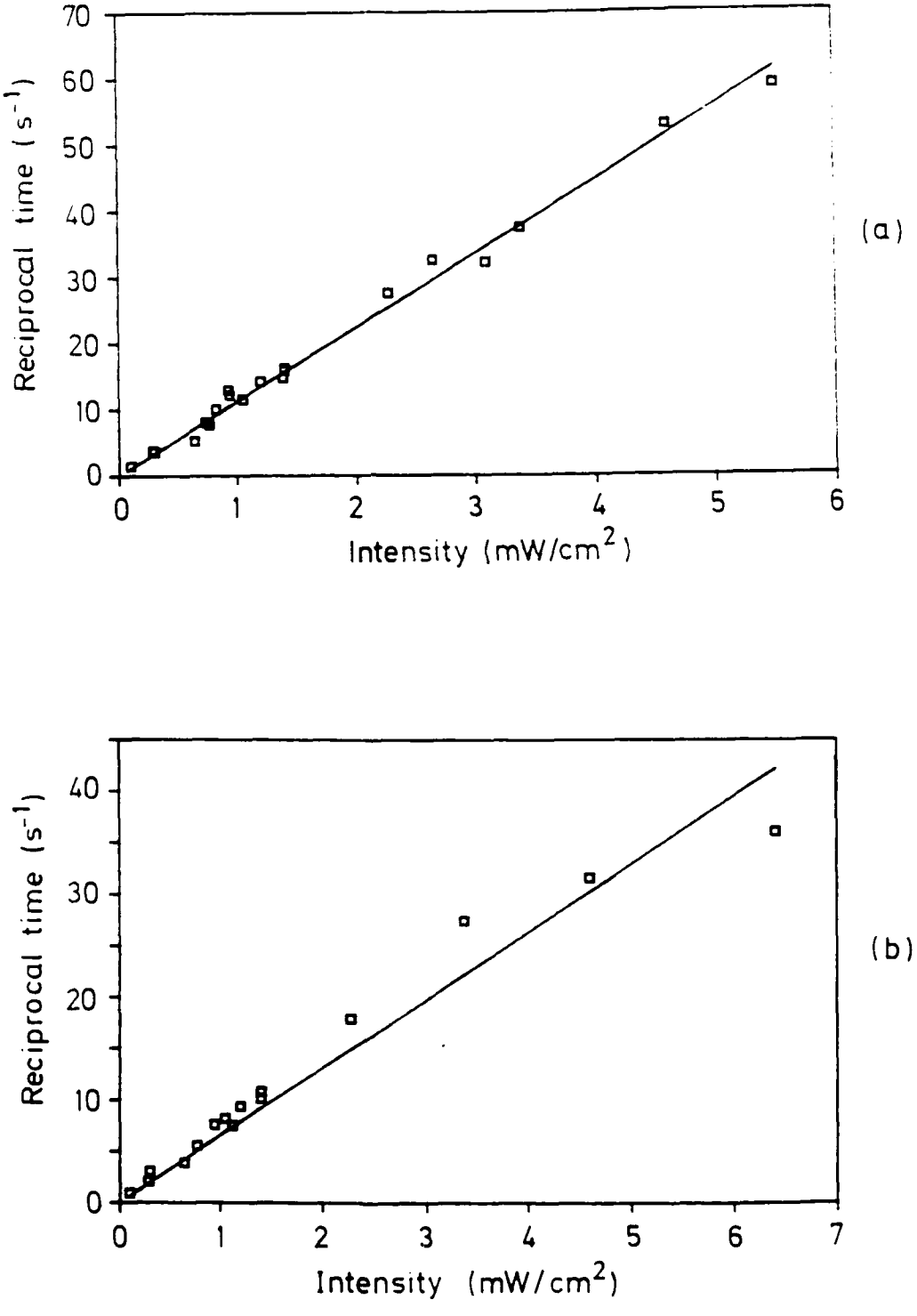

Figure 6: Reciprocal of time from the instant voltage is first applied to the first intensity peak vs incident intensity. Applied voltage is 4 kV. (a) -1 order. (b) +1 order.

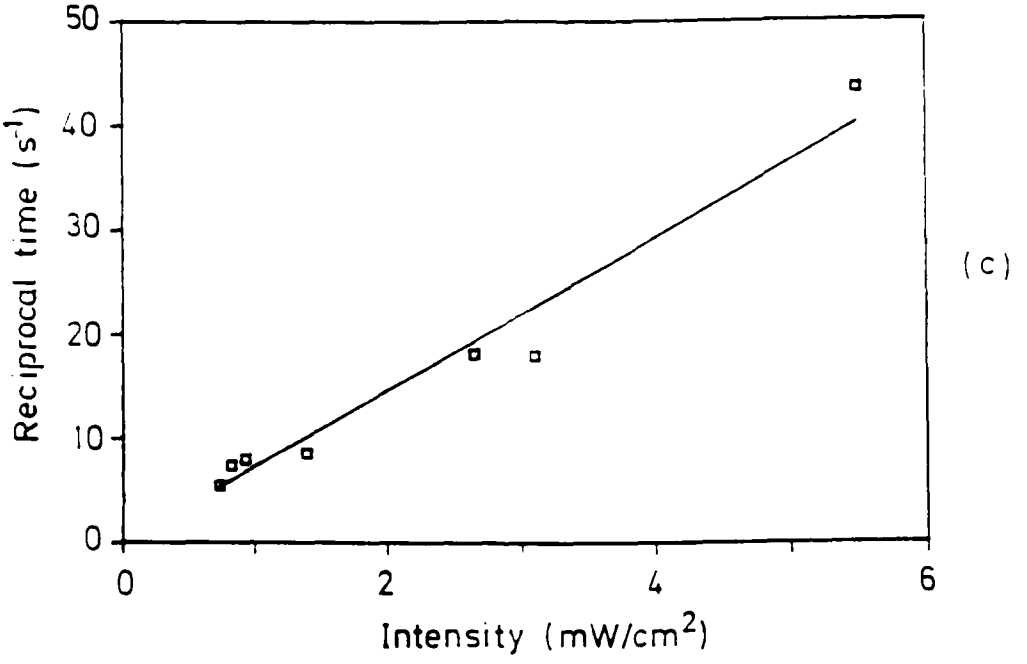

Figure 6: Reciprocal of time from the instant voltage is first applied to the first intensity peak vs incident intensity. Applied voltage is 4 kV. (c) -2 order.

linear. This suggests the time value is in some way proportional to the dielectric relaxation time constant, τ_d, which we know is inversely proportional to intensity. Figs 6b and c show similar plots for orders +1 and -2. Here the slopes of the best linear fits are very close (6.6 and 7.3 mW/cm^2-s respectively), which again suggest the emergence of these orders as a pair.

Finally we need to ask what is the dependence of the transient behaviour on applied field. In two-wave mixing an increase in applied field tended to slow down the transient effects. This is seen in higher orders as well, as evidenced in Fig 7.

Fig 8 shows the effect of applied voltage on the reciprocal time from the instant the voltage is first applied to the first intensity peak. Again we see a slowing of transient behaviour for large applied electric fields.

Our wedge angle has provided a simple means of producing highly repeatible transient effects in higher diffracted orders.

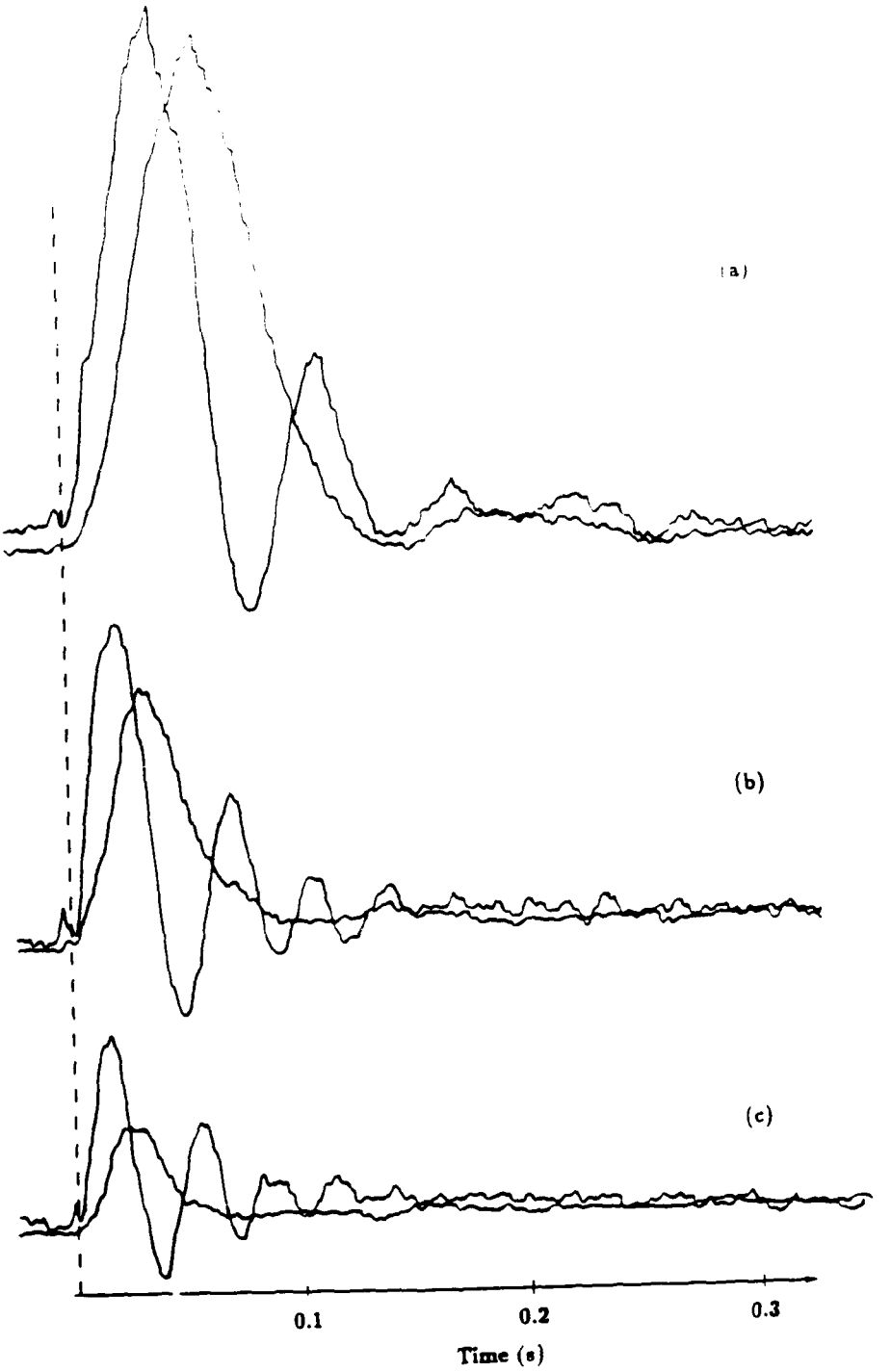

Figure 7: Simultaneous oscilloscope traces for photodiode signals of beams -1 and -2 for various applied voltages. Incident intensity is 2.6 mW/cm^2. (a) 4.5 kV. (b) 2.5 kV. (c) 0.5 kV.

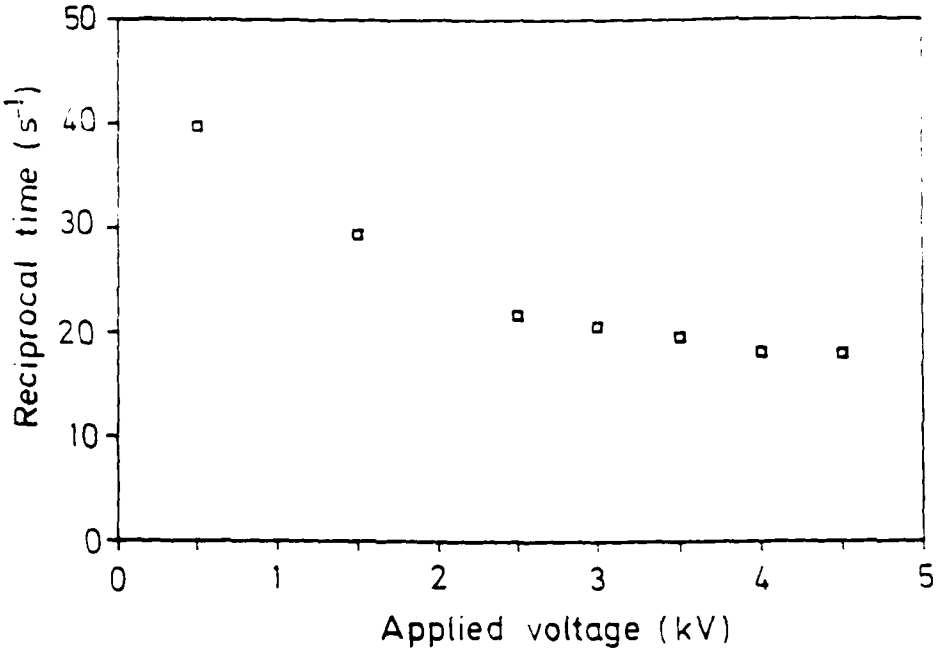

Figure 8: Reciprocal of time from the instant voltage is first applied to first intensity peak vs applied voltage. Incident intensity is 2.6 mW/cm^2.

6.2 Application to Laser Beam Steering

6.2.1 Probe of the grating

One of the exciting prospects of wave mixing using a crystal with a wedge angle is the possibility of writing holograms with very large grating spacings. This extreme drift-dominated regime has never been explored and might have some interesting features. On an optical table interbeam angles are limited by the geometry and size of optical elements such as prisms and mirrors. The smallest in-air angle we could achieve was $\approx 1.2°$. The wedge gave an effective in-air angle between beams of 0.19° which results in a grating spacing of 150 μm.

Our crystal with a wedge effectively produces very small grating vectors. We decided to write a grating using a 514 nm beam and probe collinearly with a 633 nm beam. This probe beam will not satisfy the Bragg condition exactly, however the angles involved are sufficiently small that efficient diffraction may be expected.

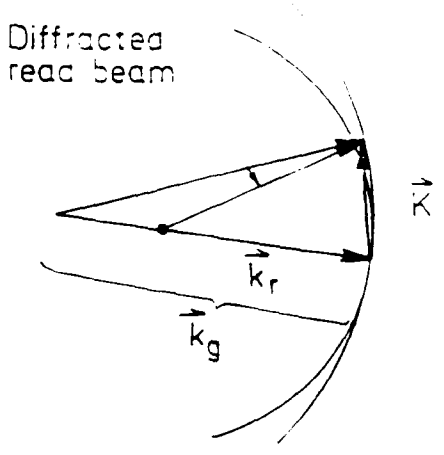

Figure 9: Probing the grating. The wavelengths of the writing (λ_g) and reading (λ_r) beams are different.

Fig 9 shows that the angle of the diffracted probe beam is

$$\theta_r = \frac{k_g}{k_r}\theta_g = \frac{\lambda_r}{\lambda_g}\theta_g \tag{2}$$

Here the subscript r refers to the reading beam and g to the grating writing beam. For $Bi_{12}SiO_{20}$ the indices of refraction at 514 and 633 nm are 2.62 and 2.52 respectively. So we expect $\theta_r = 1.28\,\theta_g$. We should see diffracted 633 nm beams at different angular spacings than the 514 nm orders.

The idea of a collinear probe beam which satisfies the Bragg condition was first investigated by Huignard and Ledu [55]. This is discussed also in the article by Mallick, et al., on spatial subharmonics [89]. The $K/2$ grating vector (for their case a grating spacing of 80 μm) produced by light of wavelength 514 nm was read by light of wavelength 1.06 μm and part of the reading beam was diffracted. This is significant because of the importance of the near-infrared in optical communications. Having the writing (514 nm) and reading (1.06 μm) beams collinear might be necessary if the beams are restricted to the same optical path, say along an optical fibre. The photorefractive crystal could act as a switch to diffract the signal beam, depending on the presence of the grating writing beam and other control parameters. Our scheme might be called collinear near-Bragg diffraction.

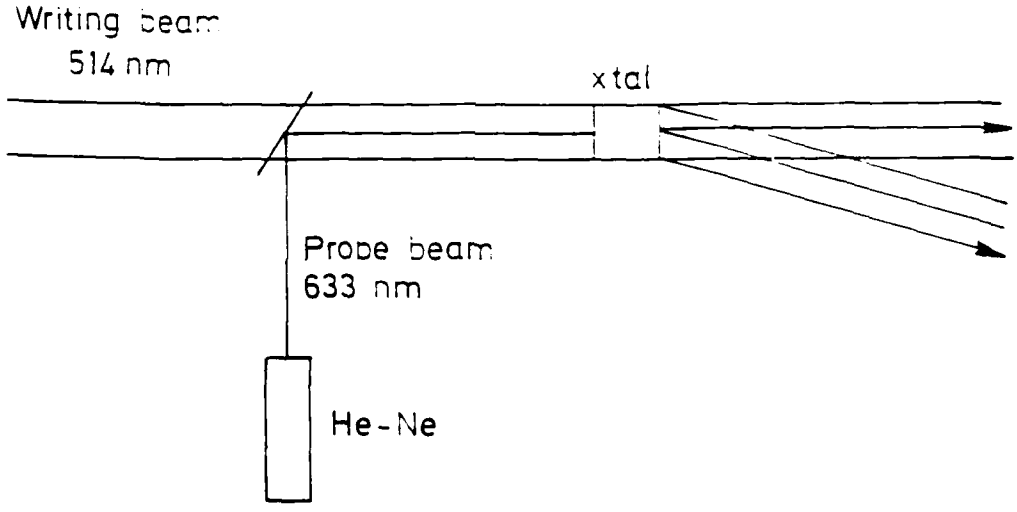

Figure 10: Use of a 633 nm probe beam to read a grating formed by 514 nm light. Probe and input writing beam are collinear.

Fig 10 shows the experimental layout for this test. An expanded, collimated, uniform intensity beam of wavelength 514 nm was at normal incidence on the crystal. A beam splitter allowed the injection of a collinear, unexpanded beam from a He-Ne laser. (An attenuating filter was used to reduce the intensity of the 633 nm in some experimental runs, but the results were the same as for an unfiltered probe beam.) A narrow band filter was used behind the crystal to remove the green light for many of the photographs.

We did not observe collinear near-Bragg diffraction. The results were much more surprising and suggest a novel means of laser beam steering.

6.2.2 Control of direction of scattered beams

Figs 11 and 12 show the results. Fig 11a depicts the main transmitted beam and its first multiple reflection for no applied field. Fig 11b is the multiple reflection pattern of the He-Ne beam with no voltage applied to the crystal. Fig 11c shows both beams. When a voltage was applied both beams produced higher diffracted orders. However, the red orders overlaid the green. There was no discernible reading of the 514 nm grating by the 633 nm light. The red higher diffracted orders seem

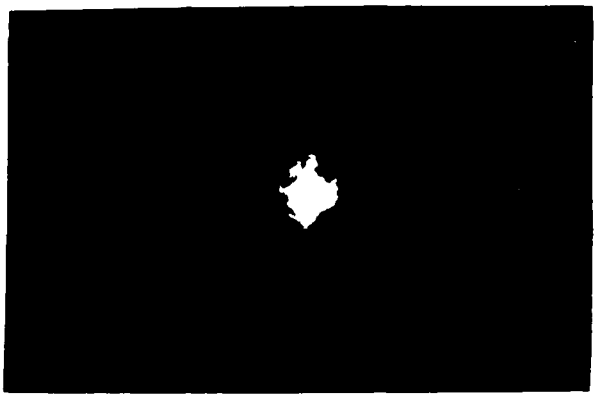

(a)

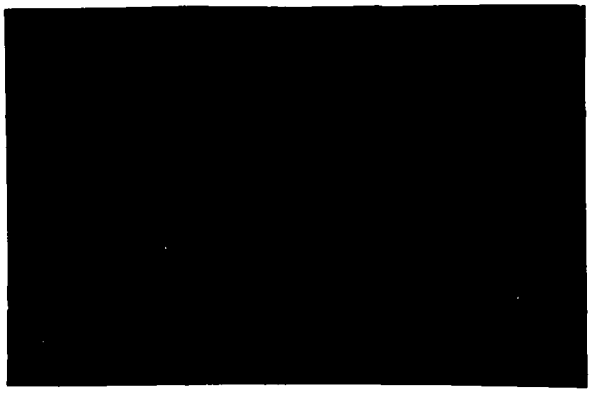

(b)

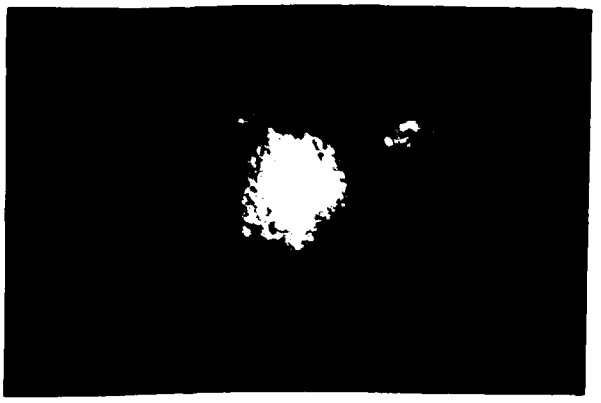

(c)

Figure 11: Superposition of 514 nm multiple reflections by 633 nm multiple reflections. (a) Transmitted 514 nm writing beam. (b) 633 nm probe beam. (c) Superposition of both beams.

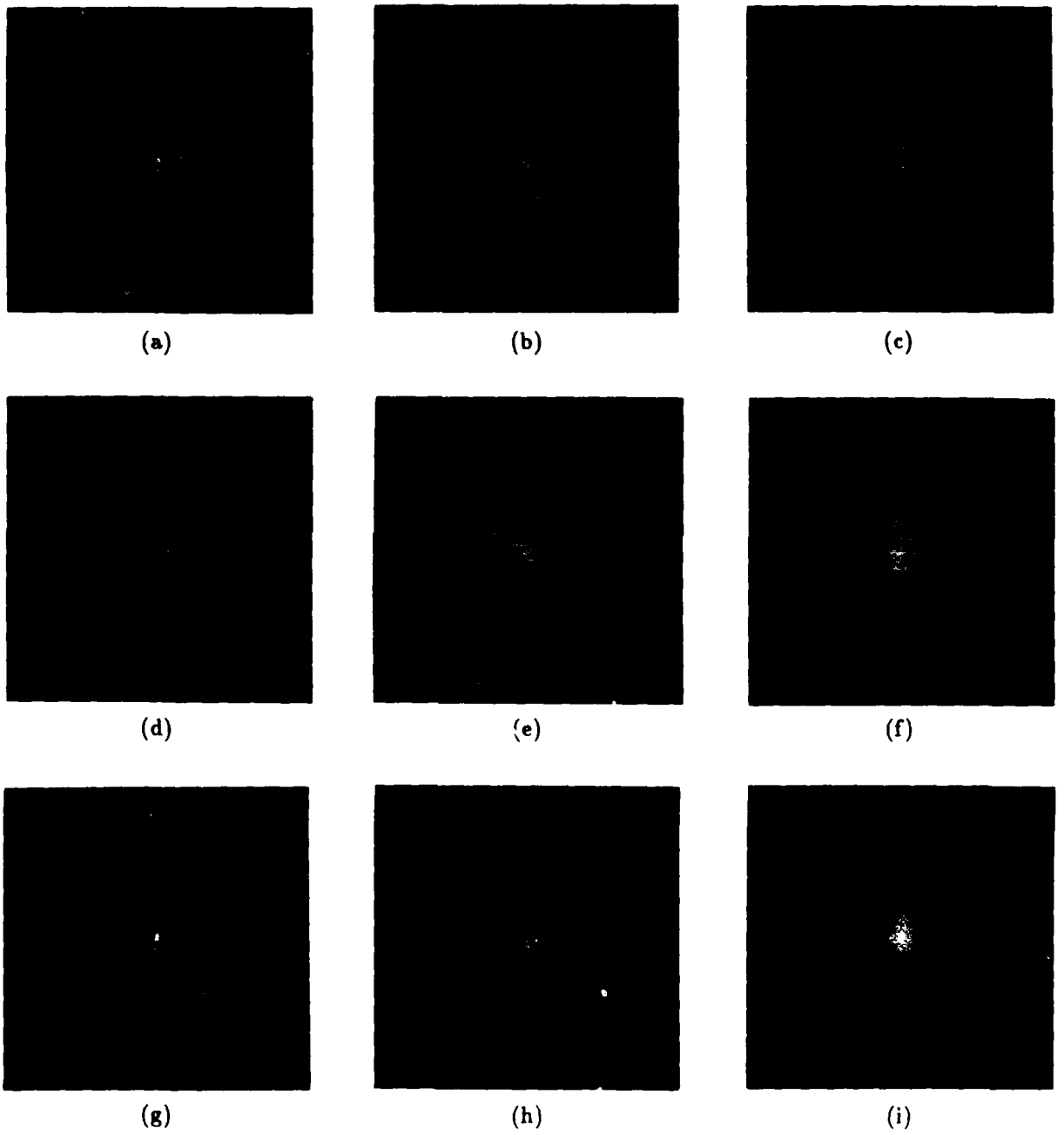

Figure 12: Apparent rotation of line of diffracted orders for applied voltage of 5 kV. Change in writing beam intensity: (a) Change in writing beam intensity: 0.2 mW/cm^2. (b) 2 mW/cm^2. (c) 4 mW/cm^2. (d) 5 mW/cm^2. (e) 9 mW/cm^2. (f) 11 mW/cm^2. (g) 15 mW/cm^2. (h) 20 mW/cm 2. (i) 30 mW/cm^2.

to arise from the same mixing mechanism as the green ones—via multiple reflection due to the wedge angle. This is somewhat unexpected because $Bi_{12}SiO_{20}$ is relatively insensitive at red wavelengths. For example, the quantum efficiency (a measure of carrier production per absorbed photon) is an order of magnitude less at 633 nm than at 514 nm [43]. However photorefractive gratings at 633 nm in $Bi_{12}SiO_{20}$ have been measured by Powell and Petts [103]. They found the sensitivity in the red could be increased by a factor of 16 if the crystal was heated to 300° C.

Figs 12a-i show the effect of increasing the intensity of the green light, with a constant applied voltage of 5 kV. The green light is filtered out for these figures. The line of diffracted orders appears to rotate. Actually the bottom diffracted orders disappear and the top orders move horizontally at spatial rates which preserve the line. This is a slow process, taking from 10 seconds to over a minute to reach steady-state. The effect can be observed as well by keeping the writing beam intensity constant and by varying voltage. If either the intensity is suddenly turned down or the applied voltage removed, the diffracted beams slowly drift back to their original positions (as in Fig 11b).

We can easily exploit this effect for laser beam steering. We know the higher diffracted orders are "copies" of the input beam (in the URR they had the same mode structure as the oscillating beam). By adjusting either the applied voltage or the intensity of the writing beam, we can direct the a copy of the 633 signal beam. Figs 13a and b show the apparent rotation of the line of diffracted orders as a function of writing intensity and applied voltage. The angle of rotation appears to be linear with intensity and quadratic with applied voltage.

How can we explain the movement of the diffracted orders? It is unlikely that it is due to a piezoelectric deformation of the crystal. Piezoelectricity is not intensity dependent. There is a slight fracture in the crystal. Could the presence of an applied field and/or high intensity light cause expansion of the fissure? It is possible, but close inspection of the diffracted orders using just 514 nm light suggests this cannot be the mechanism responsible. When a voltage is applied, increasing the incident

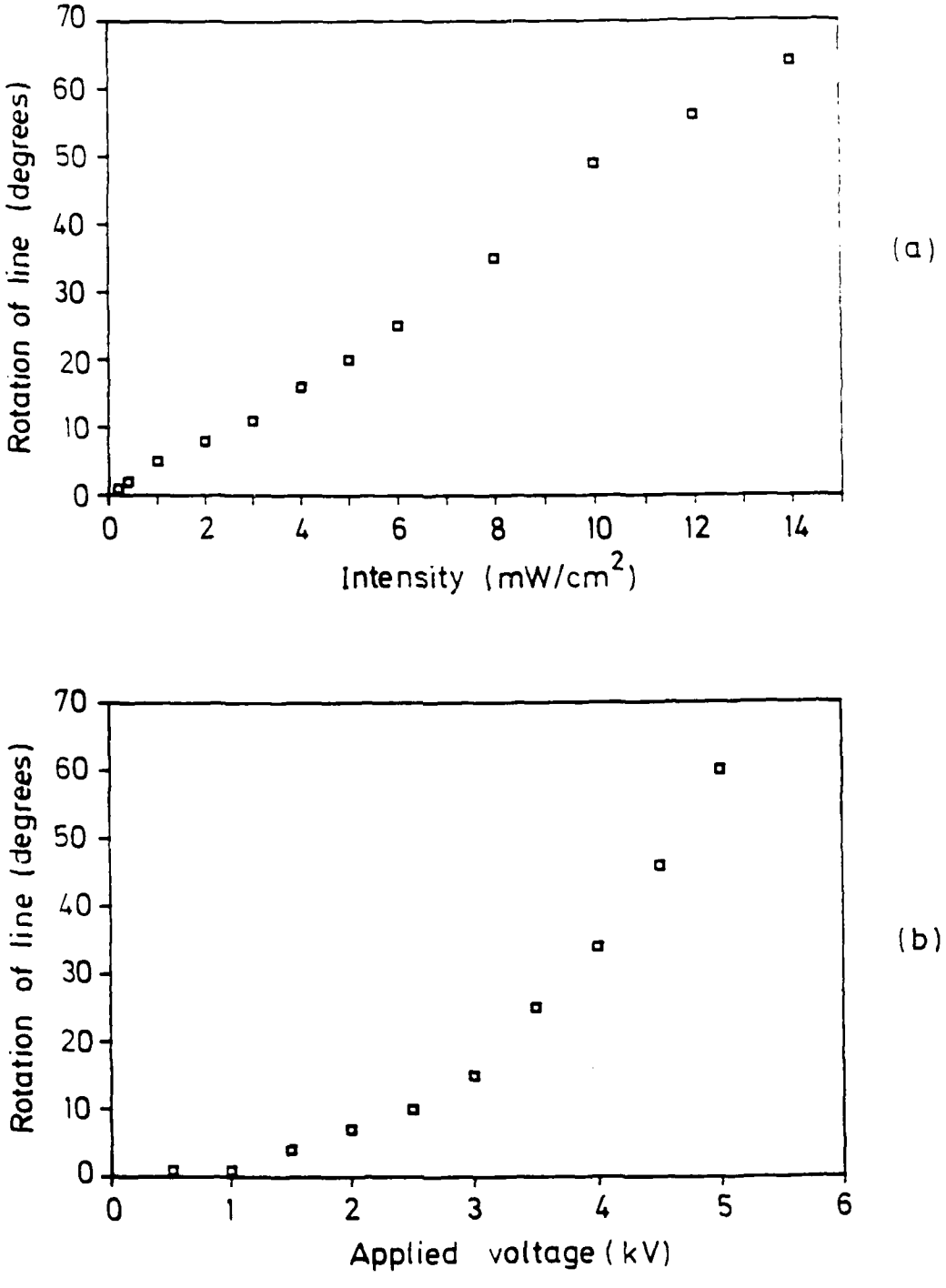

Figure 13: Rotation of line of diffracted orders (a) vs writing beam intensity (applied voltage = 4 kV), (b) vs applied voltage (writing beam intensity = 8 mW/cm^2).

intensity also shifts these diffracted orders. The outlying orders tend to smear out into regions of muted noise and only the -1 order persists. This tends to move horizontally, but as Figs 2g-i reveal there is still a vestige of the original order left behind (seen in the photograph as a crescent region). The responsible mechanism must depend on both intensity and applied electric field. It is characterised by time constants much longer than those observed for the transient effects.

What is particularly interesting about this new phenomenon is the integrity of the spatially shifted orders. As discussed above, the -1 order using 514 nm light leaves a ghost in the original location (the position corresponding to no applied voltage). But with 633 nm light the shift seems to be complete—the entire beam moves. Fig 12i shows the -1 order is stretched out somewhat for very intense incident beams. It is interesting to note that the -2 order moves twice as far as the -1 order, thus preserving the line of diffracted orders.

We will discuss two possible mechanisms. The first is a thermal effect. If a temperature gradient or a region of inhomogeneity exists in the crystal, the refractive index may vary spatially. This could divert the beams, and the heating might well depend on incident intensity and applied voltage. Such an effect would tend to preserve the line of orders. Because the angles involved are small, all the beams we observe travel through the same part of the crystal, therefore the effect of a nonuniform index will be felt by all. The main beam passes through the crystal once, the first multiple reflection makes two additional transits, and the second multiple reflection two trips beyond that. Thus we would expect an increased deviation for the higher orders. If this is the mechanism then this effect will differ from crystal sample to crystal sample, and perhaps even within a single crystal sample if the probe beam passes through a different site.

The second possible mechanism is that of noise gratings. The growth and efficiency of noise gratings depends on intensity and strength of applied electric field, and they emerge on time scales similar to those describing the movement of the diffracted orders. The effect we see may be considered similar to that which causes

the horizontal pulse of light energy at field turn-on discussed in Sec 6.1.2. That is, scattered light is amplified in a preferred direction. This effect is well-known in $BaTiO_3$ and is called fanning [34], although it has never been reported in the literature on $Bi_{12}SiO_{20}$. In $BaTiO_3$ beams interacting in the crystal can suffer significant bending, particularly in the case of a self-pumped phase conjugate mirror using internal reflections [27,28].

Another remarkable feature is that the movement is in the opposite direction to that expected for normal power transfer for vertically polarised light. Foote and Hall have demonstrated that the direction of power transfer depends on the polarisation of the mixing waves in $Bi_{12}SiO_{20}$[39]. In the presence of an applied electric field $Bi_{12}SiO_{20}$ is birefringent, and for light incident upon the $\bar{1}10$ face, two orthogonally polarised states exist in the medium. These two states correspond to different directions for power transfer. However, birefringence cannot be the complete solution to the wayward spatial shift of the orders. We would expect to see a splitting of the diffracted orders, not a unidirectional movement. Further, measurements of the polarisation states of the diffracted orders show that, as expected, they are elliptically polarised, primarily in a direction commensurate with incident vertically polarised light. Finally, only the diffracted orders move, the main transmitted 0 order does not move.

This is a very interesting phenomenon and one which merits further research.

6.3 Conclusions

Our crystal sample with a wedge angle has provided a wealth of novel, interesting effects to observe. In this chapter we concentrated on two effects with particular applications. The first concerned transient power transfer as a voltage was applied to the crystal. A first-ever study of transient effects in higher diffracted orders revealed that light energy is passed on from order to order sequentially. The orders seem to emerge in pairs. Finally we observed a new intensity/electric field dependent

scattering in $Bi_{12}SiO_{20}$ reminiscent of beam bending in $BaTiO_3$. This last effect allows for angular control of one or more of the higher diffracted orders.

Chapter 7

Conclusions and Suggestions for Future Work

Let us not go over the old ground, let us rather prepare for what is to come.

Cicero

What can I know? What ought I to do? What may I hope?

Immanuel Kant

A multitude of interesting and important optical effects arise when beams of light mix and interact inside a photorefractive crystal. Through the first six chapters and three appendices of this thesis, we have investigated a wide variety of some of these phenomena. Our main interest has been what photorefractive materials do best. They provide a medium for the coupling of beams. Like some agent or broker, they arrange for trades in energy or differential rates in the acquisition of phase. Photorefractive crystals can achieve all this in real time and in a controllable fashion. This remarkable ability stems from the nonlinear nature of the polarisation of the medium in the presence of a light wave.

This last chapter consists of three parts. The first is a brief survey of some of the accomplishments described in this thesis. The second is a guide for further

studies in photorefractives, either here at Oxford, or elsewhere. Finally we say a few encouraging words about the future of photorefractive crystals.

7.1 Accomplishments

Ignoring, for the moment, the sage advice of Cicero at the beginning of this chapter, let us make a quick review of the key points of this thesis. This will help define the directions of future work.

We began with a description of the photorefractive effect and the place of photorefractive crystals in the long, proud history of crystals. This led to a discussion of the evolution of our current understanding and applications of photorefractivity.

The nonlinear effects observed in these crystals are numerous, but they are basically variations on a theme. The theme is two-wave mixing, or a superposition thereof. Chapter 2 discussed this fundamental interaction, particularly in terms of differences in the relative sizes of the characteristic fields, and the optimising of power transfer between the mixing beams.

The preceding provided a necessary background for the understanding of novel phenomena and techniques discussed in the remaining thesis.

Two-wave mixing for counterpropagating beams was the subject of Chapter 3. We demonstrated that for the important cases involving moving intensity fringes or in the presence of an applied voltage, the degree of beam coupling varies spatially. All previous treatments of this problem assumed a constant coupling term. A comparison of the solutions of the coupled wave equations for constant and variable coupling revealed several cases in which the results differ significantly. Our numerical method was employed next to make the first systematic theoretical assessment of the control of nonreciprocal transmission and phase shift in $LiNbO_3$, a representative photorefractive crystal. For both NR effects, the velocity of the light intensity fringes offers the greatest range for control. This is particularly attractive because the photocurrent in the circuit containing the crystal was shown to depend on the

degree of wave interaction. The photocurrent has its minimum values when beam coupling is strongest. This should provide a useful, nonintrusive means to monitor NR transmission. A comparison of the theoretical results for different crystal types suggests both $LiNbO_3$ and $BaTiO_3$ should show strong NR effects, however our $LiNbO_3$ crystal samples proved too erratic in coupling to allow us to measure any effects. Our final conclusion about using photorefractive crystals for NR purposes was that they look promising for NR transmission (eg. as an optical diode), but not for NR phase shift. Moving intensity fringes and an incident beam ratio much different from 1 are required to obtain a suitably large NR phase shift ($\approx \pi/2$), a value readily realizable using NR magnetooptical devices.

In the next chapter we began a study of oscillation in resonators with photorefractive gain. We looked at the unidirectional ring resonator and made several new observations. We found a threshold for incident light intensity below which no oscillation occurred in $Bi_{12}SiO_{20}$. For our sample this was 0.8 mW/cm^2. We measured the frequency detuning of the oscillating beam (relative to the incident light) and found no measurable difference between the various resonator modes. In $BaTiO_3$ when one slightly repositions one of the mirrors forming the ring resonator, the resulting change in resonator length is accompanied by a change in frequency detuning of the oscillating beam. We discovered this was not the case for $Bi_{12}SiO_{20}$. Here the detuning, which is a function of light intensity, applied electric field, and interbeam angle, must be close to an optimum value to achieve the large gain necessary for oscillation. A surprising new result was a preponderance of higher diffracted orders for one crystal sample. Many of these additional beams were due to a slight wedge angle in the crystal. Different diffracted orders (which we dubbed companion orders) arose from two-wave mixing between a beam in the crystal and its first codirectional multiple reflection.

Chapter 5 is significant because it provides an experimental verification of a new gain mechanism for photorefractive materials. The new amplification scheme involves off-Bragg coupling and results in a power transfer from two pump beams

inward to two symmetric signal beams. The gain is readily controllable by changing the frequency detuning of the pump beams. At its optimum value, the new gain mechanism in $Bi_{12}SiO_{20}$ gives slightly larger gain than the traditional two-wave mixing mechanism. This was confirmed experimentally in a unidirectional ring resonator where the small increase in the gain coefficient using two pump beams resulted in a steady-state oscillating beam intensity four times larger than for a single pump. The increased effectiveness of resonator operation permitted the first reported quantitative measurement of oscillation in a linear resonator using $Bi_{12}SiO_{20}$. Finally we searched for evidence of spatial subharmonics between the two pump beams, but found no preferential position for the signal beams.

We then returned to a study of the crystal sample with the wedge angle. The minuteness of the wedge angle (0.036° as measured by the angular spacing of adjacent orders) allows us to investigate the case of very large grating spacings—much larger than has been looked at before. Transient effects in this region give keen insight into the transfer of power between diffracted orders. Using a single uniform input light beam, the transient phase of grating formation shows power is passed sequentially from order to order. In other words, one order must be amplified before it can effectively pass on power to an adjacent order. We have identified a transient pulse of light which occurs when a voltage is first applied to an illuminated $Bi_{12}SiO_{20}$ crystal. All our crystal samples exhibited this pulse to some extent. As an aside, we developed a new, simple, analytic formula which describes transient behaviour in two-wave mixing and which results in a remarkable savings in computation time over other numerical and analytic treatments. Finally we demonstrated a novel method of laser beam steering in which the positions of the higher diffracted orders of a collinear probe beam (of wavelength different than the writing beam) can be shifted by changing either the applied voltage or the intensity of the writing beam.

7.2 Future Work

There are many directions the work described in this thesis can go. We will consider these directions by subject.

1. *Nonreciprocal Effects.* The theory we considered in Chapter 3 assumed small modulation depth for the intensity fringes (ie. small m). There are some cases of interest where this approximation may not be valid, for example when the incident beams have roughly the same intensity and strong absorption is present. It would be worthwhile to do an analysis, such as was done recently by Au and Solymar [8], for mixing beams in the reflection geometry and large modulation depths.

   Experiments using $LiNbO_3$ as the medium were unsuccessful, however NR transmission effects have been reported in $BaTiO_3$ and $KNbO_3$. One of these materials could be used to verify our theory, particularly the aspects involving control of these effects.

2. *New Gain Mechanism.* As mentioned in Chapter 5, the best way to evaluate this new mechanism is to use three or four beams, each of which can be frequency shifted relative to the others. Besides experimental confirmation of the theoretical results, these questions should be looked at:

   - What is the relation between the signal beams? Specifically, are they phase conjugates or even near phase conjugates? On a related theme: what type of cross-talk exists between the signal beams? Is spatial and/or temporal information shared between them?
   - What effect will incompatible frequency detuning have on the gain? By incompatible we mean that the frequency differences between the beams give different speeds for the moving fringe patterns inside the medium. Our theory depended on a scaled frequency shift for the beams to give

all the fringe patterns the same velocity. However, if gain is possible or even enhanced for different combinations of frequency shift, this would be significant, and might explain why we observed oscillation in the ring resonator for such a wide range of frequency detuning of the driving pump beam.

- What is the intensity profile of the region of internal optical noise between two frequency shifted pump beams? How does this optical noise relate to the spatial subharmonics observed by Mallick, et. al. [89]? We described this phenomenon in Section 5.2.5. The optical noise, which looks rather like a swarm of irritated fireflies, seemed concentrated halfway between the two beams, but extended well out of the plane of the pump beams. As we changed the frequency of the driving pump beam, the profile seemed to stay the same, but either dimmed or brightened overall. We would expect to see the noise follow the pattern suggested by Fig 5.4, namely, for a specific frequency detuning value, the most intense peak would be in the centre, but a change in detuning should result in a symmetric, bimodal intensity distribution corresponding to a new optimum value of the scaling parameter, ζ (Fig 5.2a). Our group recently ordered a vidicam and digitizer, and this equipment would be ideal for looking at the intensity profiles.

- What would be the result if both signal beams were reinforced by (separate) unidirectional ring resonators? We made a brief attempt at this set-up, with minor success. The difficulty is insuring that one is reinforcing the second signal beam, and not just an arbitrary noise beam close to the symmetric position. If the two URRs are spot on, one might be able to achieve significantly enhanced gain in both.

3. *Linear Resonator.* The intensity of the oscillating beam in our linear resonator described in Chapter 5 was too weak to generate a phase conjugate

beam. We recently had the surfaces of a 1 cm cube of $Bi_{12}SiO_{20}$ antireflection coated. With reduced reflection loss and a longer interaction length, amplification may be high enough to produce phase conjugation. But this raises an interesting question: what type of phase conjugation, if any, is produced in a linear resonator fed by two input beams? With a single input, the counter-propagating, oscillating beams become the "pump" beams, and, if they are sufficiently intense, a phase conjugate of the input beam emerges. With two input beams do we get two phase conjugates? What if the oscillating beam does not bisect the angle between the two input beams? If each input generates a phase conjugate, and if there is a second signal beam between the two inputs, then we could have the case of seven-wave mixing—a complicated situation indeed!

4. *New Crystal Cut.* In Appendix B we suggested a new crystal cut which would result in an enhanced electrooptic effect in $Bi_{12}SiO_{20}$ for wave mixing in the absence of optical activity. Optical activity will tend to reduce the net photorefractive gain, but a question worth asking is, will the overall gain for a $Bi_{12}SiO_{20}$ crystal cut with a 111 face be higher than for a 001 face cut? The difficulty here would be a fair test— different crystal samples usually have different crystal parameters. We have a rare opportunity to make a definitive test. In Appendix A we described crystal damage in a 1 cm cube of $Bi_{12}SiO_{20}$. The undamaged part of the crystal should be large enough to cut into two samples of equal length. Both samples should have identical parameters. The original orientation and that proposed in Appendix B use polished $\bar{1}10$ and $1\bar{1}0$ faces, so the new crystal cut will merely involve a rotation of 54.7° about the normal axis through the polished faces.

5. *Wedge Angle.* Once the test on the new crystal cut is finished, a slight wedge angle can be introduced into the standard cut crystal. It would be interesting to compare wedge effects with the sample we used in Chapter 6. In particular

we need to see if the spatial shift of the higher diffracted orders of a collinear probe beam is reproducible in a different crystal sample.

7.3 Conclusions

Research in photorefractives is at a very exciting stage. The field is still young at age 20, due in part to a fallow, contemplative phase in the 1970s. But the result was a coherent charge transport/field equation theory which seems to explain, at least qualitatively, the effects seen in hundreds of experiments. Now new experimental results come fast and furious, as if straining at the leash of the theory, testing its limits.

The next stage will involve systematic exploitation of the effects being demonstrated in the laboratory today. Many devices use electrooptic crystals such as $Bi_{12}SiO_{20}$ in spatial light modulators and $LiNbO_3$ in optical waveguides, but, as of this writing, no commercial products exist which utilize photorefractive wave mixing. Still, the promise is there, and, if the quality of materials becomes more uniform, photorefractive crystals will find their place in optical interconnects, resonators, and computers of the future.

It it our sincere hope that the work represented in this thesis furthers the transition to this next stage.

Appendix A

Damage in $Bi_{12}SiO_{20}$ Crystal Samples

Chapters 4, 5, and 6 chronicle work done with a repolished piece of $Bi_{12}SiO_{20}$ from a damaged crystal. The original sample was 5 mm x 5 mm x 10 mm. The damage was first observed as a small fracture extending about 1 mm into the crystal, roughly 3 mm from one end on the long edge which served as the cathode. Over the course of several weeks of experimental work (two-wave mixing and photocurrent measurements) the fracture grew in extent and depth until the crystal split in two.

At the time we felt the damage was initiated by an air spark which passed over the front face of the crystal when the flooding illumination was interrupted and a 10 kV/cm electric field was applied. Extreme care was taken with new crystal samples to prevent a repeat occurence. We had limited success with this as evidenced by Figs 1a and 1b. These photographs show a second damaged $Bi_{12}SiO_{20}$ crystal sample. This was a 1 cm cube from Sumitomo, Ltd. Fig 1a depicts the damaged crystal and a new replacement crystal for comparison. Fig 1b shows details of the internal damage. As with the previous crystal the cracks originated on the cathode surface.

It is very easy to chip the edges of a $Bi_{12}SiO_{20}$ crystal. The best way to minimize edge damage is to limit handling of the crystal. The mere act of setting the crystal

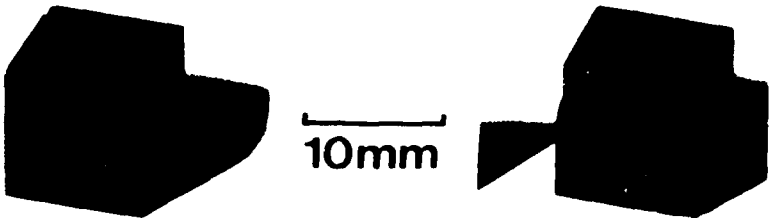

(a)

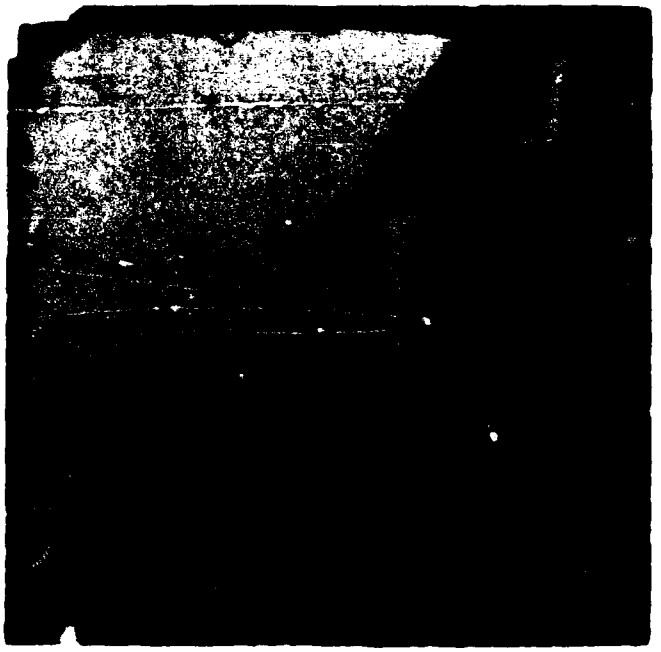

(b)

Figure 1: Damage in $Bi_{12}SiO_{20}$ crystal samples. (a) New Sumitomo sample (left) and damaged Sumitomo sample (right). (b) Interior view of damaged sample. Top of picture was crystal cathode.

in a holder with spring plunger electrical contacts invariably causes some minor chipping. But this does not seem to be the source of the fractures. The original cracks on both damaged crystals started on the sides of the crystals some distance from the edges.

The key to the damage seems to be the cathode. Bryksin, et al., reported in 1982 and 1983 the presence of strong electric fields near the cathode in a uniformly illuminated sample of $Bi_{12}SiO_{20}$[15,14]. Very close ($<$ 1 mm) to the surface the field strength could be in excess of 100 kV/cm. Oberschmid made a very thorough study of photocurrent in $Bi_{12}SiO_{20}$ and $Bi_{12}GeO_{20}$[96]. He found that electrons were injected into the crystal at localized sites on the cathode. The current from these sites spread out along conical paths. The presence of both positive and negative charges at the cathode creates instabilities and Oberschmid observed strong local fluctuations in the electric field. Anderson and Luke reported in 1987 beam induced damage in $Bi_{12}SiO_{20}$ in a PRIZ configuration [4]. The PRIZ is a spatial light modulator in which the front and real crystal faces are polished and have transparent electrodes. The authors found fractures (originating at the cathode) extending about 65 μm into the crystal. These arose using relatively low illuminations (100 $\mu W/cm^2$) and weak applied fields (2 kV/cm). It appears damage manifests itself in the form of small pits, 2–3 μm in diameter on the surface of the cathode. Striae may emanate from these pits and may run between several adjacent pits. These running striae can grow into fractures. It is very likely that the pits serve as the local electron injection sites mentioned by Oberschmid.

What can be done to minimize, or eliminate, crystal damage? We used painted silver electrodes on unpolished crystal faces. Surely the problem of pits or rough areas is worse on an unpolished surface. It might be beneficial to polish all the surfaces of a $Bi_{12}SiO_{20}$ crystal before applying electrodes. Once damage has been identified, reduced applied electric fields and low illuminations may prolong the useful life of the crystal. At least we may state confidently the reverse is true—strong fields and high intensities seem to aggravate the condition. In the Sumitomo sample

we were trying to obtain oscillation in a linear resonator configuration (see Chap 6). We knew a fracture was present in the crystal and we limited the applied field to 7 kV/cm and the intensity to 10 mW/cm^2. The crack extended approximately 2 mm into the crystal and its growth was slow. We increased the field to 10 kV/cm and the illumination to 30 mW/cm^2. The crystal suddenly lit up with bright internal sparks. We immediately turned off the applied field. The fracture was now over 5 mm long and had developed branches. After this episode the damage increased visually each time the crystal was used.

The internal sparking is a tell-tale sign of crystal damage. In our optical set-ups there is generally quite a bit of scattered light falling on the walls of the laboratory (the crystals send out a lot of scatter). The first evidence of damage in the Sumitomo crystal was a semi-periodic pulsation in a region of scattered light when an electric field was applied to the crystal. When the field was increased, the frequency of the pulses increased. Close inspection of the crystal revealed a small area near the cathode growing alternately bright then dark. This was found later to be the site of a small fracture.

I included our experiences with damage in $Bi_{12}SiO_{20}$ in a talk on crystal diagnostics given at Cambridge in September, 1987. The response of the audience was rather interesting. My confession of destroying the crystals prompted several others to bare their souls. One individual exclaimed, almost with pride, that his group had ruined two $Bi_{12}SiO_{20}$ crystals—one having literally exploded when an a.c. electric field was applied in the kilohertz range.

At a previous scientific meeting we heard the woeful tale of a research student and a crystal of $BaTiO_3$. This crystal has a Curie temperature around 5°C. Care must be taken to avoid abrupt temperature changes near this value. The well-meaning student was cleaning the surfaces of the crystal using methanol. When the methanol evaporated the temperature change was sufficient to shatter the crystal.

Relating such experiences is invaluable to research. We often learn more from mistakes than from successes. It would be useful to include a short forum, perhaps

at the end of one or more sesssions, at conferences to pass on warnings and pitfalls. Barring this, experimenters should seek out fellow workers to discuss things to be wary of.

Equally as important as understanding the uses of photorefractive materials is to be familiar with the abuses of photorefractive materials.

Appendix B

General Treatment of the Electrooptic Effect in $Bi_{12}SiO_{20}$

The appearance of the companion orders in the ring resonator, described in Chapter 4, prompted the following question: Is the electrooptic effect in $Bi_{12}SiO_{20}$ enhanced for an electric field in some direction other than along the 001 axis? If the answer is yes then the companion orders might be due to some favourable combination of grating spacing and orientation formed by the principal beam and noise.

Consider a general grating formed by the mixing of two waves in $Bi_{12}SiO_{20}$. The modulated space charge field is given by Eqn 2.20. We should mention that in the derivation of E_{sc1}, we use the projection of the applied electric field in the direction of the grating vector, $\vec{K}$, as E_{sc0}. The magnitude of E_{sc1} will determine the index modulation via the electrooptic effect. E_{sc1} has the following projections onto the principal axes of the crystal with no applied field

$$E_{sc1} = E_x\hat{x} + E_y\hat{y} + E_z\hat{z} \tag{1}$$

In the presence of E_{sc1}, the index ellipsoid is transformed to

$$\frac{x^2}{n^2} + \frac{y^2}{n^2} + \frac{z^2}{n^2} + 2rE_xxy + 2rE_yxz + 2rE_zyz = 1 \tag{2}$$

where $r = r_{63}$.

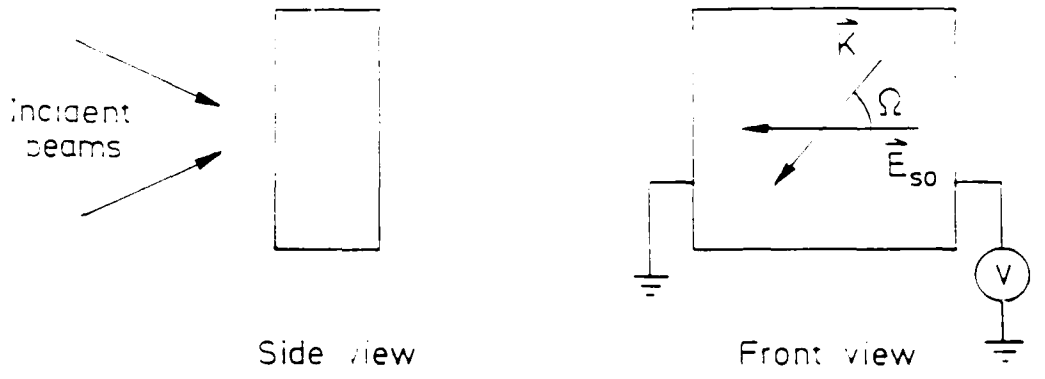

Figure 1: Two-wave mixing with grating vector not coincident with applied field.

We want to find the new principal coordinate system of the crystal. Rewrite the above as the quadratic form

$$\mathbf{Q} = \mathbf{x}^T \mathbf{C} \mathbf{x} \tag{3}$$

where $\mathbf{x}^T = (x, y, z)$ and $\mathbf{C} = \begin{bmatrix} \frac{1}{n^2} & crE & brE \\ crE & \frac{1}{n^2} & arE \\ brE & arE & \frac{1}{n^2} \end{bmatrix}$ with $a = E_x/E$, $b = E_y/E$, $c = E_z/E$, and $E = E_{sc}$. To find the new principal cooridinate system we diagonalize $\mathbf{Q}$ and to do that we need the eigenvectors of $\mathbf{C}$.

The characteristic equation for $\mathbf{C}$ is

$$\left(\frac{1}{n^2} - \lambda\right)^3 - 2r^3E^3abc - r^2E^2(a^2 + b^2 + c^2)\left(\frac{1}{n^2} - \lambda\right) = 0 \tag{4}$$

This expression can be simplified somewhat if we assume eigenvalues of the form $\lambda_i = \frac{1}{n^2} - \epsilon_i rE$ for $i = 1, 2, 3$.

$$\epsilon^3 - (a^2 + b^2 + c^2)\epsilon + 2abc = 0 \tag{5}$$

Eqn 5 is a cubic equation in ϵ whose solution in terms of the coefficients is well known, although a bit complicated [104]. The roots to this equation give the eigenvalues which represent the lengths of the axes of the transformed index ellipsoid.

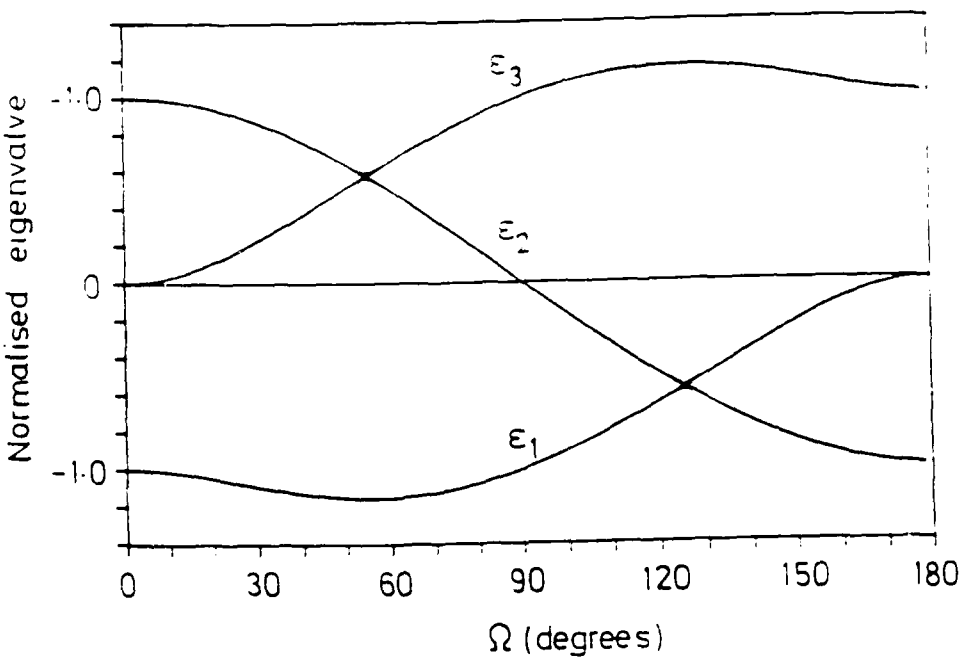

Figure 2: Eigenvalues for Eqn 8.

The eigenvectors, ω_i, satisfy

$$(\mathbf{C} - \lambda_i \mathbf{I})\omega_i = 0 \tag{6}$$

The transformation from the old primary axes system to the new one is made by

$$x' = W^T x \tag{7}$$

where T means transpose and W is the matrix whose columns are the eigenvectors ω_i. In other words, the eigenvectors are the directions of the new principal axes. To find the net electrooptic effect in the new axes system, transform the incident polarisation vector to primed coordinates and sum its projections onto the new principal axes of the index ellipsoid.

Our case of interest is shown in Fig 1. The two mixing waves are at near normal incidence to the front surface, so the grating vector, $\vec{K}$, is parallel to this surface and makes an angle Ω with the z (001) axis. Then $a = \sin\Omega/\sqrt{2}$, $b = \sin\Omega/\sqrt{2}$, and

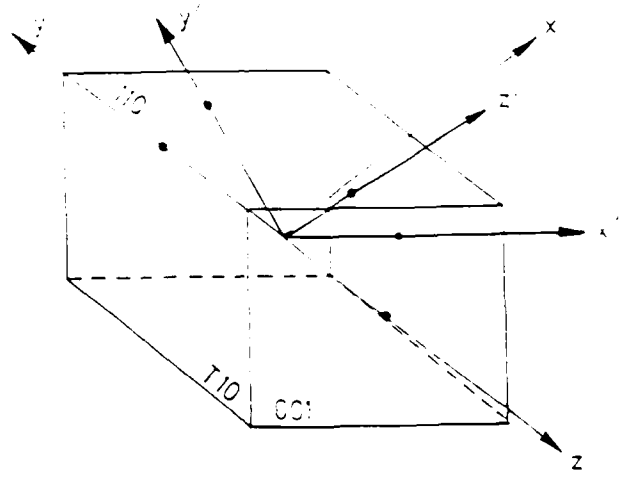

Figure 3: New principal axes system (dark axes) for electric field at an angle of 54.7° to the original 001 (light) axis.

$c = \cos\Omega$. The characteristic equation is

$$\epsilon^3 - \epsilon + \sin^2\Omega\cos\Omega = 0 \tag{8}$$

Fig 2 shows the roots of Eqn 8 for Ω between 0 and 180°. To find the maximum absolute value for a normalised eigenvalue look at the general solution to Eqn 9.

$$\epsilon^3 + a_1\epsilon + a_2 = 0 \tag{9}$$

Following Ref [104], we introduce the quantities $Q = -a_1/3$, $R = a_2/2$, and $\theta = \arccos(R/\sqrt{Q^3})$. Then our three roots are

$$\epsilon_1 = -2\sqrt{Q}\cos\left(\frac{\theta}{3}\right) \tag{10}$$

$$\epsilon_2 = -2\sqrt{Q}\cos\left(\frac{\theta+2\pi}{3}\right) \tag{11}$$

$$\epsilon_3 = -2\sqrt{Q}\cos\left(\frac{\theta+4\pi}{3}\right) \tag{12}$$

For our case $a_1 = -1$ and $a_2 = \sin^2\Omega\cos\Omega$. If we optimise, say, ϵ_1 with respect to Ω then we find we must satisfy

$$\sin^2\Omega = \frac{2}{3} \tag{13}$$

or $\Omega = 54.7°$ with a corresponding eigenvalue of -1.155. The other two eigenvalues are $\epsilon_2 = 0.577$ and $\epsilon_3 = 0.577$. The eigenvectors are

$$\underline{e}_1 = \begin{bmatrix} 0.577 \\ 0.577 \\ 0.577 \end{bmatrix}, \quad \underline{e}_2 = \begin{bmatrix} 0.707 \\ -0.707 \\ 0 \end{bmatrix}, \quad \underline{e}_3 = \begin{bmatrix} -0.408 \\ -0.408 \\ 0.816 \end{bmatrix}$$

The new principal axes are as shown in Fig 3. The first thing we should notice is that we can have an enhanced electrooptic effect. If light is polarised along the z' axis, then the normalised electrooptic effect is 1.155, or over 15% larger than for the case shown in Fig 2.4. We should recall that we also have a reduced applied field component in this case ($E_{s0}\cos\Omega$). To take full advantage of this enhancement, one should have electrodes normal to this optimum axis, namely the 111 or $11\bar{1}$ face.

The 111 cut for $Bi_{12}SiO_{20}$ is used for devices such as spatial light modulators, as is the cut shown in Fig 2.4 [53,84,4]. Marrakchi, et al., claim that the crystal cut in Fig 2.4 is the optimum one for the electrooptic effect in $Bi_{12}SiO_{20}$ for wave mixing [90]. Optical activity will have a more significant effect on the electrooptic effect for crystals cut with a 111 face. The normalised changes in refractive indicies for the two principal axes for light polarised in a plane parallel to the $\bar{1}10$ face are 1.15 and -0.577, where for the crystal in Fig 2.4 these values are 1 and 0.

However, the enhanced electrooptic effect cannot explain our companion orders, because there the angle the grating vector made with the z axis was approximately 35°. This is not the optimum angle, and the orientation of the new principal axes for vertically polarised light and this angle of grating vector gives a net normalised electooptic effect of -0.885, a magnitude less than that for the case of $\Omega = 0°$. This supports the claim that companion orders are due to a wedge in the crystal sample.

Appendix C

A Simple Analytic Formula for Transient Two-Wave Mixing

In this appendix we derive an analytic formula for the complex optical amplitude of a wave undergoing transient amplification in two-wave mixing. We show this method compares remarkably well to a previously reported numerical method [48]. This is important because our method leads to more efficient computation.

In the undepleted pump approximation for two-wave mixing the space and time differential equations describing transient behaviour are

$$\frac{\partial S_+}{\partial x} = -j\Gamma' E_{s1}^* \quad (1)$$

$$\frac{\partial E_{s1}}{\partial t} = -gE_{s1} + fS_+^* \quad (2)$$

Here $S_+ = E_+/\sqrt{I_0}$ where I_0 is the pump beam intensity, $\Gamma' = \frac{1}{2}k_0 n^3 r_{\text{eff}}$, and g and f are given in Chapter 6.

Our situation is this: a photorefractive crystal is uniformly illuminated by a single beam. An externally imposed d.c. electric field is present in the material. At time $t = 0$ a second mixing beam is introduced. The numerical method of Heaton and Solymar [48] to solve Eqns 1 and 2 for this situation is as follows. At $t = 0$, S_+ and E_{s1} are constant—$S_+ = S_{+0}$ and $E_{s1} = 0$ for all x. For a short time interval

Δt, S_- may be considered unchanged, but the space charge field grows because of the presence of a modulated intensity pattern. $E_{sc}(\Delta t)$ is calculated from Eqn 2 and this is inserted into Eqn 1. The space equation is integrated yielding values for $S_-(x, \Delta t)$. This can be inserted into Eqn 2 for the next time step and the process see-saws between time and space solutions until the required number of time steps are taken. For the case of small interbeam angles and large applied fields (drift dominated case) the solutions are highly oscillatory and many steps are required to prevent instabilities. Even with very small time steps (on the order of the dielectric time constant) our experience has shown the intensity solution may go negative (a unreal physical situation) for strong coupling and large interaction lengths. In other words, this numerical treatment is prone to give solutions which are more oscillatory than other methods [49].

Our method is similar in philosophy: we attack one differential equation, solve it, and use the solution in the other equation. Basically ours is an iterative method. We start with Eqn 2. We assume S_+ is constant and find

$$E_{sc}(x,t) = E_{sc}(x,0)\,e^{-gt} + \frac{fS_+^*}{g}(1 - e^{-gt}) \tag{3}$$

but $E_{sc}(x,0) = 0$. We put this solution into the space equation

$$\frac{\partial S_+}{\partial x} = -j\,\Gamma' C^*\,S_+ \tag{4}$$

$$C = \frac{f}{g}(1 - e^{-gt}) \tag{5}$$

This has a simple exponential solution. In theory we could continue the iterative process going back and forth between differential equations, but further iterations will require numerical solutions. Let us stop here and see how good our answer is. In terms of intensity and phase we have

$$I_+(x,t) = I_{+0}\exp\left(2\,\Gamma'\,\mathrm{Im}(C)\,x\right) \tag{6}$$

$$\phi_+(x,t) = \Gamma'\,\mathrm{Re}(C)\,x \tag{7}$$

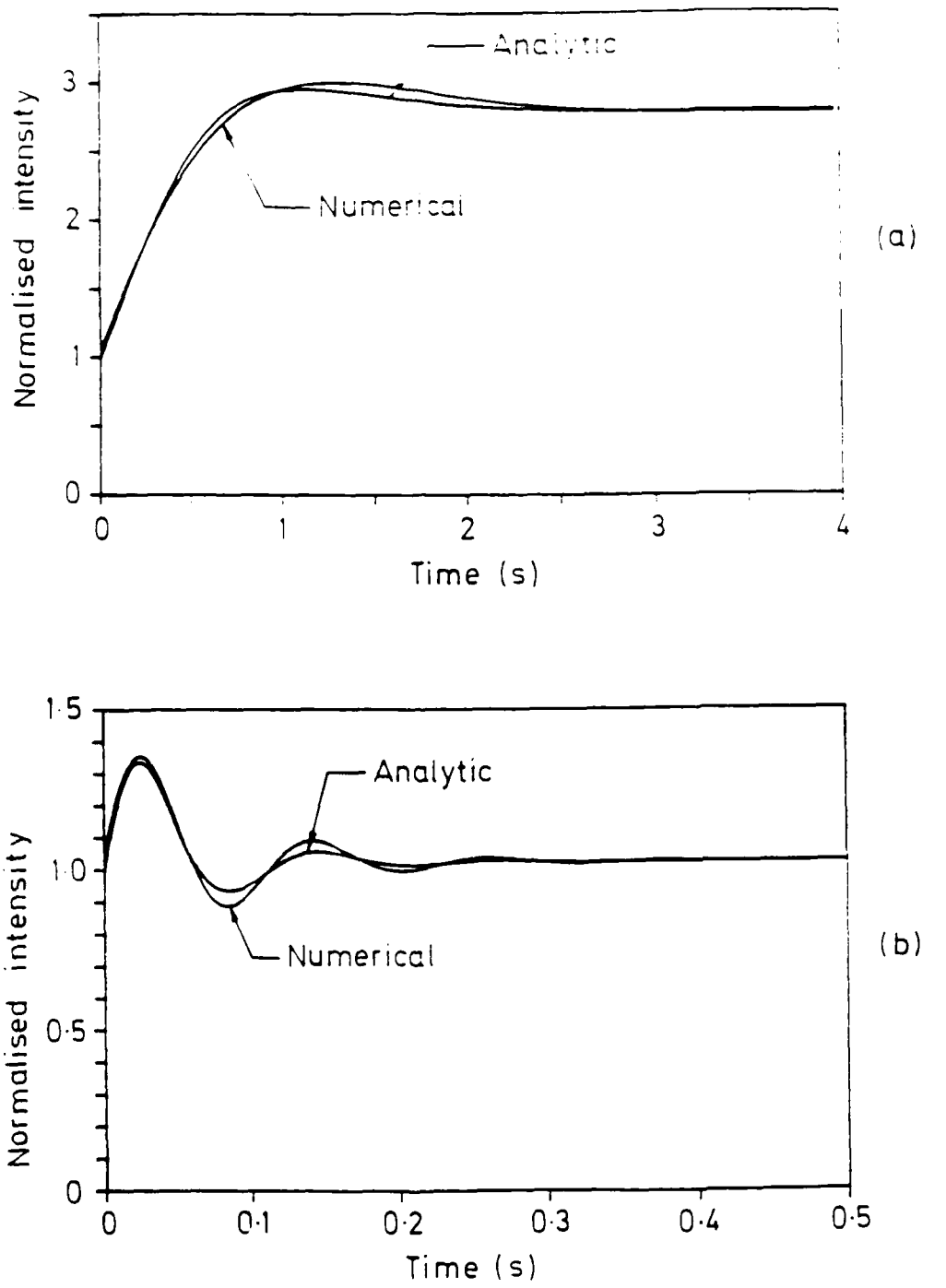

Figure 1: Normalised signal beam intensity vs time. Comparison of numerical and analytic solutions. (a) Interbeam angle = 10°, applied field = 10^6 V/m. (b) Interbeam angle = 4°, applied field = 2×10^5 V/m.

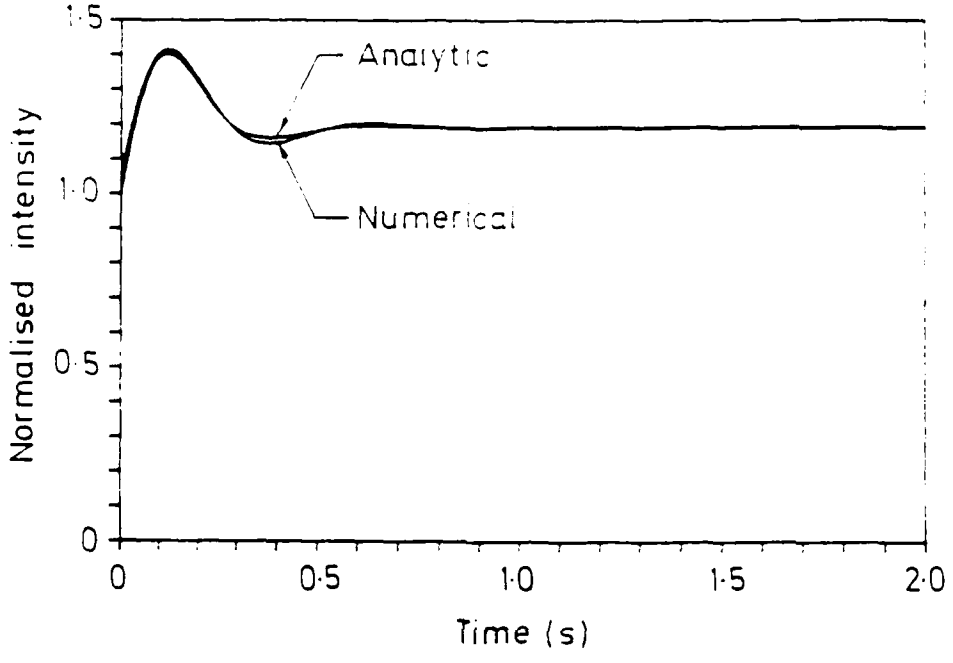

(c)

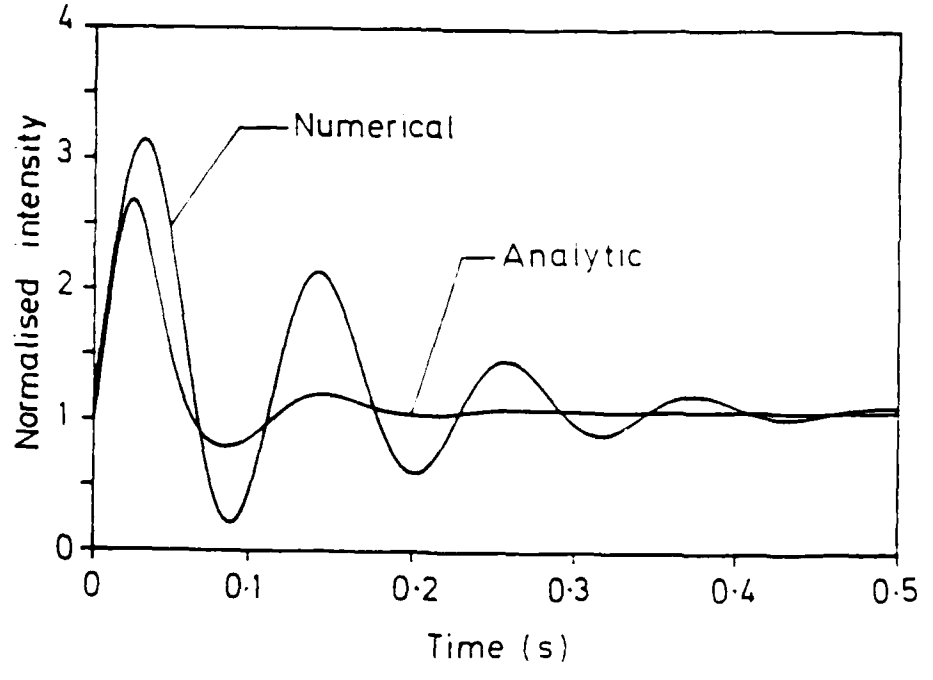

(d)

Figure 1: Normalised signal beam intensity vs time. Comparison of numerical and analytic solutions. (c) Interbeam angle = 0.5°, applied field = 2×10^5 V/m. (d) same as (c) with $r = 3.4 \times 10^{-12}$ m/V

Figs 1a-d show a comparison between the analytic and numerical methods for interbeam angles in $Bi_{12}SiO_{20}$ of 10°, 4°, and 0.5°. The crystal parameters are taken from Table 2.1 except that in Fig 1c, $\mu = 10^{-5}$ m^2/Vs, and for the first three plots $r = 10^{-12}$ m/V. In the last plot r is taken as 3.4 x 10^{-12} m/V. The crystal length is 1 cm, $I_0 = 100$ W/m^2, the wavelength is 514 nm, the crystal temperature is 300 K, and there is no frequency detuning between the beams. For the interbeam angle of 10° the applied field is 10^6 V/m and for the other plots, 2 x 10^5 V/m.

The agreement between the two methods is very good, regardless of the interbeam angle, for the case of weak coupling (small value of r or small interaction lengths). For strong coupling the two methods still agree for large angles ($> 8°$) but at smaller angles the oscillations for the analytic method are more damped.

The great savings is in computation time. Calculating and storing 220 time points using the analytic formula took less than 5 seconds on an IBM personal computer. The numerical method needed 20 minutes to compute the same number of points.

Finally we show that the analytic expression Eqn 4 is the same if we start the iteration with Eqn 1 and take one more iterative step. This fact substantiates the observation that Eqn 4 is a reasonable approximation to the transient behaviour calculated by a more thorough treatment.

The solution to Eqn 1 assuming E_{s1} constant is

$$S_+(x,t) = S_{+0}\exp(-j\Gamma' E_{s1}{}^* x) \tag{8}$$

If we put this into Eqn 2 and separate the variables we have

$$fS_{+0}\,t = \int_0^{E_{s1}(x,t)} \frac{dE_{s1}}{\exp(-BE_{s1}) - AE_{s1}} \tag{9}$$

where $A = g/fS_{+0}$ and $B = -j\Gamma' x$.

This integral cannot be solved analytically unless we can expand the exponential term in a series and ignore most higher orders. For a crystal of length 1 cm, an applied field of 10^6 V/m, assuming $E_{s1} \approx mE_{s0}$ where m is the modulation

ratio, and taking the crystal parameters of Table 2.1 we find $|BE_{s1}| \approx 4m$. Thus $|BE_{s1}| \ll 1$ for sufficiently small modulation ratios (which we assume is the case in the undepleted pump approximation). A similar check of crystal parameter values shows that $|B|/|A| \ll 1$.

Expanding the exponential to the first order term and integrating gives

$$E_{s1}(x,t) = \frac{1}{A+B}\left(1 - \exp(-fS_{+0}(A+B)t)\right) \tag{10}$$

We can neglect B with respect to A and we reproduce Eqn 3, and thus the rest of the derivation of Eqn 4 follows.

Appendix D

Publications and Talks Arising from this Research

Publications

1. D. Erbschloe, D. Jones, L. Solymar, J. Takacs, and T. Wilson, "Determination of Parameters of Photorefractive Crystals", *Proceedings on the International Conference on Holographic Systems, Components and Applications*, IERE, 1987, pp 163–167.

2. D. Erbschloe, L. Solymar, J. Takacs, and T. Wilson, "Nonreciprocal Effects in Photorefractive Materials", *Proceedings on the 14th Congress of the International Commission for Optics*, 1987, pp 501-502.

3. D. Erbschloe, L. Solymar, J. Takacs, and T. Wilson, "Two-Wave Mixing in Reflection Holograms in Photorefractive Materials, To be published in *IEEE Journal of Quantum Electronics*, May 1988.

4. D. Erbschloe and L. Solymar,"Linear Resonator in Photorefractive BSO with Two Pump Beams", to be published in *Electronics Letters*.

5. D. Erbschloe and L. Solymar, "Unidirectional Ring Resonator in Photorefractive BSO with Two Pump Beams", submitted to *Applied Physics Letters*.

6. D. Erbschloe, D. Jones, L. Solymar, J. Takacs, and T. Wilson, "Higher Diffracted Orders Produced During Two-Wave Mixing in a Unidirectional Ring Resonator", in preparation, to be published in *Journal of Physics, D*.

Talks

1. "Investigations in Photorefractive Crystals", seminar, presented to Physical Electronics Group, Department of Engineering Science, Oxford, Hilary term, 1987.

2. "Nonreciprocal Effects in Photorefractive Materials", with L. Solymar, J. Takacs, and T. Wilson, presented at the 14th Congress of the International Commission for Optics, Quebec, Canada, August 1987.

3. "Determination of Parameters of Photorefractive Crystals", with D. Jones, L. Solymar, J. Takacs, and T. Wilson, presented at the International Conference on Holographic Systems, Components and Applications, IERE, Cambridge University, September 1987.

4. "Holography: The View of the Future", an invited talk in support of the Horspath Village Church Tower Appeal, Horspath Village Manor House, March 1988.

5. "Higher Diffracted Orders Produced During Two-Wave Mixing in a Unidirectional Ring Resonator", with D. Jones, L. Solymar, J. Takacs, and T. Wilson, presented at Optics-ECOOSA '88, Birmingham, March 1988.

Bibliography

[1] *A New Dictionary on Historical Principles.* Volume II, Clarendon Press, Oxford, 1893.

[2] R. E. Aldrich, S. L. Hou, and M. L. Harvill. Electrical and optical properties of $Bi_{12}SiO_{20}$. *Journal of Applied Physics*, 42(1):493–494, 1971.

[3] J. J. Amodei. Electron diffusion effects during hologram recording in crystals. *Applied Physics Letters*, 18(1):22–24, 1971.

[4] Danny L. Anderson and Theodore E. Luke. Write-beam induced crystal damage in the conducting PRIZ. *Optics Communications*, 63(2):78–80, 1987.

[5] A. Ashkin, G. D. Boyd, J. M. Dziedzic, R. G. Smith, and A. A. Ballman. Optically-induced refractive index inhomogeneities in $LiNbO_3$ and $LiTaO_3$. *Applied Physics Letters*, 9(1):72–74, 1966.

[6] L. B. Au and L. Solymar. Amplification in photorefractive materials via a higher order wave. To be published in *Applied Physics B.*

[7] L. B. Au and L. Solymar. Higher diffracted orders in photorefractive materials. To be published in *IEEE Journal of Quantum Electronics.*

[8] L. B. Au and L. Solymar. The space charge field in photorefractive materials at large modulation. Unpublished.

[9] Erasmus Bartholinus. An account of sundry experiments made and communicated by that learn'd mathematician, Dr. Erasmus Bartholin, upon a chrystal-like body, sent to him out of Island. *Philosophical Transactions*, 67:2039–2048, 1671.

[10] A. C. Bishop. *An Outline of Crystal Morphology.* Hutchinson Scientific and Technical, London, 1967.

[11] Max Born and Emil Wolf. *Principles of Optics.* Pergamon Press, Oxford, 6th edition, 1980.

[12] W. H. Bragg and W. L. Bragg. *The Crystalline State.* G. Bell and Sons, Ltd., London, 1955.

[13] David Brewster. On the laws which regulate the absorption of polarised light by doubly refracting crystals. *Philosophical Transactions*, 11–31, 1819.

[14] V. V. Bryksin, L. I. Korovin, V. I. Marakhonov, and A. V. Khomenko. Initial stage in the redistribution of photoinduced charges and electric fields in $Bi_{12}SiO_{20}$. *Soviet Physics Solid State*, 24(10):1686–1689, 1982.

[15] V. V. Bryksin, L. I. Korovin, V. I. Marakhonov, and A. V. Khomenko. Role of electron injection in the formation of optical images in $Bi_{12}SiO_{20}$. *Soviet Technical Physics Letters*, 9(4):165–166, 1983.

[16] M. Carrascosa and F. Agullo-Lopez. Kinetics for optical erasure of sinusoidal holographic gratings in photorefractive materials. *IEEE Journal of Quantum Electronics*, 22(8):1369–1375, 1986.

[17] Chin-Lin Chen and A. Kumarswami. Nonreciprocal TM-mode thin-film phase shifters. *Applied Optics*, 25(20):3664–3670, 1986.

[18] F. S. Chen. A laser-induced inhomogeneity of refractive indices in KTN. *Physics Communications*, 3418–3420, 1968.

[19] F. S. Chen. Optically induced change of refractive indices in $LiNbO_3$ and $LiTaO_3$. *Journal of Applied Physics*, 40(4):3389–3396, 1969.

[20] F. S. Chen, J. T. LaMacchia, and D. B. Fraser. Holographic storage in lithium niobate. *Applied Physics Letters*, 13(7):223–225, 1968.

[21] A. E. T. Chiou and Pochi Yeh. Beam cleanup using photorefractive two-wave mixing. *Optics Letters*, 10(12):621–623, 1985.

[22] W. W. Chow, J. Gea-Banacloche, L. M. Pedrotti, V. E. Sanders, W. Schleich, and M. O. Scully. The ring laser gyro. *Reviews of Modern Physics*, 57(1):61–104, 1985.

[23] Robert E. Collin. *Foundations for Microwave Engineering.* McGraw-Hill Book Company, New York, 1966.

[24] Mark Cronin-Golomb, Baruch Fischer, Jeffrey O. White, and Amnon Yariv. Theory and applications of four-wave mixing in photorefractive media. *IEEE Journal of Quantum Electronics*, 20(1):12–29, 1984.

[25] Jean-Louis de Bourgrenet de la Tocnaye, Pierre Pellat-Finet, and Jean-Pierre Huignard. Effect of using a $Bi_{12}SiO_{20}$ light amplifier on the formation and competition of modes in optical resonators. *Journal of the Optical Society of America B*, 3(2):315–319, 1986.

[26] G. J. Dunning, E. Marom, Y. Owechko, and B. H. Soffer. All-optical associative memory with shift invariance and multiple image recall. *Optics Letters*, 12(9):346–348, 1987.

[27] R. W. Eason and A. M. C. Smout. Bistability and noncommutative behavior of mulitiple-beam self-pulsing and self-pumping in $BaTiO_3$. *Optics Letters*, 12(1):51–53, 1987.

[28] H. J. Eichler, P. Günter, and D. W. Pohl. *Laser-Induced Dynamic Gratings.* Springer-Verlag, Berlin, 1986.

[29] Hans J. Eichler. Introduction to the special issue on dynamic gratings and four-wave mixing. *IEEE Journal of Quantum Electronics*, 22(8):1194–1195, 1986.

[30] David Eimerl. Crystal symmetry and the electrooptic effect. *IEEE Journal of Quantum Electronics*, 23(12):2104–2115, 1987.

[31] D. Erbschloe, D. Jones, L. Solymar, J. Takacs, and T. Wilson. Determination of parameters of photorefractive crystals. In *International Conference on Holographic Systems, Components and Applications*, pages 163–167, IERE, 1987.

[32] R. C. Evans. *Crystal Chemistry.* Cambridge at the University Press, Cambridge, 2nd edition, 1964.

[33] Michael Faraday. On the magnetization of light and the illumination of magnetic lines of force. *Philosopical Magazine*, 19:294–317, 1845.

[34] Jack Feinberg. Asymmetric self-defocusing of an optical beam from the photorefractive effect. *Journal of the Optical Society of America*, 72(1):46–51, 1982.

[35] Jack Feinberg. Real-time edge enhancement using the photorefractive effect. *Optics Letters*, 5(8):330–332, 1980.

[36] Jack Feinberg, D. Heiman, A. R. Tanguay, and R. W. Hellwarth. Photorefractive effects and light-induced charge migration in barium titanate. *Journal of Applied Physics*, 51(3):1297–1305, 1980.

[37] Jack Feinberg and R. W. Hellwarth. Phase-conjugating mirror with continuous-wave gain. *Optics Letters*, 5(12):519–521, 1980.

[38] Baruch Fischer. Theory of self-frequency detuning of oscillations by wave mixing in photorefractive crystals. *Optics Letters*, 11(4):236–238, 1986.

[39] P. D. Foote and T. J. Hall. Influence of optical activity on two beam coupling constants in photorefractive $Bi_{12}SiO_{20}$. *Optics Communications*, 57(3):201–206, 1986.

[40] P. D. Foote, T. J. Hall, N. B. Aldridge, and A. G. Levenston. Photorefractive materials and their applications in optical image processing. *IEE Proceedings*, 133(1):83–90, 1986.

[41] A. M. Glass, D. von der Linde, and T. J. Negran. High-voltage bulk photovoltaic effect and the photorefractive process in $LiNbO_3$. *Applied Physics Letters*, 25(4):233–235, 1974.

[42] Joseph W. Goodman. *Introduction to Fourier Optics.* McGraw-Hill Book Company, San Francisco, 1968.

[43] R. Grousson, M. Henry, and S. Mallick. Transport properties of photoelectrons in $Bi_{12}SiO_{20}$. *Journal of Applied Physics*, 56(1):224–229, 1984.

[44] P. Günter. Holography, coherent light amplification and optical phase conjugation with photorefractive materials. *Physics Reports*, 93(4):199–299, 1982.

[45] P. Günter. Transient energy transfer between writing beams during hologram formation in $Bi_{12}GeO_{20}$. *Optics Communications*, 41(2):83–88, 1982.

[46] Hermann A. Haus, editor. *Waves and Fields in Optoelectronics*. Prentice-Hall, Inc., Englewood Cliffs, New Jersey, 1985.

[47] J. M. Heaton, P. A. Mills, E. G. S. Paige, L. Solymar, and T. Wilson. Diffraction efficiency and angular selectivity of volume phase holograms recorded in photorefractive materials. *Optica Acta*, 31(8):885–901, 1984.

[48] J. M. Heaton and L. Solymar. Transient energy transfer during hologram formation in photorefractive crystals. *Optica Acta*, 32(4):397–408, 1985.

[49] John M. Heaton. Wave interactions in static and dynamic volume holographic recording materials. D. Phil. thesis, University of Oxford, 1986.

[50] Eugene Hecht and Alfred Zajac. *Optics*. Addison-Wesley Publishing Co., Reading, Massachusetts, 1979.

[51] Robert Hooke. *Micrographia*. John Martyn, London, 1668.

[52] S. L. Hou, R. B. Lauer, and R. E. Aldrich. Transport processes of photoinduced carriers in $Bi_{12}SiO_{20}$. *Journal of Applied Physics*, 44(6):2652–2658, 1973.

[53] S. L. Hou and D. S. Oliver. Pockels readout optical memory using $Bi_{12}SiO_{20}$. *Applied Physics Letters*, 18(8):325–328, 1971.

[54] J. P. Huignard, J. P. Herriau, and T. Valentin. Time average holographic interferometry with photoconductive electrooptic $Bi_{12}SiO_{20}$ crystals. *Applied Optics*, 16(11):2796–2798, 1977.

[55] J. P. Huignard and B. Ledu. Collinear Bragg diffraction in photorefractive $Bi_{12}SiO_{20}$. *Optics Letters*, 7(7):310–312, 1982.

[56] J. P. Huignard and A. Marrakchi. Coherent signal beam amplification in two-wave mixing experiments with photorefractive $Bi_{12}SiO_{20}$ crystals. *Optics Communications*, 38(4):249–254, 1981.

[57] J. P. Huignard and A. Marrakchi. Two-wave mixing and energy transfer in $Bi_{12}SiO_{20}$ crystals: application to image amplification and vibration analysis. *Optics Letters*, 6(12):622–624, 1981.

[58] Y. H. Ja. Degenerate two-wave mixing in photorefractive crystals with multiple internal reflections. *Optics Communications*, 53(3):153–158, 1985.

[59] Y. H. Ja. Energy transfer between two beams in writing a reflection volume hologram in a dynamic medium. *Optical and Quantum Electronics*, 14:547–556, 1982.

[60] Y. H. Ja. Real-time image division in four-wave mixing with photorefractive $Bi_{12}GeO_{20}$ crystals. *Optics Communications*, 44(1):24–28, 1982.

[61] Y. H. Ja. Using the shooting method to solve boundary-value problems involving nonlinear coupled-wave equations. *Optical and Quantum Electronics*, 15:529–538, 1983.

[62] J. P. Jiang and Jack Feinberg. Dancing modes and frequency shifts in a phase conjugator. *Optics Letters*, 12(4):266–268, 1987.

[63] W. D. Johnston, Jr. Optical index damage in $LiNbO_3$ and other pyroelectric insulators. *Journal of Applied Physics*, 41(6):3279–3285, 1970.

[64] Jean-Michel C. Jonathan, Robert W. Hellwarth, and Gerald Roosen. Effect of applied electric field on the buildup and decay of photorefractive gratings. *IEEE Journal of Quantum Electronics*, 22(10):1936–1941, 1986.

[65] V. A. Kalinin and L. Solymar. Numerical solution of four-wave mixing in passive phase conjugate mirrors. To be published in *IEEE Journal of Quantum Electronics*.

[66] Hartmut Kallmann and Barnett Rosenberg. Persistent internal polarization. *Physical Review*, 97(6):1596–1610, 1955.

[67] Alexei A. Kamshilin, Jaime Frejlich, and Lucila Cescato. Photorefractive crystals for the stabilization of the holographic setup. *Applied Optics*, 25(14):2375–2381, 1986.

[68] John Kerr. Measurements and law in electro-optics. *Philosophical Magazine*, 9(55):157–174, 1880.

[69] Dae M. Kim, Rajiv R. Shah, T. A. Rabson, and F. K. Tittel. Nonlinear dynamic theory for photorefractive phase hologram formation. *Applied Physics Letters*, 28(6):338–340, 1976.

[70] M. B. Klein, G. J. Dunning, G. C. Valley, R. C. Lind, and T. R. O'Meara. Imaging threshold detector using a phase-conjugate resonator in $BaTiO_3$. *Optics Letters*, 11(9):575–577, 1986.

[71] M. B. Klein and R. N. Schwartz. Photorefractive effect in $BaTiO_3$: microscopic origins. *Journal of the Optical Society of America B*, 3(2):293–305, 1986.

[72] E. Krätzig and H. Kurz. Photo-induced currents and voltages in $LiNbO_3$. *Ferroelectrics*, 13:295–296, 1976.

[73] E. Krätzig and R. Orlowski. Light induced charge transport in doped $LiNbO_3$ and $LiTaO_3$. *Ferroelectrics*, 27:241–244, 1980.

[74] N. V. Kukhtarev, G. E. Dovgalenko, and V. N. Starkov. Influence of the optical activity on hologram formation in photorefractive crystals. *Applied Physics A*, 33:227–230, 1984.

[75] N. V. Kukhtarev, V. B. Markov, and S. G. Odulov. Transient energy transfer during hologram formation in $LiNbO_3$ in external electric field. *Optics Communications*, 23(3):338–343, 1977.

[76] N. V. Kukhtarev, V. B. Markov, S. G. Odulov, M. S. Soskin, and V. L. Vinetskii. Holographic storage in electrooptic crystals. II. Beam coupling-light amplification. *Ferroelectrics*, 22:961–964, 1979.

[77] N. V. Kukhtarev, V. B. Markov, S. G. Odulov, M. S. Soskin, and V. L. Vinetskii. Holographic storage in electrooptic crystals. I. Steady state. *Ferroelectrics*, 22:949–960, 1979.

[78] Jayant Kumar, Giovanni Albanese, and William H. Steier. Photorefractive two-beam coupling with applied radio-frequency fields: theory and experiment. *Journal of the Optical Society of America B*, 4(7):1079–1082, 1987.

[79] Sze-Keung Kwong, Mark Cronin-Golomb, and Amnon Yariv. Oscillation with photorefractive gain. *IEEE Journal of Quantum Electronics*, 22(8):1508–1523, 1986.

[80] Sze-Keung Kwong, George A. Rakuljic, and Amnon Yariv. Real time image subtraction and exclusive or operation using a self-pumped phase conjugate mirror. *Applied Physics Letters*, 48(3):201–203, 1986.

[81] Ph. Lalanne, J. Taboury, and P. Chavel. A proposed generalization of Hopfield's algorithm. *Optics Communications*, 63(1):21–25, 1987.

[82] P. Francisco Lana. Reflections upon an observation of Signor M. Antonio Castagna, superintendent of some mines in Italy, concerning the formation of crystals. *Philosophical Transactions*, 83:4068–4069, 1672.

[83] G. Lesaux, J. C. Launay, and A. Brun. Transient photocurrent induced by nanosecond light pulses in BSO and BGO. *Optics Communications*, 57(3):166–170, 1986.

[84] S. G. Lipson and P. Nisenson. Imaging characteristics of the Itek PROM. *Applied Optics*, 13(9):2052–2060, 1974.

[85] Kenneth R. MacDonald and Jack Feinberg. Theory of a self-pumped phase conjugator with two coupled interaction regions. *Journal of the Optical Society of America*, 73(5):548–553, 1983.

[86] Kenneth R. MacDonald, Jack Feinberg, Ming Zheng Zha, and Peter Günter. Asymmetric transmission through a photorefractive crystal of barium titanate. *Optics Communications*, 50(3):146–150, 1984.

[87] R. Magnusson and T. K. Gaylord. Use of dynamic theory to describe experimental results from volume holography. *Journal of Applied Physics*, 47(1):190–199, 1976.

[88] R. Magnusson, J. H. Mitchell, T. D. Black, and D. R. Wilson. Holographic interferometry using iron-doped lithium niobate. *Applied Physics Letters*, 51(2):81–82, 1987.

[89] S. Mallick, B. Imbert, H. Ducollet, J.P. Herriau, and J. P. Huignard. Generation of spatial subharmonics by two-wave mixing in a nonlinear photorefractive medium. To be published in *Applied Physics Letters*.

[90] A. Marrakchi, J. P. Huignard, and P. Günter. Diffraction efficiency and energy transfer in two-wave mixing experiments with $Bi_{12}SiO_{20}$ crystals. *Applied Physics*, 24:131–138, 1981.

[91] Peter A. Mills. Volume holographic infra-red filters in iron-doped lithium niobate. D. Phil. thesis, University of Oxford, 1985.

[92] Tetsuya Mizumoto and Yoshiyuki Naito. Nonreciprocal propagation characteristics of YIG thin film. *IEEE Transactions on Microwave Theory and Techniques*, MTT-30(6):922–925, 1982.

[93] M. G. Moharam and L. Young. Hologram writing by the photorefractive effect. *Journal of Applied Physics*, 48(8):3230–3236, 1977.

[94] R. A. Mullen and R. W. Hellwarth. Optical measurement of the photorefractive parameters of BSO. *Journal of Applied Physics*, 58(1):40–44, 1985.

[95] Yuichi Ninomiya. Recording characteristics of volume holograms. *Journal of the Optical Society of America*, 63(9):1124–1130, 1973.

[96] R. Oberschmid. Conductivity instabilities and polarization effects of $Bi_{12}(Ge,Si)O_{20}$ single-crystal samples. *Physica A*, 43(1):657–671, 1986.

[97] Ellen Ochoa, F. Vachss, and Lambertus Hesselink. Higher-order analysis of the photorefractive effect for large modulation depths. *Journal of the Optical Society of America A*, 3(2):181–187, 1986.

[98] Yasuyuki Okamura, Takayuki Negami, and Sadihiko Yamamoto. Integrated optical isolator and circulator using nonreciprocal phase shifters: a proposal. *Applied Optics*, 23(11):1886–1889, 1984.

[99] T. R. O'Meara. Compensation of laser amplifier trains with nonlinear conjugation techniques. *Optical Engineering*, 21(2):243–251, 1982.

[100] R. Orlowski and E. Krätzig. Holographic method for the determination of photo-induced electron and hole transport in electro-optic crystals. *Solid State Communications*, 27:1351–1354, 1978.

[101] J. R. Partington. *A History of Chemistry*. Volume II, MacMillan and Co., Ltd., London, 1962.

[102] Gilles Pauliat, Michel Allain, Jean-Claude Launay, and Gerald Roosen. Optical evidence of a photorefractive effect due to holes in $Bi_{12}GeO_{20}$ crystals. *Optics Communications*, 61(2):321–324, 1987.

[103] M. A. Powell and C. R. Petts. Temperature enhancement of the photorefractive sensitivity of BSO and BGO. *Optics Letters*, 11(1):36–38, 1986.

[104] William H. Press, Brian P. Flannery, Saul A. Teukolsky, and William T. Vetterling. *Numerical Recipes*. Cambridge University Press, Cambridge, 1986.

[105] H. Rajbenbach and J. P. Huignard. Self-induced coherent oscillations with photorefractive $Bi_{12}SiO_{20}$ amplifier. *Optics Letters*, 10(3):137–139, 1985.

[106] H. Rajbenbach, J. P. Huignard, and B. Loiseaux. Spatial frequency dependence of the energy transfer in two-wave mixing experiments with BSO crystals. *Optics Communications*, 48(4):247–251, 1983.

[107] H. Rajbenbach, J. P. Huignard, and P. Refregier. Amplified phase-conjugate beam reflection by four-wave mixing with photorefractive $Bi_{12}SiO_{20}$ crystals. *Optics Letters*, 9(12):558–560, 1984.

[108] D. Rak, I. Ledoux, and J. P. Huignard. Two-wave mixing and energy transfer in $BaTiO_3$ application to laser beamsteering. *Optics Communications*, 49(4):302–306, 1984.

[109] P. Refregier, L. Solymar, H. Rajbenbach, and J.P. Huignard. Two-beam coupling in photorefractive $Bi_{12}SiO_{20}$ crystals with moving grating: theory and experiments. *Journal of Applied Physics*, 58(1):45–57, 1985.

[110] K. H. Ringhofer and L. Solymar. A new gain mechanism for wave amplification in photorefractive materials. To be published in *Applied Physics Letters*.

[111] Juan Rodriguez, Azad Siahmakoun, and Gregory Salamo. Bistability and optical switching in a total internal reflection phase conjugator. *Applied Optics*, 26(11):2263–2265, 1987.

[112] Koichi Sayano, George A. Rakuljic, and Amnon Yariv. Thresholding semilinear phase-conjugate mirror. *Optics Letters*, 13(2):143–145, 1988.

[113] K. K. Shvarts. Relationship between the photorefractive and electrooptic effects in lithium niobate crystals. *Izvestiya Akademii Nauk SSSR*, 41(4):788–791, 1977.

[114] Arthur L. Smirl, George C. Valley, Ruth Ann Mullen, K. Bohnert, and C. D. Mire. Picosecond photorefractive effect in $BaTiO_3$. *Optics Letters*, 12(7):501–503, 1987.

[115] L. Solymar and D. J. Cooke. *Volume Holography and Volume Gratings*. Academic Press, London, 1981.

[116] L. Solymar and J. M. Heaton. Transient energy transfer in photorefractive materials; an analytic solution. *Optics Communications*, 51(2):76–78, 1984.

[117] L. Solymar and D. Walsh. *Lectures on the Electrical Properties of Materials*. Oxford University Press, Oxford, 3rd edition, 1985.

[118] L. Solymar and T. Wilson. Controllable nonreciprocal optical phase shifter. *Electronics Letters*, 21(6):234–235, 1985.

[119] D. L. Staebler and J. J. Amodei. Coupled-wave analysis of holographic storage in $LiNbO_3$. *Journal of Applied Physics*, 43(3):1042–1049, 1972.

[120] D. L. Staebler, W. J. Burke, W. Phillips, and J. J. Amodei. Multiple storage and erasure of fixed holograms in Fe-doped $LiNbO_3$. *Applied Physics Letters*, 26(4):182–184, 1975.

[121] S. I. Stepanov, V. V. Kulikov, and M. P. Petrov. Running holograms in photorefractive $Bi_{12}SiO_{20}$ crystals. *Optics Communications*, 44(1):19–23, 1982.

[122] S. I. Stepanov and M. P. Petrov. Efficient unstationary holographic recording in photorefractive crystals under an external alternating electric field. *Optics Communications*, 53(5):292–295, 1985.

[123] F. P. Strohkendl, J. M. C. Jonathan, and R. W. Hellwarth. Hole-electron competition in photorefractive gratings. *Optics Letters*, 11(5):312–314, 1986.

[124] S. M. Sze. *Physics of Semiconductor Devices*. Wiley-Interscience, New York, 1969.

[125] R. L. Townsend and J. T. LaMacchia. Optically induced refractive index changes in $BaTiO_3$. *Journal of Applied Physics*, 41(13):5188–5192, 1976.

[126] Theo Tschudi, Andreas Herden, Joachim Goltz, Harald Klumb, and Franco Laeri. Image amplification by two- and four-wave mixing in $BaTiO_3$ photorefractive crystals. *IEEE Journal of Quantum Electronics*, 22(8):1493–1502, 1986.

[127] David W. Vahey. A nonlinear coupled-wave theory of holographic storage in ferroelectric materials. *Journal of Applied Physics*, 46(8):3510–3515, 1975.

[128] George Valley. Simultaneous electron/hole transport in photorefractive materials. *Journal of Applied Physics*, 59(10):3363–3366, 1986.

[129] George C. Valley. Two-wave mixing with an applied field and a moving grating. *Journal of the Optical Society of America B*, 1(6):868–873, 1984.

[130] George C. Valley and Marvin B. Klein. Optimal properties of photorefractive materials for optical data processing. *Optical Engineering*, 22(6):704–711, 1983.

[131] Jeffrey O. White, Mark Cronin-Golomb, Baruch Fischer, and Amnon Yariv. Coherent oscillation by self-induced gratings in the photorefractive crystal $BaTiO_3$. *Applied Physics Letters*, 40(6):450–452, 1982.

[132] N. J. Wooder and J. C. Dainty. Real time intensity inversion by four wave mixing in bismuth silicon oxide. *Optics Communications*, 63(2):85–88, 1987.

[133] Amnon Yariv. *Optical Electronics*. Holt, Rinehart and Winston, New York, 3rd edition, 1985.

[134] Amnon Yariv, Sze-Keung Kwong, and Kazuo Kyuma. Demonstration of an all-optical associative holographic memory. *Applied Physics Letters*, 48(17):1114–1116, 1986.

[135] Amnon Yariv and Pochi Yeh. *Optical Waves in Crystals*. John Wiley & Sons, New York, 1984.

[136] Pochi Yeh. Contra-directional two-wave mixing in photorefractive media. *Optics Communications*, 45(5):323–326, 1983.

[137] Pochi Yeh. Electromagnetic propagation in photorefractive layered medium. *Journal of the Optical Society of America*, 73(10):1268–1271, 1983.

[138] Pochi Yeh. Fundamental limit of the speed of photorefractive effect and its impact on device applications and material research: author's reply to comment. *Applied Optics*, 26(16):3190–3191, 1987.

[139] Pochi Yeh. Photorefractive coupling in ring resonators. *Applied Optics*, 23(17):2974–2978, 1984.

[140] M. Z. Zha and P. Günter. Nonreciprocal optical transmission through photorefractive $KNbO_3$:Mn. *Optics Letters*, 10(4):184–186, 1985.